VHE and Multi-Wavelength Data Analysis of HESS J1741−302

DISSERTATION

zur Erlangung des akademischen Grades

doctor rerum naturalium
(Dr. rer. nat.)

im Fach Physik

Spezialisierung:
Experimentalphysik

eingereicht an der
Mathematisch-Naturwissenschaftlichen Fakultät
der Humboldt-Universität zu Berlin

von

M.Sc. Ekrem Oğuzhan Angüner

Präsident der Humboldt-Universität zu Berlin:

Prof. Dr. Jan-Hendrik Olbertz

Dekan der Mathematisch-Naturwissenschaftlichen Fakultät:

Prof. Dr. Elmar Kulke

Gutachter:
1. Prof. Dr. Thomas Lohse
2. Prof. Dr. Stefan Funk
3. Prof. Dr. Elisa Bernardini

Eingereicht am: 20. Oktober 2015
Tag der Verteidigung: 13. April 2016

I dedicate this thesis to
my mother Fatma Bilge Gürdal,
my aunt Hidayet Ege Sunal
and my friend Rabia Gökçe Aydal.

Acknowledgements

First and foremost, I would like to express my gratitude to my supervisor Thomas Lohse for accepting me as a member of the Berlin H.E.S.S. group, which gave me the opportunity to do research on this very interesting field in such a fantastic scientific group, and also for supporting me financially. A very special thanks to Ullrich Schwanke for the supervision of the work presented in this thesis, lots of useful advice and scientific discussions during entire my Ph.D..

A very special thanks goes to Igor Oya Vallejo for teaching me the concepts of VHE astrophysics, supervising my data analysis presented in this thesis and also for his close friendship during my Ph.D.. I would also like to express my gratitude to Sabrina Casanova and Johan van der Walt for our joint work on HESS J1741−302 and for their support.

I would like to thank all of the members of the H.U. Berlin group; Emrah Birsin, Matthias Füssling, Michael Gajdus, Michael Mayer, Thomas Murach, Louise Oakes, Gerrit Spengler, Iurii Sushch, Philipp Wagner, for a great and friendly atmosphere. Special thanks goes to Manuel Paz Arribas for helping me in VHE data analysis and Matthieu Kieffer for the cross-check of the VHE data analysis presented in this thesis. Extra thanks to Veronika Schneider for helping me with all the complicated bureaucratic procedures.

I acknowledge those H.E.S.S. collaboration colleagues that helped me during my Ph.D.. Particularly, I would like to thank Felix Aharonian, Pol Bordas, Ryan Chaves, Ignasi Reichardt and Victor Zabalza.

I also want to acknowledge my cat Pıtış, who died at the time I moved to Berlin, for the nice and funny moments that she has given me during her 15 years of life.

Of course, I want to thank my mother Fatma Bilge Gürdal and my aunt Hidayet Ege Sunal because of their endless love, support and trust in me during my whole life. I also thank my friend Rabia Gökçe Aydal for her support and care throughout my Ph.D..

Abstract

HESS J1741−302 is an unidentified very-high-energy (VHE) γ-ray source located in the Galactic Plane at about 1.7° away from the Galactic Center. It is one of the faintest TeV objects detected so far, with a flux $\Phi(>1\ \mathrm{TeV}) = (1.65 \pm 0.28_{\mathrm{stat}} \pm 0.33_{\mathrm{sys}}) \times 10^{-13}\ \mathrm{cm}^{-2}\ \mathrm{s}^{-1}$ corresponding to ∼1% of the Crab Nebula flux at the same energies. The data analysis of an updated high-quality dataset of ∼145 hours of VHE H.E.S.S. data taken between 2004 and 2013 has revealed the morphology of HESS J1741−302. The γ-ray spectrum of HESS J1741−302 extends beyond 10 TeV without showing any clear evidence of a cut-off. The source spectrum is well described by a power-law model with a spectral index of $\Gamma = 2.28 \pm 0.16_{\mathrm{stat}} \pm 0.20_{\mathrm{sys}}$ and a normalization at 1 TeV of $\Phi_0 = (2.12 \pm 0.42_{\mathrm{stat}} \pm 0.42_{\mathrm{sys}}) \times 10^{-13}\ \mathrm{cm}^{-2}\ \mathrm{s}^{-1}\ \mathrm{TeV}^{-1}$. Different scenarios will be considered in this thesis, including the interaction of cosmic-ray protons with molecular clouds found along the line of sight, inverse Compton scattering of infra-red photons provided by a nearby OH/IR star and the presence of a nearby pulsar wind nebula possibly related to PSR B1737−30, in order to explain the observed VHE gamma-ray emission.

Zusammenfassung

HESS J1741−302 ist eine nicht identifizierte Quelle sehr hochenergetischer Gammastrahlen, welche circa 1,7 Grad vom Zentrum der Milchstraße entfernt liegt. Diese Quelle ist eines der schwächsten Objekte im TeV-Bereich mit einem Photonfluss von $\Phi(>1\ \mathrm{TeV}) = (1.65 \pm 0.28_{\mathrm{stat}} \pm 0.33_{\mathrm{sys}}) \times 10^{-13}\ \mathrm{cm}^{-2}\ \mathrm{s}^{-1}$, was ∼1% des Krebsnebelflusses im gleichen Energiebereich entspricht. Die Analyse des aktuellen H.E.S.S. Datensatzes von 145 Stunden Beobachtungen mit hoher Qualität gibt Einblicke in die Morphologie von HESS J1741−302. Das Energiespektrum von HESS J1741−302 geht über 10 TeV hinaus, ohne dabei ein klares Anzeichen für einen spektralen Abbruch zu zeigen. Das Spektrum kann durch ein Potenzgesetz mit einem spektralen Index von $\Gamma = 2.28 \pm 0.16_{\mathrm{stat}} \pm 0.20_{\mathrm{sys}}$ und einer Normierung bei 1 TeV von $\Phi_0 = (2.12 \pm 0.42_{\mathrm{stat}} \pm 0.42_{\mathrm{sys}}) \times 10^{-13}\ \mathrm{cm}^{-2}\ \mathrm{s}^{-1}\ \mathrm{TeV}^{-1}$ beschrieben werden. In der vorliegenden Arbeit werden verschiedene Szenarien für die beobachtete Gammastrahlung und deren Entstehung in Betracht gezogen. Diese beinhalten die Wechselwirkung von Protonen der kosmischen Strahlung mit Molekülwolken entlang der Sichtlinie, IC Streuung an Infrarot-Photonen eines nahe gelegenen OH/IR Sterns und die Präsenz eines Pulsarwindnebels, welcher möglicherweise zu PSR B1737−30 gehrt.

Contents

Chapter 1

Introduction

Astronomy, which can be considered as the oldest natural science, had begun with the observations of the visible light from celestial objects by human eye. In the ancient times, people were observing the motion of celestial objects and trying to connect these motions with social phenomena and also with personal characteristics depending on the time of birth. It took thousand of years for human kind to explore that there is much more beyond what human eye can see. Consequently, astronomical observations could extend into other energy bands of the electromagnetic spectrum. It was also understood that different wavelengths of the electromagnetic radiation can penetrate the Earth's atmosphere to various depths as can be seen in Fig. 1.1. Fortunately for human kind, all of high energy X-ray and most ultra-violet (UV) wavelengths, which are quite dangerous for the life on the Earth, are filtered out long before they reach to the ground level. On the other hand, most of radio waves can make their way to the ground, along with a narrow window of infra-red, UV and optical radiation. This is basically why the radio astronomy started first after the optical astronomy.

Currently, with the modern instrumentation, astronomers can conduct observations of the cosmos in a wide spectrum from radio to γ-ray frequencies. Figure 1.2 shows how the Milky Way galaxy looks like in different wavelengths. The observed emission in different wavelengths can give crucial information about the cosmos and its evolution, which is probably one of the oldest and the fundamental philosophical questions asked. In the old times, it was believed that the Earth was located in the center of the universe and everything was orbiting around it. But thanks to modern radio astronomy and developed mathematical methods, by using the radio observations and the kinematic distance ambiguity (KDA) method (explained in detail later), astronomers can make the map of the Milky Way galaxy. Figure 1.3 shows a schematic view of the Milky Way galaxy, the observed spiral arms, the location of our solar system also by giving the relative distances, the orbit of the Sun around the Galactic Center and the Earth's orbit around the Sun. In the last two decades, very high energy (VHE) γ-ray astronomy, which utilizes ground-based Cherenkov detectors, has contributed substantially to our understanding of highly energetic processes of the non-thermal universe. A firm detection of TeV photons from a number of galactic and extragalactic sources has enabled detailed studies of intrinsic features of various astrophysical objects which give rise to the observed VHE γ-ray emission.

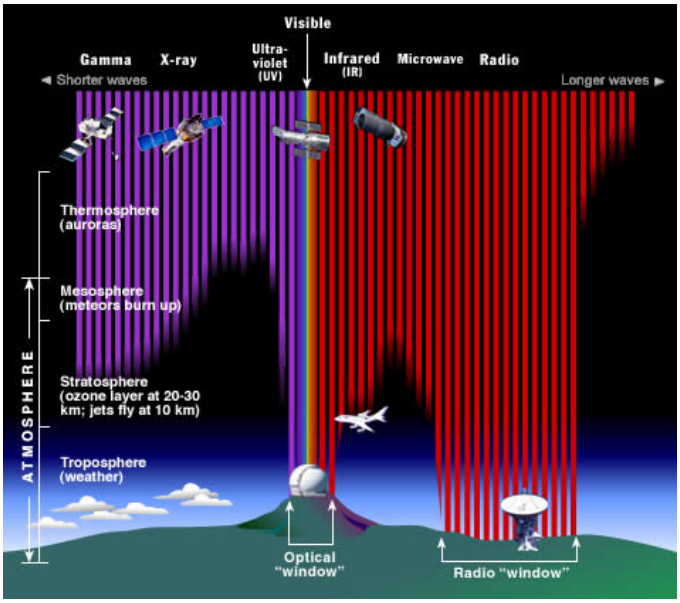

Figure 1.1: Illustration of various wavelengths of electromagnetic radiation penetrating the Earth's atmosphere. Credit: Image courtesy STCI/JHU/NASA.

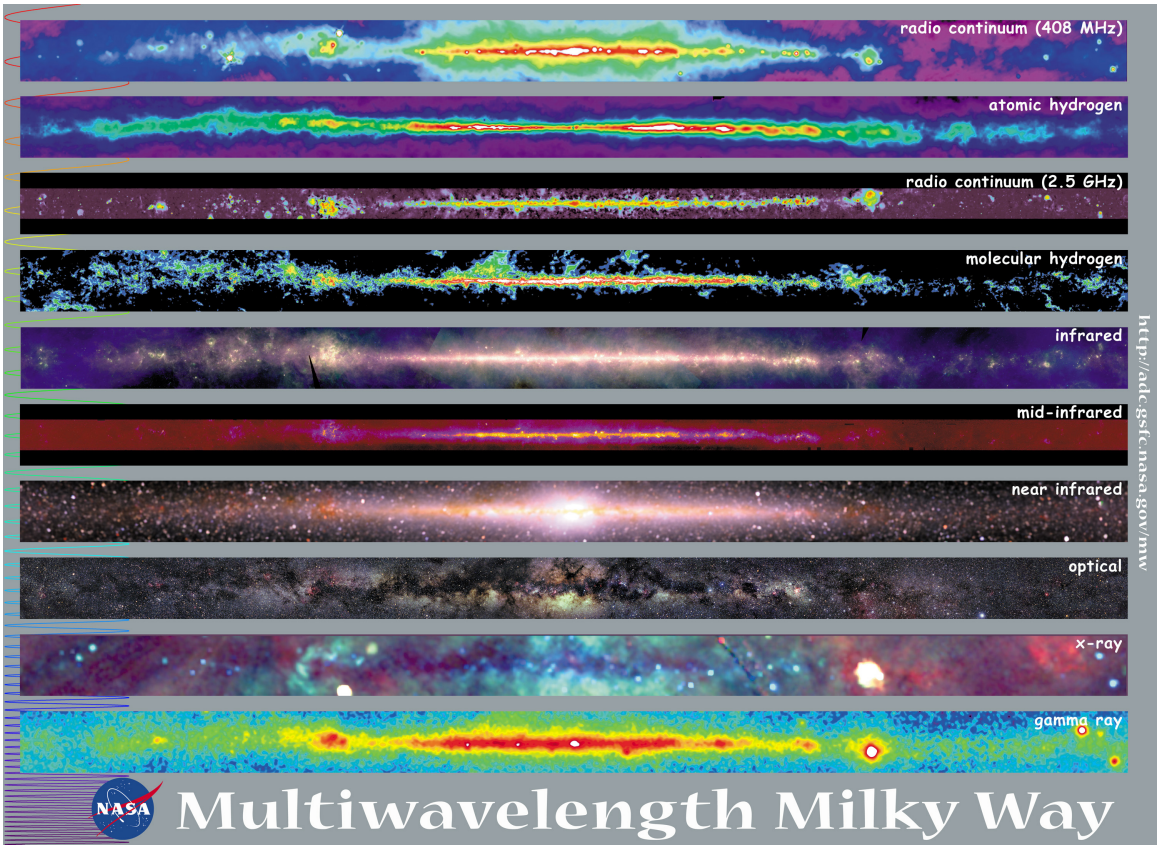

Figure 1.2: Multi-wavelength view of the Milky Way Galaxy. An image showing the Milky Way at 10 different wavelengths. The image was taken from NASA.

Research results described in this thesis are associated with the multi-wavelength observations of the unidentified VHE γ-ray source HESS J1741−302. In particular, the determination of the morphology and the (VHE) γ-ray spectrum of this object from the stereoscopic data taken with imaging atmospheric Cherenkov telescopes (IACT) of the High Energy Stereoscopic System (H.E.S.S.). Further data analysis of molecular clouds and the X-ray data analysis of the region around HESS J1741−302 were also performed to be able to understand the origin of VHE γ-ray emission from the direction of HESS J1741−302. The author of this thesis has worked in the software development for the future Cherenkov Telescope Array (CTA) project. The details of the work are given in an appendix.

This thesis is structured as follows:

- Chapter 2 is an introduction to the field of VHE γ-ray astronomy, including the description of the most relevant processes in γ-ray astronomy. Cosmic-rays are discussed in this chapter along with inverse Compton scattering and proton-proton interaction processes.

- Chapter 3 describes basic properties of interstellar molecules and molecular clouds, basic principles of molecular clouds data analysis and related methods for distance approximation. VHE γ-ray emission from molecular clouds is also discussed in this chapter.

- Chapter 4 gives brief information about IACTs including the detection techniques. A detailed description of the main characteristics and components of the H.E.S.S experiment and basic concepts of the Cherenkov Telescope Array project are also presented in this chapter.

- Chapter 5 reports on the detailed results of multi-wavelength data analysis performed on the unidentified VHE γ-ray source HESS J1741−302. This chapter concentrates on the H.E.S.S. VHE data analysis. The details of molecular cloud data analysis is given in this chapter along with X-ray data analysis results from the region around HESS J1741−302.

- Chapter 6 combines the multi-wavelength data analysis results and gives the conclusion about the origin of the observed VHE γ-ray emission from the direction of HESS J1741−302. Leptonic scenarios including the pulsar PSR B1737−30, modeling of the IC emission taking into account the OH/IR star OH 358.23+0.11 and hadronic scenarios including the molecular clouds found along the line of sight of HESS J1741−302 are discussed in this chapter.

- Appendix A gives brief information about the motivation and the structure of the medium-sized telescope (MST) prototype installed in Berlin-Adlershof.

- Appendix B reports on the software development work done by the author of this thesis in the software development group for the MST prototype.

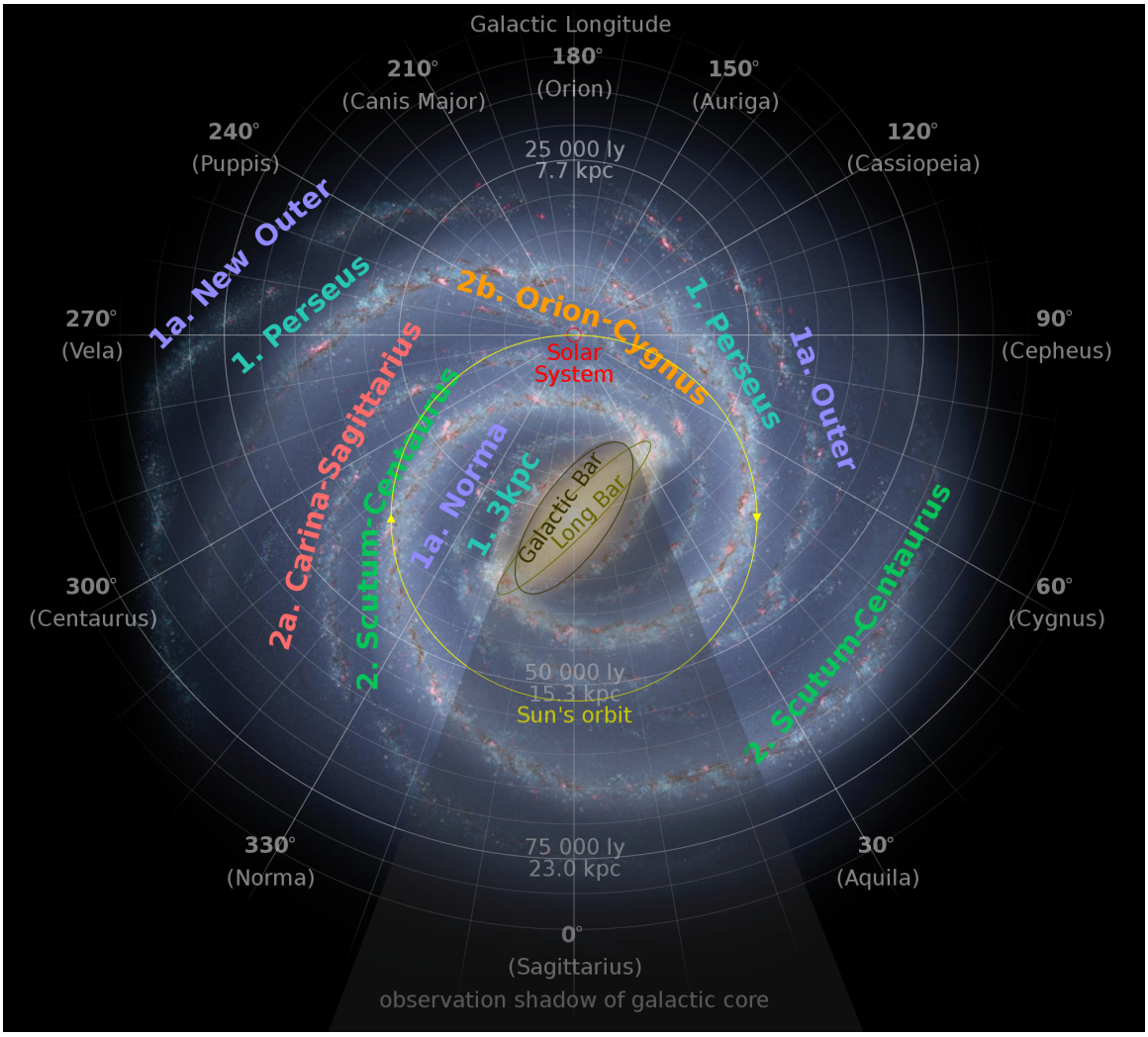

Figure 1.3: Schematic view of the Milky Way galaxy, location of the solar system and spiral arms in the Milky Way galaxy. The yellow circle shows the Sun's orbit around the Galactic Center while the red circle shows the orbit or the Earth around the Sun. The image was taken from NASA/JPL-Caltech R.Hurt (http://www.spitzer.caltech.edu/images/1923-ssc2008-10a-A-Roadmap-to-the-Milky-Way)

Chapter 2

VHE Gamma-Ray Astronomy

2.1 Introduction

The history of γ-ray astronomy is relatively young when compared to the other branches of astronomy. Both satellite and ground-based observation techniques have been developed in the second half of the 20th century. From the astrophysical point of view, the field of γ-ray astronomy above several MeV can be considered as the study of non-thermal universe, meaning that the radiation having energies above several MeV can not be blackbody radiation from hot objects. Observational γ-ray astronomy is conventionally divided into six energy ranges as summarized in Table. 2.1 .

Energy Range (MeV)	Classification	Detection Methods
$E < 10.0$	Low Energy (LE)	Balloons, Satellites
$10.0 < E < 30.0$	Medium Energy (ME)	Space Based Satellites
$30.0 < E < 30{\times}10^3$	High Energy (HE)	Space Based Satellites
$30{\times}10^3 < E < 30{\times}10^6$	Very High Energy (VHE)	Ground Based
$30{\times}10^6 < E < 30{\times}10^9$	Ultra High Energy (UHE)	Ground Based
$E > 30{\times}10^9$	Extremely High Energy (EHE)	Ground Based

Table 2.1: Nomenclature of cosmic-rays and γ-ray astronomy showing the classification and corresponding detection methods for the given energy ranges.

Astronomical observations can be done by using detectors on satellites or balloons for the low and the middle energy ranges. The sensitivity of these airborne detectors beyond 10 GeV is limited due to low statistics because of their relatively small collection areas and the low γ-ray flux from astrophysical objects. In order to explore the universe at higher energies, it is mandatory to use ground-based detectors, which have collection areas orders magnitude larger than satellite or balloon experiments.

The astronomical objects that are studied in VHE γ-ray astronomy can be summarized as Supernova Remnants (SNR), Pulsars, Pulsar Wind Nebula (PWN), Active Galactic

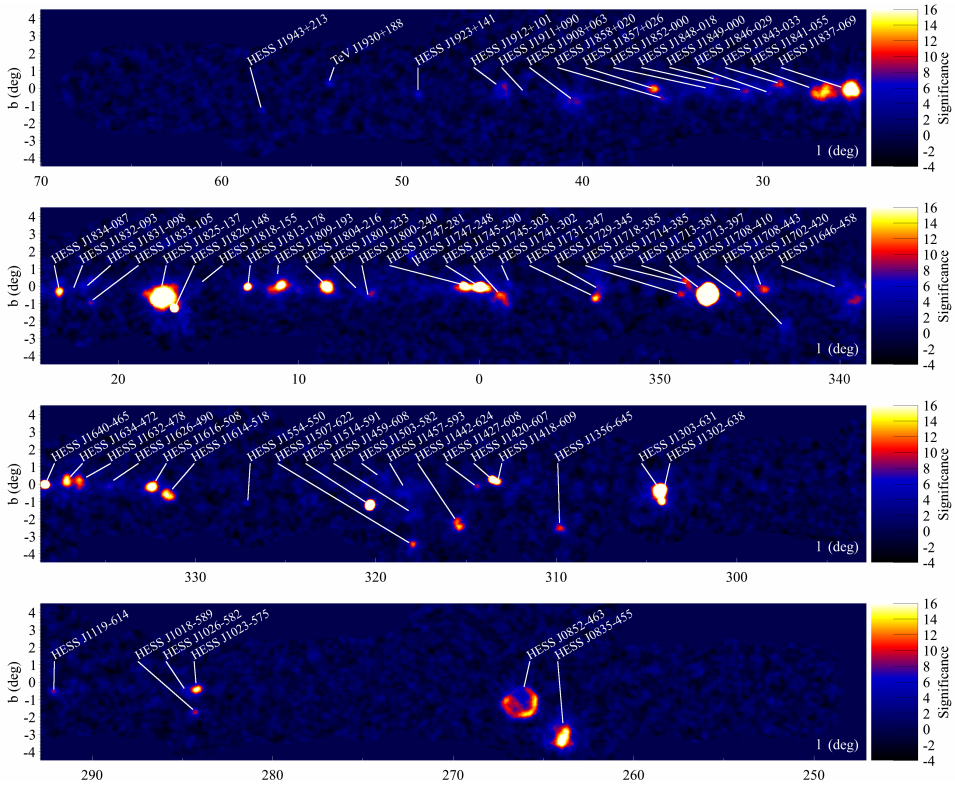

Figure 2.1: Significance map for the H.E.S.S. Galactic Plane Survey. The pre-trials significance for a correlation radius of 0.1 deg is shown. The color transition from blue to red corresponds to $\sim 5\sigma$ post-trials significance. The significance has been calculated for regions on the sky where the sensitivity of H.E.S.S. for point sources (5σ pre-trials, and assuming the spectral shape of a power law with index 2.3) is better than 10% Crab. Identifiers for sources are also included. Credit: [Carrigan et al. (2013)]

Nuclei (AGN), Galaxy Clusters, Starburst Galaxies, γ-Ray Bursts (GRB), unidentified sources from other experiments on satellites like the EGRET on CGRO and the LAT on Fermi, other sources of interest for cosmological and fundamental physics. The current distribution of known VHE sources in the plane of the Milky Way obtained by the H.E.S.S. Galactic Plane Survey (GPS) [Carrigan et al. (2013)] can be seen in Fig. 2.1.

In VHE γ-ray astronomy, the interpretation of the observed γ-ray spectra, the morphology analysis of observed sources and the identification of the involved radiation mechanisms require not only high quality observational data, but also good knowledge of the contributing production mechanisms. Basically, in the HE and VHE regime (sub-GeV to multi TeV energies), there are two dominant processes for γ-ray production, namely proton-proton (pp) interactions followed by subsequent decays of neutral pions and inverse Compton (IC) up-scattering of low-energy photons by relativistic electrons. This chapter gives brief information about these two main γ-ray production mechanisms along with cosmic-rays.

2.2 Cosmic-Rays

Cosmic-rays (CRs) are basically the particles coming from outer space and interacting with the Earth's atmosphere. The history of cosmic-rays has begun in the early 1900's when it was realized that discharge rates of electroscopes were different from zero even if they were totally isolated and shielded from sources of natural radioactivity. In 1912, Victor Francis Hess discovered [Hess (1912)] that the ionization rates increase when going up higher in the atmosphere by making manned balloon ascents experiments. He could experimentally measure that electroscopes discharge rates were doubled at 5300 meters altitude with respect to the sea level and attributed this observation to an extra-terrestrial radiation which has very high penetration power. The discovery of the CRs is normally attributed to Victor Hess, but the name "cosmic-rays" was first used by Millikan. Later, Bothe and Kolhörster showed that the CRs contain charged particles [Bothe & Kolhörster (1929)].

The word "ray" is actually used for historical reasons even though the CRs are basically individual particles. In principle, CRs have different origins, either produced in the Milky Way Galaxy (Galactic CRs) or outside the galaxy (extra-galactic CRs). The abundance of CRs is measured up to the feature, which is called "knee", as it can be seen in Fig. 2.2. Although the exact composition is not so well known, experiments indicate that the CRs are ∼99% nuclei of well known atoms and ∼1% (solitary) electrons. For the nuclei part, the composition can be approximated as ∼90% protons, ∼9% alpha particles and ∼1% nuclei of heavier elements [NASA (2012)].

CRs arrive isotropically at the Earth because of their interaction with both galactic and extra-galactic magnetic fields. Therefore, it is not possible to obtain any information about the source direction from this isotropically arriving charged radiation. The origin of a source can be traced back only by using neutral messengers, namely γ-rays and neutrinos. In addition, γ-rays can propagate freely through interstellar space, unperturbed by magnetic fields and consequently can provide direction information. Especially on galactic scales, γ-rays don't suffer from the absorption by infrared and optical photon background fields[1]. Due to the nature of emission processes, the detected γ-ray sources may show the location of potential CR emitters. It is the main reason why it is generally believed that γ-rays play an important role[2] in the determination of galactic CRs' origin.

The CR spectrum shows two distinct features seen at 10^{15} eV and 10^{18} eV, indicated by "the knee" and "the ankle" as can be seen from Fig. 2.2, respectively. Note that the spectrum steepens at the knee and it hardens again at the ankle feature. The conventionally accepted hypothesis is that the CRs up to the knee feature are accelerated in galactic objects like SNRs. Therefore, these objects are the most important targets for VHE observations to understand the nature and the origin of the galactic CRs.

The CRs beyond the ankle, namely the Ultra High Energy Cosmic Rays (UHECR), are believed to originate from extra-galactic sources. Their exact production mechanisms still remain unknown. Some classes of extra-galactic sources like blazars, radio galaxies, galaxies clusters and GRBs have been considered as the origin of the extra-galactic CRs.

[1] For the inter-galactic scales, absorption due to the extra-galactic background light (EBL) should be taken into account.

[2] For example, the diffuse galactic γ-rays are believed to originate from the interaction between galactic CRs and the molecules in the interstellar medium (ISM). This can provide useful information about the propagation of CRs throughout the galaxy.

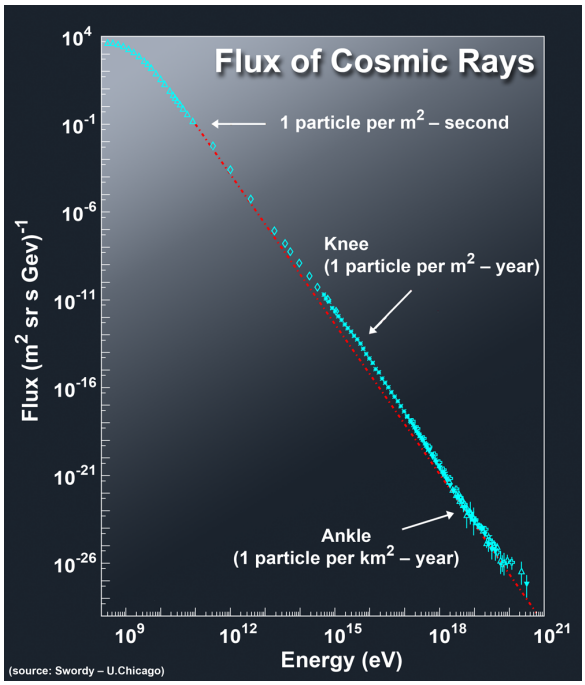

Figure 2.2: The cosmic-ray spectrum measured from the Earth. The "Knee" and the "Ankle" features are also shown on the spectrum with the corresponding flux value. Credit: HAP / A. Chantelauze

But principally, UHECR are not expected to arrive from distances[3] farther than 50 Mpc[4]. On the other hand, the Pierre Auger collaboration [Abraham (2004)] found a possible correlation between the arrival direction of 27 UHECR events with the position of nearby AGN [Abraham (2007)]. However, neither a galactic nor an extra-galactic source has been proven to be a CR accelerator site. The production and the acceleration mechanisms of these CRs are still one of the most exciting subjects of current astrophysics researches.

It is conventionally accepted that the local flux of CRs gives a correct approximation for the level of the "sea" of galactic CRs[5]. Due to a possible contamination of the sea of galactic CRs by local CR sources, one can expect significant deviations of both the spectrum and the energy density of local CRs from the spectrum and the density of galactic CRs. The CR spectrum observed in the vicinity of the Earth follows a power-law distribution. Assuming that the level of the sea of galactic CRs is the same as the proton flux measured close to the Earth, one can write the CR spectrum[6], taken from particle data group [Particle Data Group (2014)], as

$$J_{\odot}^{(\mathrm{p})} = 1.8 \times E_{\mathrm{GeV}}^{-2.7} \quad \mathrm{GeV}^{-1}\mathrm{s}^{-1}\mathrm{sr}^{-1}\mathrm{cm}^{-2} \quad . \tag{2.1}$$

[3]It is expected that the UHECRs would interact with the cosmic microwave background radiation (CMBR), which limits their mean free path on their way to the Earth.

[4]A parsec is an astronomical unit of length used to measure distances to objects outside the Solar System. 1 parsec is about 3.26 light-years (3.085×10^{16} m).

[5]Note that this is actually an ad-hoc assumption. It is not scientifically proven that the local CR spectrum should be taken as representative of the whole galactic population of relativistic particles. The expected small variations on the large galactic scales do not exclude non-negligible gradients of the CR flux on smaller scales, especially in the proximity of young CR accelerators (typically < 100 pc).

[6]The CR spectrum was first measured as $2.2 \times E_{\mathrm{GeV}}^{-2.75}$ GeV^{-1} s^{-1} sr^{-1} cm^{-2} [Simpson (1983)].

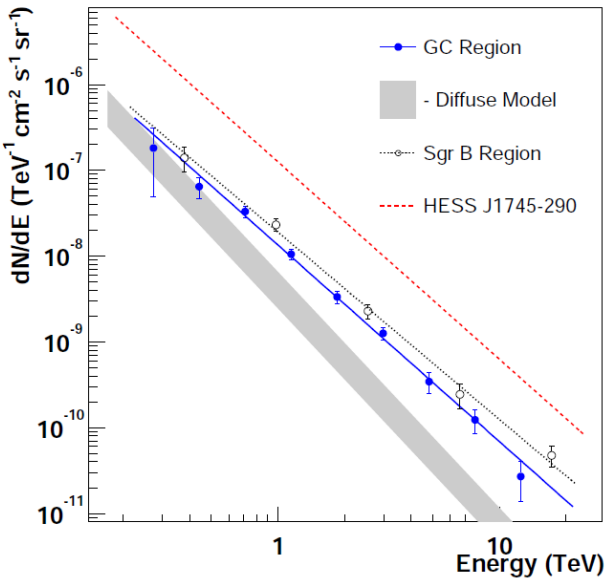

Figure 2.3: Spectrum of γ-rays from the Galactic Center Ridge [Aharonian (2006a)], γ-ray flux per unit solid angle in the GC region in comparison with the expected flux assuming a cosmic-ray spectrum as measured in the solar neighborhood. The spectrum of the region $-0.8° < l < 0.8°$, $|b| < 0.3°$ is shown by using full blue circles. These data can be described by a power law: $dN/dE = k(E/\mathrm{TeV})^{-\gamma}$, with $k = (1.73 \pm 0.13_{\mathrm{stat}} \pm 0.35_{\mathrm{sys}}) \times 10^{-8}$ TeV^{-1} cm^{-2} s^{-1} sr^{-1} and a photon index $\Gamma = 2.29 \pm 0.07_{\mathrm{stat}} \pm 0.20_{\mathrm{sys}}$. The gray shaded box shows the range of expected π^0-decay fluxes from this region assuming a CR spectrum identical to that found in the solar neighborhood.

In γ-ray astronomy, CR acceleration and propagation mechanisms are generally investigated by observing the γ-rays produced by the CRs interacting with the interstellar gas [Aharonian (2001)]. The observations carried out with the High Energy Stereoscopic System (H.E.S.S.)[7] showed that the reconstructed γ-ray spectrum for the region -0.8° < l < 0.8°, |b| < 0.3° (with point-source emission subtracted) is well described by a power law with photon index $\Gamma = 2.29 \pm 0.07_{\mathrm{stat}} \pm 0.20_{\mathrm{sys}}$ which can be seen in Fig. 2.3. Note that the measured γ-ray spectrum shows that the CR spectrum within the inner 200 pc around the Galactic Center (GC), with a spectral index close to 2.3, is significantly harder than the one measured in the solar neighborhood [Aharonian (2006a)], where an index of 2.7 was measured. This also strengthens the previous statement that the CR spectrum and the flux in the vicinity of CR accelerators can be significantly different from the local CRs.

2.3 VHE Gamma-Ray Production Mechanisms

The thermal radiation from the astrophysical objects for typical surface temperatures of ∼5000 K is produced mostly in the visible part of the electromagnetic spectrum according to the black-body radiation of thermal processes, namely Planck's radiation law. For the hottest objects observed in the universe, like the accretion discs around compact stars, the thermal radiation can go up to the hard X-ray energy range (10 keV), which is still several

[7]The H.E.S.S. experiment is explained more detailed in Section 4.2.

orders of magnitudes below the VHE γ-ray range. Therefore, any radiation exceeding these energies must be created in non-thermal processes since it is not possible to reach the required minimum temperature to produce γ-rays by thermal processes[8].

Consequently, VHE γ-rays are expected to be produced in non-thermal processes. The acceleration of electrons or nuclei in astrophysical objects leads inevitably to the production of these γ-rays. They are produced in the interactions of highly energetic particles with ambient radiation fields and matter of the interstellar medium. The most relevant and the main γ-ray production mechanisms are the decay of π^0 produced in hadronic interactions and the inverse Compton scattering of background radiation fields from relativistic electrons. For example, SNRs, where the charged particles are accelerated to TeV energies at the shock fronts, may produce these γ-rays. Also the vicinity of a highly magnetized neutron star or a jet of an AGN are possible production sites. This section describes these two main γ-ray production mechanisms, namely inverse Compton scattering and proton-proton interactions. More detailed descriptions can be found in Ramana (1993), Aharonian (2004a), Longair (1992) and in Weeks (1989).

2.3.1 Inverse Compton Scattering

The up-scattering of low energy photons by relativistic electrons or positrons to higher energies is called inverse Compton (IC) scattering. The IC scattering is a very efficient process to increase the energy of photons up to very high energies. This process becomes more relevant when the ambient photon density is relatively high. The ambient photon fields can be the 2.7 K cosmic microwave background, the diffuse Galactic radiation of the star light and dust photons or also the synchrotron photons produced by the interaction of strong magnetic fields with electron populations at astrophysical objects. Since these low energy photons fields can be provided by many different types of astrophysical objects, IC is basically at work everywhere, in pulsars, SNRs as well as in AGNs.

Figure 2.4 (bottom left) shows the illustration of a relativistic electron (or positron) moving with a Lorentz factor γ towards a photon of energy $E = h\nu$ in the laboratory frame. The top left figure shows the same system in the electron's rest frame. In this case, the photon will be seen with energy $E = \gamma h\nu$ because of the γ factor coming from the Lorentz transformation between the reference frames. Consequently after the collision, the scattered photon will have an energy of $E = \gamma h\nu$ in the electron's rest frame. An additional γ factor will again come because of the Lorentz transformation back to the laboratory frame. Finally, the energy of the boosted photon will be $E_{\rm boosted} = \gamma^2 h\nu$. So one can write

$$E_{\rm boosted} = \gamma^2 E_{\rm initial} \quad \text{if} \quad \gamma E_{\rm initial} \ll m_e c^2 \quad . \tag{2.2}$$

It is known that there are electron populations with Lorentz factors $\gamma \sim$100 - 1000 and even higher[9] in various types of astronomical objects. Consequently they up-scatter the

[8]For example, to produce 1 MeV γ-ray photon, a temperature of the order of 10^9 K would be needed. On the other hand, for some hypothetical scenarios, extremely high temperatures may be present as in GRBs.

[9]Kennel & Coroniti (1984) found that the wind from the Crab pulsar has a Lorentz factor $\Gamma_{\rm T} = 3 \times 10^6$ at the termination shock.

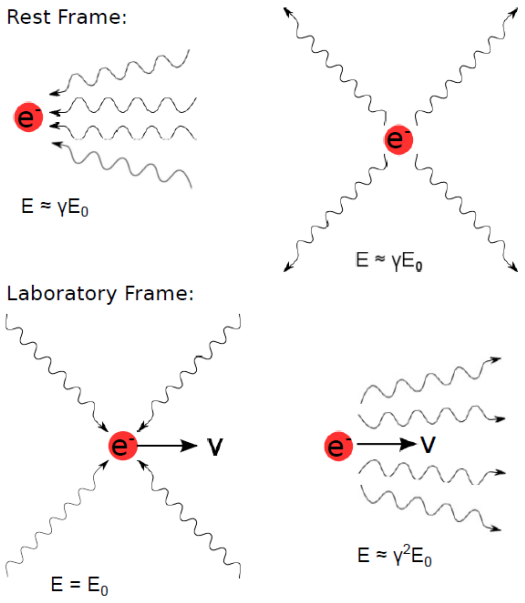

Figure 2.4: IC Scattering in the electron's rest frame and laboratory frame before collision (left upper and left bottom figures) and after collision (right upper and right bottom figures).

Initial Waveband	Initial Frequency (Hz)	Scattered waveband and frequency (Hz)
Radio	10^9	Ultra-Violet, 10^{15}
Far-Infrared	3×10^{12}	X-Rays, 3×10^{16}
Optical	4×10^{14}	Gamma-Rays, 4×10^{20}

Table 2.2: Table of up-scattered photons of different wavebands from an electron population with Lorentz factor of $\gamma = 1000$.

low energy photons to the very high energies. Table 2.2 illustrates the scattering of radio, infrared and optical photons from an electron population of Lorentz factor $\gamma = 1000$.

The cross section for IC-scattering can approximately be described by the Thomson cross section, only if the photon energy in the electron rest frame is smaller than the electron mass ($E_\gamma \ll m_e c^2$). On the other hand, when the photon energy in the electron's rest frame is greater than the electron mass ($E_\gamma \gg m_e c^2$), the cross section for IC-scattering can be described in the Klein-Nishina regime [Klein & Nishina (1929)]. The cross-sections of these regimes can be formulated as

$$\sigma_{\rm T} = \frac{8\pi}{3} r_e^2 = 6.66 \times 10^{-25} \quad \text{cm}^2 \quad \text{(Thomson Cross-Section)} \tag{2.3}$$

where $r_e = 2.8 \times 10^{-13}$ cm is the classical electron radius and

$$\sigma_{\rm KN} = r_e^2 \frac{\pi m_e c^2}{E_\gamma}\left[\ln\left(\frac{2E_\gamma}{m_e c^2}+\frac{1}{2}\right)\right] \quad \text{cm}^2 \quad \text{(Klein-Nishina Cross-Section)}. \tag{2.4}$$

The Thomson regime can be used for the interaction of electron populations with the 2.7 K CMB photons, which have energy an around $E_\gamma \approx 6{\times}10^{-4}$ eV. In this regime, the up-scattered photons follow the spectral shape of the parent photons. Assuming that the spectrum of the relativistic electron population follows a power law with index $\Gamma_{\rm e}$, the resulting up-scattered photon spectrum will follow a power law with index $\Gamma_\gamma = (\Gamma_{\rm e} + 1)/2$ up to a certain energy where a sharp cut-off exists. This cut-off is determined by the maximum energy of the incident electrons. On the other hand, if the IC scattering takes place in the Klein-Nishina regime, the electron spectrum is expected to be harder than the electron spectrum in the Thomson regime ($\Gamma_{\rm e,KN} < \Gamma_{\rm e,Thomson}$) [Moderski et al. (2005)]. This hardening effect is noticeable when the electrons are sufficiently energetic to scatter with ambient photons in the Klein-Nishina limit at energies $\gamma \geq \gamma_{\rm KN}$ where $\gamma_{\rm KN} = 1/4\epsilon_0$ and $\epsilon_0 = {\rm h}\nu_0/m_e c^2$ is the characteristic ambient photon energy. The main difference between these two cross-sections is that the electrons responsible for IC scattering lose a small fraction of their energy when the scattering takes place in Thomson regime while they lose a large fraction of their energy if the IC scattering takes place in Klein-Nishina regime. Consequently, IC scattering in the Thomson regime is more efficient than in the Klein-Nishina regime.

There is also another IC related process called "Synchrotron-Self-Compton" (SSC). SSC radiation basically results from the IC scattering of synchrotron radiation photons by the same relativistic electrons responsible for producing the synchrotron radiation itself. As an example, Fig. 2.5 shows the spectral energy distribution of radiation from the AGN RGB J0152+017 [Nedbal (2008)] where the double-hump structure can be clearly seen. The low frequency component is presumably synchrotron emission from relativistic electrons, while the origin of the high-energy component is the SSC mechanism[10]. Moreover, the contributing emission from the host galaxy can be clearly seen in the optical frequency range as a sharp peak.

2.3.2 Proton-proton Interactions and π^0 Decay

This sub-section concentrates on the γ-ray production mechanism originated from inelastic proton-proton (pp) interactions that can be observed both in HE and VHE astronomy. The produced spectrum of γ-rays from the pp interaction has a special importance in this thesis for investigating the hadronic scenario and the interpretation of the observed VHE spectral data. Therefore, proton-proton interactions and the consequent π^0 decay will be discussed in more detail.

Proton-proton interactions result in the production of secondary particles like π^0 and η-mesons, which subsequently decay into γ-rays. The decay of other products like π^+, π^- mesons and some other short-lived secondaries leads to the production of high energy

[10]Note that one can also observe the double-hump structure in the case of IC scattering of an external photon field.

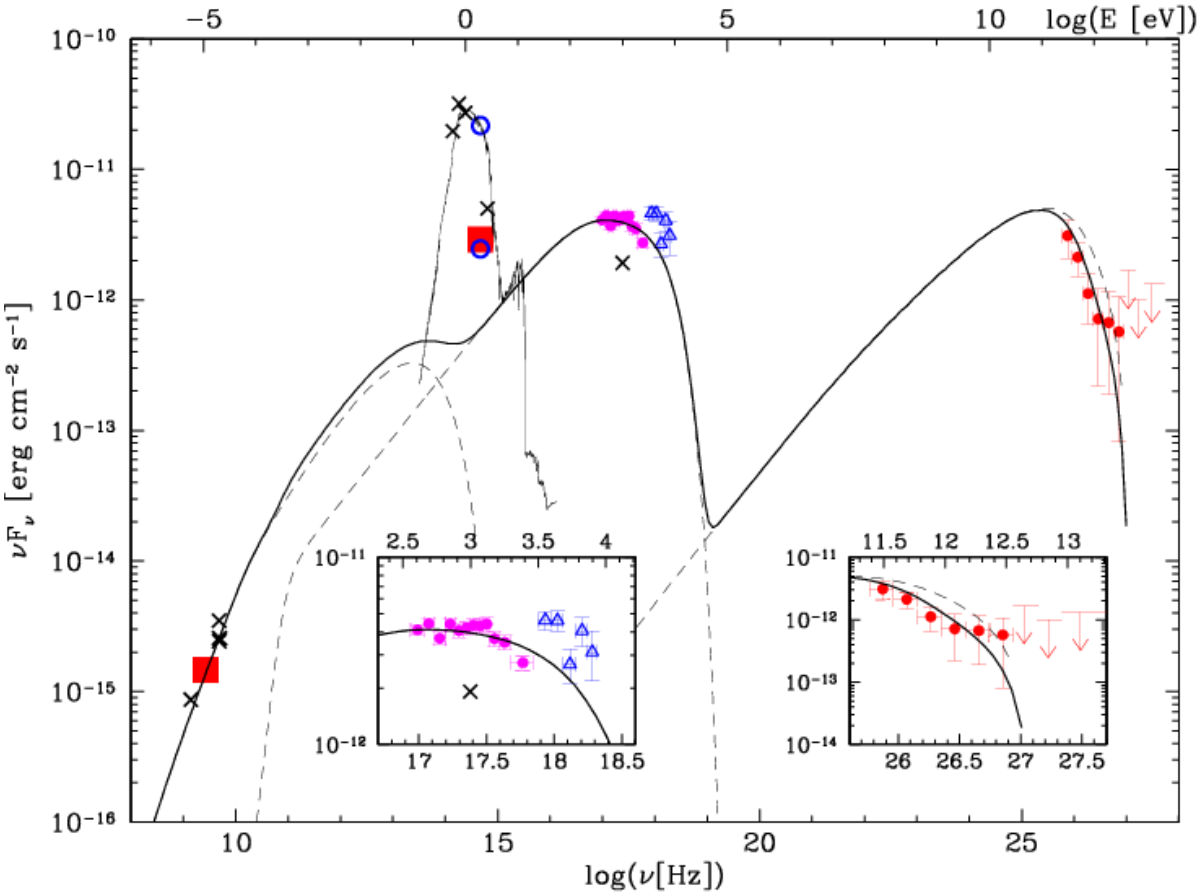

Figure 2.5: Broadband spectral energy distribution of radiation from the AGN RGB J0152+017, the contemporaneous data are shown in color. The solid lines show a 3 components model applied for this contemporaneous multi-wavelength campaign. H.E.S.S. spectrum (red filled circles and upper limits), contemporaneous RXTE (blue open triangles), Swift XRT (corrected for Galactic absorption, magenta filled circles), optical host galaxy-subtracted (ATOM) and radio (Nancay) observations (large red filled squares). The black crosses are archival data. The contribution of the dominating host galaxy is shown in the optical band. The dashed line above the solid line at VHE shows the source spectrum after correcting for EBL absorption. The left and right hand side inlays detail portions of the observed X-ray and VHE spectrum, respectively. Credit: [Nedbal (2008)]

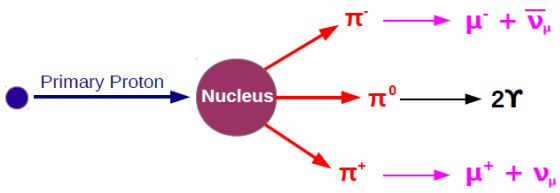

Figure 2.6: Schematic sketch of production and consequent decay of π-mesons from pp interactions.

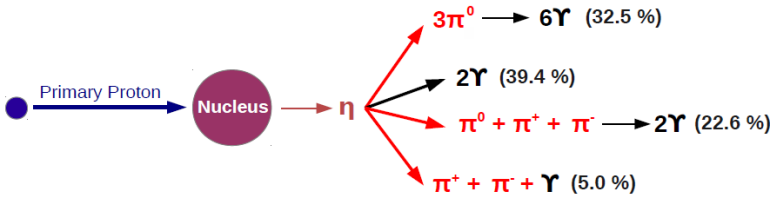

Figure 2.7: Schematic decay of η-mesons produced in pp interactions and the possible decay channels with branching ratios.

neutrinos which establishes a connection between the high energy γ-ray and the neutrino astronomy. Note that secondary electrons and positrons produced in pp interactions can also contribute to non-thermal electromagnetic radiation extending from radio to γ-ray frequencies.

In the hadronic interactions, π^0 decay is the most effective γ-ray production channel. Production of π-mesons from relativistic protons interacting with matter by inelastic collision is illustrated in Fig. 2.6. On the other hand, various secondary mesons can also be produced from these interactions like Etas and Kaons. In most hadronic models, only the π and η components are taken into account. The decay of the η component and the branching ratios are illustrated in Fig. 2.7.

If the kinetic energy of the interacting protons exceeds a minimum kinetic energy threshold of $E_{\mathrm{p,\ Threshold}} = 2m_\pi c^2\ (1+m_\pi/4m_p) \simeq 280$ MeV, where $m_\pi = 134.97$ MeV is the mass of the neutral pion, π^0s can be produced via the $\mathrm{p} + \mathrm{p_{rest}} \rightarrow \mathrm{p} + \mathrm{p} + \pi^0$ channel. This is basically the most efficient channel for transferring initial proton energy to γ-rays. The π^0 decay channels into γ-rays follow the probabilities of $\pi^0 \rightarrow 2\gamma$ (p=0.99) and $\pi^0 \rightarrow \mathrm{e}^+ + \mathrm{e}^- + \gamma$ (p=0.01). In principle, the spectrum of γ-rays from π^0 decays follows approximately the spectrum of the parent protons responsible for producing these pions. For the proton spectrum which follows a power-law distribution with spectral index of Γ_p, the observed γ-ray spectrum at higher energies will also follow a power-law distribution with spectral index of $\Gamma_\gamma = 4/3(\Gamma_\mathrm{p} - 1/2)$ [Aharonian (2004a)]. This actually implies that the observed γ-rays carry direct information about the acceleration spectrum of progenitor particles. Moreover, the decay of charged pions produces neutrinos. Especially for the high energies, the probabilities of producing π^0, π^+ and π^- from a pp interaction are more or less comparable. Because π^0s have significantly shorter lifetime (8.4×10^{-17} s) with respect to charged pions (2.6×10^{-8} s), the expected neutrino flux will be relatively smaller when compared to the observed γ-ray flux [Kelner et al. (2006)]. This reduction in the observed neutrino flux originates from the relatively longer lifetime of charged π-mesons,

since they can interact with other hadrons before decaying into neutrinos.

The γ-ray emission from pp interactions can be observed from many different astronomical objects and their surrounding media. Diffuse emission from the Galactic Ridge is predicted to originate from the interaction of background cosmic-rays with interstellar gas [Egberts (2014)]. Also, the observed emission from SNRs RX J1713.7−3946 [Aharonian (2004b)], RX J0852.0−4622 [Aharonian (2005a)] and even for the alternative models predicting high-energy γ-ray emission from AGN jets [Mücke (2003)] can be given as examples for hadronic γ-ray production.

2.3.2.1 The Spectrum of Pions from pp Interactions

The differential energy spectrum of pions resulting from pp interactions can be expressed in a general conventional way as follows

$$F_\pi(x, E_p) = \frac{d}{dx}\Phi(x, E_p) \tag{2.5}$$

where $x = E_\pi/E_p$ is described as the ratio of incident proton energy (E_p) transferred into produced pion energy (E_π) [Kelner et al. (2006)]. Note that by conventional definition, the number of produced π-mesons in the energy interval defined as (E_π, $E_\pi + dE_\pi$) per pp interaction can be written in the following form

$$dN_\pi = F_\pi(x, E_p)dx = F_\pi(x, E_p)d(E_\pi)/E_p \quad . \tag{2.6}$$

For obtaining a theoretical model for pp interactions, the function $\Phi(x, E_p)$ mentioned in Eq. 2.5 should be known. This function can be obtained from the pp interaction simulations done by well-developed public codes like SIBYLL [Fletcher (1994)] and QGSJET [Kalmykov (1997)]. Note that the QGSJET and SIBYLL codes give quite similar but not identical results for this function. In the high-energy range, the SIBYLL code describes the data relatively better [Kelner et al. (2006)]. Therefore in the following sections, the distribution of secondaries obtained from the SIBYLL code will be used for parameterizing the energy spectrum of the final products from pp interactions. The results of numerical simulations for the secondary pions are well described by the function

$$\Phi_{\rm SIBYLL}(x, E_p) = -B_\pi\left(\frac{(1-x)^\alpha}{1 + rx^\alpha(1-x)^\alpha}\right)^4 \tag{2.7}$$

with the best fit parameters given as

$$B_\pi = a + 0.25, \quad \alpha = \frac{0.98}{\sqrt{a}}, \quad r = \frac{2.6}{\sqrt{a}} \tag{2.8}$$

where

$$a = 3.67 + 0.83L + 0.075L^2 \quad \text{and} \quad L = \ln(E_p/1\ \text{TeV}) \quad . \tag{2.9}$$

By using Eq. 2.5, one can obtain the differential energy spectrum for the pions and

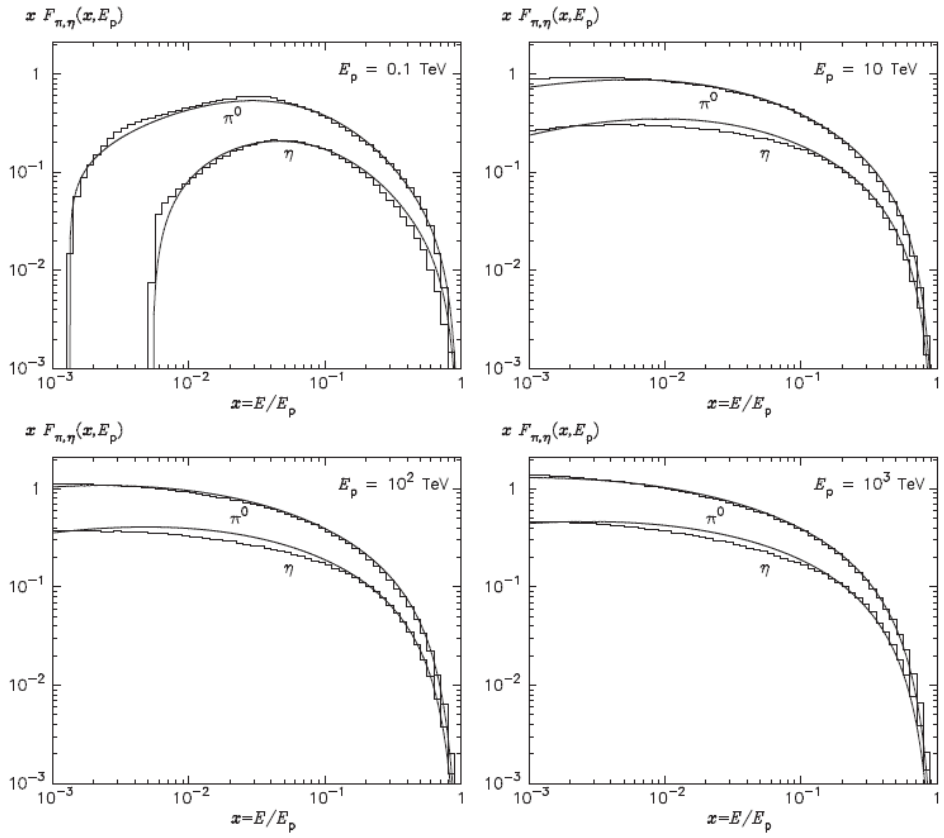

Figure 2.8: Energy spectra of π and η mesons for 4 different energies of primary protons; 0.1, 10, 100 and 1000 TeV. The histograms show numerical calculations based on simulations of production of π and η mesons using the SIBYLL code, the solid lines show the analytical presentation given by Eq. 2.10 and 2.11. Credit: [Kelner et al. (2006)]

also for the etas[11] produced from a single pp interaction. Results can be given as

$$F_\pi(x, E_p) = 4\alpha B_\pi x^{\alpha-1}\Big(\frac{1}{1-x^\alpha} + \frac{r(1-2x^\alpha)}{1+rx^\alpha(1-x^\alpha)}\Big)\Big(1-\frac{m_\pi}{xE_p}\Big)^{1/2} \tag{2.10}$$

$$\text{and } F_\eta(x, E_p) = \Big(0.55 + 0.028\ln(x)\Big)\Big(1-\frac{m_\eta}{xE_p}\Big) \quad . \tag{2.11}$$

Figure 2.8 shows the results of the simulations for the spectral energy distributions of π and η mesons taking into account 4 different incident proton energies. It can be seen from the figure that the $F_\pi(x, E_p)$ function describes the pion spectrum at $x \geq 10^{-3}$ with an accuracy better than $\sim$10% for the given energy range of the protons $[10^{-1}, 10^3]$ TeV. The results obtained for the η meson spectrum $F_\eta(x, E_p)$ is relatively less accurate. Since the γ-ray contribution from π^0-decay dominates the contribution coming from η-decay, the accuracy of $F_\eta(x, E_p)$ is acceptable.

[11]For this purpose, one should use the function $\Phi_{\rm SIBYLL}(x, E_p)$ for etas where $x = E_\eta/E_p$.

2.3.2.2 Decay of the Pions

After obtaining the spectrum of pions from pp interactions, one can discuss the decay products of the neutral pions. The energy distribution of the produced γ-rays from π^0-decay with taking into account the π^0 spectrum of $J_\pi(E_\pi)$ can be written as

$$Q_\gamma(E_\gamma) = 2 \int_{E_\gamma}^{\infty} J_\pi(E_\pi) \frac{dE_\pi}{E_\pi} \tag{2.12}$$

while the total number of produced γ-rays can be written as

$$N_\gamma = \int_0^\infty Q_\gamma(E_\gamma) dE_\gamma = 2 \int_0^\infty dE_\gamma \int_{E_\gamma}^\infty \frac{dE_\pi}{E_\pi} J_\pi(E_\pi) = 2 \int_0^\infty J_\pi(E_\pi) dE_\pi = 2N_\pi \quad . \tag{2.13}$$

Basically, Eq. 2.13 indicates that two γ-rays are produced from a single π^0-decay. Similarly, one can show that the total energy of the produced γ-rays is equal to the total energy of pions as

$$\epsilon_\gamma = \int_0^\infty E_\gamma Q_\gamma(E_\gamma) dE_\gamma = \int_0^\infty E_\pi J_\pi(E_\pi) dE_\pi = \epsilon_\pi \quad . \tag{2.14}$$

One can consider a simple example and try to obtain the γ-ray spectrum from π^0-decay, assuming a power-law shape π^0 spectrum described as

$$J_\pi(E_\pi) = \begin{cases} A/(E_\pi)^\alpha & , \text{if } E_\pi > E_0 \\ 0 & , \text{if } E_\pi < E_0 \end{cases}$$

where E_0 is the lower cut-off, A is the normalization and α is the spectral index of the pion spectrum. For $\alpha > 2.0$ one can calculate the number of pions and the total energy of the pions as

$$N_\pi = \frac{A}{(\alpha-1)(E_0)^{\alpha-1}} \quad \text{and} \quad \epsilon_\pi = \frac{A}{(\alpha-2)(E_0)^{\alpha-2}} \tag{2.15}$$

while the produced γ-ray spectrum has the following form obtained from Eq. 2.12

$$Q_\gamma(E_\gamma) = \begin{cases} \frac{2A}{\alpha E_\gamma^\alpha} & , \text{if } E_\gamma > E_0 \\ \frac{2A}{\alpha E_0^\alpha} & , \text{if } E_\gamma < E_0 \end{cases} \quad .$$

Note that above the cut-off energy E_0, the γ-ray spectrum repeats the shape of the pion spectrum, while it is energy independent below the cut-off energy.

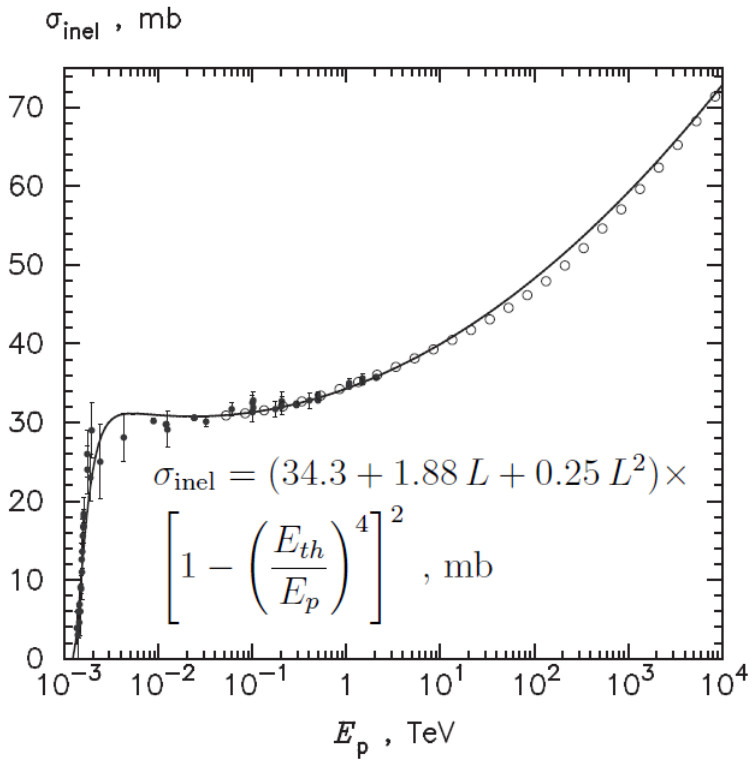

Figure 2.9: Inelastic cross-section for pp interactions. The experimental data (black points) were taken from [Eidelman (2004)], open circles correspond to the cross-section used in the SIBYLL code. Credit: [Kelner et al. (2006)]

2.3.2.3 Energy Spectrum of Photons from pp Interactions for a Wide Energy Distribution of Protons

The discussion on the produced γ-ray spectrum from pp interactions presented in the previous section is basically for a fixed proton energy E_p. It is obvious that protons generated by accelerators in astrophysical environments follow a spectral shape rather than a mono-energetic form. In this section, γ-rays produced by pp interactions of protons following a spectral shape of $J_p(E_p)$ will be discussed. At this point, it will be assumed that the gas density and the magnetic field of the ambient medium are sufficiently low that all produced secondaries decay before having any interaction with the gas or the magnetic field.

One can describe a proton spectrum as the number of protons in a unit volume in an energy interval $(E_p,\, E_p + dE_p)$ which then has units of cm^{-3} TeV^{-1}. Therefore, a function describing the γ-ray production rate in the same energy interval can be written as

$$\Phi_\gamma(E_\gamma) = \frac{dN_\gamma}{dE_\gamma} = cn_H \int_{E_\gamma}^{\infty} \sigma_{\rm inel}(E_p) J_p(E_p) F_\gamma(\frac{E_\gamma}{E_p}, E_p) \frac{dE_p}{E_p} \quad . \tag{2.16}$$

The equation 2.16 is quite important for predicting the γ-ray spectrum from the interaction between CRs[12] and molecular clouds. Consequently, it is important to understand

[12]CRs stand for both the Galactic background CRs and the injected protons from astrophysical

the structure of this formula and every single term included in it. The term n_H describes the ambient medium density of interest[13] and can be obtained experimentally from HI and ^{12}CO / ^{13}CO observations while c is the speed of light. The term $\sigma_{\rm inel}(E_p)$ is the cross-section for inelastic pp interactions and it is strongly dependent on proton energy as can be seen in Fig. 2.9. Note that in general, the total cross section is composed of different contributions and can be described as $\sigma_{\rm TOTAL} = \sigma_{\rm EL} + \sigma_{\rm SD} + \sigma_{\rm DD} + \sigma_{\rm CD} + \sigma_{\rm ND}$ where SD, DD, CD and ND stand for single, double, central and non-diffractive processes. The inelastic part of total cross section can be described as the sum of $\sigma_{\rm SD} + \sigma_{\rm DD} + \sigma_{\rm CD} + \sigma_{\rm ND}$. This inelastic part of the cross-section for pp interactions can be approximated with the formula

$$\sigma_{\rm inel}(E_p) = (34.3 + 1.88L + 0.25L^2) \times \left[1 - \left(\frac{E_{\rm th}}{E_p}\right)^4\right]^2 \quad \text{mb} \tag{2.17}$$

where $L = \ln(E_p \ / \ 1 \text{ TeV})$ and $E_{\rm th} = m_p + 2m_\pi + m_\pi^2 \ / \ 2m_p = 1.22 \times 10^{-3}$ TeV. Note that $E_{\rm th}$ is the energy threshold for π^0-meson production. This approximation is obtained from the SIBYLL code. From the Fig. 2.9, it can be seen that the approximation done in Eq. 2.17 describes the experimental data correctly even for the energies close to the threshold energy. The function $J_p(E_p)$ basically describes the injected proton spectrum. Depending on the astrophysical source, it can be taken as a basic power-law or for the sources exhibiting a cut-off in the spectrum, it can be taken as a power-law with an exponential cut-off. For the following calculations, it will be taken in the following general form of

$$J_p(E_p) = \frac{A}{E_p^\alpha} \exp\left[-\left(\frac{E_p}{E_0}\right)^\beta\right] \tag{2.18}$$

while the normalization constant A can be obtained from the condition that the energy density of protons $\omega_p = \int E_p J_p(E_p) dE_p$. Note that in realistic cases, the energy density changes depending on the proton source of interest. For example, if one assumes that the proton source is the background CRs, than the energy density should be taken as 1 eV cm^{-3} [Castellina (2012)] which is the average cosmic-ray energy density value for the interstellar medium. Another case may be that the source of the protons is a SN explosion. For such a scenario, if the SN explosion takes place within such a medium that all accelerated particles can interact with the ambient medium, then the normalization can be obtained from the following condition. If only the fraction of the particles are expected to interact, then another additional factor, the solid angle, should be implemented in the formula as

$$\int_{1 \text{ GeV}}^{1 \text{ PeV}} E_p J_p(E_p) dE_p = 10^{51} \text{erg} \times \eta \times (\Omega_{\rm solid}) \tag{2.19}$$

where η is the conversion efficiency reflecting the fraction of the explosion energy of a supernova that is transferred to CRs. It has been assumed that 1% to 10% of the total

accelerators.

[13]The density of a molecular cloud can be obtained from the column density maps (see Chapter 3 and 5 for more details) by assuming a 3D shape for the molecular cloud of interest.

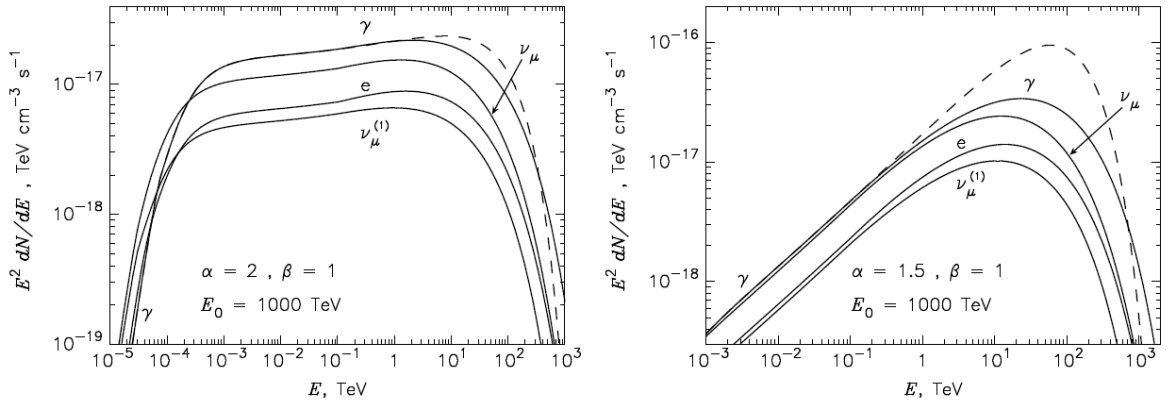

Figure 2.10: Energy spectrum of γ-rays and leptons from pp interactions calculated for the distribution of protons given by Eq. 2.18 with parameters $E_0 = 1000$ TeV (cut-off energy in the proton spectrum), $\beta = 1$ (normal exponent) and $\alpha = 2$ (left figure), $\alpha = 1.5$ (right figure) (spectral index). Credit: [Kelner et al. (2006)]

explosion energy[14] of a supernova is transferred to CRs throughout its whole life in order to explain the observational CR energy density in our Galaxy [Baade & Zwicky (1934), Ginzburg & Sryovatski (1967)]. Since there is no direct evidence for such acceleration of the CR protons, hence the energy conversion efficiency still remains elusive. Because the integration is taken over all proton energies, the lower limit of the integration is set to the proton energy which can produce π^0 mesons. For the upper limit, one can assume that the supernovas can accelerate protons above PeV energies to explain the Galactic CRs up to the knee feature.

The function $F_\gamma(\frac{E_\gamma}{E_p}, E_p)$ in Eq. 2.16 gives the total number of photons generated per collision in the interval $(x,\ x + dx)$ where $x = E_\gamma/E_p$. Note that Eq. 2.16 can be written in a less complicated form by making the conversion[15] of $x = E_\gamma/E_p$ as follows

$$\Phi_\gamma(E_\gamma) = cn_H \int_0^1 \sigma_{\rm inel}(\frac{E_\gamma}{x}) J_p(\frac{E_\gamma}{x}) F_\gamma(x, \frac{E_\gamma}{x}) \frac{dx}{x} \quad . \tag{2.20}$$

Finally, the energy spectrum of γ-rays from pp interactions calculated for the distribution of parent protons assuming the spectral shape given in Eq. 2.18, with the example parameters $E_0 = 1000$ TeV, $\beta = 1$ and $\alpha = 2$ (left figure) and 1.5 (right figure) can be seen from the Fig. 2.10. More detailed discussions on the other secondaries produced can be found in Kelner (2006).

[14]Conventionally assumed to be 10^{51} erg.

[15]Note that making this conversion also changes the integral limits. In this case, the calculations take into account all possible pp interactions where the ratio of the transferred proton energy to γ-ray energies changes between 0 (no energy is transferred) and 1 (all the proton energy is converted to γ-rays)

Chapter 3

Molecular Clouds

This chapter concentrates on the foundations for understanding the physics and chemistry of molecular clouds (MC) and investigating the interaction of CRs with them. A molecular cloud can be described as a region of the interstellar medium with densities ranging between 10^{-5} and 10^{4} cm^{-3}. Molecular clouds are the densest parts of the interstellar medium and comprise about 50% of the total interstellar gas of the Milky Way Galaxy [Tacconi (1986)]. Since their first discovery, they have been investigated as the sites of star formation. The Small Magellanic Cloud is an example of an active star-forming system in which only a small fraction of the interstellar medium is molecular [Rubio (1993)], meaning that the largest fraction has atomic structure. Molecular clouds also play an important role in the formation of galactic structures. The massive stars recently formed within them provide the main energy sources for the interstellar medium, partly by destroying their birth clouds and recycling their matter into more diffuse forms. Many complex processes are indeed involved in MCs, most of which are not yet well understood. However, detailed experimental observations of molecular clouds and star formation regions allow us describing some of the most important dominant processes at work, like the dynamics of the interstellar medium and the evolution of galaxies as a whole.

The following section summarizes the basic properties of molecular clouds, gives brief information about the interstellar molecules, the methods for detection & quantification of their properties and finally describes a way to calculate the expected γ-rays emission from MCs taking into account pp interactions.

3.1 Basic Properties of Molecular Clouds

Molecular clouds are detected by using molecular line and thermal dust emissions or absorption features. About 1% of the mass in a typical molecular cloud is made up of dust (silicates, graphites) [Di Francesco (2006)]. Conventionally, there are three main types of molecular clouds: Giant molecular clouds (GMC), small clouds (Globules) and high (galactic) latitude molecular cirrus clouds. GMCs in general have about 10^4 to 10^6 solar masses ($M_{\odot}$) with average densities in the order of 10^2 to 10^3 cm^{-3}, and sizes around tens of parsecs. Most of the mass in a MC is in the form of molecular hydrogen, H_2. The low temperatures and the shielding from galactic radiation allow the formation of H_2

Figure 3.1: A view of the stellar spire within M16, the Eagle Nebula, located at 2.1 kpc with an angular extension of 6.0 arc mins (corresponds to 3.0 parsecs). Credit: NASA, ESA and The Hubble Heritage Team (STScI/AURA)

on a timescale of 10 Myr [Bergin (2004)]. Since H_2 is a perfectly symmetric molecule, it has no suitable transitions for direct observations. Therefore, instead of H_2, observations of emission and absorption features from dust and rotational transition lines from some specific molecules, such as CO (and its isotopes), are generally used for determining the properties of MCs.

Another important characteristic of molecular clouds is that they are transient structures and do not survive without major changes for more than a few 10^7 years [Blitz (1981)]. These short lifetimes of MCs directly indicate the fact that the age range of the young stars associated with them is only about 10 to 20 Myr, comparable to the internal dynamical timescales of large molecular clouds.

A notable property of MCs is that they move through the galaxy as entities. However, they are rather highly irregular structures and have complex shapes in general. Many of them have wispy or filamentary shapes resembling those of atmospheric clouds. They are also quite inhomogeneous and have higher-density regions called "clumps" or "cores". Although the clump structures occupy only a relatively small volume of a molecular cloud, they contain a large fraction of the total mass. Within these densest clumps, star formation eventually takes place. Figure 3.1 shows an example of such a molecular cloud structure, the Eagle Nebula [Hillenbrand (1993)] & [Sana (2009)]. The other local examples of GMCs are the Orion, Taurus, Perseus and Ophiuchus clouds. Another type of MCs, which is called "Globules" are small dense isolated molecular clouds with up to a few hundred solar masses. They generally correspond to the dense clumps within GMCs. High latitude cirrus clouds are extended diffuse filamentary clouds with very low densities in the order of $3{\times}10^{-5}$ cm^{-3}. They are probably not only located at high galactic latitudes but also at low galactic latitudes where they are out-shone by the much brighter and denser GMCs and globules.

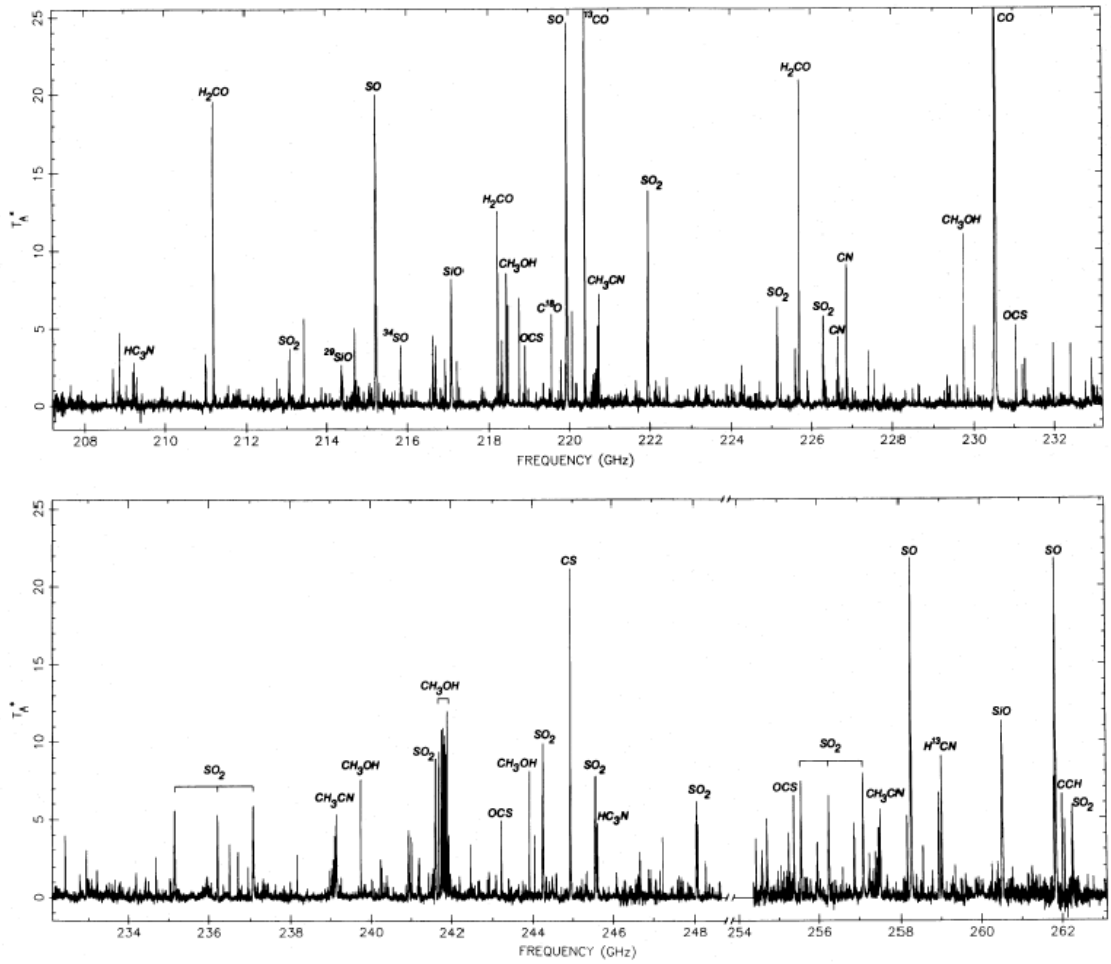

Figure 3.2: Spectrum of the Orion Molecular Cloud 1 (OMC1) in the 1.3 mm band. Each of 29 different molecule species, tagged with their names on the observed peaks, can be seen in the spectrum. The upper figure shows the detected molecules between 207 and 233 GHz while the lower figure shows the molecules detected within the 232−263 GHz waveband. Credit: [Blake (1987)]

3.2 Interstellar Molecules

In this subsection, an overview about the molecules detected in the interstellar medium is given. These molecules emit electromagnetic waves by changing their rotational or vibrational states. The first optical emission from diatomic radicals in interstellar molecular gas was detected in the 1940's from optical observations of absorption bands from electromagnetic transitions in CH, CH^+ and CN, superimposed on the spectra of bright stars [Dunham (1937)], [Swings (1938)]. The late 1960's and early 1970's were exciting times for all branches of radio astronomy. Finally the first interstellar molecule, the hydroxyl (OH) radical, was found [Weinreb (1963)] 12 years after the detection of the first atomic line, the 21 cm HI hyperfine structure (HFS) transition [Ewen (1951)]. Currently, more than 150 molecule species[1] have been observed in the interstellar space.

Infrared observations beginning in the 1970's detected H_2 in emission from forbidden

[1]See http://www.cv.nrao.edu/php/splat/advanced.php for the updated list.

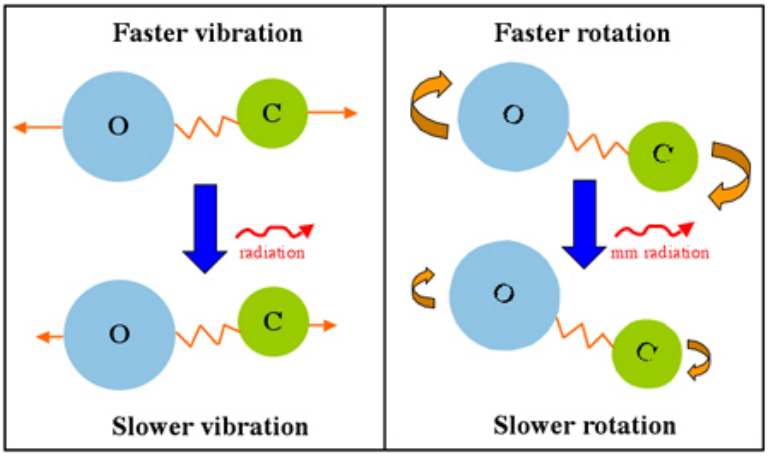

Figure 3.3: Illustration of rotational and vibrational transitions in CO molecule. The left figure illustrates the change in vibrational state while the right figure illustrates the change in rotational state.

rotational-vibrational transitions in the near-infrared (NIR) band. The study of interstellar molecules was developed significantly with the advent of new millimeter receiver technology in the 1980's. Especially after the advanced developments in IR array detectors in the late 1990's, these transitions have been studied and investigated deeply. Consequently, many different molecular species were identified. Figure 3.2 shows the spectrum of the Orion Molecular Cloud 1 in the 1.3 mm band, showing 29 molecular species detected from this region [Blake (1987)].

The most abundant molecular species in the ISM is H_2. Since it is a homo-nuclear linear molecule with no permanent dipole moment, all of the low-lying energy levels are quadrupole transitions with small transition probabilities. For this reason, the most abundant molecule in the ISM carrying most of the mass and playing a key role in excitation, thermal balance and gas-phase chemistry is virtually invisible to direct observations. As a consequence, most of what we know about molecular clouds comes from the observations of so called "tracer" species, primarily CO, observed by using its J=1→0 rotational transition at $\lambda = 2.6$ mm. Since the formation of molecular species like CO occurs under similar conditions like the H_2 formation, the amount of H_2 is generally estimated from the observed amount of CO with the assistance of a few simple assumptions. Therefore, low rotational transitions of the CO molecule, although about by 10^{-4} less abundant than H_2, have become the most important tool to study the large scale distribution of molecular gases in the interstellar medium.

3.2.1 Rotational and Vibrational Transitions in the CO Molecule

Since the emission from the CO molecules is widely used for tracing molecular clouds, it is quite important to understand the rotational and vibrational transitions in these molecules. For example, a change in the vibrational state of the CO molecule results in photons emitted at millimeter wavelengths corresponding to the IR part of the electromagnetic spectrum. IR radiation emitted by MCs can pass through the interstellar medium unaffected.

The molecules can only rotate and vibrate at certain frequencies and they need to

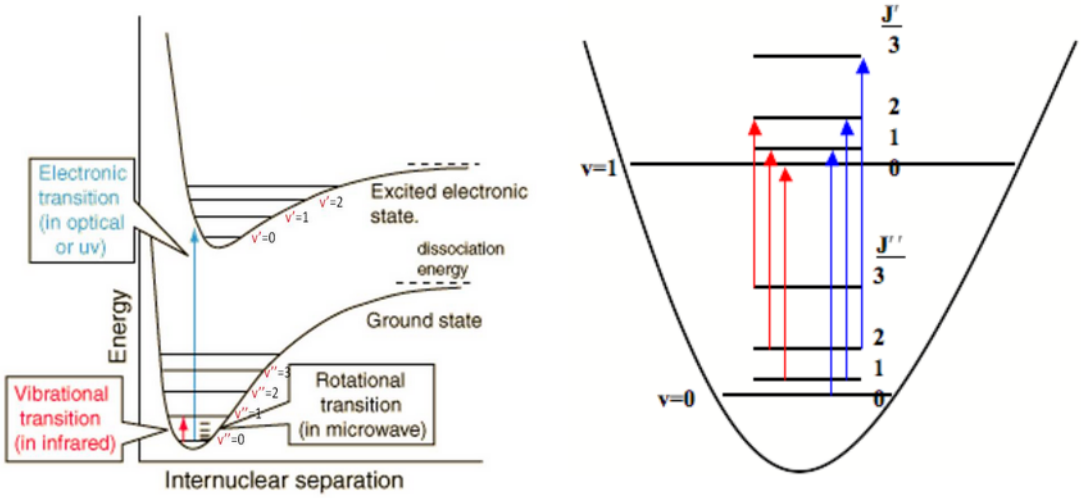

Figure 3.4: Allowed rotational and vibrational transitions in the CO molecule. The left figure illustrates the rotational (blue arrow) and vibrational (red arrow) transitions while the right figure illustrates the vibrational transitions. The red arrows show the vibrational transition for $\Delta v = -1$ case while the blue arrows show $\Delta v = +1$ cases.

absorb or release energy as they transit from one energy level to another. Specifically, some energy must be absorbed or emitted when a molecule changes its rotational state. Figure 3.3 shows the illustration of vibrational and rotational transitions for a CO molecule. As a first approach, one expects the allowed energies to be the sum of a rotational and a vibrational part which can be written as

$$E_{Total} = E_{Rot} + E_{Vib} = \left[\frac{\hbar^2}{2I}J(J+1)\right] + \left[h\omega_e(v+\frac{1}{2})\right] \tag{3.1}$$

where I is the moment of inertia[2] about an axis through the center of mass and perpendicular to the bond and J is the angular momentum quantum number. For the vibrational part, ω_e is the angular frequency and v is the vibrational quantum number.

The observed emission spectrum is determined by the selection rules which specify the allowed transitions between energy levels. In order for a potential transition to absorb a photon, the electric dipole operator must have a non-zero matrix element between the two states. For vibrational states, this basically means that v can only change by ± 1, while for the rotational states J must also change by ± 1. Figure 3.4 shows the illustration of the allowed energy levels and corresponding transitions.

Recall that although molecular hydrogen is by far the dominant molecule in molecular clouds, it is very difficult to detect since it is perfectly symmetric and has no permanent dipole moment. With no dipole moment, only quadrupole rotational transitions can occur. This means that only ΔJ=0 and ΔJ=2 rotational transitions are allowed, while ΔJ=$\pm$1 (dipole) rotational transitions are strictly forbidden. Consequently, unlike other molecules,

[2]In terms of microscopic quantities, moment of inertia can be described as $I = \mu \times r_e^2$, where μ is the reduced mass and r_e is the equilibrium inter-atomic distance.

molecule	abundance[a]	transition	type	λ	$T_\circ^b$ (K)	A_{ul} (s^{-1})	n_{crit}^c (cm^{-3})	comments
H_2	1	1→0 S(1)	vibrational	2.1 μm	6600	8.5×10^{-7}	7.8×10^{7}	shock tracer
CO	8×10^{-5}	J= 1 → 0	rotational	2.6 mm	5.5	7.5×10^{-8}	3.0×10^{3}	low density probe
OH	3×10^{-7}	$^2\Pi_{3/2}$;J=3/2	Λ-doubling	18 cm	0.08	7.2×10^{-11}	1.4×10^{0}	magnetic field probe
NH_3	2×10^{-8}	(J,K)=(1,1)	inversion	1.3 cm	1.1	1.7×10^{-7}	1.9×10^{4}	temperature probe
H_2CO	2×10^{-8}	$2_{12}\rightarrow1_{11}$	rotational	2.1 mm	6.9	5.3×10^{-5}	1.3×10^{6}	high density probe
CS	1×10^{-8}	J= 2 →1	rotational	3.1 mm	4.6	1.7×10^{-5}	4.2×10^{5}	high density probe
HCO^+	8×10^{-9}	J= 1 → 0	rotational	3.4 mm	4.3	5.5×10^{-5}	1.5×10^{5}	tracer of ionization
H_2O		$6_{16}\rightarrow5_{23}$	rotational	1.3 cm	1.1	1.9×10^{-9}	1.4×10^{3}	maser
〃	$<7\times10^{-8}$	$1_{10}\rightarrow1_{11}$	rotational	527 μm	27.3	3.5×10^{-3}	1.7×10^{7}	warm gas probe

[a] number density of main isotope relative to hydrogen, as measured in the dense core TMC–1
[b] equivalent temperature of the transition energy; $T_\circ \equiv \Delta E_{ul}/k_B$
[c] evaluated at T=10 K, except for H_2 (T=2000 K) and H_2O at 527 μm (T=20 K)

Table 3.1: Table of Galactic molecular clouds main tracers adapted from [Stahler (2004)]. The parameter λ is the detected wavelength, A_{ul} is the probability per second of spontaneous decay from excited to ground state. Transition type shows the transition of the corresponding molecule and the last column gives an idea about what these molecules are used to trace. The molecules are sorted by taking into account their abundance.

H_2 can not emit radio-wavelength rotational lines. The first pure rotational transition, J= 2→0, occurs at 28 μm. This part of the spectrum can not be observed from the ground due to water-vapor absorption in the atmosphere. Furthermore, this transition needs relatively high temperatures (around 514 K) when compared to the cores of giant molecular clouds (10 - 20 K). The next pure rotational transition is J=4→2 at 12 μm, which needs $h\nu/k$ = 1200 K temperatures. Because of the relatively high energies required for the allowed transitions in H_2, one can expect negligible H_2 emission unless looking at unusually warm (500 - 1000 K) H_2 gas in the vicinity of hot stars or in active star formation regions within or at the edges of giant molecular clouds.

Fortunately, more than 150 other molecular species have now been identified in the interstellar medium and in particular the CO molecule is an invaluable molecule for locating MCs and determining their properties. In contrast to H_2, CO line emission requires the temperature of 5.53 K. Therefore CO molecules can easily be excited by H_2 or HI collisions at temperatures of T = 10 - 20 K within the cores of GMCs. It has been shown that for every CO molecule, there are about 10^4 hydrogen molecules meaning that H_2 can be traced through the emission from the CO molecule [Glover (2010)]. Currently, this is the primary method used for locating molecular clouds.

Table 3.1, presents a list of useful molecules and their associated parameters[3]. Note that the CO molecule is the next most abundant compound after H_2. Due to the self-shielding

[3] "Λ-Doubling" stands for the hyperfine interaction with the unpaired spin of the proton causing further splits in the energy levels. Also the NH_3 molecule resembles a triangular-base pyramid, with the three hydrogen atoms at the corners of the base and the nitrogen atom at the apex. However, quantum mechanical tunneling of the nitrogen atom allows it to pass through the pyramid base to the other side, overcoming the potential barrier. A transition in which the nitrogen atoms flips the orientation of the pyramid is distinct from a simple rotation, and is called "inversion" transition since it inverts the pyramid.

effect of CO, it aggregates in a similar manner to that of H_2 (but remains dissociated to a greater cloud depth), hence it allows CO to be an accurate tracer of the Hydrogen mass of the cloud. Consequently, CO is considered as the primary tracer of molecular gas in both intra- and extra-galactic astronomy. The isotopologues[4], which are easiest to detect, according to [Stahler (2004)] are $^{12}C^{16}O$, $^{13}C^{16}O$, $^{12}C^{18}O$ and $^{12}C^{17}O$. Especially, the low critical density of CO allows it to be used to probe the lower density regions of clouds rather than the dense cores. The reason is that within the cores, the radiation of the detectable $J = 1 \rightarrow 0$ transition is completely absorbed by an optically thick[5] core medium. For this reason, the other CO isomers like $^{13}C^{16}O$ are used instead of $^{12}C^{16}O$ since they are not optically thick in these regions.

3.2.2 The Atomic Hydrogen 21 cm Line

It is well known that radio waves can reach the Earth from different parts of space, whereas optical light can not due to the attenuation through the ISM. In particular, MCs in the interstellar medium hide the optical features of our galaxy. One can obtain more information about the general structure and dynamics of a Galaxy by looking at a frequency band around 1420.4 MHz. This special feature is known as the 21 cm line and is emitted by neutral hydrogen atoms. Actually, this emission was predicted first at 21.2 cm by using the physics of the hydrogen atom [Van De Hulst (1982)]

$$\nu_{1\rightarrow 0} = \frac{8}{3} g_I \frac{m_e}{m_p} \alpha^2 R_m c = 1420.405751 \text{ MHz} \tag{3.2}$$

where $g_I \approx 5.58569$ is the nuclear g-factor for the proton[6], $\alpha = e^2/(\hbar c) \approx 1/137.036$ is the dimensionless fine-structure constant and $R_m.c$ is the hydrogen Rydberg frequency. In March 1951, the first discovery of a hydrogen emission line in the radio spectrum at 21 cm [Ewen (1951)] was done. This line can be seen with varying intensity coming from all directions in the sky and due to its extremely sharp nature, it is used widely in astronomy for spectroscopic velocity measurements.

When the hydrogen atom changes its state from the excited state into the ground state, a photon is emitted carrying away the information about the energy difference as illustrated in Fig. 3.5. This photon has a wavelength of 21 cm ($\nu = 1420.4$ MHz). The spin-flip transition, as it is termed, is a highly forbidden process, with a mean-life of approximately 10^7 years. The emission from a HI source is observed as a very sharp emission line with small ΔE energy dispersion, or line width, in this specific frequency. This feature allows the determinations of HI source velocity by simple measurements of the Doppler shift of the 21 cm line with high accuracy. By solving the relativistic Doppler

[4]Isotopologues are molecules that differ only in their isotopic composition. Simply, the isotopologue of a chemical species has at least one atom with a different number of neutrons than the parent. For example, heavy water (D_2O) is the isotopologues of ordinary water (H_2O).

[5]The optical thickness is a measure of transparency and defined as the negative natural logarithm of the fraction of radiation that is not scattered or absorbed on a path and can be described as $\tau = -\ln(I/I_0)$.

[6]In general, the g-factor is a dimensionless proportionality constant relating the magnetic moment of a charged particle to its angular momentum quantum number. Protons, neutrons, and many nuclei have spin and magnetic moments, and therefore associated g-factors defined as $\mu = g_I.\mu_N.\mathbf{I}/\hbar$ where μ_N is the nuclear magneton ($\mu_N = e.\hbar/2.m_p$) and $\mathbf{I}$ is the nuclear spin angular momentum.

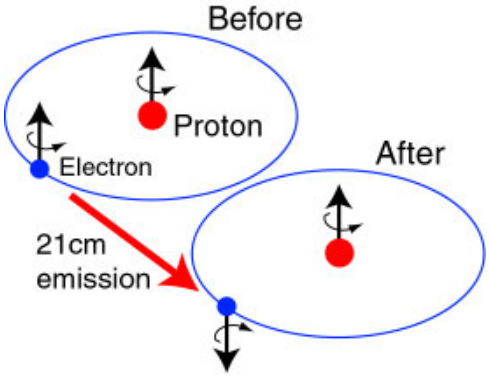

Figure 3.5: Illustration of the spin-flip transition in the hydrogen atom.

shift formula

$$\nu_{observed} = \nu_{source}\left(\frac{1 - V_{rec}/c}{1 + V_{rec}/c}\right)^{1/2} \tag{3.3}$$

where V_{rec} is the recessional velocity, one can obtain the velocity of the source. The HI observations carried out by radio telescopes basically provide the T_{exc} (which is also called T_{spin} sometimes) information similar to the CO observations. The excitation temperature again accounts for the distribution of the atoms between the two spin states. The population of these two states is determined primarily by the collisions between atoms. The probability of a spontaneous transition is around 2.85×10^{-15} s^{-1} (1 event per atom per 10^7 years), but this rate can increase up to 1 event per 400 years due to the collisions between atoms, especially in dense regions.

HI can also be observed in emission or absorption depending on the strength of the background sources as explained later in Section 3.3. Neutral hydrogen gas in the disk of our Galaxy moves in nearly circular orbits around the galactic center. Radial velocities measured from the Doppler shifts of the 21 cm emission line encode information about the kinematic distances of HI clouds. The spectra of HI absorption in front of continuum sources can be used to constrain their distances (explained detailed in the Kinematic Distance Ambiguity method in Section 3.5). HI is optically thin except in a few regions near the galactic plane, therefore the distribution of hydrogen shows the large-scale structure of the whole Milky Way Galaxy which is hidden by dust at visible wavelengths. Figure 3.6 shows the entire dataset for The Parkes Galactic All Sky Survey [McClure-Griffiths (2009)] of the atomic hydrogen emission in the Milky Way.

The 1420 MHz HI line is also an extremely useful tool for studying gas distribution in the ISM of other galaxies and for tracing the large-scale distribution of galaxies in the universe, since HI is also detectable in most spiral galaxies and in some elliptical galaxies. The observed center frequency of the HI line can be used to measure the radial velocity V_r of a galaxy[7]. If the radial velocity is significantly larger than the radial component of the peculiar velocity, the observed HI frequency can be used to estimate the Hubble

[7]The radial velocity of a galaxy is the sum of the recession velocity caused by the uniform Hubble expansion of the universe and the "peculiar" velocity of the galaxy. The radial component of the peculiar velocity reflects motions caused by gravitational interactions with nearby galaxies and is typically 200 km s^{-1} [Karachentsev (2006)] in magnitude.

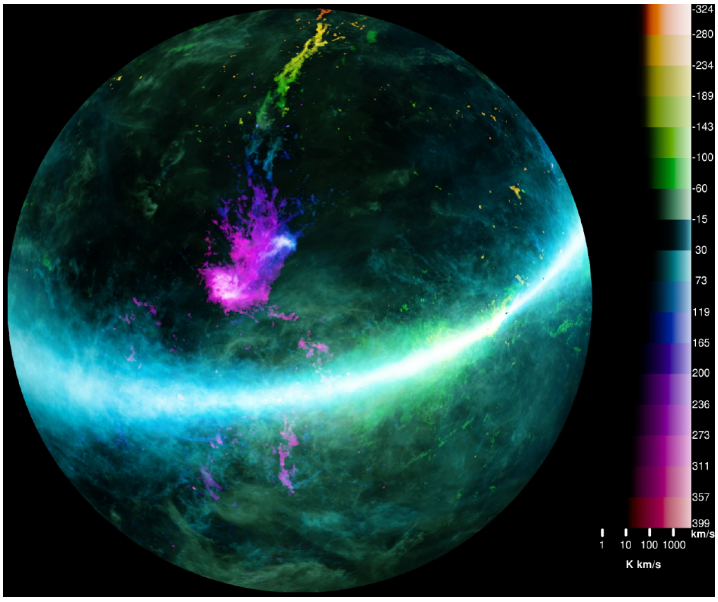

Figure 3.6: The entire dataset for The Parkes Galactic All Sky Survey (G.A.S.S.) of the atomic hydrogen emission in the Milky Way for the entire sky using the 20 cm multi-beam receiver on the Parkes Radio Telescope. The survey covers all of the velocities in the Milky Way between -400 km s^{-1} and 500 km s^{-1}. The colors correspond to integration over velocity chunks of $\sim$40 km s^{-1} as indicated by the bar on the right hand side of the image. The intensity of each color corresponds to the brightness temperature integrated over the 40 km s^{-1} velocity chunk, and is scaled logarithmically as shown by the horizontal extent of the color bar. Credit: [McClure-Griffiths (2009)]

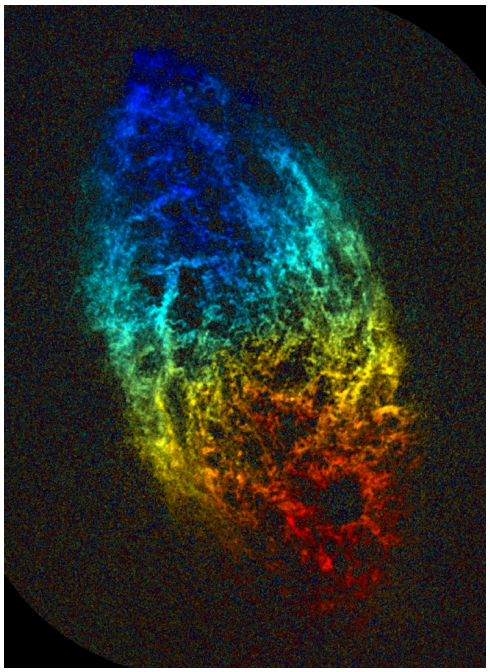

Figure 3.7: HI radial velocity field of the nearby spiral galaxy M33. The brightness in this image is proportional to the HI column density. Credit: National Radio Astronomy Observatory (NRAO)

distance[8] to a galaxy. Consequently, HI observations can also provide a tool to measure the distances to the galaxies. Figure 3.7 shows the HI radial velocity field of the nearby spiral galaxy M33 where the colors correspond to Doppler redshifts and blue-shifts relative to the center of mass. One can see that the lower right part of the M33 is moving away from the Earth while the upper blue part is moving closer to the Earth, which provides the orientation information for the rotation of M33 galaxy.

3.3 Basic Concepts of Radio Astronomy

For observations from the surface, the atmosphere is transparent to radio waves since its constituents can not absorb this radiation to a noticeable extent. The frequency of radio waves that can be detected from the Earth's surface extends from ∼15 MHz to ∼1.5 THz while these limits are not so sharp and can vary both with atmospheric and geographical conditions.

The infinitesimal power dP emitted by an infinitesimal radio source surface $d\sigma$ can be described as

$$dP = I_\nu \cos(\theta) d\Omega d\sigma d\nu \tag{3.4}$$

where dP = infinitesimal power (in Watts), I_ν = brightness or specific intensity of the source (in $\mathrm{Wm^{-2}Hz^{-1}sr^{-1}}$), $d\Omega$ = infinitesimal solid angle (in sr), $d\sigma$ = infinitesimal area of source surface (in $\mathrm{cm^2}$), θ = angle between the normal to $d\sigma$ and the direction to $d\Omega$ and

[8]The Hubble distance to a galaxy can be calculated by using the equation $D = V_r/H_0$. The Hubble velocity is proportional to the distance from the Earth and the Hubble constant of proportionality has been measured as $H_0 = 67.80 \pm 0.77$ km $\mathrm{s^{-1}}$ $\mathrm{Mpc^{-1}}$ [Planck Collaboration (2013)].

$d\nu$ = infinitesimal frequency bandwidth (in Hz). Note that Eq. 3.4 can also be considered as the definition of the brightness I_ν. The terms "intensity" or "specific intensity" are often used instead of the term brightness.

The total flux of a source can be obtained by integrating Eq. 3.4 over the total solid angle Ω_s of the source

$$S_\nu = \int_{\Omega_s} I_\nu \cos(\theta) d\Omega = I_\nu \frac{\pi R^2}{r^2} = I_\nu \Delta\Omega_s \quad . \tag{3.5}$$

where the term R is the source radius and r is the distance between the source and the observer. Note that for the derivation of above equation, one assumes a spherical source in which the brightness I_ν does not vary over the source. It is also assumed that $r \gg R$. This flux density S_ν is measured in units of $\mathrm{Wm^{-2}Hz^{-1}}$. A special radio astronomy flux density unit is introduced since the flux density of radio sources is generally very small. This unit is called the Jansky (Jy) and is given by

$$1 \text{ Jy} = 10^{-26}\mathrm{Wm^{-2}Hz^{-1}} = 10^{-23}\mathrm{ergs^{-1}cm^{-2}Hz^{-1}} \quad . \tag{3.6}$$

The brightest astronomical radio sources have flux densities of the order of one to one hundred Janskys [Longair (1983)]. This range makes the Jansky a suitable unit for radio astronomy. Note that the brightness of an extended source is a quantity similar to the surface brightness in optical astronomy and is independent of the distance to the source as long as the effects of diffraction and extinction can be neglected. On the other hand, the total flux density S_ν shows the dependence of $1/r^2$ as can be seen from the Eq. 3.5.

Since the intensity I_ν remains independent of the distance for radiation in free space, one can assume that I_ν will change only if radiation is absorbed or emitted on the way between an observer and a source. An infinitesimal change of I_ν in a slab of material of the thickness ds can be described by the "equation of transfer" and is given by

$$\frac{dI_\nu}{ds} = -\kappa_\nu I_\nu + \epsilon_\nu \tag{3.7}$$

where κ_ν is the linear absorption coefficient and ϵ_ν is the emissivity coefficient. Conventionally, both of these coefficients are assumed to be independent of the intensity I_ν. Note that there may be situations in which ϵ_ν strongly depends on I_ν, for example in an environment in which radiation is strongly scattered. However in most of the cases, ϵ_ν is independent of I_ν.

One can define several limiting cases for the equation of transfer (Eq. 3.7) in which the solution is simple as listed below.

- Emission only case: $\kappa_\nu = 0$

$$\frac{dI_\nu}{ds} = \epsilon_\nu, \quad I_\nu(s) = I_\nu(s_0) + \int_{s_0}^{s} \epsilon_\nu(s) ds \quad . \tag{3.8}$$

- Absorption only case: $\epsilon_\nu = 0$

$$\frac{dI_\nu}{ds} = -\kappa_\nu I_\nu, \quad I_\nu(s) = I_\nu(s_0) \exp\left(- \int_{s_0}^{s} \kappa_\nu(s) ds \right) \quad . \tag{3.9}$$

- Thermodynamic equilibrium (TE): If there is complete equilibrium of the radiation with its surroundings, then the brightness distribution is described by the Planck function which depends only on the thermodynamic temperature T of the surroundings

$$\frac{dI_\nu}{ds} = 0, \quad I_\nu = B_\nu(T) = \frac{\epsilon_\nu}{\kappa_\nu} = \frac{2h\nu^3}{c^2} \left[\frac{1}{\exp(h\nu/kT) - 1} \right] \quad . \tag{3.10}$$

- Local Thermodynamic equilibrium (LTE): Complete thermodynamic equilibrium can be realized only in very special cases such as stellar interiors. In the LTE case, the intensities of emitted and absorbed radiation are not independent but are related by Kirchhoff's law and can be applied independent of the material as

$$B_\nu(T) = \frac{\epsilon_\nu}{\kappa_\nu} \quad , \tag{3.11}$$

  however note that in general I_ν differs from $B_\nu(T)$ as opposed to the case of TE.

One can define the concept of "optical depth", $d\tau$, by

$$d\tau = -\kappa_\nu ds, \quad \tau_\nu(s) = \int_{s_0}^{s} \kappa_\nu(s) ds \tag{3.12}$$

as it can also be seen within the exponential term in Eq. 3.9 for the absorption only case. In this case, the equation of transfer (Eq. 3.7) can be rewritten by using the definition of $d\tau$ and Kirchoff's law as

$$-\frac{1}{\kappa_\nu} \frac{dI_\nu}{ds} = \frac{dI_\nu}{d\tau} = I_\nu - B_\nu(T) \quad . \tag{3.13}$$

The detailed solution of this differential equation (Eq. 3.13) can be found in Wilson (2009). For an isothermal medium[9], the solution to Eq. 3.13 is given by

$$I_\nu(s) = I_\nu(0) \exp(-\tau_\nu(s)) + B_\nu(T)(1 - \exp(-\tau_\nu(s))) \quad . \tag{3.14}$$

As can be seen from Eq. 3.14, for a large optical depth where $\tau_\nu \to \infty$, LTE approaches the limit of TE ($I_\nu = B_\nu(T)$). Consequently, the observed brightness I_ν for the optically

[9]Isothermal stands for the case that the temperature is constant and does not change with optical depth along the material of interest ($T(\tau) = T(s) = \text{Constant}$).

thick case is equal to the Planck's black body brightness distribution which is independent of the material. The change in the intensity ($\Delta I_\nu(s)$) can be calculated by using Eq. 3.14 as

$$\Delta I_\nu(s) = I_\nu(s) - I_\nu(0) = (B_\nu(T) - I_\nu(0))(1 - \mathrm{e}^{-\tau}) \quad . \tag{3.15}$$

Recall that the spectral distribution of the radiation from a black body in TE is given by Planck's law

$$B_\nu(T) = \frac{2h\nu^3}{c^2} \frac{1}{\exp(h\nu/kT) - 1} \quad . \tag{3.16}$$

This distribution gives the power per unit frequency interval and it reaches its maximum at

$$\frac{\nu_{max}}{\mathrm{GHz}} = 58.789 \left(\frac{T}{\mathrm{K}} \right) \tag{3.17}$$

which is known as "Wien's displacement law". If $h\nu/kT$ is far from its maximum ($h\nu \ll kT$), one can approximate the Eq. 3.16 by using an expansion of the exponential function which results in

$$B_\nu(T) = \frac{2\nu^2}{c^2} kT \quad . \tag{3.18}$$

Actually, the equation above is the classical limit of Planck's law and called "Rayleigh-Jeans law". In radio astronomy, one generally defines a "radiation temperature" T_R as

$$T_R = \frac{c^2}{2k\nu^2} I_\nu = \frac{h\nu}{k} \frac{1}{\exp(h\nu/kT) - 1} \tag{3.19}$$

which can basically be used for all thermal radio sources except for very low temperatures in the millimeter or sub-millimeter range. One of the important implications of the Rayleigh-Jeans law is that the brightness and the thermodynamic temperature of the black body that emits this radiation are proportional as can be seen from Eq. 3.19. This feature is very useful and has been used quite often in radio astronomy to measure the brightness of an extended source by measuring its brightness temperature T_b. This is actually the temperature which would result in the given brightness if inserted into the Rayleigh-Jeans law

$$T_b = \frac{c^2}{2k\nu^2} I_\nu \quad . \tag{3.20}$$

Consequently, if the radiation is emitted by a black body and $h\nu \ll kT$, then T_b gives the thermodynamic temperature of the source (T_R). It is also convenient to introduce the concept of brightness temperature into the radiative transfer equation (Eq. 3.15) as

$$T_b = \frac{c^2}{2k\nu^2} (B_\nu(T) - I_\nu(0))(1 - \mathrm{e}^{-\tau}) \quad . \tag{3.21}$$

This measured quantity is referred to as the radiation temperature or the brightness temperature. One can use Eq. 3.20 in the equation of transfer (Eq. 3.13) and obtain the

differential equation

$$\frac{dT_b(s)}{d\tau_\nu} = T_b(s) - T(s) \tag{3.22}$$

which has a solution under the assumption of isothermal medium

$$T_b(s) = T_b(0)\mathrm{e}^{-\tau_\nu(s)} + T(s)(1 - \mathrm{e}^{-\tau_\nu(s)}) \tag{3.23}$$

where $T(s)$ is the thermodynamic temperature of the medium at the position s. If one assumes $T_b(0) = 0$ for simplicity and considers the optically thick case ($\tau \gg 1$), it can be seen from Eq. 3.23 that $T_b = T$ which is also equal to T_R. It is important to realize that these relations are correct only if both the geometry of the source and the radiating medium are not important. This is generally expressed in radio astronomy as "the sources are much larger than the telescope beam".

3.4 Basic Principles of CO Analysis

Microwave radiation from the CO molecule is rather easily detectable because this molecule has a permanent dipole moment. A first approximation of the abundance of the CO molecules can be obtained by a very standard LTE analysis of the CO line radiation. This approach is realistic since the excitation of low rotational transitions is usually close to LTE. For the distribution of CO, one can adopt the simplest geometry, which is an isothermal medium that is much larger than the telescope beam. Consequently, the solution of Eq. 3.23 can be used.

Recall that the emission from the CO molecule is at the millimeter wavelengths (CO J=1→0 at 2.6 mm). For this reason, the background for such observations is dominated by the CMB background radiation which becomes the main significant background radiation field at the frequency of interest since it is present everywhere. A molecular line source is generally observed by switching the telescope beam between "on" and "off" source positions and measuring the difference in antenna temperatures. The observed brightness temperature (or antenna temperature T_A) of a line is often expressed in terms of an observed effective antenna temperature ($T_A^* = T_A/\eta$ where η is the receiver or radio telescope efficiency) as was first proposed by Dickman (1978) and is given by

$$\Delta T_A^* = \Delta T_b^* = (1 - e^{-\tau})\frac{h\nu}{k}\left[\frac{1}{\exp(h\nu/kT_{exc}) - 1} - \frac{1}{\exp(h\nu/kT_R) - 1}\right] \tag{3.24}$$

where the T_R term is the CMB background radiation with a radiation temperature of 2.725 K and the T_{exc} term is the excitation temperature[10]. So basically, the observed emission depends on the excitation temperature and the optical depth τ while T_R is known. Observations of a single line will not allow the derivation of both parameters since there are two unknowns (T_{exc} and τ) and only one observable (T_A^*).

[10]Note that the excitation temperature is the temperature responsible for the emission that originates from a specific transition (for example CO J=1→0) and is often called "rotational" or "vibrational" temperature depending on the origin of the emission. Also, this nomenclature is exactly analogous to the "spin temperature" defined for the HI 21 cm hyperfine transition in Section 3.2.2.

If τ_ν is known, then it is possible to solve for the column density N(CO). But in the case of CO one meets the difficulty that the emission line of this most abundant isotope $^{12}C^{16}O$ always seem to be optically thick. It is therefore not possible to derive any information about the CO column density from this line without assuming a model for the molecular clouds. For the CO molecule, the isotopic ratio is $^{12}CO/^{13}CO \approx 90$ as measured[11] from Orion A observations [Langer & Penzias 1990], so that one expects the relative optical depth of the ^{13}CO line to be smaller than that of the ^{12}CO line. This expectation is at the heart of the standard CO analysis. In most cases the ^{12}CO line is optically thick while its isotopic partner ^{13}CO is optically thin. Observations show that the typical relative brightness of the J=1→0 line is I(^{13}CO)/I(^{12}CO) ∼0.05 - 0.4, in agreement with this expectation. A further assumption is that ^{13}CO and ^{12}CO both arise in the same regions and share the same excitation temperature. Consequently, the following assumptions should be made for the measurements of weak isotope lines of CO molecule.

- All molecules along the line of sight possess a uniform excitation temperature in the J=1→0 transition.
- The different isotopic species have the same excitation temperatures. Usually the excitation temperature is taken to be the kinetic temperature of the gas, T_K.
- The optical depth in the ^{12}CO J=1→0 line is large compared to unity.
- The optical depth for rare transitions, such as the ^{13}CO J=1→0 line, is small compared to unity.
- The ^{13}CO and ^{12}CO lines are emitted from the same volume in space.

Given the assumptions listed above, one can write $T_{exc} = T_K = T$. Note that in this section, the expression T will be used since all temperatures are assumed to be equal with the assumptions made above. In the limit of large optical depth for the ^{12}CO line ($\tau \rightarrow \infty$), the excitation temperature can be derived form Eq. 3.24 and can be written in the simplified form as

$$T_{exc}(^{12}\mathrm{CO}) = \frac{5.53 \text{ K}}{\ln\left(1 + \frac{5.53 \text{ K}}{T_b(^{12}\mathrm{CO}) + 0.82 \text{ K}}\right)} \quad . \tag{3.25}$$

Note that in the above equation, $h\nu/k = 5.53$ K and $(h\nu/k)[\exp(h\nu/kT_R)-1] = 0.82$ K while $T_R = 2.725$ K is used. The term $T_b(^{12}CO)$ is basically the measured brightness temperature of the ^{12}CO line ($T_b^*(^{12}CO)$=$T_b(^{12}CO)/\eta$). On the other hand, since the optical depth of the ^{13}CO line is optically thin ($\tau \ll 1$), one can derive[12] the optical depth by again using Eq. 3.24 as

$$\tau(^{13}\mathrm{CO}) = -\ln\left[1 - \frac{T_b(^{13}\mathrm{CO})}{5.3 \text{ K}}\left(\left[\exp(5.3 \text{ K}/T) - 1\right]^{-1} - 0.16\right)^{-1}\right] \quad . \tag{3.26}$$

[11]Note that this ratio is not uniform along the Galaxy and may change locally.

[12]Note that the ^{13}CO emission line is observed at 110.201 GHz while the ^{12}CO emission line is observed at 115.271 GHZ. Therefore in this derivation, $h\nu/k$ term for ^{13}CO (5.3 K) is numerically different than ^{12}CO (5.53 K).

Recall that it was assumed that both ^{13}CO and ^{12}CO arise in the same regions and share the same excitation temperature, therefore $T_b(^{13}\mathrm{CO}) = T_b(^{12}\mathrm{CO})$. Usually, the total column density is the quantity of interest and can be calculated by using the formula[13]

$$N(^{13}\mathrm{CO}) = 3.0 \times 10^{14} \frac{T \exp(5.3 \text{ K}/T) \int \tau(^{13}\mathrm{CO})(\nu) d\nu}{1 - \exp(5.3 \text{ K}/T)} \quad . \tag{3.27}$$

In the above equation, $T = T_{exc}$ and can be calculated from Eq. 3.25 while $\tau(^{13}\mathrm{CO})$ can also be obtained from Eq. 3.26. Note that the integral is taken over the line profile expressed as a function of line-of-sight velocity (or radial velocity V_r), which is explained in a detailed way in the following section. After obtaining the value for N(^{13}CO), N(^{12}CO) can be derived by assuming an isotopic ratio for ^{13}CO/^{12}CO, usually the locally determined "cosmic" ratio of $\sim$1/90.

3.5 Kinematic Distance Ambiguity Method

The main goal of the Kinematic Distance Ambiguity (KDA) method is to resolve the structure of the Milky Way from observations of molecular clouds. For obtaining the structure, one needs to derive the distances to these molecular clouds and also the distribution of molecular gas in the Galaxy. Moreover, for deriving the fundamental properties of the MCs, such as mass, size and density, the distance information to these molecular clouds of interest is strictly required. Since MCs can not be characterized by a typical length nor a typical luminosity, traditional "standard ruler" or "standard candle" techniques do not work. Consequently, it becomes a quite challenging task to derive these distances.

There were some previous studies which used CO and HI spectral observations to derive the rotation curve for our Galaxy [Burton & Gordon (1978)], [Clemens (1985)]. In these studies, basically the maximum radial velocity of gas, which occurs for gas physically located at the tangent point, was measured. Note that the observed radial velocity (or the line of sight velocity) of a cloud which is basically the observed peak in the velocity spectrum is the projection of cloud's orbital velocity around the Galactic center onto the line of sight. At the tangent point[14], the orbital velocity of a cloud is parallel to the line of sight. Consequently, the velocity vector of the cloud is aligned with the line of sight and assumes its maximum value. Establishing the rotation curve was the key point for understanding gas distribution in the Galaxy. By the use of the rotation curve, one can relate the spectroscopically observed radial velocity of a cloud to its galactocentric radius and distance. The Clemens rotation curve [Clemens (1985)] which is used in the KDA method for deriving the distances, can be seen in the Fig. 3.8.

The derivation of the distances from the observed radial velocities of the MCs, by the use of the rotation curve, is called KDA method. Although the kinematic distance method

[13]Derivation of this formula uses the Einstein coefficients and can be found in Section 15.4.1 of [Wilson (2009)].

[14]See only the left part of the Fig. 3.9 for a detailed sketch and the tangent point, more detailed explanation of the HI and CO spectrum for the near and far distances that can be seen in the right part of the Fig. 3.9 will be given in the next section.

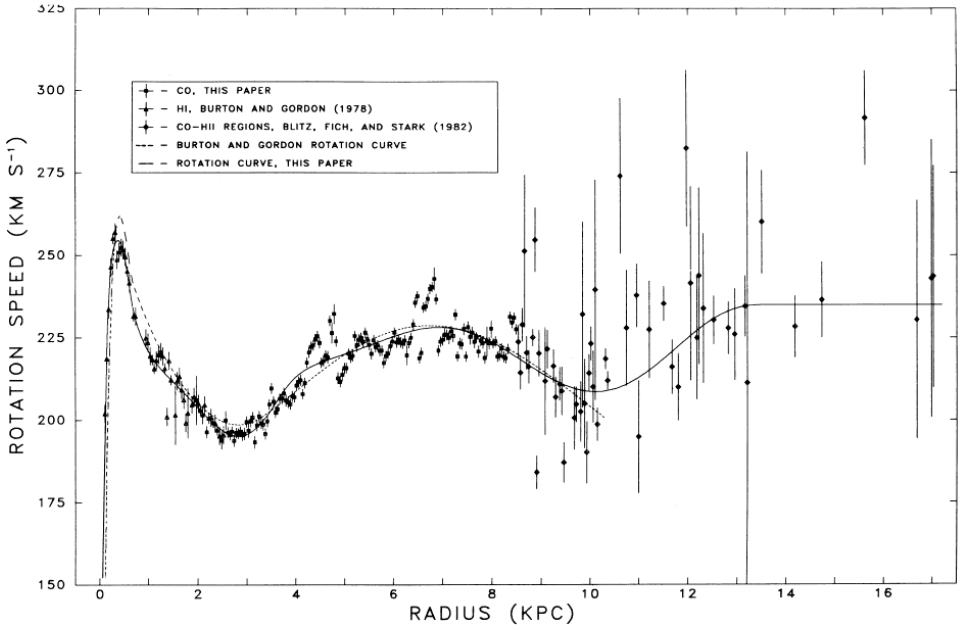

Figure 3.8: Clemens Rotation Curve of the Milky Way Galaxy. Credit: [Clemens (1985)]

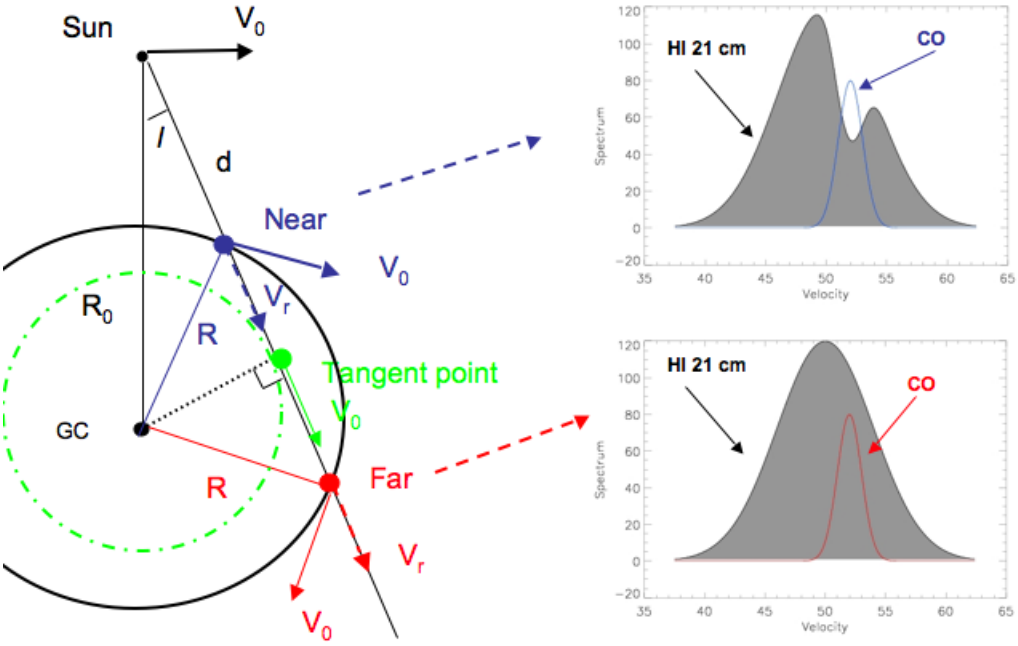

Figure 3.9: Sketch of the HI self-absorption method to resolve the KDA. The green point indicates the tangent point while the blue and the red points indicate the positions of near and far clouds which have similar observed radial velocities, consequently the same galactocentric radius. The corresponding HI & CO spectra for the near and the far clouds are shown in the upper and lower right figures, respectively. Credit: [Roman-Duval (2009)]

can have some accuracy problems because of the localized velocity perturbations due to spiral shocks, expanding shells and non-circular motions near the Galactic bar, it can still be regarded as the most efficient method to derive distances to molecular clouds.

The Doppler shift of a spectral line yields the observed line of sight velocity of the cloud. With the knowledge of the rotation curve of the Galaxy, one can relate these observed radial velocities to a unique galactocentric radius. For a given galactic longitude and the radial velocity, there is a unique solution for the galactocentric radius given by the expression

$$r_{gal} = R_0 \sin(l) \frac{V(r)}{V_{r_{gal}} + V_0 \sin(l)} \tag{3.28}$$

where r_{gal} is the distance of the observed MC to the center of the galaxy, R_0 is the galactocentric radius of the Sun, V_0 is the orbital velocity of the Sun around the galactic center, l is the angular distance of the cloud of interest from the galactic center, $V_{r_{gal}}$ is the experimentally observed radial velocity of the cloud along the line of sight and the term $V(r)$ is the orbital velocity of the cloud of interest.

Note that at this point, one has to take into account that, for the inner Galaxy observations ($r_{gal} < R_0$), this derived galactocentric radius corresponds to two different distance values along the line of sight. These two distances are defined as "the near" and "the far" kinematic distances, located on either side of the tangent point. These two solutions for the near and far distances, which indicates the distance between the Sun and the MCs, can be obtained by using the expression

$$d = R_0 \cos(l) \pm \sqrt{r_{gal}^2 - R_0^2 \sin^2(l)} \quad . \tag{3.29}$$

The near and far kinematic distances to the clouds along the line of sight can be calculated using the Clemens rotation curve of the Milky Way [Clemens (1985)] scaled to (R_0, V_0) = (8.5 kpc ± 0.5 kpc, 220.0 km s^{-1}± 7.0 km s^{-1}). Note that for the distance calculations, one can assume a flat rotation curve consequently V_R=V_0 assumption can be made. This, so-called, kinematic distance ambiguity makes the determination of kinematic distances very challenging in the inner Galaxy. It stems from the fact that the radial velocity of a cloud is the same at the near and far distances. At the tangent point, the near and far distances are identical ($d = R_0.\cos(l)$ and $r_{gal} = R_0.\sin(l)$). Consequently, the radial velocity of a cloud is maximal and equal to its orbital velocity. In the outer Galaxy ($r_{gal} > R_0$), there is a unique solution to the distance problem. The radial velocity decreases monotonically with distance to negative values. The method should be applicable to all molecular clouds, whether or not they contain a maser or a HII region.

3.5.1 HI Self-Absorption and 21 cm Continuum Absorption in the KDA Method

Studies on the structure and composition of molecular clouds have shown that there are various types of molecules located within molecular clouds. Both ^{13}CO and ^{12}CO co-exist with H_2 and HI within the cold ($T_{kin} \approx$ 10 - 20 K) central regions of molecular clouds [Goldsmith & Li (2007)]. Especially, atomic hydrogen exists in the cloud formation region

before the cloud is formed while it is consequently produced by the dissociative ionization of H_2 caused by the background Galactic cosmic-rays. It has been shown that the density of atomic hydrogen within the dense MCs is not related to the total gas density of MCs [Dyson & Williams (1980)]. Note that the Galactic CRs constitute the mechanism to heat the inner regions[15] of molecular clouds and can explain their temperature of about 10 K. Consequently, the high column densities and the low temperatures of HI in the interior parts of MCs make them quite opaque and cold, which allows the formation of the absorption lines that can be observed due to the warm background Galactic 21 cm radiation [Jackson (2004)].

This feature is at the heart of the HI Self-Absorption (HISA) method. Basically, absorption or the self-absorption feature of the 21 cm HI line can be used as a technique for discriminating the clouds located at near or far distances. Because the ISM is filled with warm HI with temperatures ranging between 10^2 to 10^4 K temperatures, the cold HI (T = 75 - 100 K) can only be found in the interior parts of the dense molecular clouds. For example, one can imagine two molecular clouds, namely "N" and "F", located at the near and the far distances, respectively, as it can be seen in the left part of the Fig. 3.9. Consequently, they have same the observed radial velocities. The cloud N is located in front of most of the warm Galactic background HI 21 cm radiation, located at the far distance and emitting at the same velocity as that of the cloud. Because the cold HI located within the molecular cloud N is much colder than the warm HI background, the radiation emitted at the far distance by the warm HI background will be absorbed by the cloud N on its way to the Earth. Consequently, if one investigates the observed HI 21 cm spectrum, there will be an absorption feature in the HI spectrum exactly at the same velocity that is observed from the CO spectrum as can be seen both for cloud N and F in the right part of the Fig. 3.9. Note that at this point, both CO and HI spectrum are required to resolve HISA. The CO spectrum is used for the comparison, while the distance (near or far) information is hidden in the HI spectrum. Therefore by comparing the CO and HI spectrums, one can resolve if the distance to MC is near or far. This phenomenon is basically known as HI self-absorption and is schematically illustrated in Fig. 3.10.

Similarly, the cloud F located at the far kinematic distance lies in front of warm HI Galactic 21 cm background radiation. In this case, the background radiation has a different radial velocity than the velocity of the cloud F as illustrated in the top right panel of Fig. 3.10 due to the nature of the Galactic rotation curve. Consequently, cloud F cannot absorb the radiation emitted by the warm HI background. Moreover, there will be warm HI in the foreground of the cloud F, which is emitting at the same velocity as the cloud F. Therefore, in the spectrum, there will not be any HI self-absorption feature toward a cloud F. Thus, an analysis of the HI 21 cm spectrum along the line of sight to a molecular cloud can resolve the kinematic distance ambiguity. If HI self-absorption is coincident at the same velocity as CO emission, then the molecular cloud is located at the near kinematic distance. Whenever HISA feature is absent, the cloud is located at the far kinematic distance.

[15]The atomic hydrogen is shielded from outside radiation due to the thicker outer layers of the MC. So the HI in the interior regions of MCs is much colder than the rest of the Galactic atomic hydrogen, which has a temperature of 75 - 100 K and up to 10^4 K for the warm component [Kulkarni (1982)].

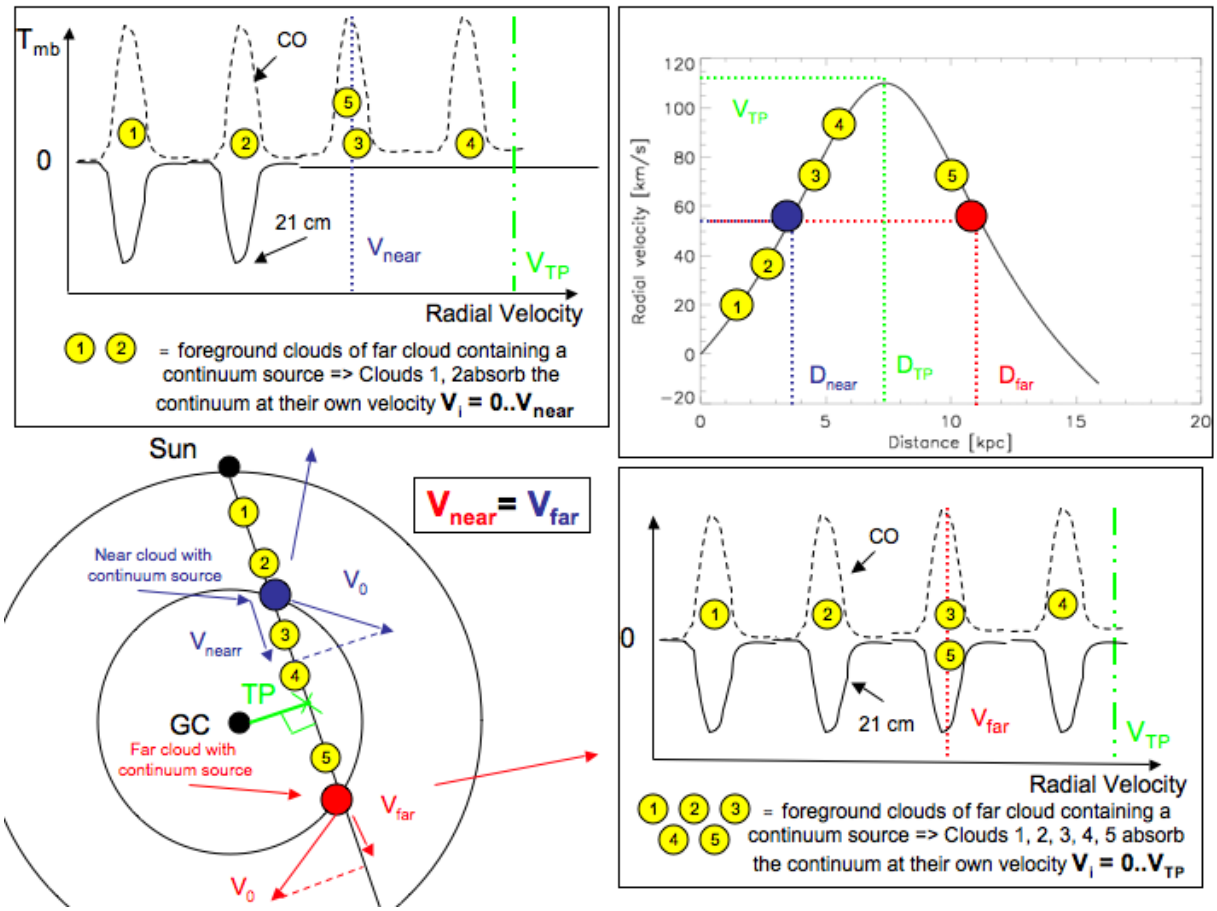

Figure 3.10: Schematic of the 21 cm continuum absorption method to resolve the KDA. The 21 cm continuum emitted by the source embedded in the cloud of interest is absorbed by all foreground molecular clouds. If the cloud of interest is located at the near kinematic distance (cloud in blue), the foreground molecular clouds (clouds 1 and 2) have velocities smaller than the velocity of the cloud (see the top right panel). As a consequence, the foreground molecular clouds absorb the 21 cm continuum emitted from the cloud of interest up to its radial velocity only. The HI 21 cm spectrum shows absorption lines at velocities up to the velocity of the cloud of interest (top left panel). On the other hand, if the cloud of interest is located at the far kinematic distance (cloud in red), the foreground molecular clouds (clouds 1, 2, 3, 4, 5) can have velocities up to the velocity of the tangent point (marked with green cross). As a result, the HI 21 cm spectrum exhibits absorption lines up to the velocity of the tangent point (V_{TP}), each absorption line corresponding to a CO emission line from the foreground molecular clouds. Credit: [Roman-Duval (2009)]

3.5.2 Error Sources in the KDA Method

Note there there are several error sources for the KDA method when estimating the distance to molecular clouds. One basically measures the radial velocity of clouds, or in other words the projection of their velocity vector around the GC onto the line of sight. Note that the terms V_R and R_0 in Eq. 3.28 are taken as 220 km s^{-1} and 8.5 kpc respectively by assuming a flat rotation curve as suggested by Roman-Duval (2009) while calculating the distances to molecular clouds. This assumption leads to a systematic error in the kinematic distance estimation of MCs. Furthermore, spiral arms of the galaxy induce shocks associated with non-circular velocity discontinuities and velocity gradients, so basically the motions are not strictly circular anymore as one gets closer to the Galactic Center. This produces again a systematic error in the observed velocity of a cloud compared to pure circular orbital motions which was estimated around $\sim$10 km s^{-1} [Clemens (1985)]. Another error source in the kinematic distance estimation of MCs is the $\sin(l)$ term which is the angular distance of the cloud of interest from the GC and should be taken into account. Finally, additional errors are related finding of the peaks in the velocity spectrum. These are the errors coming from fitting the peaks to a Gaussian function. All of the errors mentioned in this subsection were taken into account for calculating the kinematic distances in Section 5.3.

3.6 Gamma-Rays from Molecular Clouds

The γ-ray emission from molecular clouds is assumed to originate from the pp interaction between the cosmic-rays and the material included in MCs. Therefore this emission can give unique information about the proton acceleration sites inside or around MCs and also about the background galactic CRs.

The VHE region of γ-rays from 100 GeV to 100 TeV is of a special interest, since these γ-rays carry direct information about the sources responsible for formation of the spectrum of galactic CRs extending to the so-called 'knee' around 10^{15} eV. The existence of a CR accelerator is a necessary but not a sufficient condition for effective γ-ray production. Surely a target component is needed and GMCs are great candidate objects to play that role in our Galaxy. Consequently, the emission from giant molecular clouds located in the vicinity of CR accelerators can provide important information to solve the origin of galactic CRs.

3.6.1 Emissivity of π^0-decay Gamma-Rays

The emissivity of the π^0-decay γ-rays originating from pp interactions can be described as the number of photons produced per second per hydrogen atom. In its general form for an arbitrary proton spectrum J_p (E_p), it can be written as

$$q_\gamma(E_\gamma) = 2 \int_{E_\pi}^{\infty} \frac{q_\pi(E_\pi)}{(E_\pi^2 - m_\pi^2 c^4)^{1/2}} dE_\pi \quad , \tag{3.30}$$

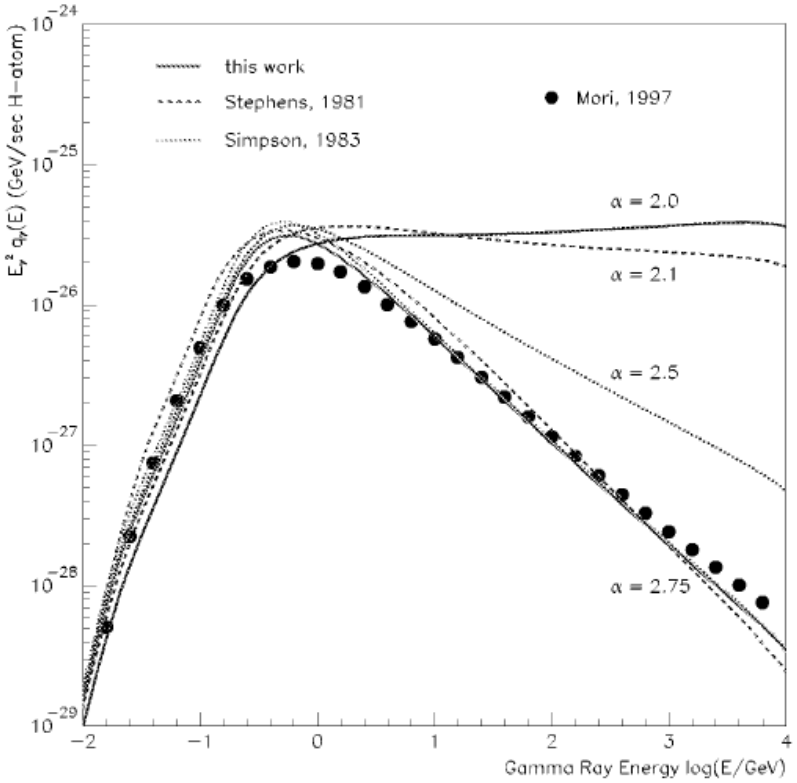

Figure 3.11: The emissivities of π^0 γ-rays for different power-law spectral indexes. The black data points were taken form [Mori (1997)]. Credit: [Huang (2003)]

where $q_\pi(E_\pi)$ is

$$q_\pi(E_\pi) = 4\pi\eta \int_{E_p}^{\infty} dE_p J_p(E_p) \frac{d\sigma_\pi(E_\pi, E_p)}{dE_\pi} \tag{3.31}$$

where most of the parameters are described in detail in Section 2.3.2.3. Note that η here is the correction factor taking into account the π^0 production from the channels involving heavier nuclei. For the standard composition of the cosmic-rays and the interstellar gas, η was estimated to be around $\approx$ 1.4 - 1.5 [Dermer (1986)].

Figure 3.11 shows the comparison of the emissivities of π^0 γ-rays obtained from Eq. 3.30 for power-law spectra with different spectral indexes. Note that the CR proton energy spectrum was normalized by using the CR energy density of 1 eV cm^{-3}. By using the Eq. 3.31 and assuming the proton spectrum is the cosmic-ray spectrum measured around the Sun as

$$J^p_\odot(E_p) = 2.2 \times E^{-2.75}_{\rm GeV} \quad {\rm GeV}^{-1}{\rm cm}^{-2}{\rm s}^{-1}{\rm sr}^{-1} \quad , \tag{3.32}$$

one can also calculate the emissivity around the solar neighborhood. For the γ-ray emissivity above 100 MeV, Eq. 3.30 can be reduced to

$$q_\odot(E > 100 \text{ MeV}) = 1.53 \times 10^{-25} \eta \text{ s}^{-1}(\text{H-Atom})^{-1} = q_{-25}(E > 100 \text{ MeV}) \tag{3.33}$$

where $q_{-25}(E >$100 MeV) is the emissivity of γ-rays above 100 MeV around the Sun,

provided by the background galactic cosmic-rays.

3.6.2 Giant Molecular Clouds as Tracers of Cosmic-Rays

Assuming that the observed γ-rays originate from the pp interaction of cosmic-rays with the ambient gas in molecular clouds, the expected γ-ray flux can be written in the general form as

$$F_\gamma = \frac{\int\limits_{Volume} n(\mathbf{r}) q_\gamma(E_\gamma) d^3(\mathbf{r})}{4\pi d^2} \tag{3.34}$$

where $n(\mathbf{r})$ is the number density and d is the distance to the molecular cloud from the Earth. Note that the integral is taken over the volume of the MC and that it is assumed that the distance to the molecular cloud (d) is much greater than the diameter of the molecular cloud of interest. Because the emissivity term has no spatial dependence, the integration of the gas density over the volume of the molecular cloud will basically give the total mass of the molecular cloud. Therefore, Eq. 3.34 can be written in the following reduced form

$$F_\gamma = \frac{M_{Cloud}}{m_p} \frac{q_\gamma}{4\pi d^2} \tag{3.35}$$

where M_{Cloud} is the mass of the molecular cloud that can be obtained from CO and HI observations. Note that M_{Cloud} can be written as $M_{Cloud} = m_p.n.V_{Cloud}$, where n is the gas number density, V_{Cloud} is the volume of the cloud and m_p is the mass of the proton[16]. At this point, for the theoretical calculations, one should make an assumption about the shape of the cloud. In general, it's taken as a sphere but surely MCs do not generally have rigid well-defined shapes.

The integral γ-ray flux above a given energy E_γ, originating from the background Galactic cosmic-rays, can be expressed as

$$F_\gamma(\geq E_\gamma) = 10^7 \frac{M_5}{d^2_{\rm kpc}} q_{-25}(\geq E_\gamma) \quad \mathrm{cm}^{-2}\mathrm{s}^{-1} \tag{3.36}$$

where $M_5 = M_{Cloud}/10^5 M_\odot$ and $d_{\rm kpc} = d/1$ kpc. Actually, $M_5/d^2_{\rm kpc}$ is one of the principal parameters that determines the γ-ray visibility of giant molecular clouds. The γ-ray visibility concept is related whether the emission from the molecular cloud can be detected from Earth or not. The γ-ray emissivity q_γ can differ from GMC to GMC and also from the local emissivity $q_\odot$. Consequently one can define a ratio K_{cr} to quantify the relative change as

$$q_\gamma = K_{cr} q_\odot \quad . \tag{3.37}$$

The γ-ray emissivity of a GMC can be compared with the local emissivity around the Sun by using K_{cr}. For making this comparison, one should assume that the distribution of the background CR flux does not vary significantly across the entire Galaxy. If K_{cr} is found around 1, then the GMC is called "passive", which means that it is being illuminated

[16]Note that it is assumed that the mass of Hydrogen atom is equal to the mass of the proton

by the Galactic background CRs. On the other hand if K_{cr} significantly exceeds unity, then one can conclude that the GMC is being illuminated by a nearby accelerator, which can be close by or located within the cloud. Note that an uncertainty up to a factor of 3 on K_{cr} is possible because of the unknown contribution coming from the bremsstrahlung and the IC channels.

Up to now, the γ-ray spectrum created by pp interactions, the column density and also the emissivity of molecular clouds were discussed. One can combine these results to produce the expected γ-ray spectra from the molecular clouds observed from Earth. In the general formalism, the differential photon flux at Earth produced by CRs interacting with the gas from a given region in the Galaxy is given in its general form [Casanova (2010)] as

$$\frac{dN_\gamma}{dAdE_\gamma dtd\Omega} = \int_{E_{p,min}}^{E_{p,max}} dE_p \frac{d\sigma_{pp}}{dE_p} J_p(E_p) \int_{l_{d,min}}^{l_{d,max}} dl_d n(l,b,l_d) \tag{3.38}$$

where the first integral is taken over the energy of the protons and the second is taken over the galactic distance l_d, which is the distance from the Sun. The term $n(l,b,l_d)$ is the gas density profile along the line of sight as function of the galactic coordinates, latitude, b, longitude, l, and l_d, and $J(E_p)$ is the assumed proton spectrum. The spectral dependence of the photons emitted by CR protons, expressed in terms of the differential cross section, $d\sigma_{pp}/dE_p$, is calculated using the parametrization of Kelner [Kelner et al. (2006)] as already discussed and shown in Fig. 2.9. Note that the correction factor η=1.5 should also be applied to the proton spectrum for taking into account the contributions coming from the emission from heavier nuclei. The first integration in Eq. 3.38 is the expected γ-ray emission from the pp interactions, while the second integration over l_d is summing all $n(l,b)$ values over the line of sight, which is equal to the "column density" over the line of sight, that can be easily obtained from CO and HI observation data. The observed flux in terms of $\mathrm{TeV}^{-1}\mathrm{cm}^{-2}\mathrm{s}^{-1}$ can be written as

$$\Phi_{observedFlux} = \frac{dN_\gamma}{dAdE_\gamma dt} = \frac{\Phi_\gamma(E_\gamma) \times \text{Column Density} \times \text{Area Of the Molecular Cloud}}{4\pi \times (\text{Distance to the MC})^2} \tag{3.39}$$

where the area of the molecular cloud is the area taken into account for the analysis, the column density is the average column density of the MC within the used solid angle. Both column density and distance information can be obtained from the analysis of CO and HI data.

Chapter 4

Imaging Air Cherenkov Telescopes

As mentioned in the Section 2.2, the Earth is continuously bombarded by an isotropic flux of background CRs, which consist mainly of protons, heavier nuclei and a small fraction of electrons and positrons, spanning over 10 orders of magnitude in energy. Because these charged CRs are deflected by the magnetic fields on their way, they lose their direction information and that makes it impossible to trace them back to their origin.

The photons, as well as the neutrinos, are not affected by these deflecting magnetic fields, they can be used for tracing back to the origin of their astrophysical sources, consequently, they can serve as messenger particles as illustrated in Fig. 4.1. But at this point, another problem arises because of the small magnitude of the photon flux when compared to the flux of cosmic rays, especially at energies above a few tens of GeV. The γ-rays can be directly detected by satellite experiments up to energies of around 10 GeV. But as the energy of the primary γ-ray increases, it becomes extremely difficult to detect them with detectors having the few square meters detection areas of satellite experiments and also because of the steep decline of the γ-ray flux with increasing energy. Therefore, for detecting the higher energy γ-rays, ground-based IACTs use indirect measurements of the produced secondary light. This produced secondary light can be recorded by IACTs which use the Earth's atmosphere as a calorimetric detector.

This chapter gives brief information about IACTs including the detection techniques. A detailed description of the main characteristics and components of the H.E.S.S experiment and basic concepts of the Cherenkov Telescope Array project are also presented.

4.1 The IACT Technique

The imaging atmospheric Cherenkov technique was first pioneered by the Whipple Observatory located in Arizona. The first VHE γ-ray source, the "Crab Nebula" [Weekes (1989)] was detected in 1989. In this approach, ground-based Cherenkov telescopes are used for catching the Cherenkov light emitted by extensive air showers. The extensive air showers are initiated when a VHE particle enters the atmosphere and interacts with the atmospheric material. Recorded Cherenkov images from extensive showers can be used for reconstructing the direction and the energy of primary particle. In this approach, it is also extremely important to discriminate the images initiated by photon-induced and

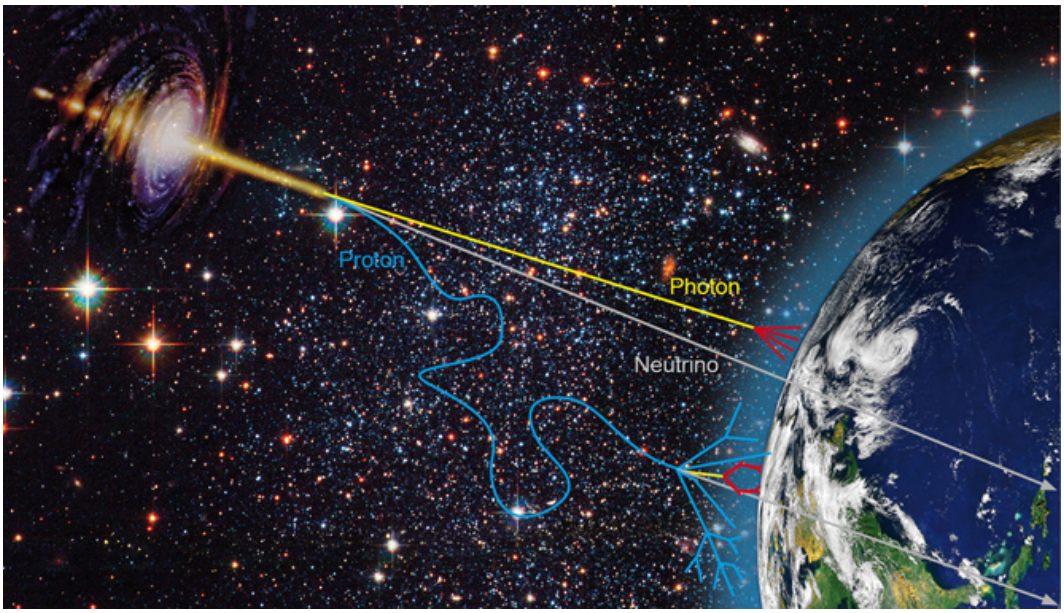

Figure 4.1: The path followed by protons, neutrinos and photons. Protons are deflected on their way by magnetic fields while photons and neutrinos are not affected. Credit: http://www.hap-astroparticle.org/

CR-induced air showers.

Cherenkov radiation is emitted when a charged particle passes through a dielectric medium at a speed faster than the speed of light in that medium as illustrated in Fig. 4.2. The Cherenkov light is emitted with the opening Cherenkov angle φ described as

$$\cos(\varphi) = \frac{1}{\beta n(\lambda)} \tag{4.1}$$

where $n(\lambda)$ is the refractive index of the medium and $\beta = v/c$ is the speed of the particle. Basically, when a charged particle passes an insulator with a speed above the speed of light in that medium, the particle's charge disturbs the local electromagnetic fields of the atoms of the insulator. Consequently, the electrons in the atoms are displaced which causes polarization. As this stimulated state restores itself back to equilibrium state after the particle has passed, the Cherenkov photons are emitted. When the speed of the charged particle is less than the speed of light in this medium ($v < c/n$), the produced Cherenkov photons destructively interfere with each other, therefore no radiation can be detected. On the other hand, if the particle travels faster than the speed of light in that medium ($v > c/n$), the photons constructively interfere and the Cherenkov radiation becomes observable. The Nobel prize in physics was awarded to P. A. Cherenkov, I. M. Franck and I.Y. Tamm for the discovery and the interpretation of this effect in 1958.

The number of Cherenkov photons in the frequency interval (ν, $\nu + d\nu$) emitted by a particle with charge Z moving with a velocity β in a medium with a refractive index of n, is given by the formula

$$N(\nu)d\nu = 4\pi^2 \frac{(Zq)^2}{hc^2}\left(1 - \frac{1}{n^2\beta^2}\right)d\nu \quad . \tag{4.2}$$

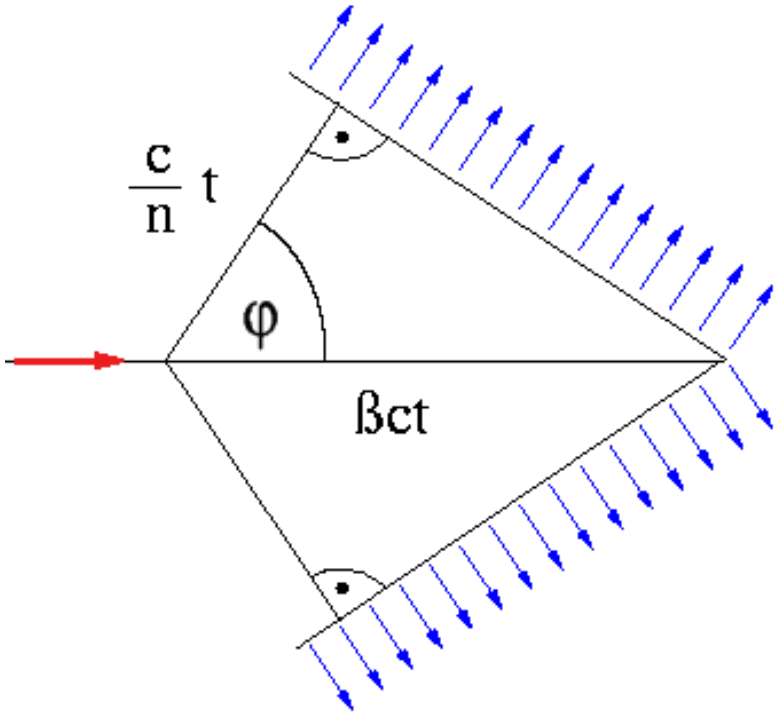

Figure 4.2: Illustration of emitted Cherenkov radiation from a charged particle moving with a speed faster than the speed of light in that medium.

Note that this formula has the following important features.

- The emitted photon spectrum is exactly identical for particles having the same charge Z, independent of the nature of the particle. For instance, the same spectrum will be emitted for protons, electrons, pions, muons and for their antiparticles.
- As the charge of the particle (Z) increases, the number of emitted photons increases as Z^2.
- $N(\nu)$ increases with the velocity of the particle.
- $N(\nu)$ is approximately independent of ν. So one observes that $dN(\nu) \propto d\nu$.
- As the spectrum is uniform in frequency, and $E = h\nu$, this means that the main energy output of the radiation is concentrated in the extreme short-wave region of the spectrum, $dE_{Cherenkov} \propto \nu \; d\nu$.

By using the principles of the Cherenkov radiation emission, imaging of the air showers can be recorded by ground-based Cherenkov telescopes, consequently the recorded images can be interpreted and the properties of the primary particle can be obtained. Figure 4.3 shows the leading IACTs in the world with their location.

4.1.1 Extended Air Showers

As a VHE particle (CR or γ-ray) enters the Earth's atmosphere, it interacts with the molecules and the atmospheric nuclei creating secondary particles. The first interaction

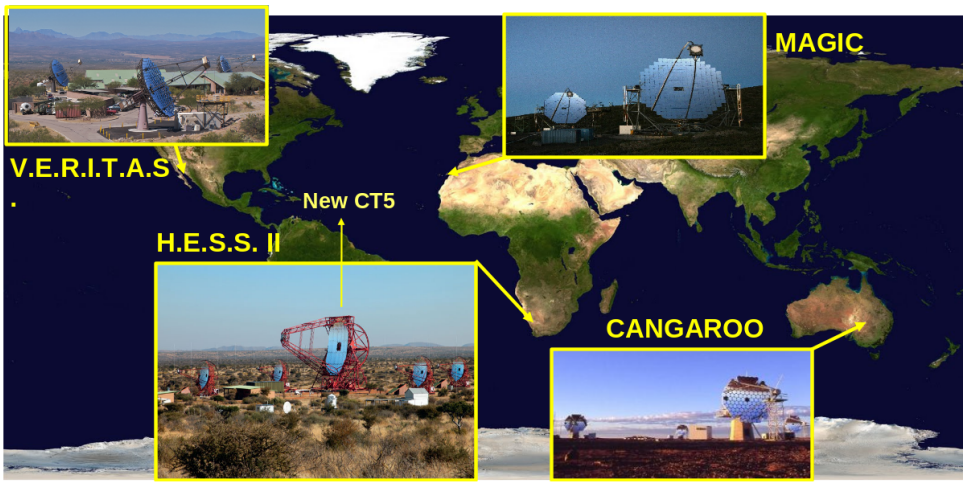

Figure 4.3: Current Imaging Air Cerenkov Telescopes in operation. Each IACT location is also shown on the map.

height is typically around 10 km. The created secondary particles in the shower carry most of the kinetic energy and momentum of the primary particle and continue interacting with the atmospheric nuclei via pair production and bremsstrahlung processes. This series of interactions forms a structure called "Extended Air Shower" or "Extensive Air Shower".

As these created secondaries move faster than the speed of light in air because they are extremely energetic, they emit Cherenkov radiation. The evolution of air showers is mainly governed by the initial particle energy and the energy loss processes. The longitudinal development of air showers follow the initial direction of the primary particle that enters the atmosphere, which allows the direction reconstruction of the primary particle. Also, the total number of particles produced in a shower is governed by the primary particle energy. Consequently, energy reconstruction of the primary particle is available by using the information of the collected amount of the produced Cherenkov photons. After each interaction in the shower development process, the number of particles increases until reaching a maximum while the average energy per particle decreases to a threshold energy where no further shower development, or in other words no particle creation takes place. In addition, the particle composition of extensive air showers and the geometry of the Cherenkov light on the ground depend on the type of primary particle. Electrons, positrons and photons undergo electromagnetic interactions and thus induce "Electromagnetic showers". Air showers induced by hadrons evolve differently in the atmosphere. In the hadronic shower process, new particles such as pions and kaons are produced which lead to hadronic sub-showers and a different composition, consequently a different shape of the Cherenkov light on the ground.

4.1.1.1 Electromagnetic Showers

An electromagnetic air shower is the cascade of particles induced by a VHE photon or electron. Basically, γ-rays and electrons (or positrons) behave in a quite similar way when they enter the Earth's atmosphere at high energies. In both of these cases, the shower evolves by the generation of particles via pair production and the bremsstrahlung

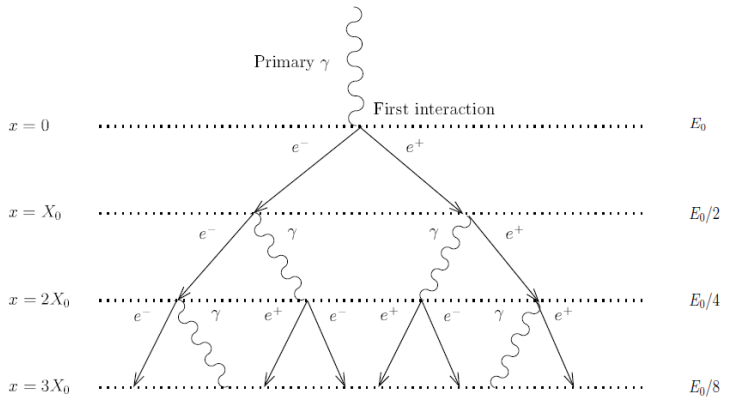

Figure 4.4: Bethe-Heitler model of electromagnetic shower showing both pair production and bremsstrahlung process in each radiation length.

processes.

When a VHE photon enters the atmosphere, it interacts with an atmospheric nucleus resulting in a pair production of e^+ and e^-. The pair creation process is the dominant energy loss mechanism for γ-rays for energies above 100 GeV. Pair creation typically takes place after traversing a radiation length in the air, which is (for air) $X_0 = 37.2$ g cm^{-2} [Eidelman (2004)]. The total thickness of the Earths atmosphere is $\sim$1000 g cm^{-2}. For this reason, γ-rays can not reach to ground level without getting into any interaction. That's why it is impossible to detect directly the VHE γ-rays by ground-based detectors. The produced electron and positrons are deflected by the air molecule and emit bremsstrahlung radiation. The created bremsstrahlung photons again generate a cascade of ultra-relativistic charged particles. In each interaction step, a new generation of photons and e^+ e^- pairs are produced and the total number of particles increases while the average energy per particle decreases. This model of the shower, where the radiation lengths for both the pair production and bremsstrahlung processes are set equal, is called Bethe-Heitler model [Heitler (1954)] and is illustrated in the Fig. 4.4.

Primary Photon Energy	X_{max} (g cm^{-2})	z_{max} (km)	N_{max}
10 GeV	175	12.8	1.6×10^1
100 GeV	261	10.3	1.3×10^2
1 TeV	346	8.4	1.1×10^3
10 TeV	431	6.8	1.0×10^4
100 TeV	517	5.5	9.3×10^4

Table 4.1: Shower characteristics for primary γ-ray energies of 0.01, 0.1, 1.0, 10.0 and 100.0 TeV. X_{max} is the shower maximum, z_{max} is the altitude and N_{max} is the maximum number of the particles at X_{max}. The data were taken form [Weekes (2003)].

Finally, the cascade dies out when the ionization losses of the produced electrons and positrons are greater than the ones caused by the bremsstrahlung. This happens when

the average particle energy falls below a critical energy threshold of 80 MeV after ∼10 cascade steps[1] in a typical atmospheric height of around 10 km. At this point, the shower maximum is reached where the shower contains the maximum number of particles. Table 4.1 shows some characteristics of the showers initiated by primary γ-rays having different energies.

The particles in the shower emit Cherenkov light if they have energies greater than $E > m_x c^2/(1-n^{-2})^{1/2}$ where m_x is the mass of the particle of interest. The longitudinal extent of the shower is always related to the energy of the primary particle and to the subsequent energy losses of the secondary particles. Because the total thickness of the atmosphere is more than $20X_0$, the shower maximum is reached well above the sea level. The dominant process determining the lateral shower development is multiple Coulomb scattering. A charged particle traversing the air has many small-angle Coulomb scatterings from atmospheric nuclei. Both bremsstrahlung and pair production contribute to the lateral spread of the secondary particles with respect to the shower axis, but this is a small contribution. For example a radiated bremsstrahlung photon from an electron has an emission angle of $\sim(1/\gamma)$, where γ is the Lorentz factor of the electron. Therefore, the high energy electrons having quite large Lorentz factors radiate with relatively small opening angle and directional divergence from the shower axis. Therefore the shower particles travel in a narrow front with a width of a few nanoseconds while the full shower develops within a few microseconds. The Coulomb scattering distribution, which has a Gaussian shape for small scattering angles, can be well described by the Moliere theory [Bethe (1953)]. The lateral distribution of electromagnetic showers in different materials is given by the Moliere radius (R_{mol}) as

$$R_{mol} = 0.0212 \times \frac{X_0}{E_c} \tag{4.3}$$

where E_c is the critical energy for a given material. For the electromagnetic air showers, R_{mol} is around 80 m at the sea level [Heck (1998)]. On average 90% of the shower energy is deposited in a cylinder around the shower axis with radius of R_{mol}.

The typical opening angle of the Cherenkov light is around 1.4°. So the Cherenkov photons will be emitted into a light pool of ∼100 m radius for a typical ground-based observation height of ∼2000 m above the sea level with a typical first interaction altitude of 10 km. Also the photon density on the ground scales approximately linearly with the energy of the primary γ-ray and is around 100 photons per square meter for the energy of 1 TeV. The Cherenkov photons arrive at the ground within a very narrow time window of a few tens of nanoseconds[2].

On the other hand, if a primary particle is an ultra-relativistic electron, the shower development is approximately the same as for the γ-rays. The first interaction in this case is not the pair creation but the bremsstrahlung process. In VHE observations, electron and positron initiated air showers constitute a background for the γ-ray detection. The mean free path length for pair creation at high energies is slightly larger than a radiation length for bremsstrahlung (factor 9/7). The usage of this feature has been discussed

[1]The number of steps depends logarithmically on the energy of primary particle.

[2]Note that images of Cherenkov showers in a large field of view Cherenkov telescope can last ∼100 ns.

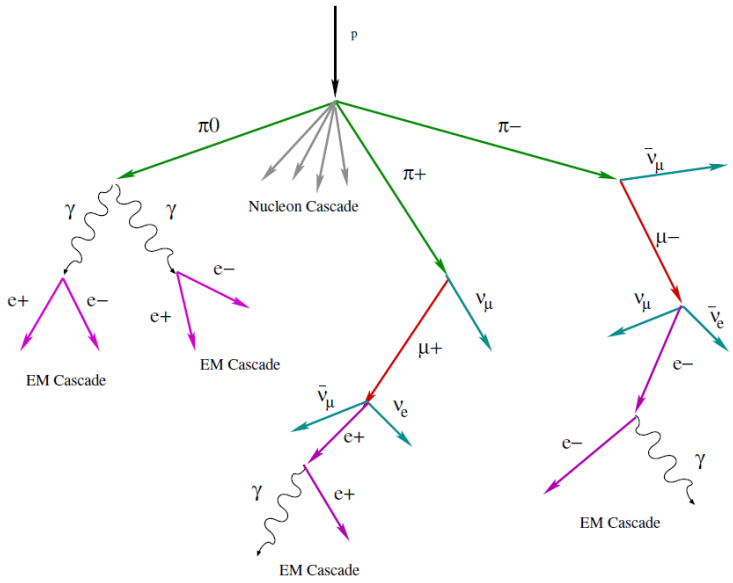

Figure 4.5: Development model of a hadron-induced air shower. This figure is adapted from [Jelley (1958)]

for separating the electron(positron) induced showers from the γ-rays induced showers [H.E.S.S. Collaboration (2008a)].

4.1.1.2 Hadronic Showers

The protons and heavier nuclei entering the atmosphere constitute the major part of the cosmic particles interacting with the Earth's atmosphere. Fortunately, the development of the hadron-induced showers differs significantly from the shower development for photons and electrons, which can basically be used for separating them. For the first interaction, hadrons interact nearly only via strong interaction with the atmospheric nuclei. The nuclear interaction length in air is $\sim$90 g cm^{-2} [Eidelman (2004)] which is nearly $\sim$3 times larger than the radiation length for the γ-ray interactions. Hadronic interactions are much more complex and the shower induced by them evolves in a complicated way. The strong interaction results in the production of secondaries, mainly mesons like pions and kaons, but also nucleons (neutrons, protons) and hyperons[3] (Λ, Σ), are created. Again a hadronic cascade is generated from these secondary particles that also interact strongly with the air nuclei.

The hadron-induced air showers have two components, namely an electromagnetic and a hadronic component. The shower core generally consists of hadronic particles which constantly feed the electromagnetic component via decay of neutral and charged mesons. Especially the pions play an important role in the shower development. The neutral pions decay instantly after a mean lifetime of 8.4×10^{-17} s into two photons, consequently these photons generate electromagnetic sub-showers. On the other hand the charged pions having relatively longer lifetime of 2.6×10^{-8} s, decay mainly into muons which later decay into electrons and neutrinos. The charged pions with sufficiently large Lorentz

[3]Note that in particle physics, a hyperon is any baryon containing one or more strange quarks, consequently strangeness $S \neq 0$.

factor can have strong interactions and transfer ∼1/3 of their energy into neutral pions. The development of a hadronic shower is illustrated in Fig. 4.5. In each interaction, approximately more than 1/3 of the energy is transformed to the electromagnetic part. Eventually, most of the primary hadron energy entering the earth atmosphere is transferred to electromagnetic sub-showers [Engel (2011)]. The main energy losses are due to neutrino and muon production and also the ionization losses of electrons.

4.1.1.3 Comparison of Electromagnetic and Hadronic Showers

Since hadronic and electromagnetic showers have different development processes in the atmosphere, one expects to have different images recorded by the ground based IACTs from these showers. By using the knowledge of the shower development, hadronic and electromagnetic showers can be discriminated from each other. The main differences between these 2 types of showers can be listed as follows :

- Since the interaction length of hadrons is ∼3 times larger than the radiation length X_0, the longitudinal size of hadronic showers is larger than that of γ-ray showers with similar energies. Therefore, hadrons penetrate deeper into the atmosphere, leading to a larger maximum shower depth.

- The lateral development of hadronic showers is wider than that of electromagnetic showers. The secondary particles produced by strong interactions and weak decays in hadronic showers have high transverse momenta, consequently the lateral extension of the hadronic showers are larger with respect to the electromagnetic showers.

- Complex multi-particle creation processes are involved in the development of hadronic showers when compared to electromagnetic showers. Therefore the hadronic shower is less regular because of the higher statistical fluctuations. Consequently, hadronic showers have a less uniform and symmetric development [Longair (2011)].

Figure 4.6 shows the simulation [Bernlöhr (2000)] of the development of an electromagnetic shower for a 300 GeV γ-ray (a) and a hadronic shower for a 1 TeV proton (b), also the corresponding Cherenkov photon density on the ground. As it can be seen in the figure, the hadronic shower is much more irregular than the electromagnetic shower. Figure 4.7 also shows the comparison of the electromagnetic and hadronic shower images recorded by IACTs camera.

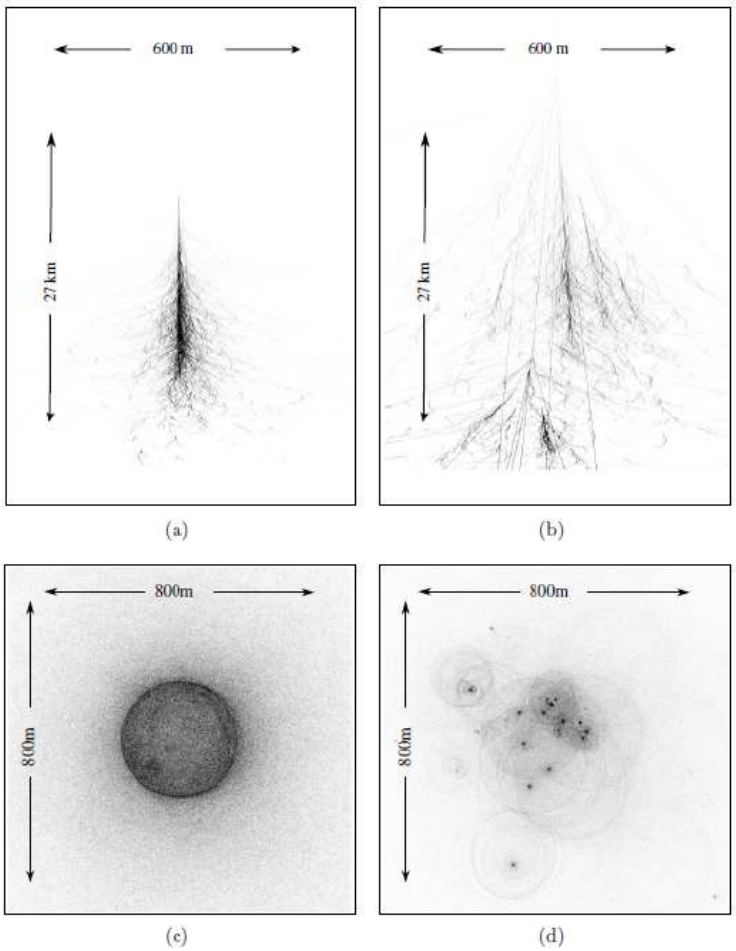

Figure 4.6: Development of electromagnetic and hadronic showers. Figure (a) shows the development of a 300 GeV γ-ray while figure (b) shows the development of 1 a TeV proton. Figures (c) and (d) show the corresponding density of Cherenkov photons on the ground for 300 GeV γ-ray and 1 TeV proton, respectively. Credit: [Bernlöhr (2000)]

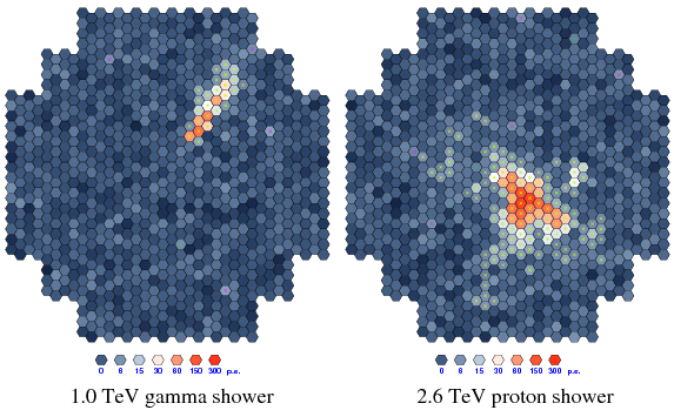

Figure 4.7: Comparison of electromagnetic and hadronic shower Cherenkov photon densities in a IACT camera. The left figure shows the Cherenkov photon density from an electromagnetic shower initiated by a 1.0 TeV photon while the right figure is for a hadronic shower initiated by a 2.6 TeV proton. Credit: [Voelk (2009)]

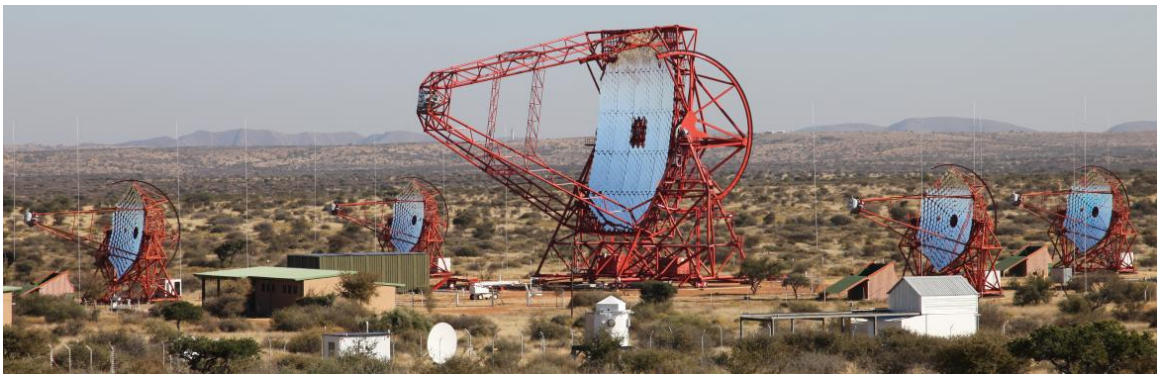

Figure 4.8: High Energy Stereoscopic System (H.E.S.S.).

Figure 4.9: Picture of High Energy Stereoscopic System first phase.

4.2 The High Energy Stereoscopic System

The High Energy Stereoscopic System (H.E.S.S.), which is shown in Fig. 4.8, is an array of 5 Imaging Atmospheric Cherenkov Telescopes. The H.E.S.S. is located in the Khomas Highland in Namibia (23°16'18" South, 16°30'00" East) around 100 km south-west of the Namibian capital Windhoek, at an elevation of 1800 m above sea level. The name of the observatory references to Victor Franz Hess, an Austrian-American physicist who won the Nobel Prize in physics in 1936 for the discovery of CRs. The first phase of H.E.S.S. experiment, operated since 2003, includes four telescopes that are positioned at the corners of a square of 120 m side length while H.E.S.S. phase II includes an additional large fifth telescope at the center that was added in July 2012. The phase I is sensitive to γ-rays in the energy interval between 100 GeV and several 10s of TeVs. The energy threshold is lowered to some 10s of GeVs with the addition of the large fifth telescope (CT5).

4.2.1 Introduction to the H.E.S.S. Telescopes

4.2.1.1 H.E.S.S. Phase I

The picture of the H.E.S.S. phase I array can be seen in Fig. 4.9. The spacing between the telescopes was chosen in order to allow for a simultaneous view of Cherenkov light emitted by γ-ray induced air showers by at least two telescopes while keeping a maximum distance between the telescopes for good stereoscopic viewing conditions.

The total reflector of one IACT has a flat-to-flat diameter of 13 m and 15 m focal

Figure 4.10: The H.E.S.S. I Camera is shown in the middle figure. The left figure shows the schematic view of the H.E.S.S. I camera profile with the Winston cones and PMTs while the right figure shows a front picture of the camera. The PMTs illustrated in the left figure can be seen clearly in the right figure.

length. The total collection area of the mirrors is 107 m^2, consisting out of 382 small mirror facets of 60 cm diameter each. The facets are arranged spherically while the camera is located at the focal plane. The mirrors have a high reflectivity O(80%) which depends on the wavelength and the degradation of mirrors due to aging. The telescopes are built in a "Davis-Cotton design" to reduce the spherical aberration [Davies-Cotton (1957)] and have an imaging accuracy of 0.03° on axis while 0.06° for optical photons at 2° off axis. A more detailed overview of the H.E.S.S. telescopes' optical reflector design can be found in [Bernlöhr (2003)].

The H.E.S.S. phase I cameras, providing a total camera field of view of 5° in the sky consist of 960 Photonis XP2960 photo-multiplier tubes (PMTs) arranged in a plane and packed in electronic modules called "drawers". The PMTs are chosen to be sensitive to the light between 300 nm to 600 nm with a typical quantum efficiency of O(25%) in the most sensitive wavelength band between 320 nm to 420 nm [Bernlöhr (2003)]. Each drawer consists of 16 PMTs and each PMT corresponds to an area of 0.16° diameter in the sky. The drawers contain required electronics for triggering and data read-out as well as high voltage supply. Every PMT in a drawer is equipped with a hexagonal shaped Winston cone to increase the light yield by capturing and focusing the light that falls between the PMTs. Consequently, the Winston cones reduce the background light by behaving as collimators which keep stray light or light coming from larger angles off the PMTs. The Cherenkov light emitted in the atmosphere is reflected and imaged on the camera by the IACT mirrors and detected by PMTs using a short integration time of 16 ns to suppress night sky background (NSB). Also the PMTs seeing the bright stars during data taking are removed from the camera trigger and their high voltage powers supplies are turned off until the bright star leaves the PMT's field of view. One of the H.E.S.S. cameras and its schematic sketch can be seen in Fig 4.10. A more detailed overview on the mechanics and electronics of H.E.S.S. cameras can be found in [Vincent (2003)].

In the H.E.S.S. experiment, simultaneous observations of air showers with multiple telescopes are carried out at the hardware level by the central trigger system. The trigger system consists of two main parts, namely the camera trigger and the central trigger. A single H.E.S.S. telescope camera trigger system includes two levels to increase the sensitivity of the camera for the detection of γ-rays, the first trigger is on PMT level and the second trigger is on the camera level. The central trigger is done on the array level.

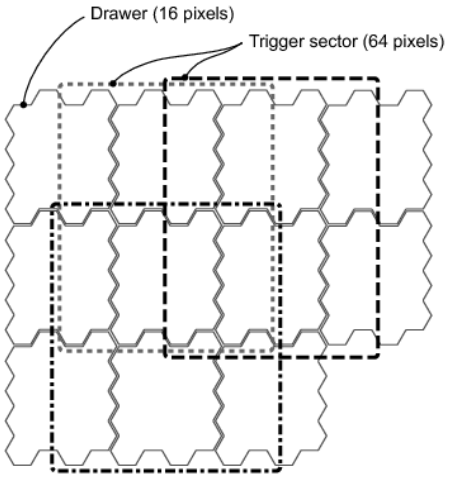

Figure 4.11: The H.E.S.S. camera trigger schematics showing the drawers with 16 pixels and the trigger sectors with 64 pixels.

The H.E.S.S. camera is sub-divided into 38 overlapping trigger sectors each consisting of 64 (8x8 pixels) PMTs as illustrated in Fig. 4.11, which basically provides an homogeneous trigger efficiency over the entire camera. At pixel level, the PMT comparator checks if the number of photoelectrons (p.e.) in the signal exceeds the critical threshold of 5.3 p.e. defined as the PMT threshold, which is programmable and creates a trigger pulse. The length of the pulse carries the information about how much time the input signal exceeds the given threshold. Generally, typical noise signals trigger short signals. The effective resolving time of the pixel coincidence is in the 1.3 to 2 ns range which efficiently rejects uncorrelated PMT signals from the night sky background and provides a high suppression of random coincidences. The second level, which is the camera trigger (or telescope trigger) is achieved when a signal above the PMT threshold is seen in at least 3 PMTs (defined as sector threshold) within one sector within a time window of the effective resolving time ($\sim$1.5 ns). Whenever a camera creates a trigger, a signal is sent via optical fiber to the central trigger system, which allows for multiple telescope coincidence requirements. At the array trigger level, it is demanded that at least two of four telescopes should be triggered (telescope multiplicity) within a time window of 80 ns. If all trigger requirements are fulfilled, the ADC[4] values of 960 PMTs of each triggered telescope are read out and stored for further offline processing. The array trigger level is significantly reducing background events due to muons produced in hadronic air showers. Typical H.E.S.S. I array trigger rates are O(200 Hz). The central trigger also logs the current read-out status of the cameras and thus allows for measurement of the system dead-time. To each individual event, a GPS time stamp is assigned by the central trigger system. More information on the trigger system of H.E.S.S. array can be found in [Funk (2004)].

[4]Analogue to Digital Converter.

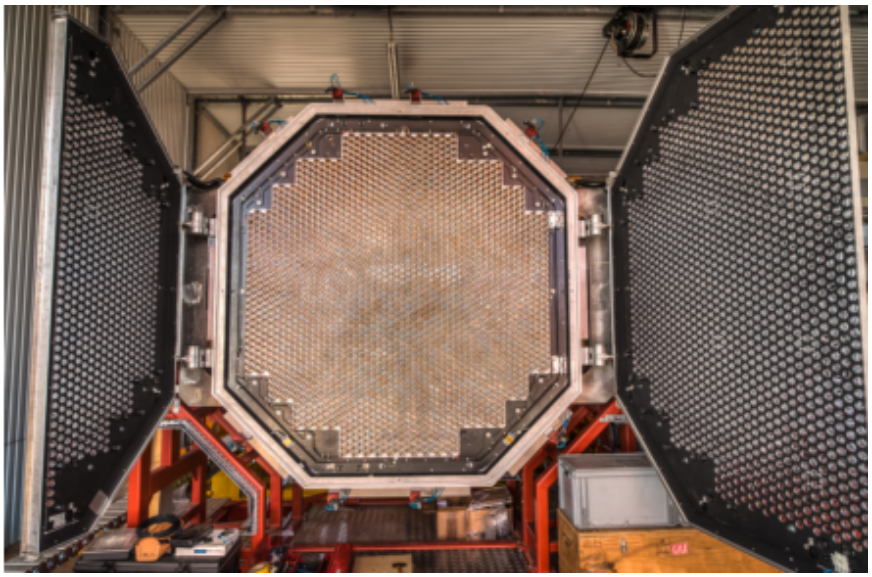

Figure 4.12: The picture of CT5 camera from the front view with an open lid.

4.2.1.2 H.E.S.S. Phase II

In the second phase of H.E.S.S., a large new Cherenkov telescope (CT5) was placed at the center of the four H.E.S.S. I telescopes in 2012. The large telescope is sensitive to γ-ray showers with a primary energy of some 10 GeV when compared to the energy threshold of the phase I array which is around 100 GeV, therefore enlarges the observatory capabilities to the lower energies. The CT5 telescope had its first light in July 2012. The lower energy threshold is reached by the larger mirror of CT5 which is $\sim$600 m^2. The 28 m diameter telescope uses a parabolic mirror to minimize the time dispersion[5] between incoming photons. The dish is composed of 875 hexagonal facets with flat-to-flat size of 90 cm and the focal length of CT5 is 36 m.

The CT5 camera (see Fig. 4.12) basically follows the design of the H.E.S.S. I cameras, but is much larger. It is equipped with 2048 PMTs in 128 drawers. The physical pixel size of each PMT is 42 mm equivalent to a 0.067° FoV in the sky. The CT5 camera pixels actually have the same physical size like the H.E.S.S. I camera pixels sizes but due to the larger focal length, shower images are resolved much better. The total field of view of the CT5 camera in the sky is $\sim 3.5°$. A more detailed system description of the CT5 camera can be found in [Bolmont (2014)].

The trigger system of H.E.S.S. II comprises three levels. Level 1 trigger (camera level), Level 2 trigger (CT5 level) and the stereoscopy (array level) trigger. In addition to time coincidences between H.E.S.S. Phase I level 1 triggers, the central trigger system checks for time coincidences of large and small telescopes' triggers. The result of the latter coincidence test (monoscopic or stereoscopic event) is sent back to the CT5 trigger management. As in H.E.S.S. phase I, the stereoscopic events will always be accepted. Each sector in the CT5 camera again consists of 64 pixels, with 96 overlapping sectors to ensure trigger homogeneity. The effective time window for a coincidence is 1.3 ns. A

[5]Note that spherical mirrors introduce time dispersions between photons reaching the camera in the focal plane from different points on the mirror.

camera level 1 trigger occurs if the signals in M pixels (pixel multiplicity) of a camera sector, exceed a threshold of N photoelectrons (pixel threshold). The small Cherenkov telescopes are not equipped with a level 2 trigger, since they do not operate in mono mode. The CT5 was built to lower the energy threshold of triggered gamma events. Normally, the background rejection is achieved in the stereoscopic mode when more than one small telescope is triggered at the same time with the large telescope. The stereoscopy with the large telescope allows to lower the energy threshold down to 50 - 60 GeV. The CT5 telescope has to work in mono mode below this energy range but the mono mode suffers from high trigger rates caused by single muons. The solution is a level 2 trigger to reduce the trigger rate. The step after the camera trigger level (level 1 trigger) is the so-called central trigger. The central trigger system looks for coincidences of telescope triggers inside a 40 ns time window. A coincidence of at least 2 telescopes is required in the central trigger time window. The CT5 monoscopic events are accepted or rejected depending on the result of level 2 system evaluation. In normal operation, any of the small telescopes is triggered only in case of a coincidence with another telescope, but low energy photons can not trigger the small telescopes. To increase the acceptance of low energy photons, standalone CT5 triggers have to be accepted. A more detailed study of the CT5 trigger system can be found in [Barnacka (2013)].

The large telescope is in principle sensitive to photons down to some 10 GeV. This region is so far only accessible with the current generation of satellite-borne detectors in the HE range. This lowered energy threshold can allow detecting astrophysical transient phenomena like γ-ray bursts. Another important fact for the detection of transients is the H.E.S.S. II drive system which, with a design speed of about 200°/min, is much faster than that of the old telescopes with a design speed around 100°/min. All the data analyzed in this thesis were taken by H.E.S.S. phase I, consequently, no CT5 data are analyzed in this thesis.

4.2.2 Data Quality

The H.E.S.S. telescopes collect ∼1000 hours of data per year, but not all of the collected data can be used for the analysis. Reduction of the unreliable data, which were taken under non-optimal conditions, is very important for minimizing systematic effects on the measured parameters before going to the further steps. Normally, the H.E.S.S. telescopes take data only if the meteorological conditions during the dark time and the tracking deviations are within some acceptable limits. These limits are defined for the trigger rates, tracking of the source and the unexpected light sources effecting the observations. For each observation runs, the individual telescope trigger rates, the participation fraction of each telescope in the array trigger and the array trigger rate are monitored. A constant trigger rate is preferred which shows that the observations are taken under good atmospheric conditions. The presence of clouds or excessive dust in the atmosphere leads to the enhanced absorption of the Cherenkov light produced by the air showers. This absorption causes fluctuations in the system trigger rates, consequently it causes systematic uncertainties in the reconstructed photon energies and in the measured flux. The pointing precision of the telescope tracking system is tested by comparison with the position of bright stars on the sky. The runs having non-precise tracking lead to uncertainties in the determination

of the source position. Moreover, unexpected light sources like meteorites, lightnings, satellites and airplanes cause PMTs to be switched-off. The runs having more than 10% of switched-off pixels are rejected. A more detailed explanation of the standard quality selection criterias can be found in [Aharonian (2006b)].

4.2.3 Data Calibration

In order to analyze data and obtain reliable scientific results, the data passing the quality criterias are then calibrated by using a standard calibration chain as explained in [Aharonian (2004c)]. The pulse information generated by a photon in a single pixel is measured by the ADC in counts. In order to convert the ADC values into physically meaningful values, a source of light with precisely known wavelength, pulse duration, and intensity distribution similar to Cherenkov light has to be used for illuminating and measuring the response of PMTs. For this purpose, a set of calibration runs must be performed as listed below.

- **Electronic pedestal calibration runs** are used to estimate the noise level in a single pixel. This calibration procedure takes into account the counts recorded by ADCs in the absence of any light source. This basically provides the information of the electronic background noise. It is performed with closed lid of the camera and with the high voltage (HV) turned on. In the absence of any light, electronic noise creates a narrow Gaussian ADC distribution. The mean of this distribution is defined as the pedestal position. The pedestal position varies with the temperature of the camera due to seasonal changes and also with the heating of electronics during operation.

- **Single photoelectron calibration runs** (SPE) are used for estimating the conversion coefficient from 1 p.e. to ADC counts. SPE calibration uses light-emitting diode (LED) pulses recorded by the camera at 70 Hz with an intensity such that on average, there is 1 p.e. per pixel (or PMT), per event. It is performed with the camera lid open and HV on. In order to avoid contamination from NSB, SPE calibration runs are performed inside the camera shelter. On average 1 p.e. corresponds to $\sim$80 ADC counts.

- **A flatfielding calibration run** is performed for correcting the differences in single PMT efficiencies (gain of the PMTs) which is done every second night. Although the electronics of PMTs is calibrated in SPE calibration, some pixels may give slightly different responses to a uniform illumination. This is basically because of the inhomogeneities in the camera due to different quantum efficiencies of the pixels and also due to the collection efficiencies of Winston cones. The LED mounted in the center of the dish uniformly illuminates the whole camera with short light pulses with a FWHM[6] of 5 ns. The wavelength of the LED pulses are in the range of 390 - 420 nm which triggers the camera in the same way as for Cherenkov light from air showers, but with an increased pixel multiplicity ($>$ 9 pixels) to reduce

[6]Full Width at Half Maximum.

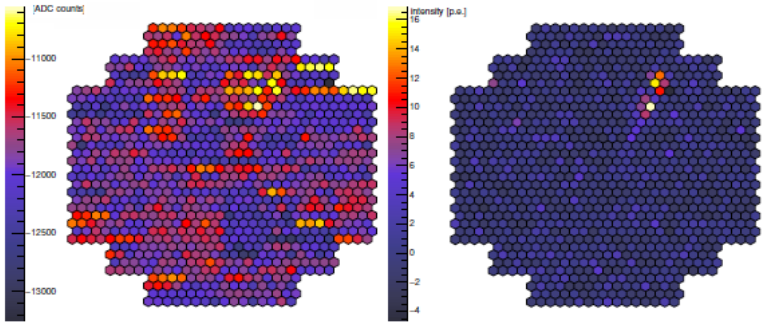

Figure 4.13: Comparison of the raw data and calibrated image. A raw camera image before the calibration is shown at the left figure while the same event after calibration is shown at the right figure. Credit:[Komin (2005)]

the background of air showers. The mean ADC count of all pixels is calculated and a flatfield correction coefficient for each single pixel is obtained to correct these differences and equalize the sensitivity of the PMTs over the camera. It should also be noted that the broken pixels are not used in the calibration process.

- Muon rings are also recorded to estimate the changes in mirror reflectivity, occurring with time due to pollution and degradation of the mirror coating. The Cherenkov light produced by muons is well understood and modeled. The mirror efficiency can be estimated as the ratio of measured pixel intensities to simulated Cherenkov photons from a muon. The image intensities are then scaled according to this ratio as explained in more detail in Leroy (2003).

Comparison of the raw data and calibrated image can be seen in Fig. 4.13. The image of the shower can hardly be seen before calibration while the shower image is clearly enhanced after the calibration. The rest of the camera is dominated by small fluctuations due to electronic noise and NSB.

4.2.4 Data Analysis

The main purpose of analyzing the data is to reconstruct the primary photon's arrival direction and also the energy. It is also important to obtain the flux level of the source for being able to interpret and understand the nature of the emission. In this section, it is explained how the stereoscopic shower reconstruction and the energy estimation of the primary photons are done.

4.2.4.1 Monte Carlo Simulations

Monte Carlo simulations of the Cherenkov light and of the H.E.S.S. detectors are necessary for understanding the detected showers and the response of detectors to different types of showers. A better discrimination between the γ-ray and hadron induced showers can be achieved by simulating both shower types in different energies and statistically study the observed properties of the showers on the simulated detectors. Moreover, the experimentally measured parameters of the shower images can not help to estimate the

energy of the primary photon on their own without using the results of the simulations. The responses of the H.E.S.S. telescopes must be obtained from the MC data for γ-ray induced showers.

For this purpose, there are some sophisticated air shower simulation packages currently used by the scientific community. The one that is used by H.E.S.S. is called CORSIKA (COsmic Ray SImulations for KAscade) [Heck (1998)] and was first developed for the KASCADE [Doll (1990)] experiment. The EGS4 code system[7] [Hirayama (2005)] is used for the implementation of the different electromagnetic particle interactions. For being able to describe the effect of the γ-rays realistically, the simulation of the showers and the propagation of Cherenkov photons in the atmosphere are done by taking into account the atmospheric and the geographic conditions of the H.E.S.S. site.

For understanding the response of the H.E.S.S. detectors to the simulated γ-ray showers, the sim hessarray package [Bernlöhr (2008)] is used in different array configurations. The sim hessarray package uses the CORSIKA generated Cherenkov photons as input and takes into account the experimentally measured properties of the H.E.S.S. array. These properties are quantum efficiencies for the camera PMTs obtained from calibration runs, NSB rate, trigger conditions, electronic noise and the pulse shape of the trigger signal. The simulation results provide the ADC counts for each pixel which can be translated into intensity. After that, the shower reconstruction is applied to the simulated data to obtain expected shower parameters for the event selection. Consequently, calculation of the effective areas of the instrument and estimation of the energy of primary particle based on the observed shower parameters can be done.

4.2.4.2 Image Cleaning

After data quality selection and calibration, an event image is the collection of all signals of the PMTs in photoelectrons. Note that this calibrated image still includes random fluctuations that are not related to the Cherenkov shower image and are likely to be caused by electronic noise of PMTs or the NSB. Note that there are noise sources in the electronics used by PMTs. For example, amplifiers used for amplifying the output signal of PMTs have internal noise sources. Therefore, the calibrated image should be cleaned from these random fluctuations for the further steps of the data analysis. This is done by the process called "image cleaning". The image cleaning procedure is achieved by applying a two-level tail-cut procedure, the levels are named as T_{high} and T_{low}. These thresholds values are $T_{high} = 10$ p.e. and $T_{low} = 5$ p.e. for the standard H.E.S.S. I image cleaning procedure. In the first level, all the pixel containing photoelectrons less than T_{low} are discarded and not considered in the calculation of the Hillas parameters. Only the pixels containing more photoelectrons than T_{high} with a neighboring pixel above T_{low} and vice-verse are kept in the image. In addition to these two fixed threshold values, another additional NSB threshold is defined for excluding the pixels suffering from bright star light. Therefore the pixels that pass the tail cuts, but whose intensity does not exceed 3σ of the pedestal RMS obtained from the electronic pedestal calibration runs, are excluded from

[7]The EGS* system of computer codes is a general purpose package for Monte Carlo simulations of the coupled transport of electrons and photons in an arbitrary geometry for particles with energies above a few keV up to several TeV.

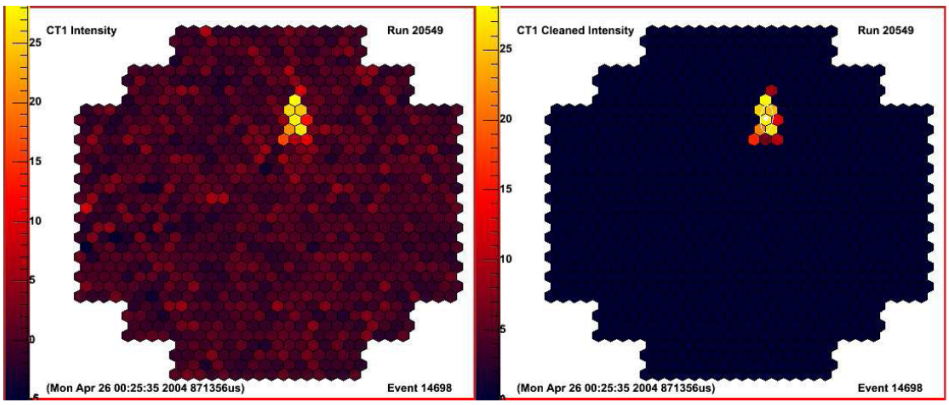

Figure 4.14: The left figure shows the calibrated image while the right figure shows the cleaned image. Credit:[Funk (2005)]

the analysis. Finally, a large number of noisy pixels are discarded in the calibrated image as can be seen from comparison of the calibrated and the cleaned image in Fig. 4.14.

4.2.4.3 Hillas Parametrization

The shape of the Cherenkov light from an air shower on the camera can be approximated as an elongated elliptic shape. Therefore, the shape on the camera can be parameterized by an ellipse and these parameters can be written in terms of moments of the light intensity distribution. The parameters basically correspond to position, orientation, shape and brightness of the image on the camera. These parameters are called Hillas parameters [Hillas (1985)] as illustrated in Fig. 4.15. After cleaning an image from NSB and electronic noise effects, the next step is to calculate the Hillas parameters. By using these parameters, energy and direction reconstruction can be done and physical properties of the primary photon can be estimated. The parameters of this ellipse can be described as follows.

- Image Size (S) is the total number of photoelectrons in a Cherenkov shower image. It can be calculated from the zeroth moment of the intensity distribution of the image.
- The position of the Hillas ellipse in the camera is given by the center of gravity (CoG) of the light intensity distribution. The first moments of this two-dimensional intensity distribution have the mathematical form of a center of gravity, or the mean value of the distribution. After calculating the CoG parameter, the distance (D) between the camera center and the CoG can be calculated.
- The length (L) specifies the rms length of the semi-major axis of the ellipse, while the parameter Width (W) represents that of the semi-minor axis. The matrix of second moments can be interpreted as an ellipse around the CoG, giving the information about the distribution along the major and the minor axes.
- The angle α, which gives the orientation of the ellipse, or in other words, the angular difference between the line connecting CoG to the camera center and the line along

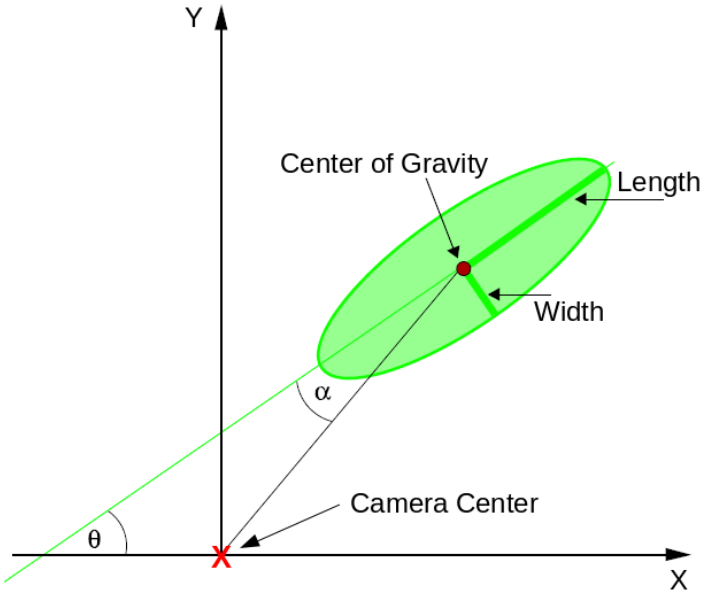

Figure 4.15: Illustration of Hillas parameters. The green region is the recorded camera image with an ellipse approximation. The length and the width of the ellipse are shown with camera center and center of gravity of the ellipse.

the major axis of Hillas ellipse, is used for the direction reconstruction. Note that the angle α depends on where the (assumed) source is.

The image parameters provide important information about the primary particle's properties. The width and the length parameters are used for rejecting the shower morphologies which are initiated by the hadronic showers and can therefore be used for gamma/hadron separation. The amount of light collected by the telescopes, which corresponds to the size parameter, is connected to the energy of the primary photon, thus the size parameter can be used for reconstructing the energy of the primary photon. The CoG and the orientation of the ellipse (α) are connected to the shower geometry and can be used for reconstructing the primary photon direction. The details of the calculation of Hillas parameters can be found in [Eidemüller (2002)]. Note that there are also other reconstruction methods used which do not use classical Hillas approach. For example the Model++ analysis [Naurois (2009)] is based on the comparison of the raw Cherenkov camera pixel images of a photon induced atmospheric particle shower with the predictions from a semi-analytical model. This reconstruction technique provides a more precise direction and energy reconstruction of the photon induced shower compared to Hillas Parametrization technique.

4.2.4.4 Gamma-ray Selection and Background Suppression

The majority of the events recorded by the H.E.S.S. telescopes originates from hadronic showers. These hadronic showers are the most important background events that must be suppressed and filtered-out while keeping a large fraction of γ-ray events. The idea of discriminating between γ-ray and hadron induced events lies in the difference of longitudinal and lateral development of electromagnetic and hadronic showers as discussed before.

Therefore, the morphological differences of the camera image can provide a method to be used for separating them. In order to reconstruct the primary photon properties accurately, the parameters of the Hillas ellipse should be defined well. For this reason, a set of cuts should be applied to the calibrated and cleaned data images.

H.E.S.S. software applies a set of cuts, called "pre-selection cuts" on the size and distance parameters. The events with a low image size are rejected if they are below a given threshold since the parameters and the errors on these parameters can not be determined well for faint shower images. Furthermore, the events whose center of gravity is close to the camera edges are also rejected, since the signal acceptance[8] drops off towards the edge of the camera.

The basis of separating the γ-ray signal from the hadronic background is to apply the cuts to the mean reduced scaled parameters. The scaled parameter concept, which was first used by the HEGRA collaboration [Daum (1997)] and is described as

$$X_{i,scaled} = \frac{X_i - \langle X_i \rangle}{\sigma(X_i)} \tag{4.4}$$

where X_i is the observed value of the parameter, $\langle X_i \rangle$ is the mean value of the parameter which is obtained from Monte Carlo simulations for γ-rays[9] and the term $\sigma(X_i)$ is the root mean square value of the simulated parameter. Note that X_i here can either be the length (L) or the width (W) parameter of the ellipse. In the data analysis, the reconstructed impact parameter is used along with the image amplitude for each telescope image to find $\langle X_i \rangle$ and $\sigma(X_i)$ in a lookup table filled from γ-ray showers MC simulations. For obtaining the mean reduced scaled parameters, the obtained scaled parameters are averaged over all telescopes as indicated by the subscript i in Eq. 4.4. In its general form, mean reduced scaled parameter can be written as follows

$$X_{i,MRS} = \sum_{tel}^{N_{tel}} X_{i,scaled} \quad . \tag{4.5}$$

By using the calculation method above, mean reduced scaled length (MRSL) and mean reduced scaled width (MRSW) can be calculated for each event passing the pre-selection cuts. Therefore MRSL and MRSW represent the mean deviation from the width of the shower images with respect to the one expected from simulations in units of σ. Figure 4.16 shows the comparison of Monte Carlo simulation results for hadron and γ-ray initiated events. As can be seen from Fig. 4.16, MRSW and MRSL distribution of γ-rays events are approximately Gaussian with a mean value of zero while cosmic rays events have a wider distribution centered at higher values, therefore allowing to set cuts on these parameters to discriminate γ-rays from the hadrons.

Additionally, in order to define a region of interest, a cut on θ^2 which is the squared angular distance from the position of the source of interest, is performed. This cut

[8]The acceptance of the detector can be described as the response of the detector to the detected light and it is expected not to be homogeneous over the entire camera field of view. It basically drops rapidly towards the edge.

[9]Note that simulations take into account the image intensity, reconstructed impact parameter and zenith angle of the shower.

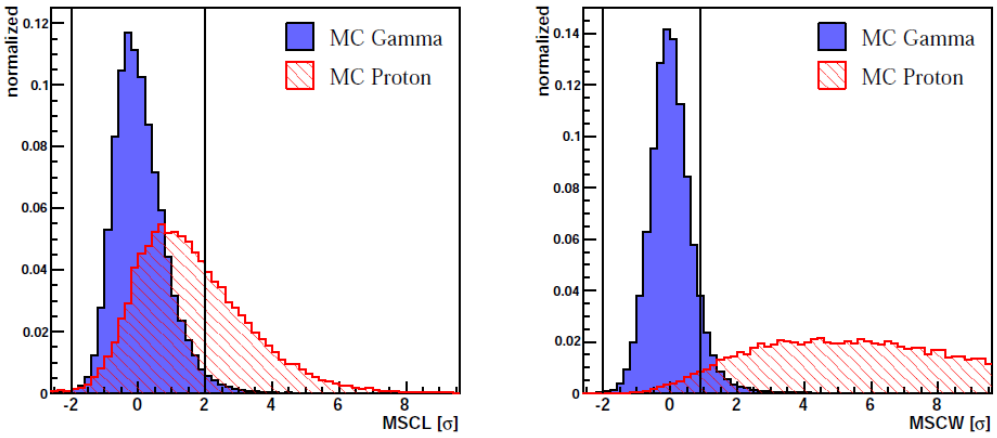

Figure 4.16: Comparison of MSRL and MSRW between gamma and hadron induced events. The left figure shows the comparison of MSRL parameter between γ-ray induced and hadronic induced shower while the right figure shows the comparison of MSRW parameter. Note that in both figures, the blue area shows the distribution of a parameter obtained from MC simulation of γ-ray induced shower while the red area shows the distribution of a parameter for hadron induced shower. Credit: [Prokoph (2009)]

defines a circular region around the source position which is considered as on-source region. It should also be noted that the optimum selection cuts depend on the assumed γ-ray energy spectrum of the source. Therefore several different types of cuts have been defined as shown in Table 4.2 for maximizing the significance[10] for different source types [Aharonian (2006b)].

Configuration	MRSL Min.	MRSL Max.	MRSW Min.	MRSW Max.	θ^2_{Cut} Max. (Degree^2)	Image Amp. Min. (p.e.)	Distance Max Max. (Degree)
Standard	-2.0	2.0	-2.0	0.9	0.0125	80	2.0
Hard	-2.0	2.0	-2.0	0.7	0.01	200	2.0
Loose	-2.0	2.0	-2.0	1.2	0.04	40	2.0
Extended	-2.0	2.0	-2.0	0.9	0.16	80	2.0

Table 4.2: Description of cuts and corresponding values for the cut parameters used in the H.E.S.S. data analysis. Cuts are applied on MRSW and MRSL, as well as on the distance (θ) from the reconstructed shower position to the source. A minimum of two telescopes passing the per-telescope cuts, on image amplitude and distance from the centre of the field of view, are also required. Standard cuts, as well as hard, loose and extended cuts are listed.

The cuts defined in Table 4.2 are used for different types of analysis aiming at different purposes. The usage of the cuts can be listed as follows.

[10]Note that in the presence of background, the significance of a source increases with the square root of observation time, t_{obs}. The optimized cuts yield the maximum σ / $\sqrt{t_{obs}}$ for a source of a given type.

- **Standard Cuts:** They are optimized for strong sources with a flux of 10% of the Crab Nebula with a power law spectrum and a photon index of 2.6. These cuts are used mainly for spectral studies.

- **Hard Cuts:** They are optimized for relatively faint sources with a flux of 1% of the Crab Nebula and a power-law spectrum with a photon index of 2.0. These cuts are generally used for morphology studies since they provide better angular resolution with respect to the standard cuts. They can also be used for spectral studies in the presence of a strong nearby source which contaminates the spectrum of the source of interest.

- **Loose Cuts:** They are optimized for bright sources with a flux level around Crab nebula and a power law spectrum with a photon index of 3.2. These cuts are used mainly for spectral studies with a low energy threshold.

- **Extended Cuts:** They are optimized for analyzing extended sources. For analysis of large extended sources the cut on θ^2 is usually set to be larger than the extension of the source, so that all γ-rays from the source can pass this cut.

For the existing IACTs, an increased background reduction improves the sensitivity considerably. The applicability of multivariate analysis techniques (MVA), with the application of the Boosted Decision Trees (BDT) method, provided by TMVA package [Höcker (2007)] provides a better background rejection when compared to the classical Hillas approach. The MVA technique combines several shower parameters into one parameter which gives the likelihood of an event to be a γ-ray like. In the TMVA approach of gamma/hadron separation, several parameters are defined for the selection of γ-ray like evens. These parameters are also called "BDT training variables". A more detailed information about the TMVA technique can be found in Ohm (2009).

4.2.4.5 Direction Reconstruction

The stereoscopic imaging technique basically uses the images of same Cherenkov shower from different angles simultaneously. Therefore it requires more than one camera of the system should be triggered. By using these simultaneous images from different angles, the direction of the primary photon can be reconstructed. For each Cherenkov image on the cameras, the origin of the shower called "shower core", lies on the major axis of the ellipses. The core position can be estimated from the relative alignment of the shower images with respect to each other as illustrated in Fig. 4.17. Actually each shower image on the camera determines an orthogonal plane to the camera plane. This plane contains also the shower axis and therefore the shower core. The intersection of these orthogonal planes can be connected to the ground with a straight line, defined as the impact point of the shower on the ground. So the shower core must be located on this straight line.

The core position is obtained by averaging the intersecting points of the major axes from multiple shower images as explained above. A more detailed explanation of the reconstruction process can be found in Berge (2006). The angular resolution of the stereoscopic direction reconstruction is around $\sim 0.1^\circ$ and $\pm$ 10 m for the core location.

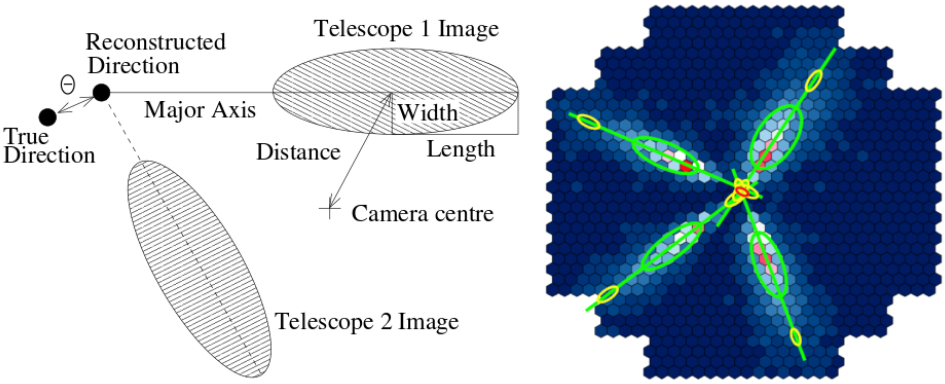

Figure 4.17: Direction reconstruction in stereoscopic mode. The left figure shows the illustration of intersecting two Hillas ellipses while the right figure shows the intersection of four Hillas ellipses on the camera.

4.2.4.6 Energy Reconstruction

The estimation of the primary γ-ray energy from Hillas reconstruction is done by taking into account the total shower image, namely the size parameter and the core distance from each telescope. Energy reconstruction procedure needs lookup tables generated from detailed shower simulations taking into account the instrument responses. The energy of the primary photon is approximately proportional to the total number of Cherenkov photons produced. The core distance is needed in this procedure since the photon intensity on the ground varies with the distance from the shower core. The energy of the primary γ-ray is determined by using the mean of the independently estimated energies for each telescope. The systematic uncertainty in the energy estimation is around $\sim$15%. Energy reconstruction needs the lookup tables which contains the true MC energy depending on the lookup parameters like zenith angle, angular distance between shower direction and camera center in focal plane (offset). All of these parameters affect the total image intensity in the camera for a given energy. The reconstructed energy is sensitive to various systematic effects as listed below.

- Atmospheric Effects: Monte Carlo simulations of air showers in the atmosphere are used to predict the light yield as a function of energy and shower position assuming good, stable weather conditions. In the case that the atmospheric conditions change and are variable, the interaction of particles and the propagation of Cherenkov light in the atmosphere is affected significantly. The uncertainties arising from the atmosphere are in the order of 20% and introduce the largest uncertainties.

- The optical response of the instrument: The reflectivity of the mirrors and the Winston cones, also the shadowing effect of the telescope masts introduces uncertainties to the energy estimation. This response is monitored by studying Cherenkov light from single muons passing close to the telescope and is described in Bolz (2004).

- Camera Response: SPE gain of each PMTs is monitored by SPE calibration runs. Small differences between the gains of PMTs in the camera introduce uncertainties to the energy estimation.

4.2.4.7 Signal Determination and the Modeling of the Background

Despite the significant reduction of the events originated from CRs after the application of event selection cuts (around a factor of ∼100), there still remains background events in the data that originate from the hadronic showers or CR electrons, which look like γ-ray events in terms of the parameters used for the gamma/hadron separation. Depending on selection cuts and the source strength, this background can be of the same order (or even larger) of the γ-ray events. Although it is usually assumed that the distribution of background events are azimuthally symmetric within the camera field of view, this may not always be the case. Therefore, for extracting the γ-ray signal from the remaining γ-ray-like events, a statistical estimation of the background is strictly required.

In order to estimate the background from H.E.S.S. data, several models have been developed for choosing a background region. A general description of the two most frequently used methods, namely "Ring Background Method" and "Reflected Background Method" will be explained in detail. Both of these methods choose the suitable OFF region from the same field of view. For being able to estimate the background, the reconstructed shower direction for each γ-ray like events are filled in a two dimensional histogram which is called "Skymap". The size of the signal region for a given point in the sky is determined by selecting events within a circular region around the given point with radial θ cut. For point-like sources, the size of the signal region is adjusted according to the angular resolution of the selected cuts and is in general slightly larger than the H.E.S.S. point spread function, which can be approximated by the sum of two or three one-dimensional Gaussian functions. The PSF function which is the sum of two 1D Gaussian functions can be written as

$$\mathrm{PSF} = A\left[\exp\left(\frac{-\theta^2}{2\sigma_1^2}\right) + \exp\left(\frac{-\theta^2}{2\sigma_2^2}\right)\right]. \tag{4.6}$$

Signal Determination

For determining the excess number of γ-rays (N_γ) and the statistical significance S of this excess, an estimation of the irreducible background is strongly needed. The excess number of γ-rays can be given as

$$N_\gamma = N_{On} - \alpha N_{Off} \quad \text{where the error is} \quad \sigma(N_\gamma) = \sqrt{N_{On} + \alpha^2 N_{Off}} \tag{4.7}$$

where N_{On} and N_{Off} are the number of events obtained from the defined ON and OFF regions and α is the normalization factor. For the background normalization factor, one should take into account that the solid angle or the exposure time can be different for the ON and the OFF regions. Note that the acceptance of the H.E.S.S. camera changes within the field of view and are dependent on the zenith angle and the exposure time. Therefore, for obtaining a reasonable normalization factor, all of these effects have to be taken into account. Since the exposure time and the zenith angle of observation are similar for the ON and OFF regions in Wobble mode observations[11], the normalization factor depends

[11] In Wobble mode observation, the source of interest is observed with an offset while keeping the source in the camera field of view. Therefore the background can be extracted from the anti-source position

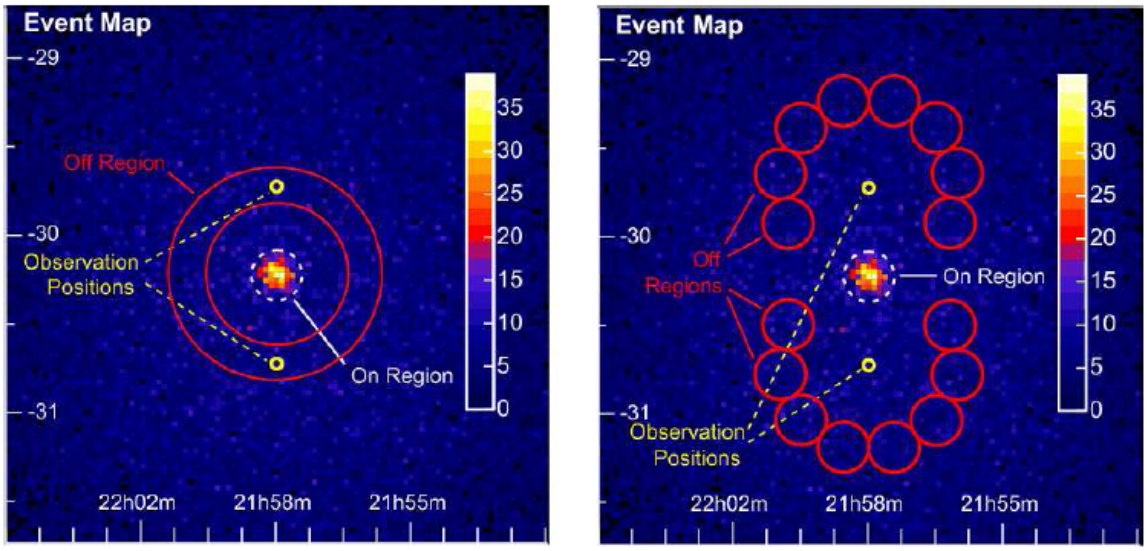

Figure 4.18: The skymap showing the ring background region (Off region) taken into account for determining the background events is shown in the left figure with the red ring while the right figure shows the background regions for reflected background method (the red circles). In both figures, the On regions are indicated as dashed white circles. Observation positions are also marked with the small yellow circles. Credit:[Funk (2005)]

only on the ratio of the ON to OFF regions weighted for the camera acceptance. The significance of the γ-ray signal observed from the each position in the field of view can be determined by Li&Ma approach [Li & Ma (1983)].

By determining N_{On}, N_{Off} and α for each position in a region of the sky, a two-dimensional excess and the significance map of the region of interest can be produced. The background models, which use different regions in the field of view for estimating the background events, should take into account the change of acceptance, thus, this acceptance function of the camera should be precisely determined.

Ring Background Method

The ring background method estimates the number of events in the OFF region defined between the inner and the outer circles with radius R_{in} and R_{out} centered at the source position of interest as can be seen from Fig. 4.18 (left). R_{in} and R_{out} are chosen such that the ratio of the areas of the OFF region to ON regions minimizes any statistical fluctuations. The default value for this ratio is 7. The inner radius of the ring should be chosen larger than the ON region radius to avoid the source position to be selected as background region. The default value for R_{in} in H.E.S.S. data analysis is 0.5°. Note that the regions including known γ-ray sources have to be excluded from the area of the ring. The normalization factor (α) is given basically by the ratio of the ON to OFF region areas modified by a weight factor for taking into account the radial acceptance in the camera.

The ring background method can be applied to any position within the field of view. This method has the advantage of providing the background for the whole field of view and thus allows the determination of excess and significance maps after being corrected for

which is symmetrical with respect to the camera center.

the camera acceptance. The ring background method is suitable for morphology studies of a source. The disadvantage is the dependence on the modeling of the background acceptance. Since the background acceptance is typically energy dependent, the ring background method is not suited for spectral analysis for the determination of energy spectrum of a source.

Reflected Background Method

The reflected region background model is well suited for observations taken with standard Wobble mode. It is important that the Wobble offset is large enough so that the camera center does not overlap with the ON region. In order to apply this method, H.E.S.S. observations are usually taken in Wobble mode, where the source is observed with a typical offset of 0.5° with respect to the camera center. This background method estimates the number of events from multiple numbers of OFF regions having equal distances from the camera center and the same size as the signal region as can be seen from Fig. 4.18 (right). These OFF regions for background estimation are obtained by rotating the ON region around the observation position. In the case of a large ON region, the number of background regions are reduced therefore they don't overlap with the chosen ON region. As the acceptance of H.E.S.S. is radially symmetric in the camera, both the ON and the OFF regions have the same acceptance value. Consequently, no camera acceptance correction is needed and the normalization α is just the ratio of number of ON regions to OFF regions. In order to minimize the systematic effects due to non-radial acceptance variations, the Wobble position is altered around the target position between different observation runs. Finally, total number of OFF events from these OFF regions are used for estimating the background in the ON region, just scaled by the normalization factor α. Additionally, if known γ-ray sources exist in the field of view, these regions have to be excluded. The reflected background is best suited for the flux and the spectral measurements.

Note that it is not possible to apply the discussed background models for very extended sources having sizes comparable to the H.E.S.S. field of view. There are some other background models suitable for very extended sources like template background model, field-of-view background model or the classical ON/OFF approach. More detailed information about the alternative background methods can be found in Berge & Funk & Hinton (2007).

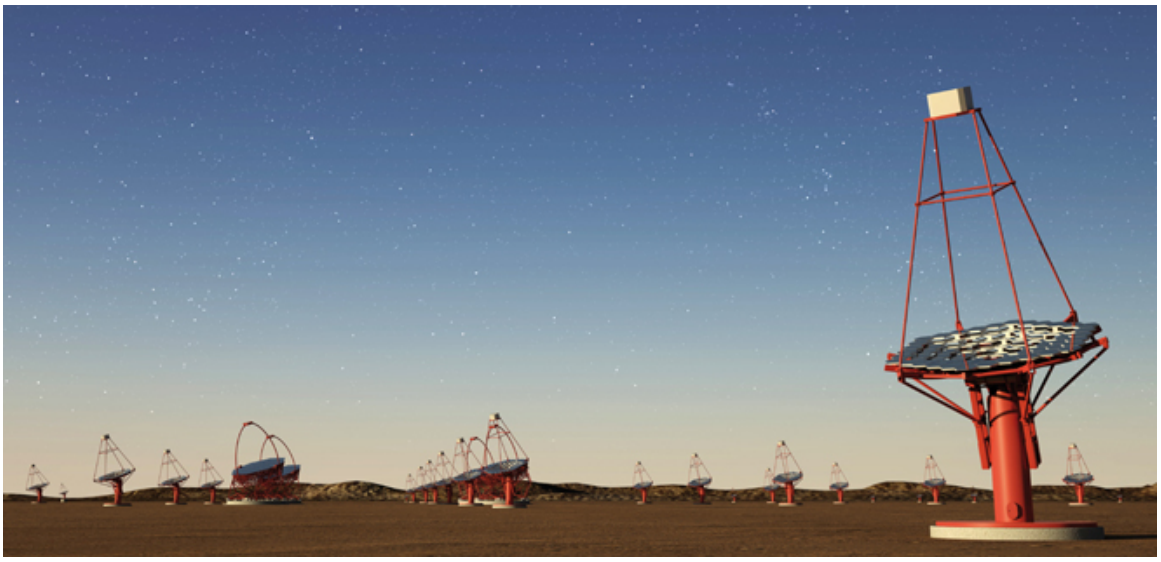

Figure 4.19: The artistic picture of Cherenkov Telescope Array (CTA). Credit:G. Perez, IAC (SMM)

4.3 The Cherenkov Telescope Array Project

The VHE part of the electromagnetic spectrum is currently being investigated by means of ground-based imaging array Cherenkov telescopes (H.E.S.S., MAGIC, and VERITAS). It is believed that improving the sensitivity and lowering the energy threshold of such a ground-based γ-ray astronomy system will lead to the discovery of many more γ-ray sources, which will surely improve the knowledge and the understanding of the Universe. In order to dramatically boost the current IACTs' performance and to widen the VHE science, a new Cherenkov Telescope Array (CTA) project has been proposed.

CTA is an initiative to build the next generation ground-based γ-ray instrument. The CTA array will allow studies in the VHE domain in the range from a few tens of GeV to more than a hundred TeV, extending the existing energy coverage and increasing the sensitivity by a factor 10 compared to the current installations, while also improving other aspects like angular and energy resolution [Actis (2011)]. The improvement in the sensitivity, energy coverage, angular and energy resolution will lead to the discovery of more than 1000 sources among galactic, extra-galactic and unidentified sources [Hinton & Hoffman (2009)]. Achieving these goals requires the construction of many tens of telescopes divided in three different types, having different sizes and the use of two arrays located in the northern and in the southern hemisphere in order to provide full sky coverage.

CTA will represent a major step towards the understanding of the VHE Universe, by means of a 10-fold improvement in the sensitivity. This project will allow to address the scientific topics in a two-fold approach. From one side, CTA will investigate a much larger number of already known classes of sources, going to further distances in the Universe, performing population studies, accurate variability and spatially-resolved studies. On the other side, such performance figures will allow new light to be shed on possible new classes of TeV sources such as GRBs, cluster of Galaxies and address fundamental physics studies [Persic (2013)]. Moreover, pushing the high-energy limit to E $>$ 100 TeV will allow a thorough exploration of the cut-off regimes of the cosmic accelerators. CTA will be

operated as an observatory open to the scientific community.

This section is added to the thesis because the author has worked in the CTA Array Control and Data Acquisition (ACTL) (see Appendix B for the details of the work) software development group for the MST prototype in Berlin-Adlershof (see Appendix A for the details of the MST prototype). CTA is a very huge and detailed science project that covers many different research areas. For this reason, only brief information about the CTA and motivation of this project will be given in the following sections.

4.3.1 Science Motivation for the CTA Project

The main scientific aims of the CTA can be roughly grouped into three subjects, serving as key science drivers:

- Understanding the origin and propagation of leptonic and hadronic CRs and their role in the universe.
- Understanding the nature and variety of black holes, and their use as a probe of the star-formation history of the universe.
- Searching for the ultimate nature of matter and physics beyond the Standard Model.

4.3.1.1 The Origin and Propagation of Leptonic and Hadronic CRs and Their Role in the Universe

The CR spectrum observed near the Earth can be described by a pure power law up to an energy of a few PeV, where it slightly steepens as discussed in Section 2.2. The cosmic-rays are believed to be accelerated in the shocks of supernovas. However, while particle acceleration up to energies well beyond 10^{14} eV has now clearly been demonstrated with the current generation of instruments, it can still not be proved that supernovae accelerate the bulk of cosmic-rays.

Even if a SNR can be detected by the current generation Cherenkov telescopes during a significant fraction of its lifetime (up to several 10^4 years), they can produce CRs having PeV energies only for a much shorter time when compared to their lifetime (several hundred years). The further detection of such an SNRs would be extremely important, as it would be clear evidence for the acceleration of CRs up to PeV energies. A sensitive scan of the galactic plane with CTA would be an ideal way of searching for these sources, which can produce PeV CRs and are called "Pevatrons". On the other hand, the spectrum of radiating particles (both electrons and protons) and therefore the spectra of γ-ray radiation should show a characteristic curvature, reflecting the acceleration at CR modified shocks. However, to be able see such curvature, one needs a coverage of a few decades in energy. CTA will be able to provide this energy coverage. Therefore, the large sample of supernovae will be observable with CTA, in some scenarios several hundreds of objects. In particular, the increased energy coverage at lower and higher energies with respect to current generation IACTs will allow sensitive population studies. The improved angular

resolution (arc min level) will help to resolve fine structures[12] in supernova remnants which are essential for the study of particle acceleration and the interactions between the particles.

CTA offers the possibility of real breakthroughs in the understanding of cosmic rays. There is also a potential to directly observe CRs diffusion[Aharonian & Atoyan (1996)], the presence of a massive molecular cloud located in the proximity of a SNR (or any kind of CR accelerator) provides a thick target for CR hadronic interactions and thus enhances the γ-ray emission. Hence, studies of molecular clouds in γ-rays can be used to identify the sites where CRs are accelerated.

The main key science topics related to observation of Galactic sources include Cosmic Rays and Supernova Remnants, Pevatrons, Diffusion of Cosmic Rays, Cosmic rays in galaxies, Star Clusters, Pulsar wind nebulae, Pulsars and Ultra high energy cosmic rays.

4.3.1.2 The Nature and Variety of Black Holes, and Their Use as a Probe of the Star-formation History of the Universe

The most massive black holes in our Universe are presumably hosted by the centers of active galaxies, namely active galactic nuclei (AGN). Matter accretion into a black hole provides one of the most efficient energy sources known in the Universe and explains the extreme luminosity of these objects [Dermer (2009)]. These objects generally show jet structures of relativistic plasma which are most luminous at γ-ray energies. The blazars[13] are the dominant class of extra-galactic VHE emitters known so far and the observed VHE flux from such objects shows very fast variability down to minute scales [Aharonian (2007)]. Multi-wavelength observations with high temporal and spectral resolution can help to understand how these relativistic jets are launched, what their structures and composition are and by what physical mechanism the particles are accelerated to very high energies. CTA will be able to provide new insights about the underlying physics of these sources by accessing to the VHE emission for a large population of blazars. In particular, CTA will be able to probe variability time scales of seconds and put constraints on acceleration and cooling times, instability growth rates and the time evolution of shocks and turbulences.

As it is known, VHE γ-rays traveling from distant sources interact with photons of the extra-galactic background light (EBL) via pair production. This causes an energy-dependent absorption of the intrinsic source spectrum. The integrated EBL density towards these sources can be measured by knowing the intrinsic spectra [Raue (2010)]. The EBL density as function of redshift can be constrained by sampling a large number of extra-galactic VHE sources with CTA.

The main key science topics related to observation of extra-galactic sources include AGNs, radiogalaxies and Seyfert galaxies, star formation history and inter-galactic magnetic fields.

[12]The concept of resolving the fine structure in SNRs is called "The horizon of resolvability" [Gabici (2012)] and basically described as the maximum distance that the shell of the SNR can be distinguished from a simple Gaussian.

[13]AGNs with jets structures which are aligned with the line-of-sight are called "Blazars"

4.3.1.3 Searching for the Ultimate Nature of Matter and Physics beyond the Standard Model

A major open question for modern physics is the nature of dark matter[14] (DM). At scales from kpc to Mpc, there are numerous lines of evidence for the presence of an unknown form of mass that cannot be accounted for by the Standard Model (SM) of particle physics. By comparing the galaxy distribution in large galaxy redshift surveys and through N-body simulations of structure formation, it emerges that the particles constituting the DM had to be moving non-relativistically at freeze-out to reproduce the observed structure of the Universe, hence it is termed "cold DM" (CDM). One of the most popular scenarios for CDM is that of weakly interacting massive particles (WIMPs), which include a large class of non-baryonic candidates with a mass typically between few tens of GeV and few TeV and an annihilation cross section of the order of the weak interaction. Natural WIMP candidates are found, e.g., in super-symmetric (SUSY) extensions of the SM. This cross-section ($\approx 3 \times 10^{-26}$ cm^3 s^{-1}) is therefore a baseline benchmark that CTA has the potential to reach through searches for the annihilation of dark matter particles, as has been attempted already by all operating IACTs. Concerning indirect detection, CTA will have a better chance of DM detection compared to the current generation of IACTs. Its extended energy range will allow searches for WIMPs with lower mass while the improved sensitivity in the entire energy range will improve the probability of detection or identification of DM through the observation of spectral features. Increased FoV with a homogeneous sensitivity as well as the improved angular resolution will allow for more efficient searches for extended sources and spatial anisotropies and finally, improved energy resolution will increase the chances of detecting a possible spectral feature in the a DM-induced photon spectrum. By observing the region around the Galactic Center, and by adopting dedicated observational strategies [Doro (2012)], CTA will be able to reach the canonical velocity-averaged annihilation cross-section in only 100 h observations. This will be the first time for ground-based IACTs to reach this sensitivity level.

CTA will also be an excellent experiment for other fundamental physics searches, and especially for possible Quantum Gravity (QG) induced Lorentz Invariance Violation (LIV)[15] and Axion-like particle (ALP) searches. The observation of very distant, strong flaring blazars will provide the strongest constraints of LIV compared to the current generation of IACTs since AGN observation will be routine astrophysical targets for CTA. On the other hand, axions, which are a proposed solution to the strong-CP problem of QCD (or ALPs in general), are also valid candidates to constitute a part or all of CDM. They are expected to convert into photons (and vice versa) in the presence of magnetic fields. In the case of a very distant AGN, the ALP/photon can cause either attenuation or enhancement of the photon flux (in competition with the EBL absorption), depending on the ALP mass.

[14]The observation of the acoustic oscillations imprinted into the cosmic microwave background measured by the WMAP satellite quantifies this dark component as contributing to about 25% of the total Universe energy budget being over dominant with respect to the baryonic component which accounts for only about 4% of the total energy density.

[15]It has been suggested that QG effects may induce time delays between photons with different energies traveling over large distances due to a non-trivial refractive index of the vacuum.

4.3.2 CTA Specifications

Improved performance specifications compared to current IACTs are needed for being able to meet the science goals mentioned above. For this reason, the CTA project is required to achieve high technical performance within a reasonable budget. CTA goals is based on few general ideas as listed below.

- CTA should use proven IACT technology.
- The array should be increased from currently 4 - 5 telescopes (VERITAS, HESS) to several tens of telescopes.
- CTA should cover the energy range from ∼10 GeV to ∼100 TeV. Since this wide energy range can not be covered with an uniform array of identical telescopes, use of 3 different telescope sizes covering 3 sub-energy ranges is appropriate.
- These telescopes should be distributed over a large area (∼1 - 10 km^2) on the ground.
- CTA should provide high automatization liable to remote operation and run as an observatory open to the astrophysics community.

4.3.2.1 Energy Ranges of CTA

A uniform array of identical telescopes with fixed spacing is not the most efficient solution for covering the wide energy range desired. Total energy range should be separated into three energy ranges without sharp boundaries for being covered. These three energy ranges are described below.

The low-energy range, $E < 100$ GeV:

For being able to detect showers down to a few tens of GeV, the Cherenkov light needs to be collected efficiently. Since the event rates and the systematic background uncertainties are quite high for this low energy range, this can limit the achievable sensitivity. Efficient photon detection can be achieved either with few large telescopes or many telescopes of modest size. The area of this part of the array can be relatively small, being of order of a few 10^4 m^2. Actually the MAGIC collaboration has led the access to the sub-100 GeV domain. Building on that experience, CTA will further lower the low-energy threshold. One major reason to push the energy reach of CTA to lower energies is the wish to enlarge the spectral overlap between CTA and space-borne telescopes operating in the HE regime by direct detection of γ-ray photons, such as LAT. For example, over a limited bandwidth, hadronic and leptonic emissions from SNRs look similar with current observations. Over a bandwidth more extended to low energies, detailed profiles characterizing the two emission spectra should become apparent, so clarifying the nature of the emission whether it is purely hadronic, purely leptonic, or a combination of both. Moreover, this energy range is also important to observe GRBs and for EBL studies. The low-energy regime of CTA holds the key to uncovering for the first time completely new phenomenology opening up the time domain astronomy in timescales shorter than half an hour.

In the case small to medium-sized telescopes are used in this energy range, the challenge is to trigger the array since no individual telescope detects enough Cherenkov photons to

provide a reliable trigger signal. Trigger systems which combine and superimpose images at the pixel level in real time, with a time resolution of a few ns represent a significant challenge. Because of this reason, CTA design conservatively assumes a small number of very large telescopes, typically with about a 20 to 30 m dish diameter, to cover the low energy range.

The core energy range from 100 GeV to 10 TeV:

This is the central and most natural regime for IACTs and addresses most of the core science themes. It is well understood from current experiments like H.E.S.S., VERITAS and MAGIC. In this energy range, most of the action in VHE astrophysics occurs. The good reconstruction of the arrival direction of primary photons, the high statistics, and the efficiency of gamma-hadron separation allow deep sensitivity and arc min angular resolution to be reached.

The flux sensitivity of 10^{-13} erg cm^{-2} s^{-1} is aimed for by CTA, which corresponds to source luminosities of 10^{33} $(d/10$ kpc$)^2$ erg s^{-1} for Galactic sources and 10^{41} $(d/100$ Mpc$)^2$ erg s^{-1} for extra-galactic objects. This sensitivity should allow the detection of all types of CR accelerators, including SNRs (and the interaction of cosmic-ray particles accelerated by them with nearby MCs), PWNe, clusters, as well as AGNs, radio galaxies and is expected to lead to the detection of over 1000 sources. The large FoV will allow deep surveys relatively fast with respect to the current surveys and exploring the possible diffuse emission of the Galactic disc, as well as the origin of the extended features in the GC.

The best approach for the shower detection and reconstruction is a grid of telescopes of the 10 to 15 m class with a spacing of about 100 m. Improved sensitivity will be obtained by both the increased area covered and the higher quality of shower reconstruction. Currently, the showers are typically imaged by a few telescopes. For the first time, with the addition of many middle sized telescopes, array size will be larger than the Cherenkov light pool. It ensures that images will be uniformly sampled across the light pool and that a number of images are recorded close to the optimum distance from the shower axis (about 70 to 150 m). A further advantage is that an extended telescope grid operated with a two-telescope trigger condition will have a lower threshold than a small array, since there are always telescopes sufficiently close to the shower core.

The high-energy range above 10 TeV:

Above 10 TeV, the knowledge of the γ-ray sky is very limited. At these energies, current instruments typically run out of photon statistics for all but the extremely bright objects. The key limitation in this energy range is the number of detected γ-ray showers, therefore the array needs to cover multi-km^2 areas. At high energies the light yield is large, so showers can be detected well beyond the 150 m radius of a typical Cherenkov light pool.

There are several cases where high-energy observations with CTA may provide crucial information. Extension of the spectral window to higher energies than current IACTs will allow the exploration of unknown parts of source spectra. The highest energy domain of CTA will provide the opportunity to measure the emergence of any pion-decay component and thus unambiguously identify hadronic cosmic-ray accelerators. The peak energy output from pion decay occurs at γ-ray energies a factor of 10 lower than the parent proton energy. "Galactic Pevatrons" should therefore produce hard spectrum power-law γ-ray emission

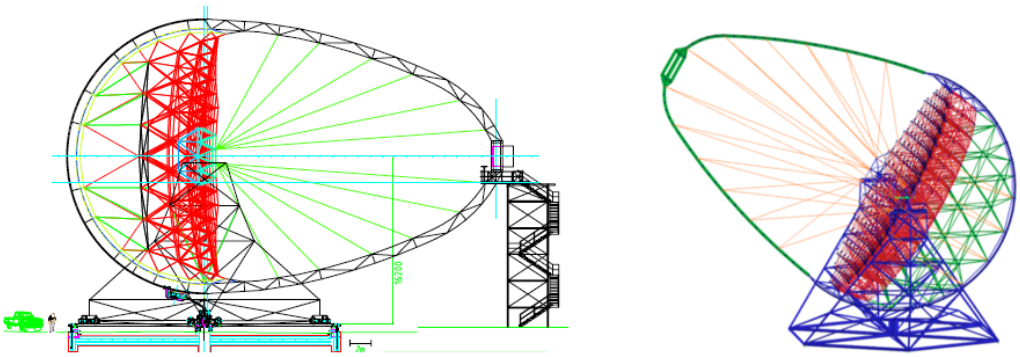

Figure 4.20: Large size telescope design. Credit:[CTA Consortium (2011)]

with gradual cut-offs in the 100 - 300 TeV energy range. CTA, with sensitivity up to 300 TeV, will be able to measure such cut-off energies and identify these acceleration sites.

4.3.2.2 CTA Telescope Types

As mentioned before, the CTA project will use three different sizes of telescopes for covering the full energy range. These three telescope types are Large Size Telescope (LST), Medium-Sized Telescope (MST) and Small Size Telescope (SST). This section gives brief information about each telescope type.

Large Size Telescope :

The purpose of LSTs is to enhance the sensitivity below 200 - 300 GeV and to lower the effective threshold down to 20 - 30 GeV. Therefore, design concept of LST takes into account the maximization of the sensitivity at low energy range. The science case of LST is the observation of high redshift AGNs up to $z \leq 3$, GRBs up to $z \leq 10$, pulsars and galactic transients. For being able to achieve the science goals, LST should have a long focal distance for optimizing the optical performance of the telescope. It should also be designed in the way that allows quick movement and rapid positioning for being able to catch the GRBs. Moreover, LST should have a high level of dynamical mechanical stability of the structures supporting the camera to minimize the camera misalignment and to optimize the angular resolution.

Extended Monte Carlo simulation studies have been conducted in order to explore and decide on the basic design parameters for the telescope and these have been fixed at a focal length of $F = 28$ m, field of view of FoV $= 4.5°$, pixel size fixed to $0.1°$, and a dish diameter of $D = 23$ m which satisfies the ratio $F/D = 1.2$. A specification of 20 s maximum delay to re-point the LSTs in the direction of a GRB alert at 180 angular distance from the previous pointing position is one more severe constraint on the telescope system design. The reflector with its diameter of 23 m diameter consists of 198 units of hexagonal shape 1.5 m flat to flat segmented mirrors of 2 m^2. Total area of the reflector is about 400 m^2. The LST Camera Support Structure (CSS) is designed to satisfy the critical requirements aimed for being able to provide the best optical properties of the telescope and a high level of mechanical stability while minimizing both the weight of

the masts and the shadow projected onto the mirror due to their geometry. Current LST design structure can be seen in Fig. 4.20. More information about the design of LST can be found in Deleglise (2013).

Medium-Sized Telescope :

Medium-Sized Telescopes of 10 - 12 m diameter, covering the energy band from 100 GeV to a few TeV, will be the workhorse of the CTA observatory. MSTs will be built for achieving the sensitivity of a milli-Crab level in this energy domain. Shower detection and reconstruction in this energy range has been well-understood from currently active IACT systems, and an appropriate solution is a grid of telescopes of the 10 to 15 m class with a spacing in the 100 m range. Aimed improved sensitivity will be obtained both by the increased area covered and by the higher quality of shower reconstruction since showers will be typically imaged by a larger number of telescopes with respect to current few-telescope arrays. Consequently, quite a number of telescopes should be built. Simplicity, robustness, reliability and the ease to maintenance are therefore particularly important features. Monte Carlo simulations studies suggest that an F/D of around 1.4 and a FoV of about 8.0° is required to achieve the key science drives. Two design options were considered for the MSTs, one is similar with the H.E.S.S. I telescopes, and the other design was similar with VERITAS design.

A prototype of one of the design concepts of the MST is under development and deployed in Berlin (Adlershof Campus). More detailed description of MST prototype is given in Appendix A.

Small Size Telescope :

The SST component of CTA will extend the energy range beyond the limits of current IACT setups which allows exploring the high energy end of galactic and extra-galactic sources and also probe the limits of particle acceleration in TeV emitters. A sufficiently large number of SSTs (on the order of 70) are needed to cover a surface area of 3 km^2 for being able to achieve this objective. A small effective mirror area of at least 5 m^2 is sufficient for the SSTs, because of the expected bright signal from air showers in the high energy range. Additionally, the FoV of the telescopes needs to be large, around $\sim 10°$, to allow imaging the showers that are far away from each single telescope. This will permit the installation of a spread-out SST array with a large inter-telescope spacing (up to ∼300 m). Finally, these properties of SSTs will improve the angular resolution in the $0.1-10$ TeV energy range and will allow studies of galactic plane sources to be extended beyond 100 TeV.

Currently, three different SST designs are being considered by the CTA consortium. One of them is using single-mirror Davies-Cotton (DC) optics with a GAPD based camera [Moderski (2013)] similar to the FACT telescope [Anderhub (2013)] and two others, the ASTRI [Pareschi (2013)] and SST-GATE projects, are based on Schwarzschild-Couder(SC) dual-mirrors optics [Vassiliev (2007)]. Figure 4.21 (left) shows the SST DC design while Fig 4.21 (right) shows the SST-ASTRI design. The plate-scale is much smaller in SC design when compared to DC design permitting the use of a small, light-weight camera, while still providing the required wide FoV. The challenge lies in the fact that such a SC mirror based telescope has never been built before and that practical solutions for the non-spherical mirrors still need to be tested.

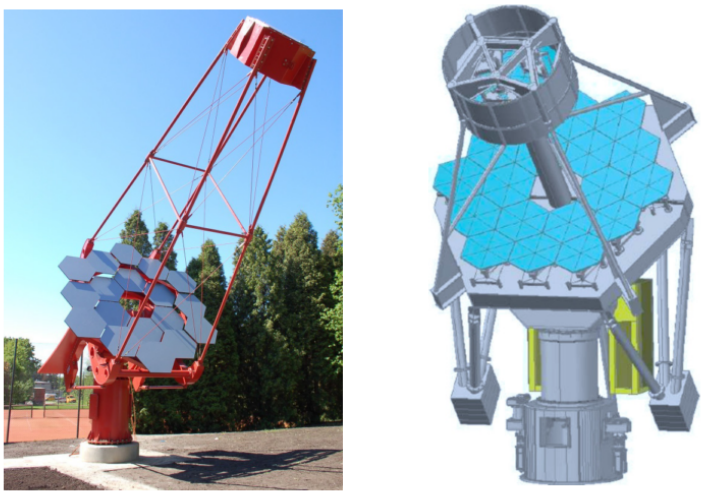

Figure 4.21: Small size telescope designs. The left figure shows the SST DC design while the right figure shows the SST ASTRI design. Credit:[CTA Consortium (2011)]

4.3.2.3 Array Layout

For being able to provide full-sky coverage, CTA consortium plans to build two sites, one in the southern and one in the northern hemisphere. The southern site will cover the central part of the galactic plane and see most of the galactic sources and will therefore be designed to have high sensitivity over the full energy range with respect to the currently existing experiments. The northern site will be optimized for extra-galactic astronomy and therefore there is no need for the high energies part coverage.

Monte Carlo simulations are a crucial tool in the design of CTA. The ultimate goal of these simulations is to find the most cost-effective solution for given physics goals and thus sensitivity goals or to find, for a given cost, the solution best suited for different types of targets with CTA. For this reason, different array layouts are being studied. Different candidate array configurations can be seen in Fig. 4.22.

4.3.2.4 CTA Sensitivity

Over the core energy range of 100 GeV to 10 TeV, CTA aims to be about a factor of 10 more sensitive than any existing instrument. The current installations consist of up to 5 Cherenkov telescopes[16]. They reach sensitivities of about 1% of the flux of the Crab Nebula at energies between 100 GeV and 1 TeV range. At 1 TeV, the goal of CTA is to achieve a 1 milli-Crab sensitivity. It will therefore for the first time allow detection and in-depth study of large samples of known source types. Consequently, CTA will explore a wide range of classes of suspected γ-ray emitters beyond the sensitivity of current instruments and will be sensitive to new phenomenas. This dynamic range will not only allow study of weaker sources and of new source types but also reduce the selection bias in the taxonomy of known types of sources.

The results of CTA simulation studies about the prediction of CTA time and energy

[16]5 telescopes with the H.E.S.S. II upgrade.

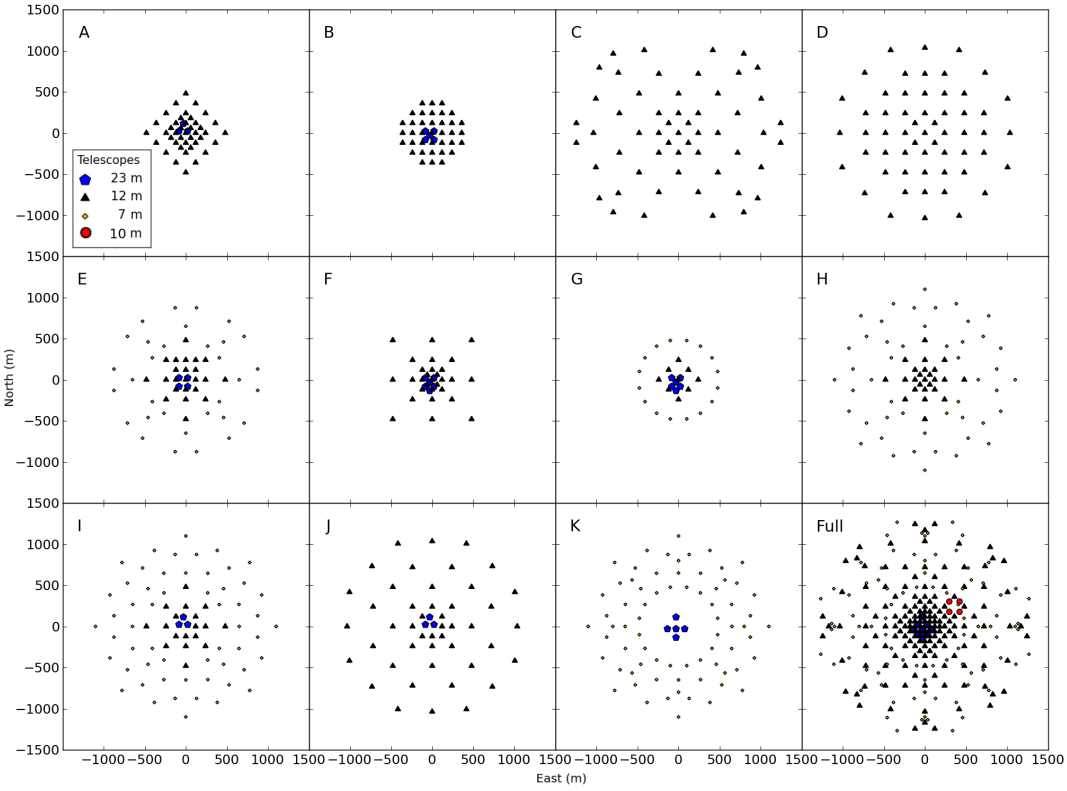

Figure 4.22: Different telescope array layouts currently being discussed for CTA. Each of the configurations is a subset of the large array shown in the bottom-right corner. Credit:[CTA Consortium (2011)]

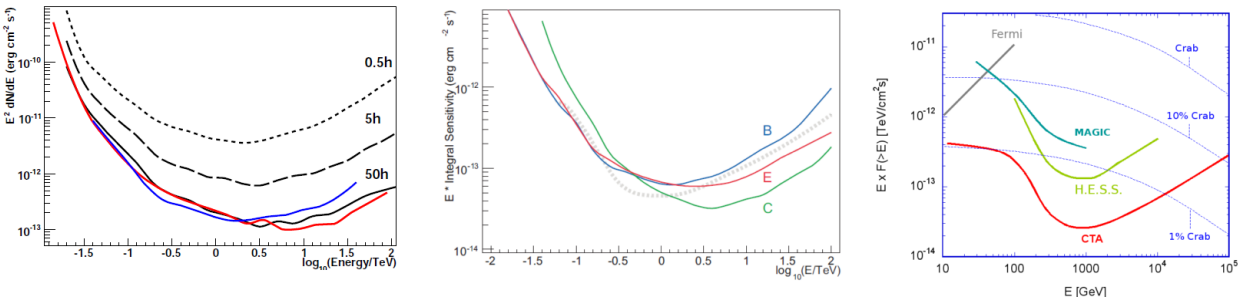

Figure 4.23: Left Figure: Time and energy dependence of the differential sensitivity for configuration E. Exposure times of 0.5, 5 and 50 hours are shown. For the 50 hour curve two alternative analysis methods are also shown. The red curve is for an analysis procedure with an image cleaning procedure and a Random Forest-based method for hadron rejection. An independent analysis using TMVA for hadron rejection is shown as a blue curve. Center Figure: Integral sensitivity for the candidate configurations B, C and E, for point sources observed for 50 hours at a zenith angle of 20. The goal curve for CTA (dashed line) is shown for comparison. Right Figure: Point-source sensitivity of current and future γ-ray observatories to constant sources. For pointed instruments like H.E.S.S. (green line) and MAGIC(cyan line), the sensitivity is shown for a 50 h exposure. Crab flux levels are also shown for comparison. Credit:[CTA Consortium (2011)]

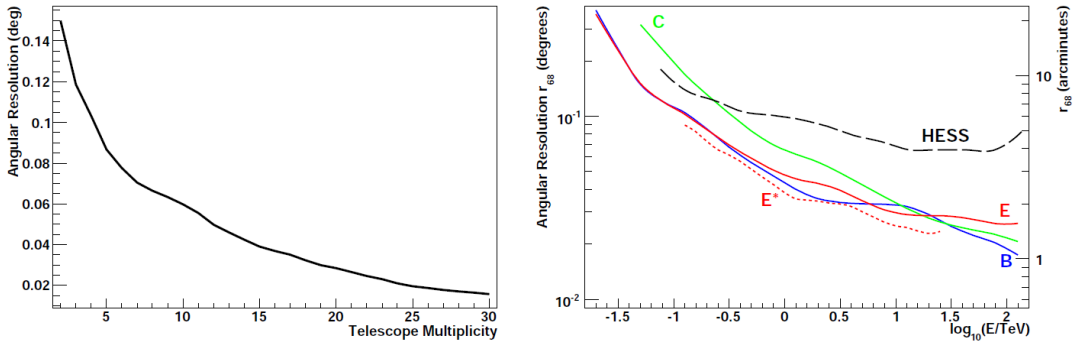

Figure 4.24: Left figure: Angular resolution (68% containment radius) for array configuration E, as a function of the number of telescopes with good shower images. Right figure: Angular resolution (68% containment radius of the γ-ray PSF) versus energy for the candidate configurations B, C and E. The resolution for a more sophisticated shower axis reconstruction method for configuration E is shown for comparison (dashed red line - E*). The angular resolution of H.E.S.S. (basic Hillas analysis, standard cuts) is shown as a reference. Credit:[CTA Consortium (2011)]

dependence of the differential sensitivity, integral sensitivity for the candidate configurations and the comparison of current and future γ-ray observatories sensitivities are shown in Fig. 4.23. High sensitivity over a wide energy range requires an instrument that is able to detect a sufficient number of Cherenkov photons for low energy showers and which covers a very large area for high-energy showers. Sensitivity degrades towards lower energies due to threshold effects and towards higher energies, due to the limited detection area.

4.3.2.5 CTA Angular Resolution

Current ground based Cherenkov telescopes are able to resolve extended sources, but in most cases they cannot probe the fine structures visible in other wavebands. Gamma-ray induced cascades detected simultaneously by many of telescopes will provide CTA to reach angular resolutions in arc-minute range, a factor of 5 better than the current instruments. The high telescope multiplicity (and event quality) is a key element of the CTA design. By using many telescopes, resolutions of $<0.02^\circ$ can be reached for the most energetic showers.

Figure 4.24 (left) shows how the angular resolution evolves with the increasing number of telescopes that record a shower image. By recording the shower images with 4 telescopes (like in H.E.S.S. Phase I or VERITAS) a resolution of about 0.1° is reached, while by using 12 telescopes the resolution is around 0.05°. The angular resolution for different CTA candidate systems is shown in Fig. 4.24 (right). Resolution at 1 TeV is at the 0.04° - 0.05° range for the configurations B and E, and a little bit worse for the larger area configuration C. A simultaneous minimization to find the best shower core and direction, using pixel timing information, provides a significant improvement with respect to the traditional intersection of image axes technique (see dashed line in Fig. 4.24 (right)). The resolution approaches 1 arc minute at high energies. Fiducial cuts on core location and/or harder telescope multiplicity cuts improve the performance at the expense of collection

area.

Significant increase in the angular resolution provides the ability to resolve the morphology of extended sources. Improved angular resolution will help to resolve fine structures in SNRs which are essential for the study of particle acceleration and particle interactions. Moreover, with an angular resolution of the order of 1 arc min one could resolve the inner part of the molecular clouds and measure the degree of penetration of cosmic rays.

Chapter 5

HESS J1741−302 Multi Wavelength Data Analysis

The aim of the multi-wavelength (MWL) data analysis described in this chapter is to understand the nature of the VHE γ-ray emission detected from the direction of the unidentified H.E.S.S. source HESS J1741−302. The source was investigated before and the results were published in the ICRC proceedings, Tibolla et. al (2008). The emission mechanism could not be addressed in detail because of the lack of statistics in H.E.S.S. data and the lack of multi-wavelength data analysis, consequently HESS J1741−302 was tagged as an unidentified source. The development of analysis techniques and the increased amount of collected high-quality VHE data allow the investigation of the nature of this source in more detail. Recall that there are ∼20 unidentified VHE γ-ray sources which have plausible MWL counterparts but the associations have not been confidentially established yet, while few (∼7) of them have no plausible counterparts at any wavelengths and are tagged as "dark sources". This kind of multi-wavelength data analysis presented in this thesis for HESS J1741−302 is a quite common approach for understanding the nature of the detected VHE emission from the direction of such unidentified sources. Similar MWL data analyses have been performed in Mizukami (2009), Etten (2009), Eger (2010), Perades (2013) and Shahinyan (2015).

In this chapter, general information about the VHE γ-ray source HESS J1741−302 and the nearby objects which can be responsible for the observed VHE γ-ray emission are given, also the details and results of multi-wavelength data analysis for the HESS J1741−302 region are presented. The MWL approach presented in this chapter includes the analysis of H.E.S.S. VHE γ-ray data, ^{12}CO and HI molecular clouds data and the X-ray data from Swift XRT observations. The joint interpretation of the results obtained from the MWL analysis comes later and is discussed in Chapter 6.

5.1 General Information about HESS J1741−302

HESS J1741−302 was first discovered by the H.E.S.S. Collaboration and the analysis results were published in a proceedings paper [Tibolla et al.(2008)]. The source was reported as a faint source with an integrated flux level of ∼1% Crab flux. The H.E.S.S. VHE data used

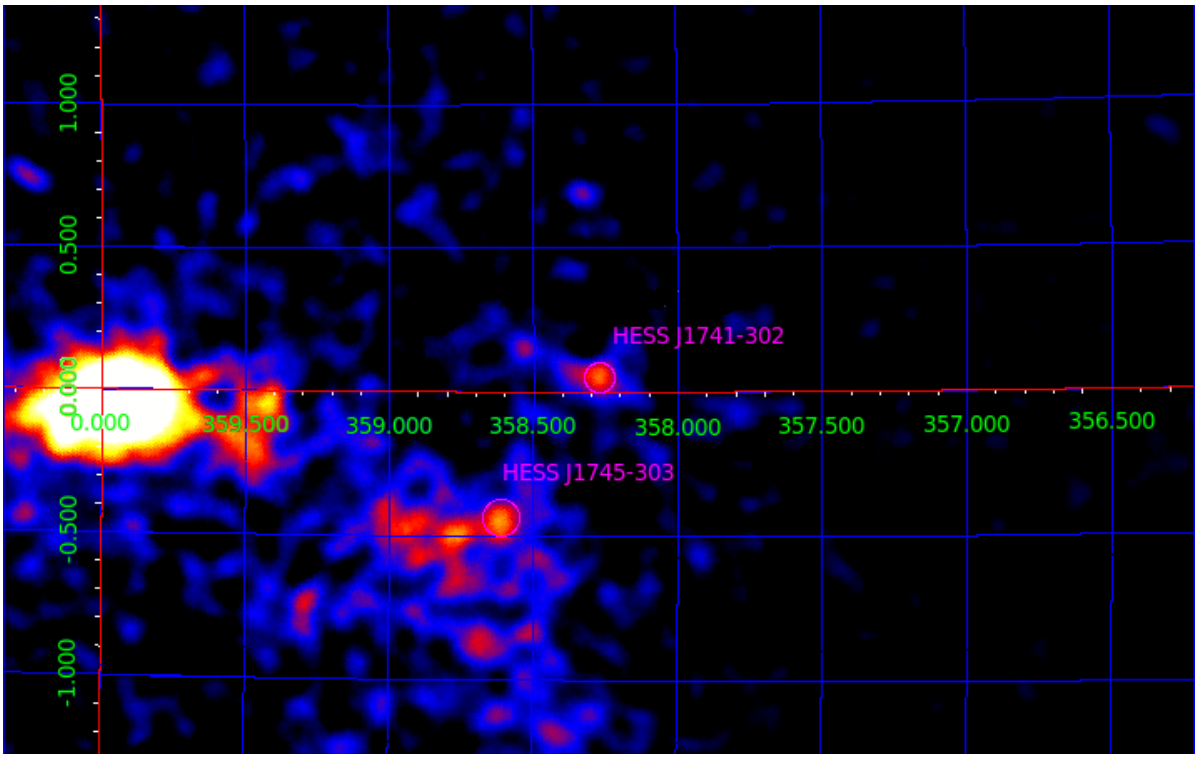

Figure 5.1: Location of HESS J1741−302 on the Galactic plane. The magenta circles show the location of HESS J1741−302 and HESS J1745−303. The GC ridge can be seen around $(l, b) = (0,0)$. The excess map is saturated for better visualization.

for the analysis presented in Tibolla et. al (2008) included 143.5 hours of observations collected from the VHE Galactic Plane Survey (GPS) of H.E.S.S. taken in 2004 - 2005 [Aharonian (2005b)] and also the extension of the survey between 2006 and 2008. The exact source position and the spectrum information was not available in the published proceedings paper. At that time, the statistics did not allow detailed studies on the source spectrum and the exact morphology. Only the integral flux level was mentioned. A proceedings paper about all known GPS sources was published one year later in 2009 [Chaves et al.(2009)], providing a preliminary spectral results for the first time without showing the VHE γ-ray spectrum of HESS J1741−302.

The position and the spectral information of the source currently given in TeVCat[1], collected from these two published proceedings papers mentioned above, are R.A.: $17^{\mathrm{h}}41^{\mathrm{m}}00^{\mathrm{s}}$, Dec.: $-30°12^{\mathrm{m}}00^{\mathrm{s}}$, corresponding to Galactic coordinates of $l = 358.4°$, $b = 0.19°$, and a spectral index of $\Gamma = 2.78 \pm 0.24_{\mathrm{stat}} \pm 0.20_{\mathrm{sys}}$, respectively. The integral flux above 1 TeV is given as $\mathrm{F}(> 1\ \mathrm{TeV}) = (6.3 \pm 1.3_{\mathrm{stat}} \pm 1.1_{\mathrm{sys}}) \times 10^{-13}\ \mathrm{cm}^{-2}\ \mathrm{s}^{-1}$. This source is tagged as an extended source in TeVCat, but no quantitative statement was made about the extension (size) of HESS J1741−302 in both proceedings papers. Figure 5.1 shows the location of HESS J1741−302 on the Galactic plane. As it can be seen from the figure, HESS J1741−302 is very close (angular distance of $\sim 0.5°$) to the relatively bright VHE γ-ray source HESS J1745−303 [Aharonian (2008a)]. Note that the bright GC ridge [Aharonian (2006a)] can also be seen in the figure.

[1]Online catalog for TeV Astronomy, http://tevcat.uchicago.edu/?mode=1&showsrc=189.

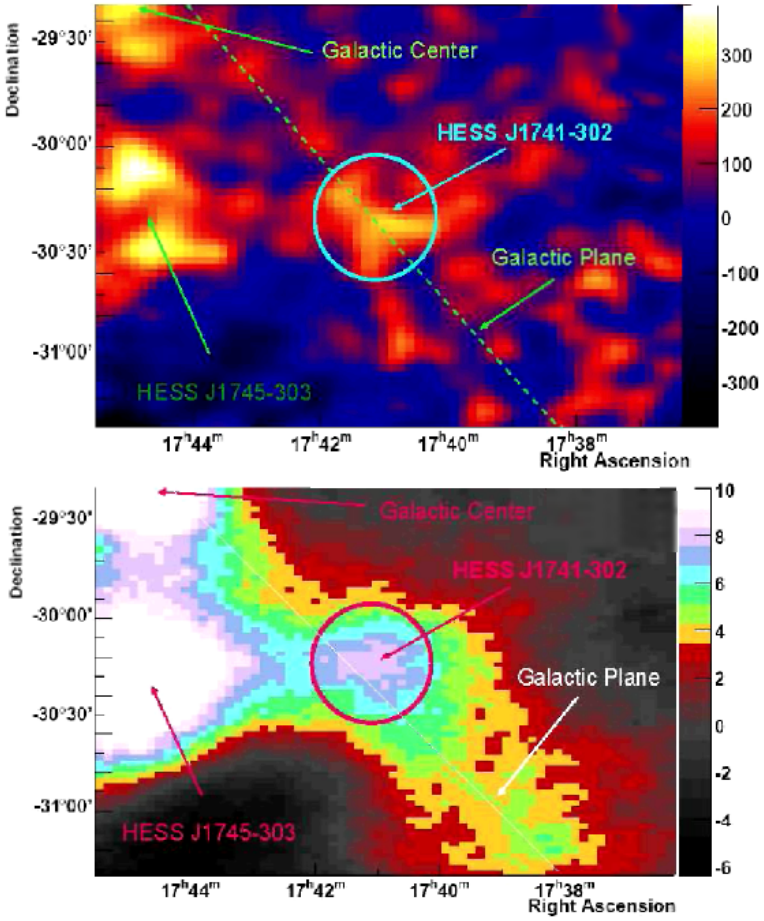

Figure 5.2: The excess (top figure) and the significance map (bottom figure) of HESS J1741−302. The excess map was smoothed with a Gaussian kernel of 0.05° radius. The source is marked with the cyan (top) and the red (bottom) circles. Credit: [Tibolla et al.(2008)]

Figure 5.2 shows the excess map (top) and the significance map (bottom) of HESS J1741−302 published in the proceedings paper. The standard cut configuration was used for producing the skymaps and the background was estimated by using the ring background method. As it can be seen from the figures, HESS J1741−302 seems to be connected with the nearby source HESS J1745−303 when using standard cuts.

The first morphological study done on the source was to investigate whether HESS J1741−302 is an extension of HESS J1745−303 or not. For this study, a slice of the excess map along the line connecting these two sources was chosen. The hard cut configuration, which provides improved angular resolution with respect to standard cuts, was used for producing the excess map. Note that using hard cuts allow the reduction of the contamination coming from the nearby source because of the increased energy threshold with respect to standard cuts. The obtained excess profile along the slice was fitted to a single and a double Gaussian to see if these two sources can be discriminated statistically from each other. The double Gaussian fit ($\chi^2/N_{d.o.f} = 10.2/14$) gave a significantly better fit with respect to the single Gaussian fit ($\chi^2/N_{d.o.f} = 30.2/17$). Consequently, it was concluded that HESS J1741−302 and HESS J1745−303 are two different VHE γ-ray

sources.

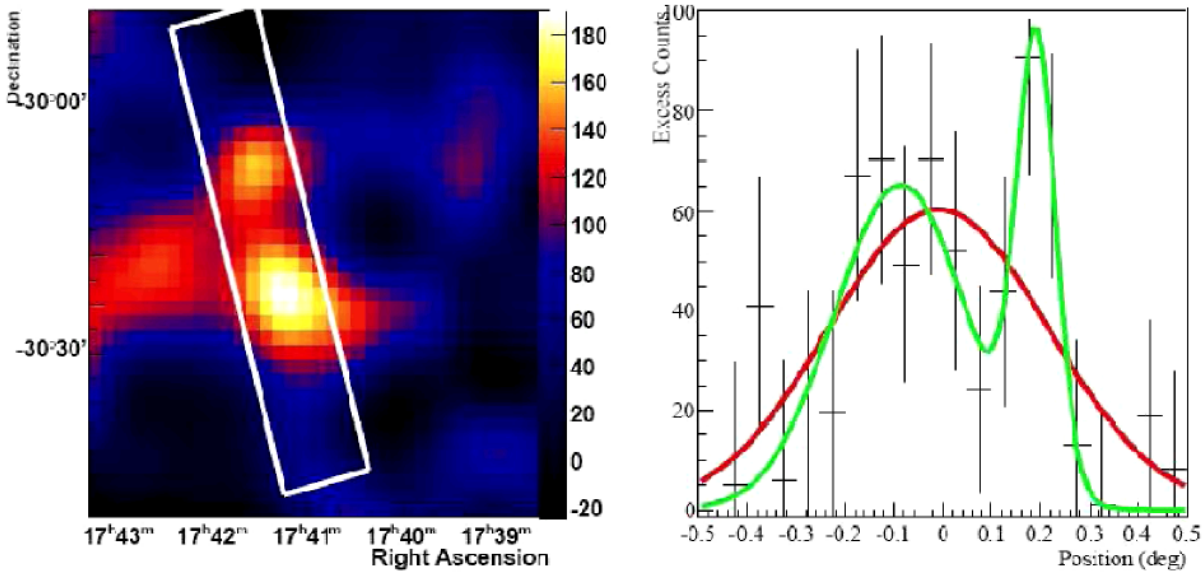

Figure 5.3: Separation of HESS J1741−302 and the nearby hotspot. The left figure shows the zoomed excess map for the HESS J1741−302 region obtained with hard cuts. The white box is the region used for the slice analysis. The right figure shows the excess slice profile for the box region shown in the left figure. The red line is the single Gaussian fit while the green line is the double Gaussian fit. Credit: [Tibolla et al.(2008)]

A hotspot appeared in the northern part of HESS J1741−302 when the hard cut configuration was used for producing the excess map as it can be seen in Fig. 5.3 (left). Therefore, an additional morphological investigation was required, again fitting the excess slice (indicated by the white rectangle in Fig. 5.3 (left)) both to single and double Gaussian to see whether this hotspot is a counter part of HESS J1741−302 or not. The double Gaussian fit to the excess profile ($\chi^2/N_{d.o.f} = 5.9/14$) did not significantly improve the fit with respect to the single Gaussian fit ($\chi^2/N_{d.o.f} = 15.8/17$) as it can be seen from Fig. 5.3 (right). Consequently, the statistics did not allow detailed morphological statements about this hotspot and the hotspot was found to be consistent with statistical fluctuations within the data.

As conclusions, the authors mentioned a probable association of the VHE γ-ray emission with molecular clouds. The reason was due to some overlapping molecular clouds found in the Dame survey [Dame (2001)] and NANTEN data (mentioned as a private communication with Y. Fukui) with the observed VHE γ-ray emission. But these molecular clouds data were not investigated. Another suitable scenario mentioned in the proceedings paper was a possibility of VHE emission originated from a pulsar with an offset PWN that can be associated with the powerful nearby pulsar PSR B1737−30 [Clifton & Lyne (1986)]. The pulsar PSR B1737−30 has an angular offset around $\sim 0.2°$ from the source position. The third but very unlikely scenario was a PWN scenario related to the extremely faint pulsar PSR 1741−3016 [Morris (2002)].

5.1.1 HESS J1741−302 Surroundings

For understanding the nature of the VHE emission coming from the direction of HESS J1741−302, it is important to investigate the objects located around the source. Figure 5.4 shows the excess map with 0.5° FoV radius centered at the source position obtained by using the TMVA hard cut analysis configuration. In the vicinity of HESS J1741−302, there are three pulsars which may be related to the observed VHE γ-ray emission. The properties of these pulsars are listed in Table 5.1. The nearby OH/IR star[2] OH 358.23+0.11 [Caswell (1998)] and a nearby Wolf-Rayet[3] (WR) binary WR 98a [Monnier et al. (1999)] are also shown in Fig. 5.4.

Pulsar Name PSR	R.A. hh:mm:ss	Dec. dd:mm:ss	τ_c kyr	$\dot{E}$ erg s^{-1}	Distance kpc	$\dot{E}/d^2$ erg s^{-1}kpc^2	Offset Degree
J1741−3016	17:41:06.96	−30:16:30.0	3340	5.2×10^{31}	5.02	2.06×10^{30}	0.1
B1737−30	17:40:33.84	−30:15:43.2	20.6	8.2×10^{34}	0.4	5.1×10^{35}	0.19
					3.28	7.6×10^{33}	
J1739−3023	17:39:39.80	−30:23:12.0	159	3.0×10^{35}	3.41	2.6×10^{34}	0.35

Table 5.1: Pulsars around HESS J1741−302. The R.A. and Dec. columns give the pulsar position while the $\dot{E}$ and $\dot{E}/d^2$ columns give the spin-down luminosity and the spin-down flux observed at the Earth, respectively. The offset column gives the relative offset of the pulsars with respect to the best fit position of HESS J1741−302 while τ_c column gives the characteristics age of the pulsar. Data were taken from [ATNF Pulsar Database].

Previous studies about the PWN population at VHE regime showed that pulsars with $\dot{E}/d^2 \approx 10^{34}$ erg s^{-1} kpc^{-2} can produce a PWN that is detectable by the H.E.S.S. telescopes [Carrigan et al. (2007)]. In this study, a conversion efficiency of ∼1% of pulsar spin-down energy loss ($\dot{E}$) into TeV γ-rays was measured. Therefore, distance and $\dot{E}$ information of the pulsars around HESS J1741−302 can provide useful information about possible PWN scenarios. Note that the pulsar PSR J1741−3016 is quite old with a characteristic age of 3.34 Myr and has a relatively low spin-down luminosity. Taking into account the distance of 5.02 kpc, the observable flux at the Earth position is rather low. Consequently, it is unlikely that this pulsar can provide any TeV emission detectable by the H.E.S.S. telescopes and can be directly discarded from leptonic scenarios. The other two pulsars, PSR B1737−30 and PSR 1739−3023, have reasonable $\dot{E}/d^2$ values and therefore can be considered as candidates. But the offset of these pulsars from the best fit position of HESS J1741−302 should be explained.

Since PSR 1739−3023 has a relatively large offset, PSR B1737−30 can be considered as the best candidate. The distance information for this pulsar is not so clear. Two different distance values of 0.4 kpc and 3.28 kpc are provided in the ATNF Pulsar Database.

[2]OH/IR stars are late type stars enshrouded in a dense dust shell which absorbs all the radiation emitted by the star and re-emits it in infra-red (IR) wavelengths.

[3]Wolf-Rayet stars are a heterogeneous set of stars with unusual spectra showing prominent broad emission lines of highly ionized helium and nitrogen or carbon. The spectra indicate very high surface temperatures of 3×10^4 K to around 2×10^5 K.

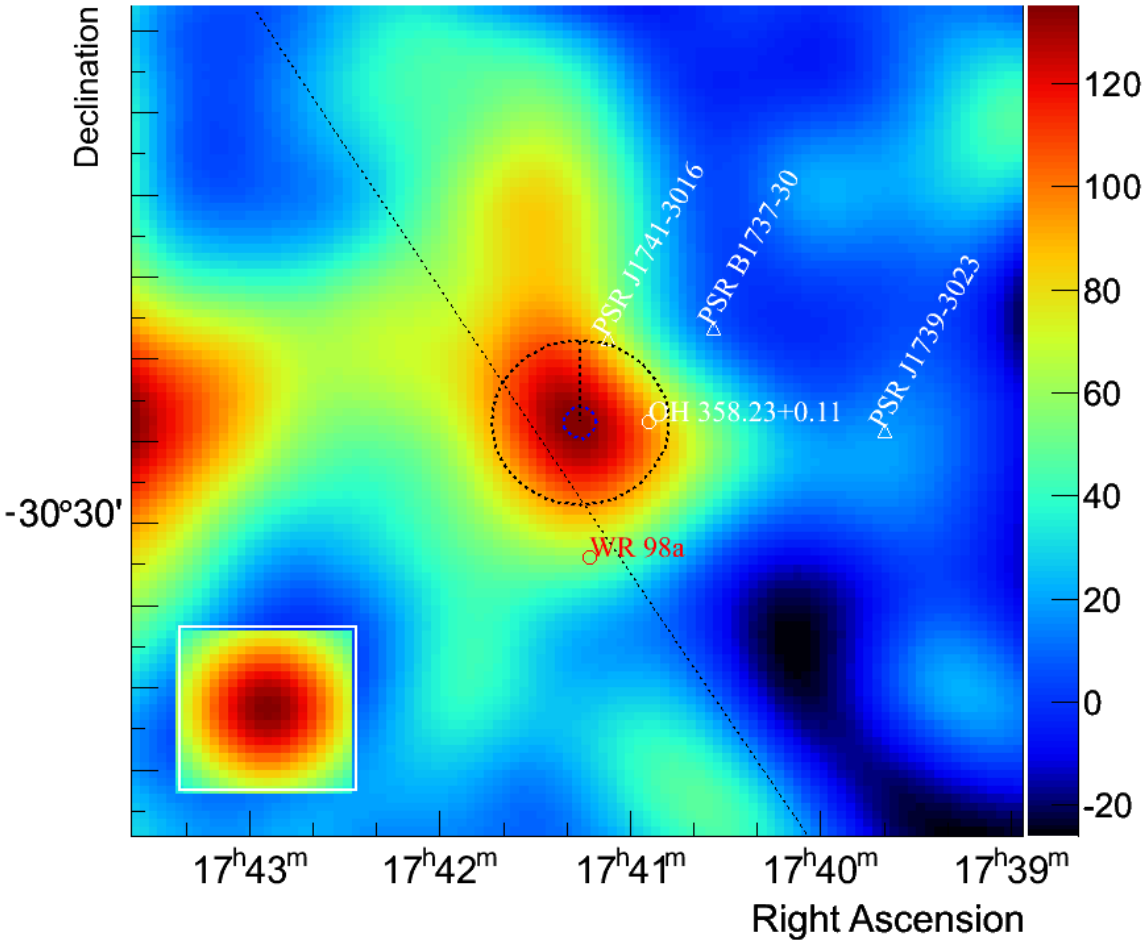

Figure 5.4: HESS J1741−302 surroundings. The dashed black circle which is centered at the best fit position of HESS J1741−302 (explained in more detail in Section 5.2.2) shows the extension (0.1°) of the point-like morphology of HESS J1741−302. The dashed blue circle shows 1σ error interval of the best fit position (both in R.A. and Dec.) of HESS J1741−302. The white triangles indicate the pulsar positions given in Table 5.1 while the white circle indicates the OH/IR star OH 358.23+0.11 position. The red circle shows the position of Wolf-Rayet binary WR 98a.

These two distance values were estimated by using the dispersion measure (DM) method [Taylor (1993)]. Technically, the dispersion measure is proportional to the integrated column density of free electrons between an observer and a pulsar. The distance of 0.4 kpc to the pulsar PSR B1737−30 was calculated by the latest electron density estimate in Janssen (2006) by using the DM method explained in Taylor (1993) and is accepted as the default value in the ATNF Pulsar Database currently. On the other hand, the 3.28 kpc distance was calculated by using the same method and taking into account the electron density model given in Taylor (1993). Consequently, for the rest of this study, the distance to PSR B1737−30 will be accepted as 0.4 kpc, but the calculations will also be repeated for the distance approximation of 3.28 kpc.

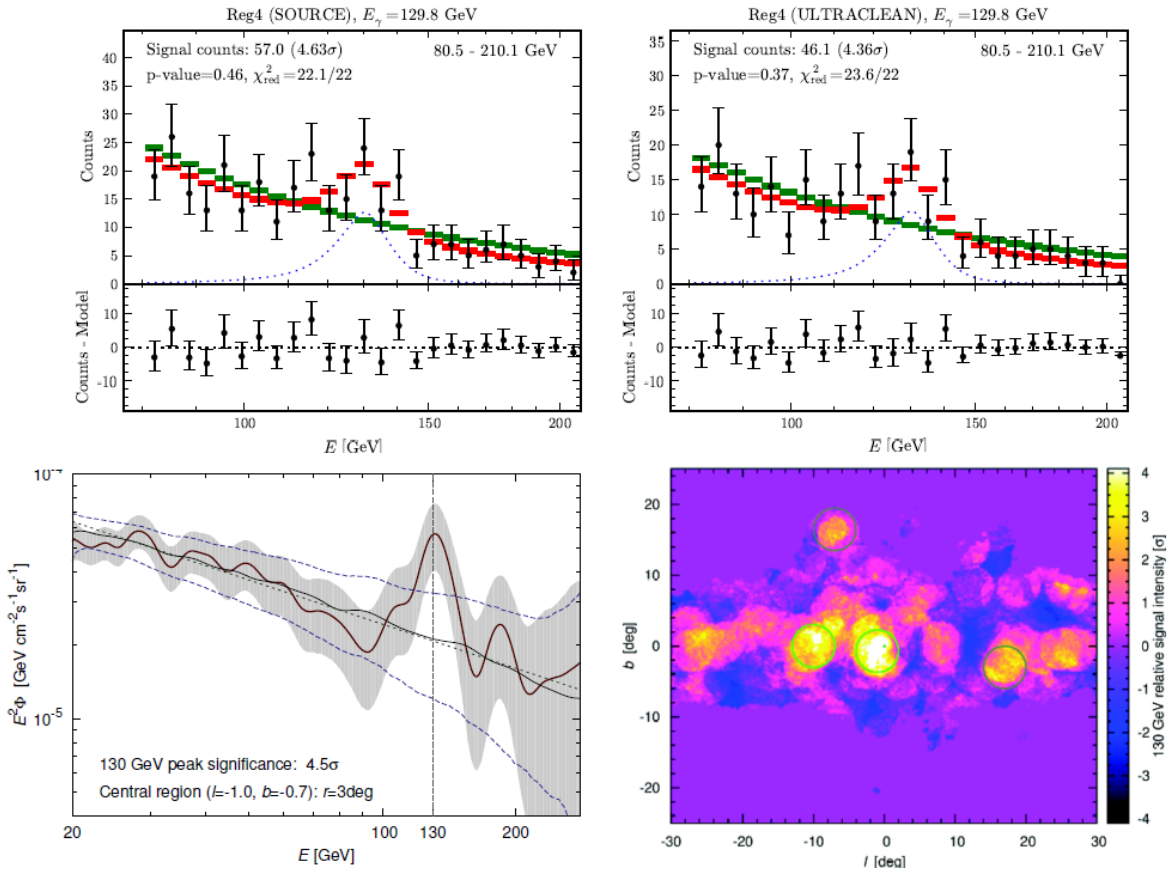

Figure 5.5: First 130 GeV line studies. Top left and top right figures show the evidence for a line spectral feature at $E = \sim$130 GeV found in the Fermi-LAT data [Weniger (2012)] obtained by using different cut configurations, respectively. The measured events with statistical errors are plotted in black. The horizontal bars show the best fit models with (red) and without (green) dark matter signal. The lower left figure shows the Fermi line flux extracted from a region centered at $(l, b) = (-1.0°, -0.7°)$ with a radius of 3° [Tempel (2012a)]. The lower right figure shows the significance map of 130 GeV photons in the Galaxy. The green circles denote the signal regions that provide the excess with highest statistical significance with the green point indicating the maximum significant bin.

5.1.2 The Fermi 130 GeV Line Feature

The Fermi Gamma-ray Space Telescope carries two instruments, namely the Large Area Telescope (LAT) and the GLAST Burst Monitor (GBM). The LAT, which is exploring the γ-ray sky in the energy range between 20 MeV and 300 GeV, is Fermi's primary instrument while the GBM is the complementary one. Detailed descriptions of the LAT, its performance and calibration procedures can be found in Atwood (2009) and Ackermann (2012). The LAT data analysis is event-based, individual events are reconstructed so their energies and directions can be estimated. CR background rates can exceed γ-ray rates by factors of up to 10^4, therefore requiring powerful event selection criteria to obtain pure γ-ray samples.

In 2012, a tentative evidence for a line-like spectral feature at $E = \sim$130 GeV in the Fermi-LAT data has been found [Weniger (2012)] as shown in Fig. 5.5 (upper panel).

The local significance[4] of this line structure was around $\sim 4.3\sigma$ while the global significance was around $\sim 3.2\sigma$ for both sets of cuts[5] used for data analysis. The line structure was interpreted as the 130 GeV dark matter annihilating into two photons with a cross section approximately 24 times smaller than needed for the thermal relic density. Afterwards, the signal was independently confirmed [Tempel (2012c)], [Finkbeiner (2012a)], [Tempel (2012a)]. In another study [Tempel (2012a)], authors tried to localize the spatial origin of the 130 GeV excess by looking at the significance distribution of the relative signal intensity of 130 GeV photons in the Galaxy as shown in the lower right Fig. 5.5, within the energy interval of 120 GeV$< E <$140 GeV. The point of maximum significance in Fig. 5.5 (lower right) corresponds to Galactic coordinates of $(l, b) = (-1.0^\circ, -0.7^\circ)$, which is coincident with the H.E.S.S. source HESS J1745−303 having the Galactic coordinates of (l, b)=$(-1.24^\circ, -0.64^\circ)$ [Aharonian (2006d)]. The standard deviation from this maximum was around 2.0° on both l and b, which also includes the Galactic Central source HESS J1745−290 [Acero (2010)].

Another study on the localization of the spatial origin of the line structure was done in Finkbeiner (2012b). The authors used another approach by considering the individual photon events (not maps) and assuming that the exposure across the GC is slowly varying. Projecting the event locations into histograms of galactic l and b coordinates and studying the distributions allowed them finding the parameters of a best-fit Gaussian[6]. The results are shown in Fig. 5.6. Two datasets were investigated, the first dataset includes all events while the second one takes into account the events with $\theta > 40^\circ$. Such a choice allows the elimination of γ-ray events produced by CR interactions in the Earth's atmosphere. For both datasets, the line structure was found to be in the energy interval between 124.7 GeV and 133.0 GeV and centered at the Galactic coordinates[7] of $(l, b) = (-1.5^\circ \pm 0.3^\circ, 0^\circ \pm 1.0^\circ)$. Consequently, the obtained best Fermi line spatial position is coincident with HESS J1741−302 which is located at $(l, b) = (-1.71^\circ \pm 0.03^\circ, 0.05^\circ \pm 0.03^\circ)$. The possibility that the γ-ray line is a fake instrumental effect was discussed and disfavored in Finkbeiner (2012a).

Finally, the Fermi Collaboration has performed a search for γ-ray spectral lines from 5 GeV to 300 GeV within 5 different ROIs as shown in Fig. 5.7 (upper left panel). The total 3.7 years of data have been re-processed by using updated calorimeter calibration constants and the 2D energy dispersion model, which provides improved energy resolution with respect to the 1D energy dispersion model by using an additional parameter (P_E) that

[4]Local significance can be described as the pre-trial significance which does not take into account the trial factors of the analysis while global significance is the post-trial significance which takes into account the trial factors of analysis.

[5]Two different cut selections were used in this analysis. "SOURCE" event selection is used for analyzing the point sources and regions of bright diffuse emission while "ULTRACLEAN" selection is used for analyzing the regions of faint diffuse emission above a few GeV.

[6]In order to test for the existence of a line structure, the authors compared $\ln(L_0)$ for the null hypothesis (no line structure), to a model with an additional Gaussian of FWHM F_l, centered at l_0 with peak height A_l. Finally, the authors computed $\Delta\ln(L) = \ln(L/L_0)$ and expressed the results using the test statistic TS $= 2\Delta\ln(L)$.

[7]Note that in the latitude direction, the fit is complicated by the concentration of conventional continuum emission in the plane. The peak was found not to be significantly offset in the b direction, but sits in the region of highest background, so addition of the peak is not demanded strongly by the fit. Therefore, determination of errors on b_0 requires much more data.

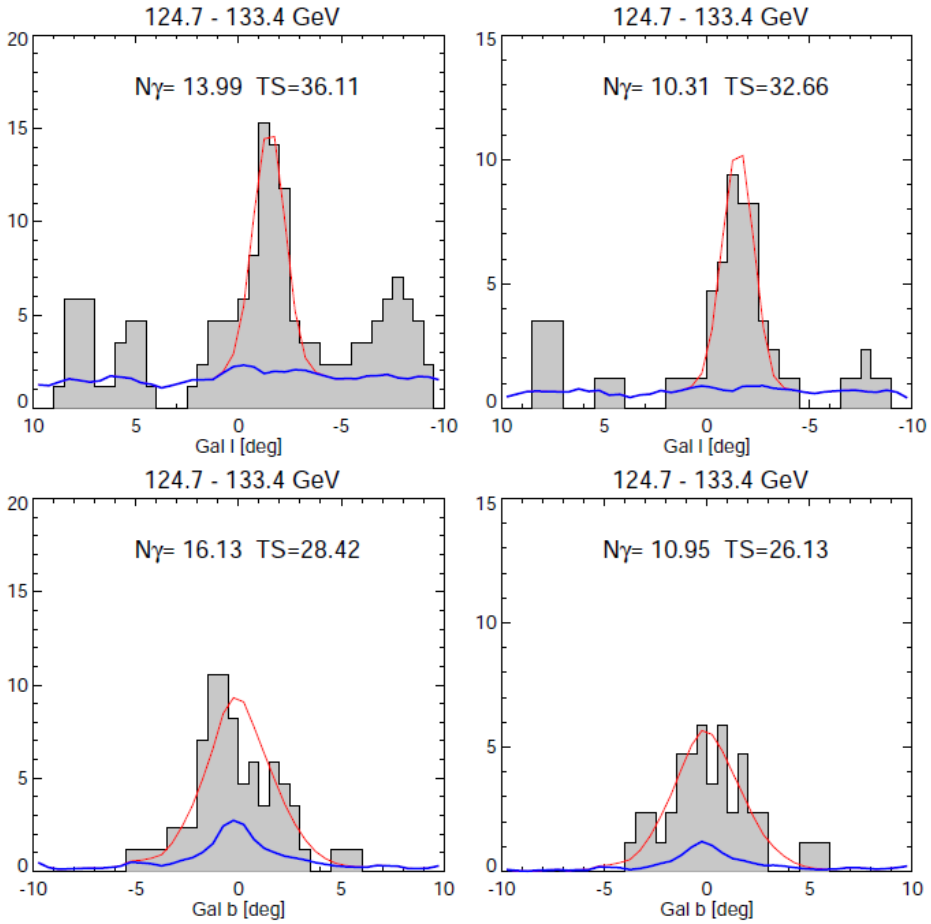

Figure 5.6: Spatial origin of the Fermi 130 GeV line. Figures are the excess profiles for both l and b. The left figures show the results obtained by taking into account all events, while the right figures show the results by taking into account the events with $\theta > 40°$. The angle θ is the γ-ray incidence angle which is defined as the angle between the boresight of LAT instrument and the direction of limb γ-ray production by CR interactions in the Earth's atmosphere.

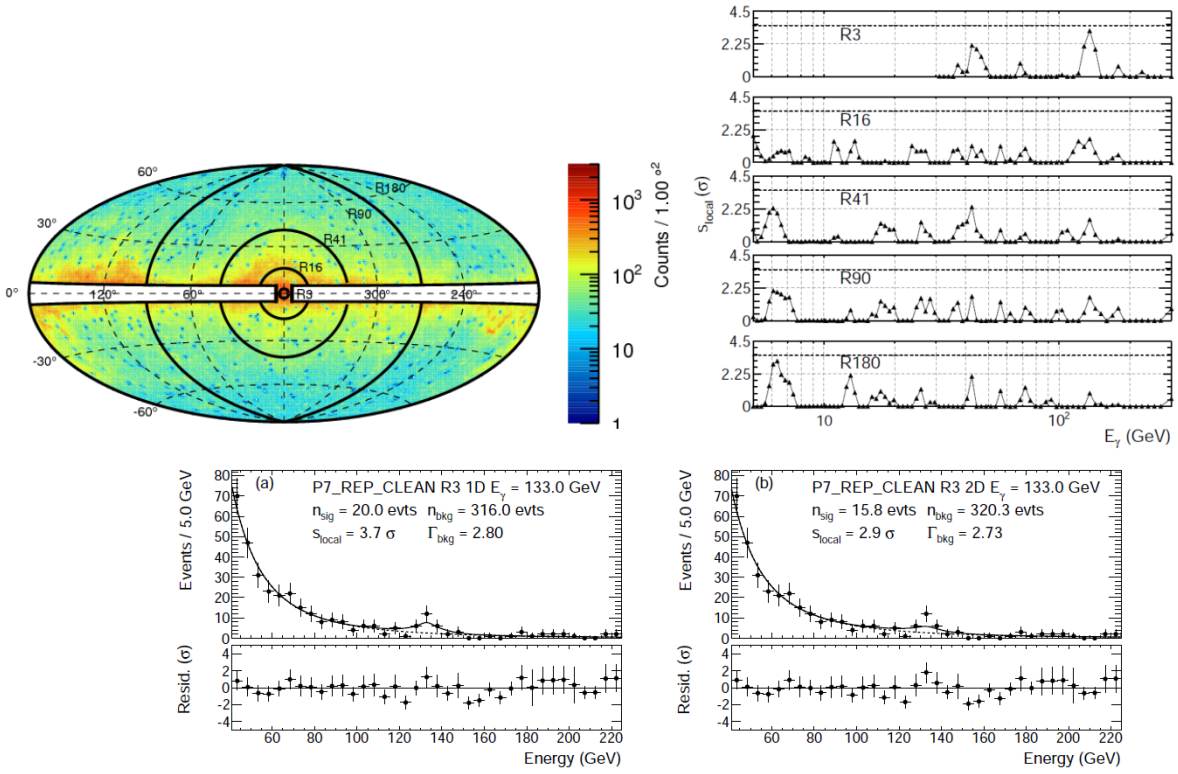

Figure 5.7: Fermi 130 GeV line final results. The upper left panel shows the ROIs used for searching the line structure. The upper right panel shows the result of the line search studies in all the ROIs taken into account. The dashed line at the top of this plot indicates the local significance corresponding to the 2.0σ global significance. The lower panel shows the fit for a line-signal signal at 133 GeV in R3 using a 4.4 year P7REP CLEAN dataset for (a) the 1D energy dispersion model (b) the 2D energy dispersion model. Credit: Fermi Collaboration (2013)

describes event-by-event energy reconstruction quality. It was reported that no globally significant spectral line signal was found [Fermi Collaboration (2013)]. Although the local significances were found around 3.6σ and 2.9σ for 1D and 2D energy dispersion models for the ROI R3, respectively, no line structure model could go beyond 2.0σ global significance level. It was also mentioned in this paper that the 133 GeV feature in ROI R3 cannot be entirely explained in terms of known systematic effects, but this feature does have certain characteristics that disfavor interpreting it as a DM signal. Therefore, more data are needed to clarify the origin of this feature.

5.2 VHE Data Analysis

In this section, the analysis results of VHE data from the H.E.S.S. observations of the region around HESS J1741−302 will be described in detail. The VHE data analyzed in this section were taken with H.E.S.S. phase I array configuration.

5.2.1 Available Data and Analysis Methods

HESS J1741−302 data was analyzed by taking into account 343 (detection selection, 145 hours live-time) and 303 (spectral selection, 128 hours live-time) observation runs located within 2.0 degree offset from the HESS J1741−302 catalog position R.A.: $17^{h}41^{m}43^{s}$, Dec.: −30°17'35". The runs with detection selection[8] were used to gain as many excess events as one can get from the observation data for producing skymaps and to perform a morphology analysis. The runs with spectral selection[9] were used for extracting the VHE γ-ray spectrum of the source HESSJ1741−302.

The data were analyzed with the H.E.S.S. Analysis Package[10] for shower reconstruction, and a multivariate analysis technique [Ohm (2009)] was applied for improved discrimination between hadrons and γ-rays after the application of quality selection criteria [Aharonian (2006b)]. The cosmic-ray background level was estimated by using the ring background model [Berge & Funk & Hinton (2007)] for the morphology analysis of HESS J1741−302, while the reflected background model [Berge & Funk & Hinton (2007)] was used for the spectral analysis of this source.

Recall that in the proceedings paper, it was mentioned that 143.5 hr of data were analyzed. These data were analyzed by using the "Wobble-chain" software since the hap software did not exist at that time. The Wobble-chain software was using a very old calibration and was known to have higher systematics. This software was not applying selection criteria to the VHE data as they are defined in the current hap software. Note

[8]Detection criterion applies the cuts on the hardware quality which is based on the run duration (>10 mins), participation fraction (relative participation to trigger rates of each telescope should be > 0.4), broken pixels and tracking quality. This criterion also needs at least 2 telescopes participating in a run.

[9]Spectral criterion includes the cuts used in detection criterion and the additional atmospheric effects like relative change of the system trigger rate, the fluctuation of the system trigger rate and the combined effect of muon efficiency, camera gains and telescope trigger rates. Spectral criterion is needed for the spectrum because the Cherenkov light can be absorbed due to the atmospheric conditions and this can result in the misinterpretation of the images produced in camera. This criterion also needs a minimum number of 3 telescopes participating in a run.

[10]HAP-HD 13-06

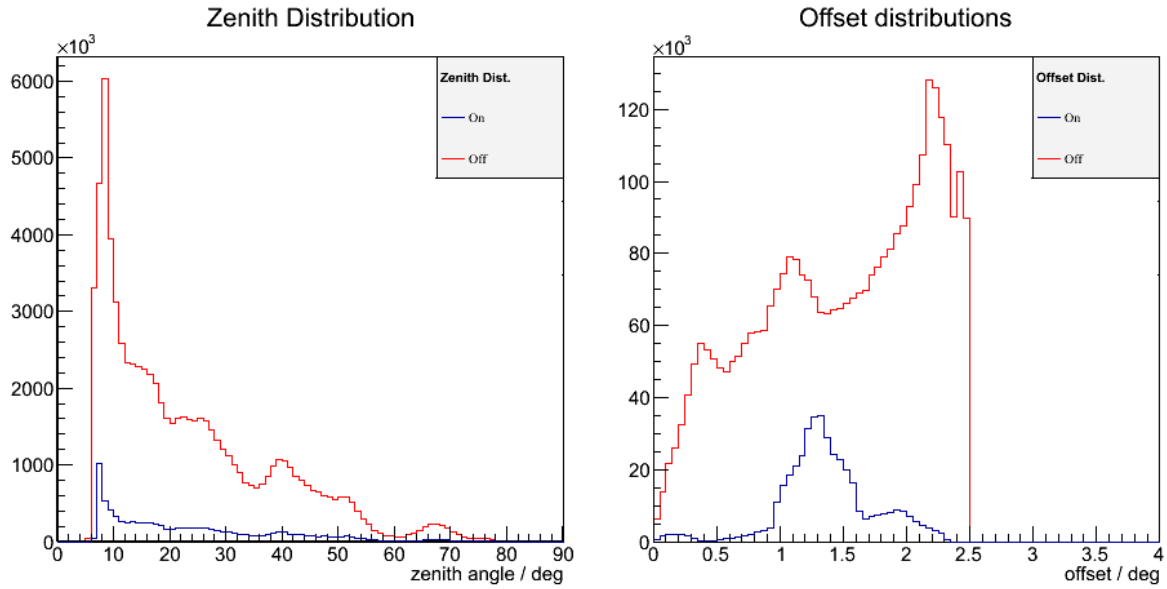

Figure 5.8: Left figure: Zenith distribution of ON and OFF events for detection runs. Right figure: Offset distribution of ON and OFF events for detection runs. Note that ON and OFF events are obtained by using the ring background maker. The red lines show the zenith angle (offset) distribution of OFF events while the blue lines show the zenith angle (offset) distribution of ON events in both of the figures.

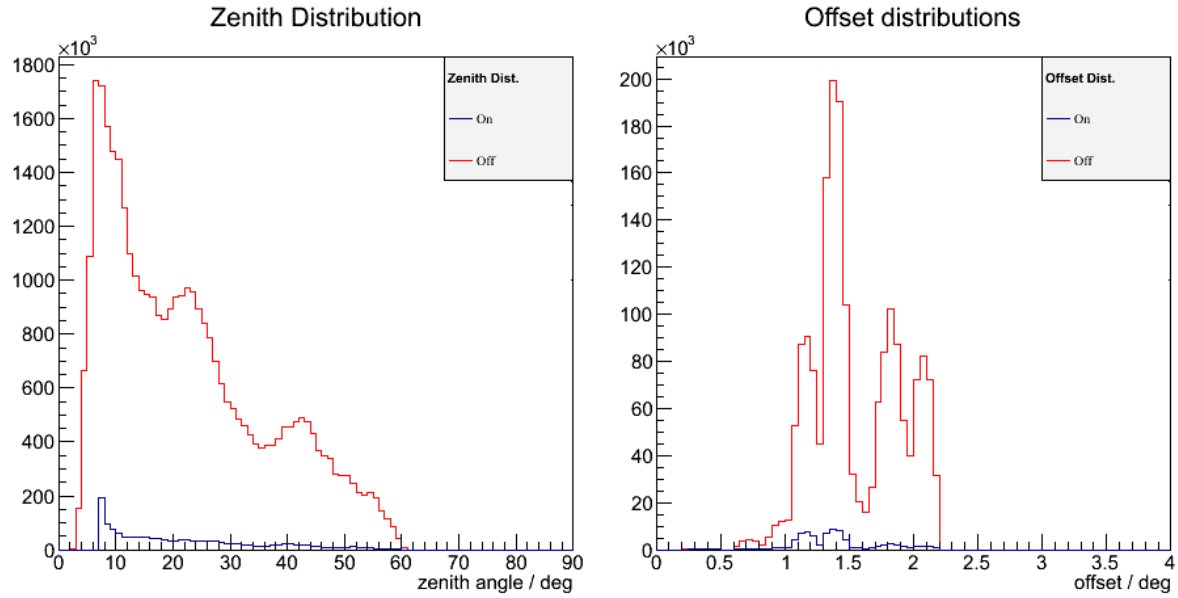

Figure 5.9: Zenith and offset distributions as shown in Fig. 5.8 but for spectral runs. Note that ON and OFF events are obtained by using the reflected background maker.

that the application of current selection criteria (detection selection) to the H.E.S.S. data taken before 01.01.2009, which were used in the data analysis presented in Tibolla et. al (2008), gives ∼97 hr of good-quality data. Therefore, 143.5 hr data used in the previous analysis corresponds to ∼97 hr of good-quality data. Consequently, the VHE data analyzed in this thesis include additional ∼48 hr of data. In this analysis, only the good-quality runs passing the mentioned criteria were analyzed. This explains why there is not much difference between the live-times of the analyzed data (143.5 hours) in Tibolla et. al (2008) and in this thesis (145 hours).

Figure 5.8 shows the zenith and offset distributions of ON and OFF events from detection runs used in the HESS J1741−302 analysis while the same distributions for spectral selection runs are shown in Fig. 5.9. For detection runs, the zenith angle distributions of both ON and OFF events give the mean values of 23.1°, while the offset distribution mean values for ON and OFF events are 1.37° and 1.49°, respectively. For spectral detection runs, the mean values for the zenith angle distribution of ON and OFF events are 21.5° and 22.5° while the mean values for ON and OFF events' offset angle distributions are 1.39° and 1.54°, respectively.

5.2.2 Detection and Morphological Analysis

Understanding the morphology of HESS J1741−302 is important because it could not be resolved in the previously published analysis leading to a choice of larger extraction region for deriving the spectrum. Moreover, the detailed morphology of the source can give hints about the emission mechanism that gives rise to the observed VHE γ-ray signal.

The ON region with a radius of 0.1° centered at the source position R.A.: $17^{h}41^{m}15^{s}$, Dec.: −30°22'37" was used for detection. H.E.S.S. J1741−302 was detected[11] with a statistical significance of 7.6σ, determined by using Equation 17 in Li&Ma (1983), after background estimation with the reflected background model. In order to minimize the contamination coming from the nearby powerful source HESS J1745−303 (Aharonian et al. 2006), hard ζ cuts, which imply a cut on θ^2 of 0.01 degree^2 and a cut on the individual image charge of 160 photo-electrons, were used. The application of hard ζ cuts provides an improved angular resolution for morphological studies with respect to standard ζ cuts.

Figure 5.10 shows the excess and the significance maps for the HESS J1741−302 region while Fig. 5.11 shows the corresponding background diagnostics plots. As it can be seen from Fig. 5.11 (right), the significance distribution of the background is compatible with the expected background distribution[12], indicating that the background was modeled well for this analysis.

The previous morphological analysis of the HESS J1741−302 region presented in the proceedings paper and also the produced excess maps for this study suggest the possible elongation of HESS J1741−302 or the presence of a second source in the field of view. For investigating this possibility, a slice analysis of the source along the visible extension direction was performed as it was done in the proceedings paper. Figure 5.12 (top) shows the slice region taken into account for slice analysis while the bottom figure shows the

[11]Note that in the proceedings paper, only the peak significance of 8.1σ was mentioned.

[12]The significance distribution of background is expected to have a mean value of 0 with a standard deviation of 1.0.

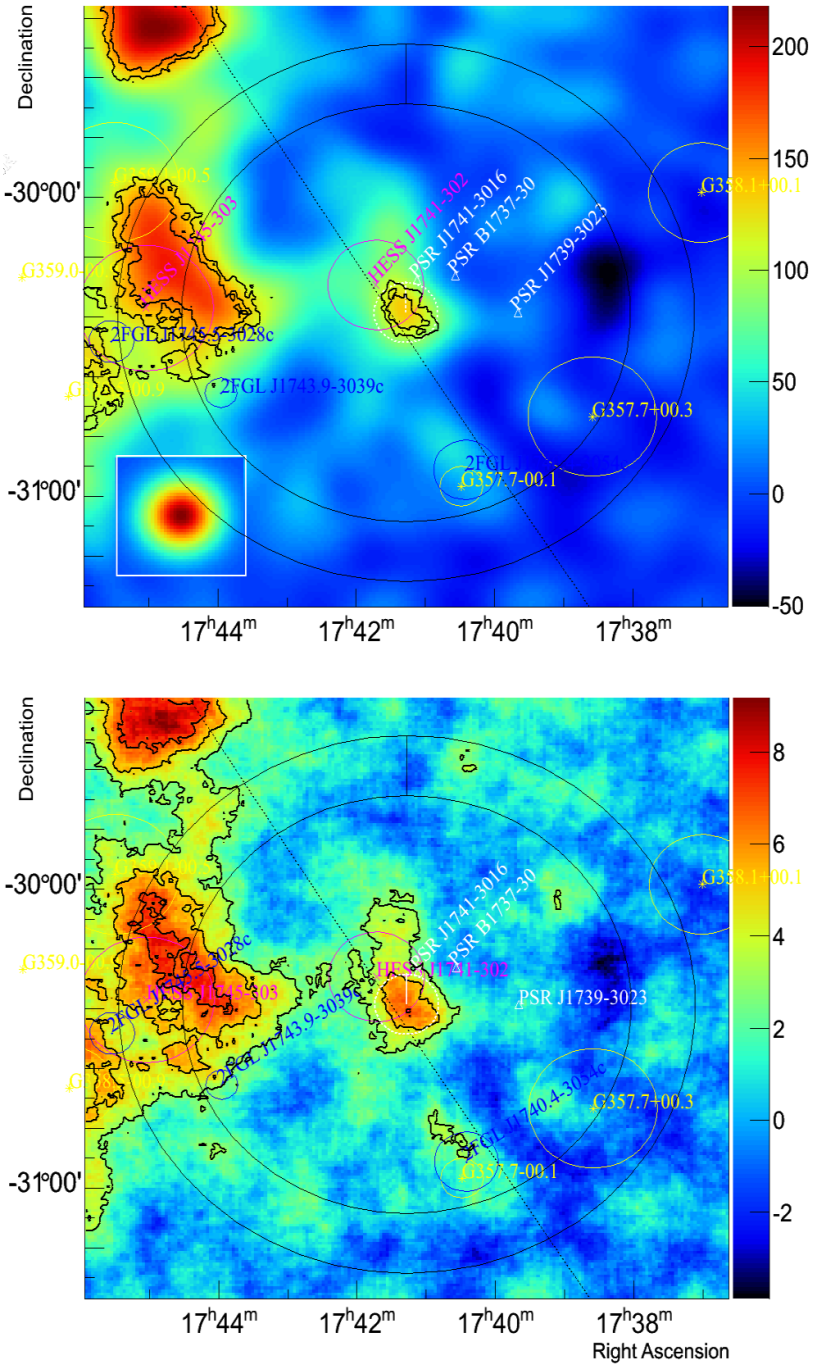

Figure 5.10: Top figure: The excess map of the HESS J1741−302 region smoothed with a Gaussian of width 0.07°. The white dashed circle shows the ON region used for this analysis while the black ring shows the ring region used for background estimation. Note that the H.E.S.S. objects are marked with the magenta circles while the Fermi objects are marked with the blue circles. The pulsars shown in Table 5.1 are marked with the white triangles while the SNRs are shown with the yellow circles. The black contours indicate 5σ and 6σ significance contours. The H.E.S.S. PSF is shown inside the white box in the bottom left corner. Bottom figure: The significance map of the HESS J1741−302 region. The black contours indicate 3σ, 5σ and 7σ significance contours.

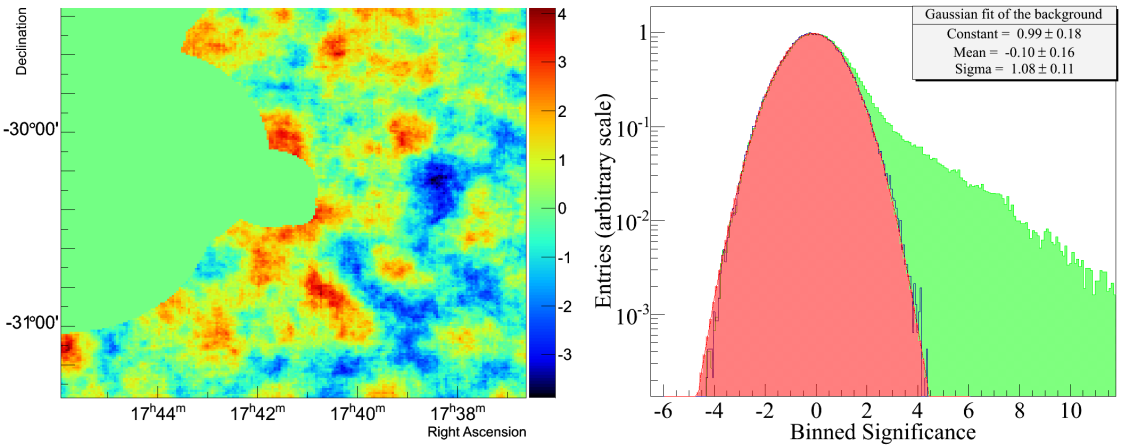

Figure 5.11: Left figure: The significance map with excluded regions used in this analysis. Right figure: Significance distribution of the background. Note that the green region shows the total significance distribution while the red region shows a Gaussian fit to the background significance distribution. Best fit values for a Gaussian fit to the background significance distribution are given in the upper right corner.

corresponding excess distribution within the chosen slice region. The double Gaussian fit to the excess profile can not be statistically separated (1.7σ by using the F-Test) from a single Gaussian fit. Therefore, a 2D fitting procedure was performed for investigating the exact morphology of the source in more detail.

A morphology analysis of HESS J1741−302 was done by using CIAO Sherpa v4.5[13] [Freeman (2001)] which allows performing simultaneous 2D model fitting. An addition to TMVA hard ζ cuts, the same fitting procedure was repeated for the TMVA hi-resolution direction maker [Chia-Chun Lu et al. (2013)] cut configuration which offers better angular resolution with respect to hard ζ cuts and is more suitable for the morphology study of this complicated region. Note that the `hires_zeta_dm` cut configuration (hi-res ζ) provides an angular resolution down to 0.08° at 20° zenith angle with an image size cut of 160 p.e. for sources with spectral index of 2.0. This configuration also uses the runs with spectral selection quality which allows better reconstruction of showers with respect to hard ζ cuts using runs with detection selection quality. The fitting procedure was performed step by step, following the procedure of adding an additional 2D Gaussian to the previous model and comparing the results by using the Log-Likelihood Ratio Test (LLRT). For each step, an elongation of the added 2D Gaussian was also tested to assess the significance of the improvement with respect to the nested model. Note that a 2D Gaussian has 4 parameters. These parameters are the x and y position on the excess map, the FWHM value which gives source extension and the amplitude. In 2D elongated Gaussian case, there are 6 parameters. An addition to 4 parameters describing the 2D Gaussian, there are two more parameters called "ellipticity", a parameter related to the ratio of the ellipse's major and minor axes, and "theta" which is a parameter related to the orientation of major axis of the ellipse. For a morphology model to be valid, the fit should converge and all parameters of the combined model should be constrained well. The 2D Gaussian functions used for

[13]See http://cxc.harvard.edu/sherpa/ for detailed information.

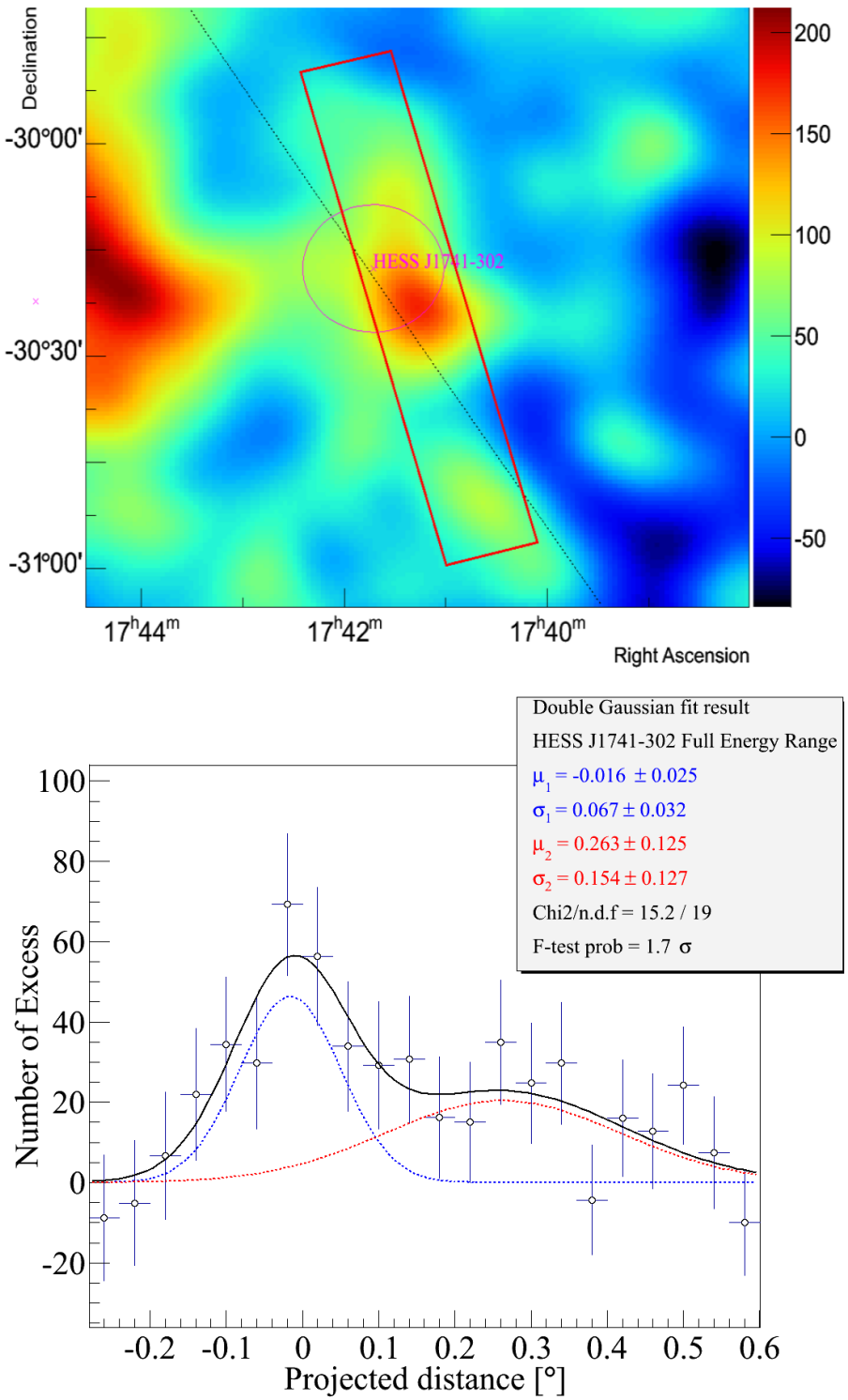

Figure 5.12: Top figure: Zoomed excess map of the HESS J1741−302 region. The red box shows the slice region taken into account for the slice analysis. Bottom figure: Spatial excess distribution within the chosen slice region. The black line, which is the sum of 2 Gaussians, shows the total fit to the excess profile. The blue line shows the 1st Gaussian used for modeling HESS J1741−302 while the red line shows the second Gaussian modeling the possible second source (or possible elongation).

modeling the morphology were convolved with the PSF of the instrument[14]. All tested morphology models were fitted to the excess map extracted as FITS[15] files from the hap analysis.

The excess maps for both configurations are shown in Fig. 5.13. As it can be seen from the figures, the HESS J1745−303 region has an extremely complicated morphology. Therefore, only a fraction of the produced excess map, called region of interest (ROI) as shown in Fig. 5.13, was used for avoiding the complicated morphological effects of HESS J1745−303. The separation between HESS J1741−302 and the hotspot that can be seen in the northern part of HESS J1741−302 is more clear in Fig. 5.13 (top) with respect to the bottom figure even by eye, since the excess map at the top was produced by using the hi-res ζ cut configuration. The results obtained from the 2D fitting procedure for different 2D morphology models are shown in Table 5.2 for each configuration while the residual maps of the tested models for the hard ζ configuration are shown in Fig. 5.14.

Since there is a contamination coming from the relatively powerful nearby source HESS J1745−303, one of the 2D Gaussians is used for the background contamination correction and the second Gaussian is used for modeling the source HESS J1741−302. This combined model (referred to as 2 × G in Table 5.13) is assumed to be a "nested model" for comparing further 2D combined morphological models.

When modeling the region of interest with two 2D Gaussians by using hard ζ cuts (model Hard ζ (N) in Table 5.13), a blob like structure can be clearly seen in the residual map (Fig. 5.14 (left)). This basically suggests the elongation of HESS J1741−302 or to add another 2D Gaussian at the blob structure position. Modeling the region with an elongated 2D Gaussian representing HESS J1741−302 (model Hard ζ (D) in Table 5.13) could not be well fitted to the data. The parameters of the elongated 2D Gaussian, namely theta and ellipticity, could not be well constrained and the total fit did not converge. On the other hand, modeling the data by using an additional 3rd non-elongated Gaussian (model E) could well represent the data and all parameters of the 2D Gaussians could be well constrained. This model (E) improved the fit by 4.0σ with respect to the nested model. Allowing elongation of the source HESS J1741−302 (model F) again could not represent the data well and the fit did not converge.

The same procedure was repeated by using the hi-res ζ cut configuration. In contrast to hard ζ cuts, modeling the data by using an elongated 2D Gaussian representing HESS J1741−302 could be fitted well to the data and the fit converged (model A and C in Table 5.13). Comparing the LLRT results given in Table 5.13 suggests that the best morphology model representing the data obtained by using hi-res ζ cut configuration is model C which is the combination of 2 × Gaussians + 1 Elongated Gaussian (with an improvement of 5.3σ with respect to the nested model). In this model, an elongated 2D Gaussian is the function used for modeling the source HESS J1741−302.

Consequently, the addition of a third 2D Gaussian (model B and E) improved the fit significantly for both configurations. This third 2D Gaussian refers to the nearby hotspot structure that can be seen in the excess maps. The theta and ellipticity parameters of the

[14]The PSF was extracted from the hap analysis by using the obtained spectral index (2.28) assuming a power-law model. Afterwards, the PSF was fitted to a triple exponential function for determining the parameters which were used as input for modeling the PSF of the instrument.

[15]Flexible Image Transport System

Model	R.A. Degree	Dec. Degree	Extension Degree	Theta Degree	Ellipticity	Log-likelihood	LLRT σ
Hi-Res ζ (N) 2 × G	265.303 ± 0.013	−30.393 ± 0.011	0.026 ± 0.010	–	–	−26139.5	–
Hi-Res ζ (A) G + EG	265.322 ± 0.013	−30.369 ± 0.017	Maj: 0.074 ± 0.020 Min: 0.019 ± 0.005	116.9 ± 10.0	0.742 ± 0.146	−26133.3	3.1
Hi-Res ζ (B) 3 × G	265.314 ± 0.020	−30.377 ± 0.026	0.036 ± 0.020	–	–	−26126.8	4.1
Hi-Res ζ (C) 2 × G + EG	265.322 ± 0.012	−30.369 ± 0.015	Maj: 0.074 ± 0.020 Min: 0.017 ± 0.005	118.6 ± 9.4	0.723 ± 0.142	−26117.7	5.3
Hard ζ (N) 2 × G	265.314 ± 0.014	−30.377 ± 0.014	0.032 ± 0.017	–	–	−23677.2	–
Hard ζ (D) G + EG	Constrained	Constrained	Constrained	Failed	Failed	Fit did not converge	–
Hard ζ (E) 3 × G	265.316 ± 0.015	−30.377 ± 0.015	0.041 ± 0.018	–	–	−23665.0	4.0
Hard ζ (F) 2 × G + EG	Constrained	Constrained	Constrained	Failed	Failed	Fit did not converge	–

Table 5.2: Comparison of 2D morphological models for the hi-res ζ and hard ζ cut configurations that can be seen in Fig. 5.13 (top) and Fig. 5.13 (bottom), respectively. The model column describes the cut configuration and the 2D model used for fitting. The character "G" refers to 2D Gaussian model with 4 parameters while "EG" refers to 2D elongated Gaussian with 6 parameters. The characters A, B, C, D, E and F are references to models for simplicity while the character "N" stands for the "Nested Model". R.A. and Dec. columns give the best fit position of the 2D Gaussian representing the source HESS J1741−302 while the extension column gives the intrinsic extension of the source. Note that the theta column gives the orientation of the ellipse while the ellipticity column gives flattening (or oblateness) of the elongated Gaussian. The LLRT column gives the improvement of the model with respect to the nested model (2 × G) in σ. In this table, 2D Gaussian parameters are given for the Gaussian describing HESS J1741−302 while improvement and log-likelihood values are given for the combined model.

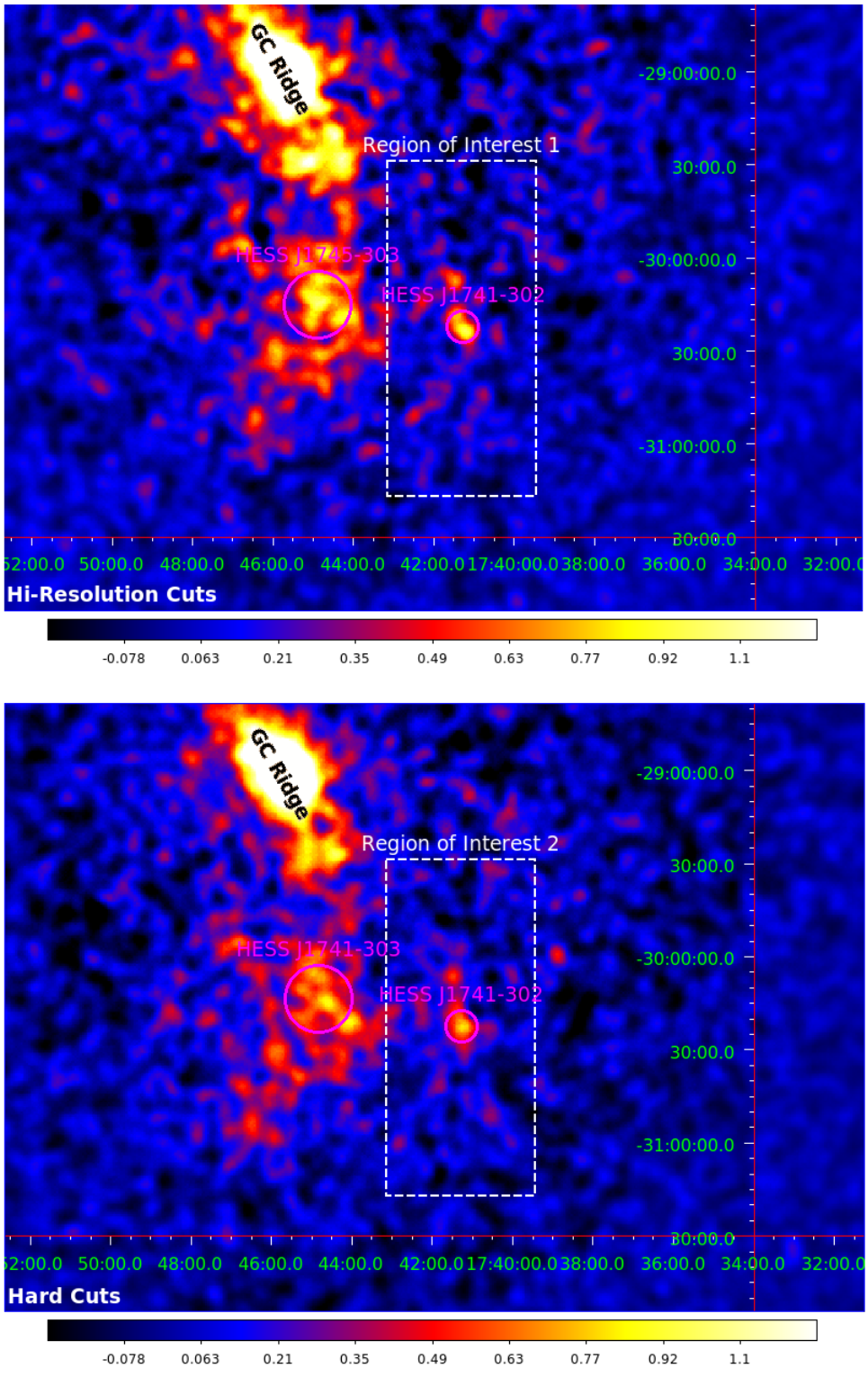

Figure 5.13: The excess maps derived by applying hi-res ζ (top figure) and hard ζ (bottom figure) cut configurations. Both maps were smoothed with a Gaussian kernel of 0.07° for a better visualization. Region of interests taken into account for 2D morphology fitting are shown with the dashed white boxes. The HESS J1741−302 and HESS J1745−303 positions are marked with the magenta circles. The bright GC ridge can also be seen in both excess maps.

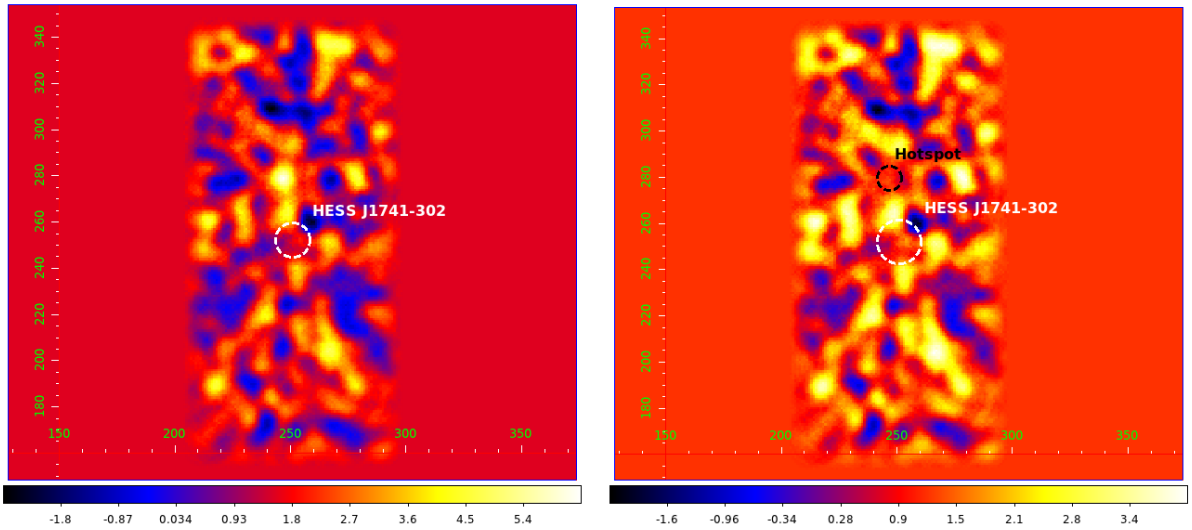

Figure 5.14: Residual count maps for converged 2D combined models for the hard ζ configuration. Note that both figures show the residual map for the ROI shown in Fig. 5.13 (bottom). Left figure: Residual map for the model Hard ζ (N) given in the Table 5.2. Right figure: Residual map for the model Hard ζ (E) given in the Table 5.2. The white dashed circles show the best fit position of HESS J1741−302 in both figures while the black dashed circle in the right figure shows the best fit position of the hotspot structure. The axes are given in physics coordinates of the excess maps used in 2D fitting. The z-axis gives the difference of excess counts between the data and the converged morphology model.

2D elongated Gaussian could not be well constrained when allowing the elongation of the 2D Gaussian representing HESS J1741−302 for hard ζ cuts (model D and F) as can be seen from the Table 5.2. On the other hand, all elongated model parameters (model A and C) are well constrained and the fit converged when fitting tested morphology models to the excess data produced by hi-resolution cuts. As a conclusion, the hotspot structure can be statistically discriminated in both configurations from HESS J1741−302 while an elongation of HESS J1741−302 can only be obtained when using hi-resolution cuts.

As a result, HESS J1741−302 is found to be slightly extended along the galactic plane by using hi-res ζ cuts (model C) while the source is found to be point-like when using hard ζ cuts (model E). Note that the intrinsic extension value obtained from hard ζ cuts is $0.041° \pm 0.018°$. For a source to be "point-like", the intrinsic extension value should not significantly exceed the H.E.S.S. PSF extension uncertainty of 0.05°. Since the intrinsic extension of the 2D Gaussian was found to be smaller than 0.05°, HESS J1741−302 was tagged as a point-like source. It is also important to remind the reader that using hi-res ζ cuts increases the trial factors for the analysis. Since the post-trial detection significance of HESS J1741−302 by using hard ζ cuts is at the limits of conventionally accepted detection significance of 5σ, using hi-res ζ cuts reduces the post-trial detection significance slightly below 5σ. Therefore, for the rest of the analysis presented in this thesis, HESS J1741−302 will be accepted as a point-like source to be at the safe side with the best fit position of R.A.: $17^{h}41^{m}15.8^{s} \pm 3.6^{s}_{stat} \pm 1.3^{s}_{sys}$, Dec.: $-30°22'37.2" \pm 50"_{stat} \pm 20"_{sys}$.

In all cases (models B, C and E), the hotspot structure was found to be point-like

with a best fit position[16] of R.A.: $17^{h}41^{m}28.8^{s} \pm 4.5^{s}_{stat} \pm 1.3^{s}_{sys}$, Dec.: $-30°07'22.5" \pm 16"_{stat} \pm 20"_{sys}$. Running an TMVA hard ζ point-like analysis centered at the best fit position of this hotspot gave a significance of $\sim 3.7\sigma$ (reflected background), consequently, no significant emission could be detected from this hotspot structure.

5.2.3 Spectral Analysis

The circular region with a radius of 0.1° around the best fit position of HESS J1741−302 R.A.: $17^{h}41^{m}15.8^{s}$, Dec.: $-30^{d}22'37.2"$ obtained from the 2D Sherpa morphology analysis was used as an integration region for extracting the VHE γ-ray spectrum of HESS J1741−302. The TMVA hard ζ configuration was applied for reducing the contamination effects coming from the nearby source HESS J1745−303 and the background was estimated by using the reflected background method. The forward folded algorithm [Piron et al. (2001)] was applied for spectral fitting procedure that takes into account the assumed spectral shape.

The spectral analysis of an updated high-quality dataset of ∼128 hours of data taken between 2004 and 2013 has revealed that the VHE γ-ray spectrum of HESS J1741−302 can be well described by a power-law model with a spectral index of $\Gamma = 2.28 \pm 0.16_{stat} \pm 0.20_{sys}$ and a normalization at 1 TeV of $\Phi_0 = (2.12 \pm 0.42_{stat} \pm 0.42_{sys}) \times 10^{-13}$ cm^{-2}s^{-1}TeV^{-1}. The integrated flux above 1 TeV is $\Phi(>1 \text{ TeV}) = (1.65 \pm 0.28_{stat} \pm 0.33_{sys}) \times 10^{-13}$ cm^{-2}s^{-1} corresponding to ∼1% of the Crab Nebula flux at the same energies. A fit to a power-law model yields a χ^2/d.o.f = 4.6/7, with a p-value of 0.71. A power-law with an exponential cut-off model (ECPL) fit was also performed to investigate the possibility of a cut-off in the γ-ray spectrum. The fit has not been improved significantly (0.4σ from LLRT) by the addition of one more parameter with respect to a power-law model, consequently the ECPL model was rejected. The VHE γ-ray spectrum of HESS J1741−302 assuming both power-law and ECPL models can be seen in Fig. 5.15. Both spectra were re-binned in such a way that each point in the spectrum should have a significance level above 1.5σ while the significance of the last points are $\sim 2.5\sigma$. The diagnostic plots for a preferred power-law fit are shown in Fig. 5.16. As it can be seen from the 2D contour plot (Fig. 5.16 (right)), profile likelihood of both power-law parameters can be well constrained. It is also clear from the right and middle figure that the profile likelihoods for normalization and spectral index parameters have Gaussian shape.

Recall that the results of the spectral analysis ($\Gamma = 2.78 \pm 0.24_{stat} \pm 0.20_{sys}$ and $F(> 1 \text{ TeV}) = (6.3 \pm 1.5_{stat} \pm 1.1_{sys}) \times 10^{-13}$ cm^{-2} s^{-1}) presented in the proceedings paper are significantly different than the results given in this thesis. The reason for this significant difference, especially for the spectral index, is basically due to the choice of the integration region used for extracting the VHE γ-ray spectrum of HESS J1741−302. Since the exact morphology of HESS J1741−302 could not be resolved and the nearby hotspot could not be statistically separated from HESS J1741−302 in the analysis presented in the proceedings paper, the authors chose an integration region which also encloses the hotspot structure. This led to a choice of significantly larger integration region with respect to the one used in the analysis presented in this thesis, consequently leading to significantly

[16]Note that only the best fit position obtained from model E is given here. The best fit positions obtained from other models B and C are compatible within 1σ error interval.

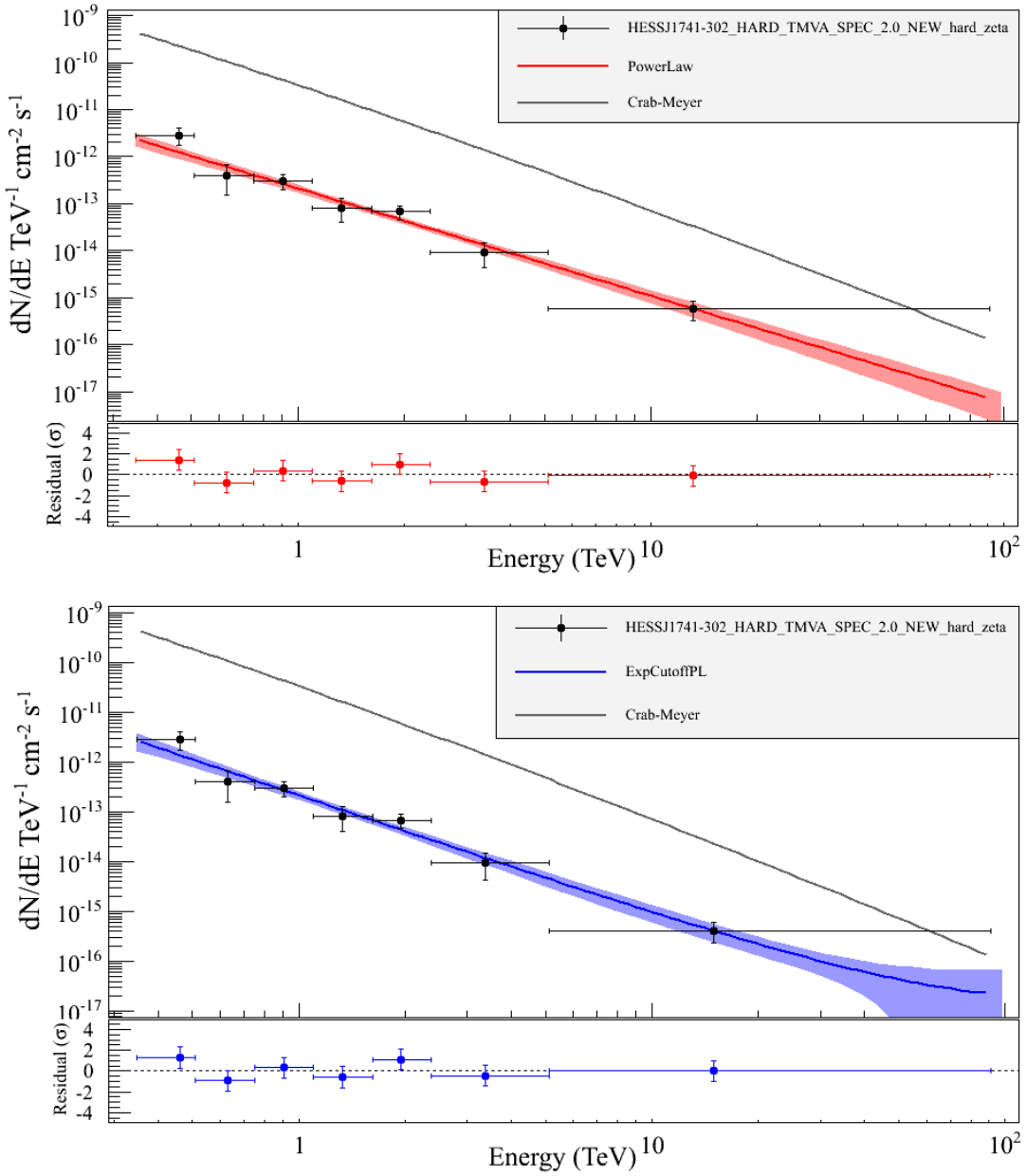

Figure 5.15: Top figure shows the spectrum of HESS J1741−302 with a power-law model assumption while the bottom figure shows the spectrum of HESS J1741−302 with an exponential cut-off power-law model assumption. In both figures, black dots show the flux points with errors while red (blue) shaded region is 1σ (68%) confidence interval for the flux with a power-law (an exponential cut-off power-law) assumption. The thin black lines represent the Crab nebula spectrum.

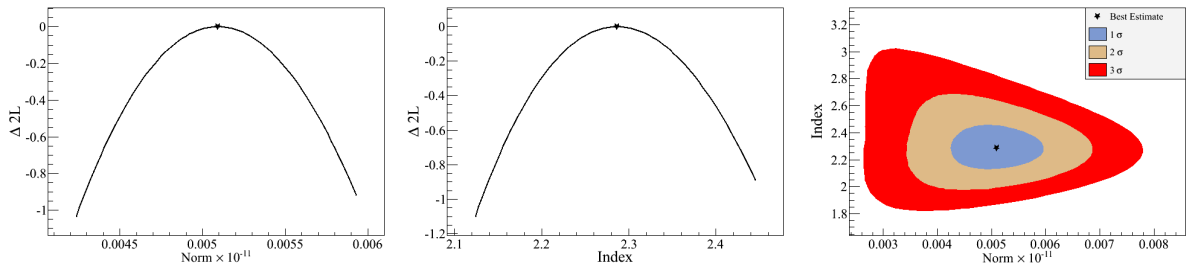

Figure 5.16: Diagnostics plots for the preferred power-law fit. The left figure shows the profile likelihood for the normalization parameter while the central figure is the profile likelihood for the index parameter. The right figure shows 2D contour plot for index and normalization parameters. 1σ, 2σ and 3σ confidence intervals are shown with blue, brown and red regions, respectively.

different derived spectral parameters. With the increased statistics, the morphology of HESS J1741−302 can be better understood in this analysis. Therefore, the VHE γ-ray spectrum of the source can be more precisely derived with respect to the one presented in Tibolla et. al (2008).

5.3 Data Analysis of Molecular Clouds

As explained in Section 3.2 and Section 3.3, observations of transitions in ^{12}CO and HI can provide useful information for determining molecular cloud properties. Therefore, ^{12}CO and HI data were investigated to determine molecular clouds and their properties along the line of sight for the HESS J1741−302 region. The results obtained in this subsection will be used later (in Section 6.2) for discussing a possible hadronic origin of VHE γ-ray emission coming from the direction of HESS J1741−302.

5.3.1 Molecular Cloud Data and Distance Calculation

For the analysis of MCs along the line of sight of HESS J1741−302, atomic hydrogen data were taken from the Galactic All Sky Survey (G.A.S.S.) [McClure-Griffiths et al. (2009)] while ^{12}CO data were taken from the Dame Galactic Plane Survey [Dame (2001)]. The data are provided as FITS data cube which is a set of FITS frames, each showing the brightness temperature distribution for a given velocity value between [−320.0 km/s, 320.0 km/s] for ^{12}CO and [−450.0 km/s, 450 km/s] for HI, respectively. Velocity distributions for both HI data and ^{12}CO data extracted along the line of sight for HESS J1741−302 are shown in Fig. 5.17.

The ON region used for extracting the velocity distribution was chosen as a circle centered at the best fit position of model E given in Table 5.13 with a radius of 0.1°. As it can be seen from the figure, there is clear evidence for the existence of molecular clouds along the line of sight. Note that the gap seen in the HI velocity distribution plot (centered at $V = 0$ km/s, between the velocity interval [−10.0 km/s, +10.0 km/s]) is actually the excluded Galactic Center region since it is extremely bright and should be excluded in

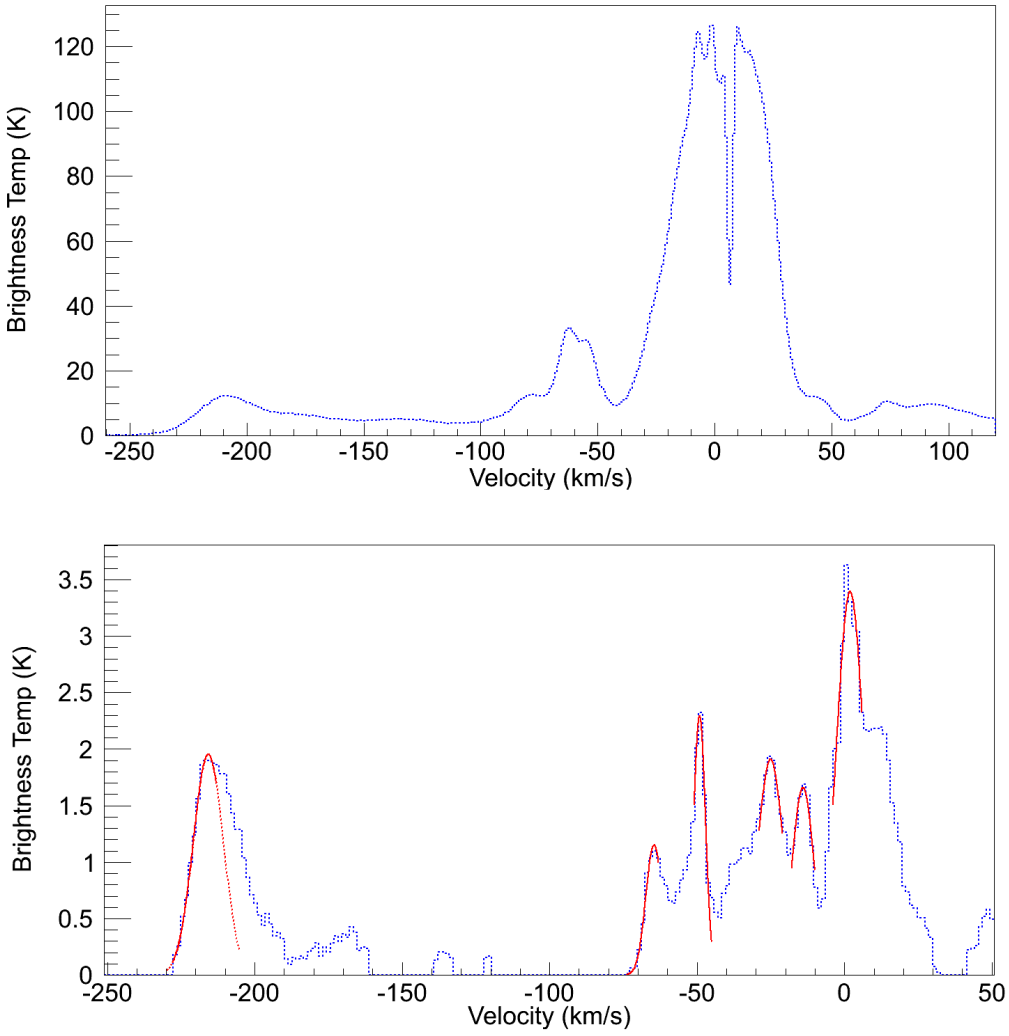

Figure 5.17: Top figure: Velocity distribution for HI data from the G.A.S.S. survey. Bottom figure: Velocity distribution for ^{12}CO data from the Dame survey. Both velocity distributions were extracted along the line of sight for HESS J1741−302 taking into account the point-like morphology (0.1° radius) centered at the best fit position. The blue lines indicate the brightness temperature as a function of observed velocities while the red lines (in the bottom figure) show the Gaussians fitted to observed peaks for the determination of molecular clouds properties along the line of sight of HESS J1741−302.

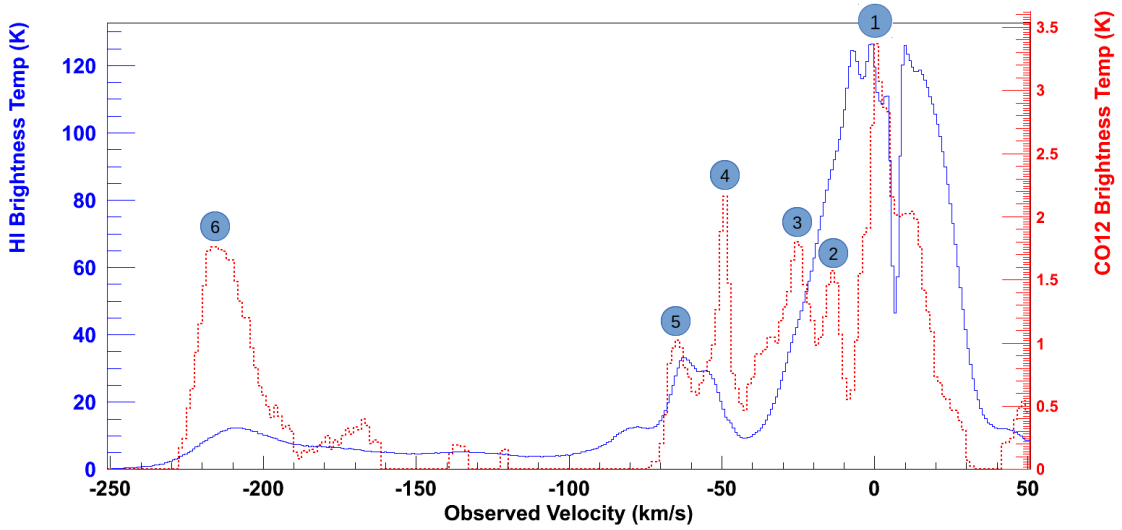

Figure 5.18: Observed velocities for molecular clouds along the line of sight for HESS J1741−302. The red dashed line indicates ^{12}CO data from the Dame survey while the blue line shows HI data from the G.A.S.S. survey. The x-axis shows the observed velocity of molecular clouds in km/s while the y-axis shows the brightness temperature (the left axis for HI and the right axis for ^{12}CO) in K. HI and ^{12}CO data are scaled for comparison and for being able to determine near and far clouds as suggested by the KDA method. Each observed peak in the velocity distribution was tagged with a number which points out the corresponding MC.

standard HI data processing.

MC Number	Velocity Interval km/s	Peak Velocity km/s	D_{GC} kpc	D_{Sun} kpc
1 (N)	[−8, +8]	+2.0 ± 5.2	–	–
2 (F)	[−18, −10]	−14.0 ± 3.7	2.73 ± 0.55	11.21 ± 1.05
3 (N)	[−29, −21]	−25.0 ± 4.3	1.78 ± 0.29	6.73 ± 0.79
4 (N)	[−51, −45]	−49.1 ± 2.0	1.01 ± 0.10	7.52 ± 0.60
5 (N)	[−74, −63]	−64.6 ± 2.8	0.79 ± 0.08	7.74 ± 0.58
6 (N)	[−228, −213]	−215.8 ± 5.1	0.26 ± 0.04	8.39 ± 0.50

Table 5.3: Distance information of the molecular clouds located along the line of sight for HESS J1741−302. MC number column shows the corresponding clouds from Fig. 5.18, it also indicates if the cloud is located at a near distance (N) or at a far distance (F). Velocity interval column shows the velocity intervals used for Gaussian fitting of the observed peaks in Fig. 5.18. Peak velocity column is the peak velocity obtained from Gaussian fitting for each cloud within the given velocity interval. D_{GC} column shows the corresponding distance of the cloud from the Galactic Center while D_{Sun} is the distance of the cloud from the Sun.

Figure 5.18 shows the comparison of HI and ^{12}CO data used for determining distances to molecular clouds. HI and ^{12}CO data were normalized to each other by using the brightness temperature to be able to discriminate between near and far clouds. Near and far clouds were determined by following the KDA method as explained in Section 3.5. Distances to these clouds were calculated from Eq. 3.29 with the use of Clemens Rotation Curve shown in Fig. 3.8. In this calculation, assumptions of $V_0 = 220.0 \pm 7.0$ km/s, $R_0 = 8.5 \pm 0.5$ kpc and $V_R = 220.0 \pm 7.0$ km/s were made as suggested by the KDA method [Roman-Duval (2009)]. In addition to the errors of the parameters mentioned in V_0, R_0 and V_R, errors coming from the Gaussian fitting of ^{12}CO data (the red lines in Fig. 5.17 (lower)) were also taken into account for distance calculation. Table 5.3 gives the calculated distances by using the KDA method. Note that the distance to the GC for MC 1 can not be determined by using the KDA method because of huge errors in the determination of the peak velocity from the ^{12}CO data. Therefore, this molecular cloud was excluded for the rest of this analysis.

5.3.2 Column Densities and Mass Determination

For being able to determine the masses of the observed molecular clouds, column density maps of the HESS J1741−302 region are required. Total column densities corresponding to each cloud can be calculated by integrating the brightness temperature over the velocity intervals as explained in Section 3.4. The velocity intervals used for integrating the brightness temperature for each molecular cloud along the line of sight can be found in Table 5.3. Since the velocity information is provided as a data cube, one needs to integrate the data cube between the velocities that cover each of the observed peaks. Afterwards, the mass of each cloud can be calculated by taking into account the assumed projected area of the molecular cloud[17]. The CIAO-v4.5 "dmcopy" tool[18] was used for integrating the data cube within the desired velocity intervals.

The total column density calculation can be summarized in the following order:

- HI Column Density $N(\mathrm{HI}) = I(\mathrm{HI})_{\mathrm{Integrated}} \times V_{Delta}(\mathrm{HI}) \times X_{\mathrm{HI}}$

- $\mathrm{H_2}$ Column Density $N(\mathrm{H_2}) = I(^{12}\mathrm{CO})_{\mathrm{Integrated}} \times V_{Delta}(^{12}\mathrm{CO}) \times X_{^{12}\mathrm{CO}}$

- Total Column Density $N_{\mathrm{H}} = N(\mathrm{HI}) + 2.N(\mathrm{H_2})$

Note that in the above expressions, $I(\mathrm{HI})_{\mathrm{Integrated}}$ and $I(^{12}\mathrm{CO})_{\mathrm{Integrated}}$ are the integrated brightness temperatures, or in other words, they are the integrated data cubes between the velocity intervals of interest for both HI and ^{12}CO data, respectively. Consequently, they provide the integrated brightness temperature maps for each molecular cloud. The velocity resolutions for the corresponding surveys, namely $V_{Delta}(\mathrm{HI})$ and $V_{Delta}(^{12}\mathrm{CO})$, are

[17]For this analysis, the circular ON region used for extracting the velocity profiles was used for the assumed projected MC area.

[18]See http://cxc.harvard.edu/ciao/ahelp/dmcopy.html for detailed information about the dmcopy tool.

provided in the data cube headers and are given as V_{Delta}(HI) = 0.82 km/s and V_{Delta}(^{12}CO) = 1.30 km/s. Note that the G.A.S.S. survey has an angular resolution of 0.08° while the Dame survey's angular resolution is 0.125° in both galactic latitudes and longitudes. The other terms, $X_{\rm HI}$ and $X_{^{12}{\rm CO}}$, are the X-factors for the corresponding surveys. The X-factor can be described as the ratio of H_2 column density to CO^{12} (or HI) intensity and is found to be more or less constant in Galactic molecular clouds [Shettys et al. (2011)]. The X-factor (HI) = 1.823×10^{18} cm^{-2} (K km s^{-1})$^{-1}$ and the X-factor (^{12}CO) = 1.8×10^{20} cm^{-2} (K km s^{-1})$^{-1}$ for HI and CO^{12} were taken from the Dame and the G.A.S.S. surveys, respectively. The total column density map for the HESS J1741−302 region, obtained by integrating the data cube over all provided survey velocities can be seen from Fig. 5.19 (top) while the total column density map for the MC 6 is shown in the bottom panel of Fig. 5.19.

The obtained solid angle averaged H_2 column densities for each molecular cloud found along the line of sight for the HESS J1741−302 region are given in Table 5.4. Note that one can underestimate the solid angle averaged column density if the integrations along line of sight are performed by taking into account only the velocity integrals given in Table 5.3 since they do not always cover entire peaks. For this reason, velocity integrations were also performed taking into account the fitted Gaussians within 3σ velocity intervals around the best fit peak velocity $V_{\rm peak}$ which then would cover 99.5% of the observed peak[19]. The results are given in H_2 Col. Dens. (Theo) column of Table 5.4. Moreover, it can also be seen from Fig. 5.18 that not all ^{12}CO peaks are clearly correlated with HI peaks. Actually, one can see that the MC 6 HI peak is correlated with the MC 6 ^{12}CO peak. Note that HI is mostly found in the diffuse clouds which are found throughout the Galaxy with a peak at about 10 kpc (see Fig. 10 of Nakanishi et. al (2003).). Molecular clouds include different type of molecules which can be detected through the emission lines. Basically the thermal and turbulent broadening determine the width of a line. If there are a lot of HI associated with a MC, then corresponding HI spectrum will have the same structure as ^{12}CO spectrum. Consequently, the lack of correlation indicates that the mass of the MC is dominated by molecules (H_2) instead of HI atoms. For this reason, the second and the third columns in Table 5.4 give the solid angle averaged column density by taking into account only the ^{12}CO data while the fourth column gives the solid angle averaged column density by taking into account the ^{12}CO + HI data. Note that the relative increase values given in the last column of the Table 5.4 are directly reflected in the calculated masses of clouds since these cloud masses are proportional to column densities. This increase in the calculated mass is strongly dependent on the cloud of interest as it can be seen from Table 5.5.

Note that the total ^{12}CO column density for the source region is $\sim 1.3 \times 10^{23}$ cm^{-2} while this value increases to $\sim 2.0 \times 10^{23}$ cm^{-2} if one takes into account the total HI column density. Dividing this value by the total number of pixels located within the source area, one can obtain the solid angle averaged ^{12}CO average column density for the HESS J1741−302 region, which is $\sim 6.5 \times 10^{22}$ cm^{-2} ($\sim 8.0 \times 10^{22}$ cm^{-2} if HI column density is taken into account). In this study, the total column density maps for each clouds were produced. By assuming the same source area shown in Fig. 5.19 (the white circle), one

[19]This approach may overestimate the calculated column densities since there exist background below the Gaussians.

MC Number	H_2 Col. Dens. (Exp) 10^{21} cm^{-2}	H_2 Col. Dens. (Theo) 10^{21} cm^{-2}	H_2 Col. Dens. (+HI) 10^{21} cm^{-2}	Increase % w.r.t. H_2
1 (N)	–	–	–	–
2 (F)	5.14 ± 0.78	7.23	7.06 ± 0.83	37.3
3 (N)	6.34 ± 2.28	9.72	7.32 ± 2.31	15.4
4 (N)	4.34 ± 0.64	5.41	4.55 ± 0.65	4.8
5 (N)	3.08 ± 0.28	3.77	3.70 ± 0.30	20.1
6 (N)	11.20 ± 2.80	11.60	11.60 ± 3.00	3.6

Table 5.4: H_2 column density table for the molecular clouds located along the line of sight for HESS J1741−302. MC Number column shows the corresponding clouds from Fig. 5.18. H_2 Col. Dens. (Exp) column gives the solid angle averaged column densities obtained experimentally from ^{12}CO data by integrating the velocities between the given values in Table 5.3. H_2 Col. Dens. (Theo) column gives the solid averaged column densities obtained theoretically by integrating velocities between the interval [$V_{\rm peak} - 3\sigma_{\rm peak}$, $V_{\rm peak} + 3\sigma_{\rm peak}$]. H_2 Col. Dens. (+HI) column gives the the solid averaged column densities obtained by taking into account the HI column density from the G.A.S.S. survey data. Increase column gives the relative increase of the average column density (H_2+HI) in % with respect to the column densities obtained by using only ^{12}CO data (H_2).

can calculate the masses for each molecular cloud by using the formula

$$\mathrm{M_{Cloud}(M_\odot) = \ Area\ (cm^2) \times Solid\ Angle\ Averaged\ Column\ Density\ (cm^{-2}) \times M_H/M_\odot} \quad (5.1)$$

where M_H and $M_\odot$ are the masses of the Hydrogen atom[20] and the Sun in grams, respectively. Additionally, one can calculate the gas number density (n_{Gas} in cm^{-3}) for each molecular cloud. Note that in general, molecular clouds do not have exactly defined shapes like sphere or ellipsoid but have irregular shapes. Therefore, one needs to assume a shape of a molecular cloud for determining the gas number density. Conventionally, the shape of molecular clouds is assumed to be a perfect sphere, an ellipsoid or a suitable shape that is matching to the observed morphology of a MC. For this analysis, a perfect spherical shape is assumed for each molecular clouds along the line of sight. Consequently, n_{Gas} can be calculated for each molecular cloud by using the formula

$$n_{Gas} = \text{Solid Angle Averaged Column Density} \times \text{Source Area / Volume} \quad (\mathrm{cm^{-3}}) \quad (5.2)$$

where the assumed volume of a MC is basically the volume of a sphere in this case. Obtained gas number density vales for each molecular cloud along the line of sight are given in the n_{Gas} column of Table 5.5.

By assuming that all the observed VHE γ-ray emission comes from a particular

[20]In this calculation, the mass of the Hydrogen atom was assumed equal to the mass of proton, which is $\sim 1.67 \times 10^{-30}$ g.

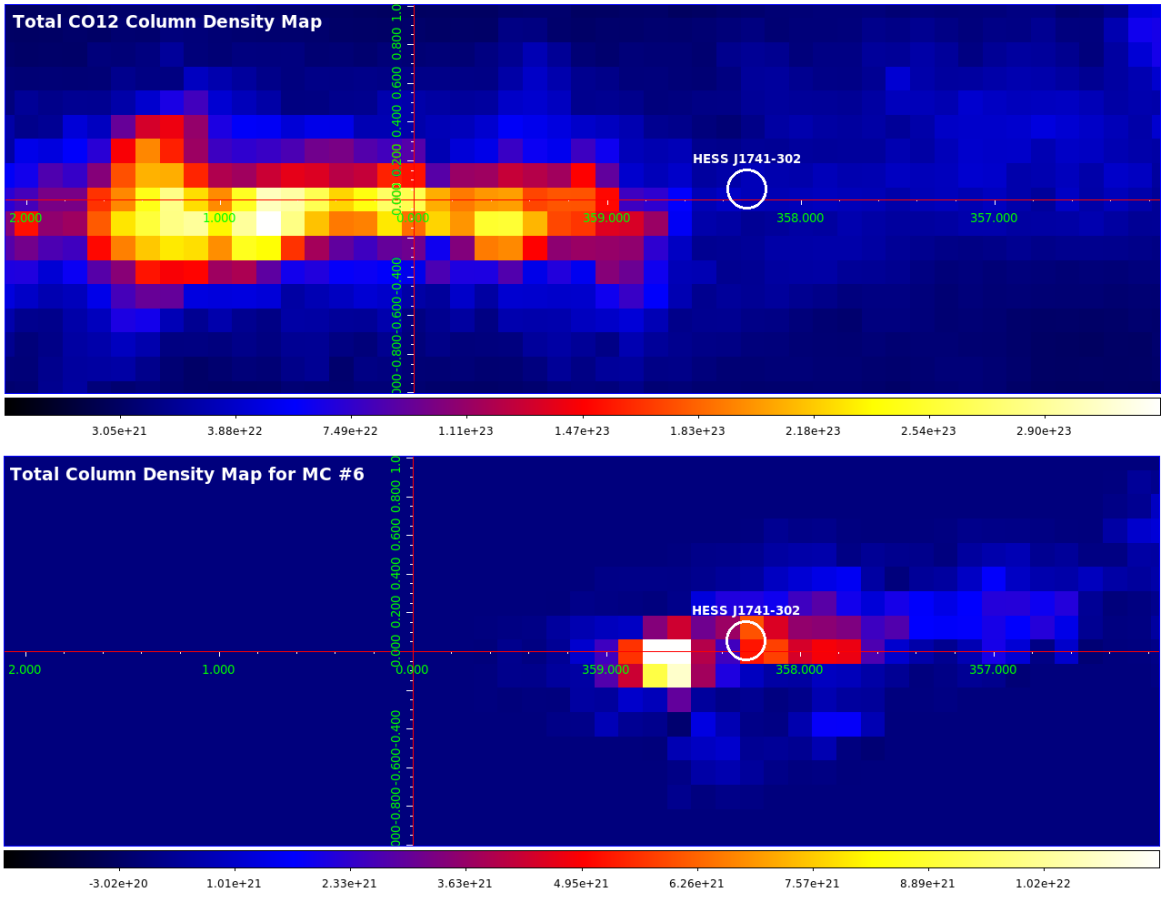

Figure 5.19: Top figure: Integrated total ^{12}CO column density map for the HESS J1741−302 region for the velocity interval between [−320.0 km/s, 320.0 km/s]. Bottom figure: Integrated total ^{12}CO column density map for the MC 6 for the velocity interval between [−230 km/s, −205 km/s]. The white circle in both figures shows the location of HESS J1741−302.

molecular cloud of interest, one can obtain a ratio, K_{cr}, named as "cosmic-ray enhancement factor". This ratio is defined as the ratio of required cosmic-ray density in a particular cloud for being able to produce the observed VHE γ-ray flux to the density of background Galactic CRs observed in the vicinity of the Earth. Recall that the gamma-ray emissivity in the vicinity of the Earth is given by the formula

$$q(> E_\gamma) = 1.0 \times 10^{-31} (E_\gamma / 1 \text{ TeV})^{-1.75} \quad \text{s}^{-1}(\text{H-Atom})^{-1} \tag{5.3}$$

for the background cosmic-ray spectrum assumption of

$$J_\odot^{(p)} = 1.8 \times E_{\text{GeV}}^{-2.7} \quad \text{GeV}^{-1}\text{s}^{-1}\text{sr}^{-1}\text{cm}^{-2}. \tag{5.4}$$

Finally, the masses, n_{Gas} and K_{cr} values were calculated for each molecular cloud along the line of sight that can be seen in the ^{12}CO velocity distribution. Table 5.5 shows the obtained results from the MC data analysis. Note that the results shown in the Table 5.5 will be used when discussing possible hadronic scenarios later in Chapter 6.

MC Number	Mass $M_\odot$	K_{cr} (E > 0.35 TeV)	n_{Gas} (cm^{-3})	Mass (Theo) $M_\odot$	Mass (HI+^{12}CO) $M_\odot$
1 (N)	–	–	–	–	–
2 (F)	49400 ± 11900	172 ± 50	85 ± 22	69500 ± 16700	67800 ± 16300
3 (N)	22000 ± 9400	140 ± 45	175 ± 79	33700 ± 14400	25400 ± 10800
4 (N)	18800 ± 4100	204 ± 56	107 ± 25	23400 ± 5100	19700 ± 4300
5 (N)	14100 ± 2500	288 ± 77	74 ± 14	17200 ± 3100	17000 ± 3000
6 (N)	60700 ± 7400	79 ± 20	249 ± 35	62900 ± 7700	62900 ± 7700

Table 5.5: Mass information of the molecular clouds located along the line of sight for HESS J1741−302. MC Number column shows the corresponding clouds from Fig. 5.18, it also indicates if the cloud is located at a near distance (N) or at a far distance (F). Mass column gives the mass of the molecular cloud in terms of $M_\odot$ calculated by taking into account only H_2 column densities while K_{cr} column shows the corresponding cosmic-ray enhancement factor. n_{Gas} column gives the calculated gas number density of each molecular clouds. Mass (Theo) column gives the masses of the molecular clouds by taking into account the theoretical H_2 column density given in the third column of Table 5.4 while Mass (HI + ^{12}CO) column gives the masses of the molecular clouds calculated by taking into account the HI column density.

5.4 X-Ray Data Analysis

The HESS J1741−302 region has been observed by the Suzaku [Mitsuda et al. (2007)], Chandra [Daniel et al. (2004)] and Swift [Burrows et al. (2005)] X-ray Telescopes (XRT). The Suzaku X-ray Imaging Spectrometer (XIS) observed the regions around the pulsar PSR B1737−30 and the VHE γ-ray source HESS J1741−302 twice. The first observation was part of Suzaku deep survey project of the Galactic Center region and the second one was a pointing observation of the unidentified TeV γ-ray source HESS J1741−302.

The Suzaku XIS consists of four sets of X-ray CCD camera systems (XIS 0, 1, 2, and 3) placed on the focal planes of four X-ray telescopes aboard the Suzaku satellite. XIS 0, 2, and 3 have front-illuminated (FI) CCDs, while XIS 1 has a back-illuminated (BI) CCD. One of the FI CCD cameras (XIS 2) has been out of function since November 2006. Detailed descriptions of the Suzaku satellite, the XRT and the XIS can be found in Mitsuda et al. (2007), Serlemitsos et al. (2007) and Koyama et al. (2007), respectively. The Suzaku observations showed neither significant X-ray emission from the HESS J1741−302 region nor from the position of the pulsar PSR B1737−30 after the analysis of ∼96 ks observation data [Uchiyama et al. (2011)]. Instead, a new intermediate polar candidate[21], Suzaku J174035.6−301416, in the vicinity of PSR B1737−30 was discovered. Note that the fine-tuned position of Suzaku J174035.6−301416 (R.A.: $17^h40^m35.6^s$, Dec: −30°14'16.0") is significantly different from the position of PSR B1737−30 (R.A.: $17^h40^m33.84^s$, Dec.:

[21]Intermediate polar object is a sub-class of a magnetized white dwarf binary. These objects are also called cataclysmic variables (mCV).

$-30°15'43.2"$). The angular distance between these two objects is $\sim$90" while 1σ overall uncertainty of the X-ray emission best fit position is $\sim$14". The X-ray flux upper limits for the HESS J1741$-$302 region and for the pulsar PSR B1737$-$30 were given as $F_{X,\,HESSJ1741-302}$ (1$-$9 keV) $< 1.6 \times 10^{-13}$ erg cm^{-2} s^{-1} and $F_{X,\,PSRB1737-30}$ (1$-$9 keV) $< 3.5 \times 10^{-13}$ erg cm^{-2} s^{-1} at 90% confidence level, respectively. Note that the Suzaku X-ray upper limits are the only limits available and therefore the most constraining ones. On the other hand, because of the low photon statistics and the contamination coming from Suzaku J174035.6$-$301416, the limits are not very constraining.

Swift is a multi-wavelength space-based observatory dedicated to the study of γ-ray burst science. It has three instruments working together to observe GRBs and afterglows in the γ-ray, X-ray, ultraviolet and optical wavebands. The XRT is a focusing X-ray telescope with 110 cm^2 effective area, 23.6 $\times$ 23.6 (arc min)^2 FoV, 18 arc sec resolution and operates in the 0.2$-$10 keV energy band. Swift XRT has approximately $\sim$8 ks observational data for the HESS J1741$-$302 region (Obs. ID : 00035330001). These data have not been investigated in detail before. The total observation time of $\sim$8 ks is significantly less than the data used for the Suzaku X-ray analysis ($\sim$96 ks). The skymap of the HESS J1741$-$302 region obtained from standard reprocessed clean events is shown in Fig. 5.20. The advantage of the Swift X-ray observations with respect to the Suzaku observations is that the FoV of Swift observations cover a larger fraction of the HESS J1741$-$302 region. At this points, recall that the Suzaku observations were not pointed exactly at the updated best fit position of the source HESS J1741$-$302. The result of the morphology analysis presented in this thesis showed that only a small fraction of HESS J1741$-$302 was in the FoV of the Suzaku observations as can be seen in Fig. 5.20.

Note that slightly extended X-ray emission can be clearly seen in the vicinity of PSR B1737$-$30 in Fig. 5.20. But as mentioned by Uchiyama et al. (2011), this X-ray emission is not related to PSR B1737$-$30. A soft X-ray point like source spatially coincident with the HESS J1741$-$302 position can be seen in Fig. 5.20 (marked as the green circle). Note that this point-like source was not within the FoV of the Suzaku observations, therefore no X-ray data analysis could be performed on this source. Since this point-like source can be clearly seen in Swift XRT data, a spectral analysis of this source was performed by using the available $\sim$8 ks of Swift XRT data. The Swift analysis framework XSpec[22] was used. Standard data analysis cuts were applied as recommended by the data analysis documentation and also the latest Swift CALDB[23] was used. The resulting spectrum was fitted to two different models, namely a blackbody spectrum and an absorbed power-law, to see if the observed X-ray emission is thermal or non-thermal in nature. Due to the lack of statistics, these two models can not be significantly discriminated from each other. Note that the given information and the obtained results in this sub-section will be used when discussing the leptonic scenario later in Section 6.1.

[22]See `http://swift.gsfc.nasa.gov/proposals/swift_xspec_sim.html` for details.

[23]CALDB is the calibration database providing RMFs (Redistribution Matrix File) and ARFs (Auxiliary Response File) that are necessary for the calibration of Swift observations data.

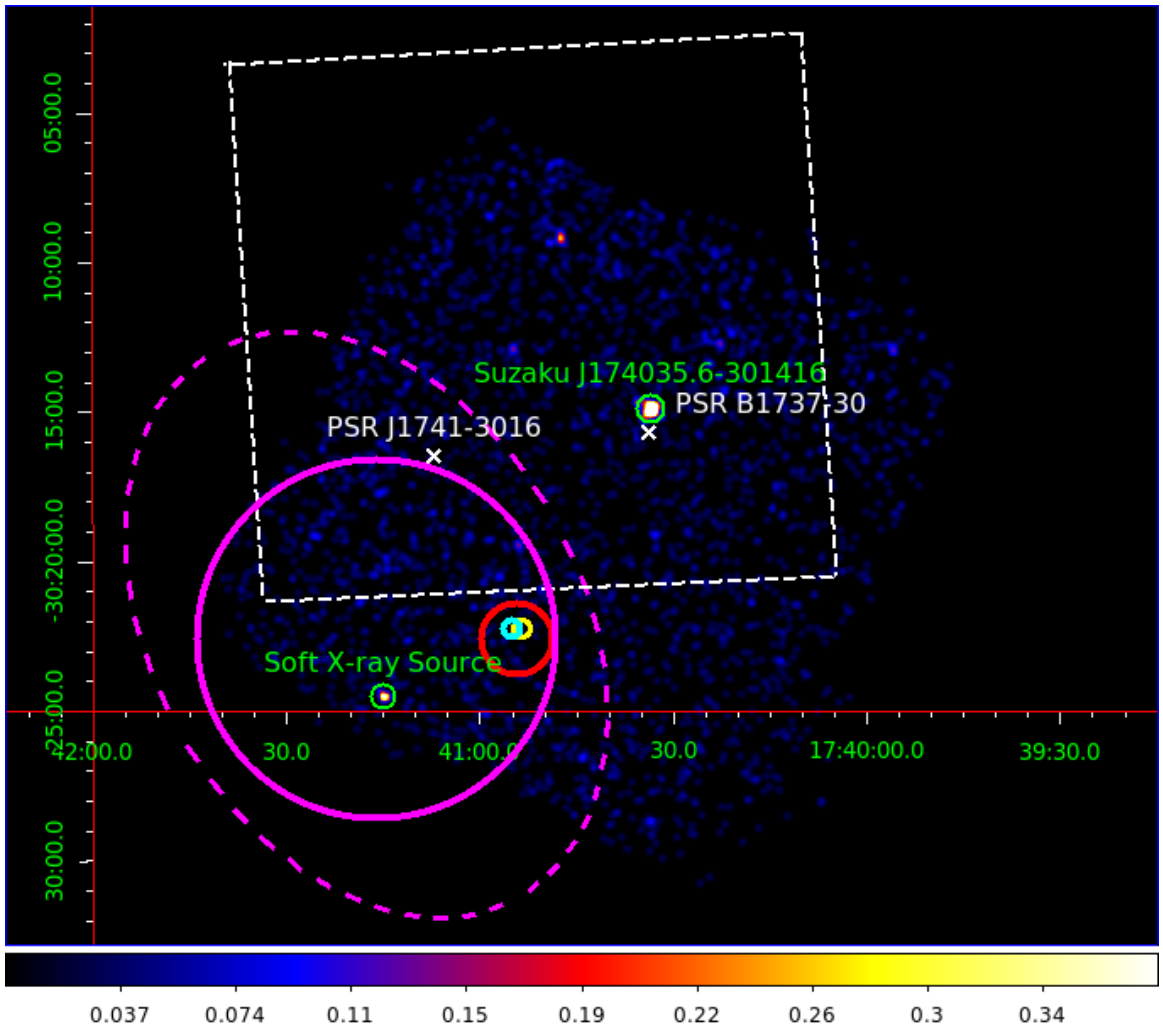

Figure 5.20: Swift X-ray map of clean events in RA-Dec (J2000) coordinate system. The map is smoothed with a Gaussian kernel of radius 0.05° for better visualization. The magenta circle, which is centered at the best fit position, shows the extension (0.1°) of the point-like morphology of HESS J1741−302 (obtained from hard ζ cuts). The dashed magenta ellipse shows the elongated morphology of HESS J1741−302 obtained from hi-res ζ cuts. The white crosses show the 2 nearby pulsars whose properties are given in Table 5.1. The cyan and yellow circles show the position of water and OH masers found close to HESS J1741−302, respectively. The red circle shows the position of the very powerful OH/IR star (2MASS OH/IR K-band (2.2 micron) source 2MASS J23525579+0006091 [Caswell (1998)]). The green circles point out the X-ray emission regions which can be seen in the clean events map. The white dashed box shows the FoV of the Suzaku observations.

Chapter 6

Discussion

HESS J1741−302 is an unidentified VHE γ-ray source with a power-law index of 2.28 $\pm$ $0.16_{\rm stat}$ $\pm$ $0.20_{\rm sys}$. One can discuss several possible leptonic and hadronic scenarios to explain the observed VHE γ-ray emission coming from the direction of HESS J1741−302. Hereafter, various scenarios including the emission from a pulsar with an offset pulsar wind nebula (PWN), IC scattering of CMB photons and also IR photons emitted by an OH/IR star, molecular clouds illuminated by the galactic background cosmic-rays and interaction between molecular clouds and accelerated protons will be discussed.

6.1 Leptonic Scenarios

Recall that there are 3 detected pulsars in the vicinity of HESS J1741−302 with their properties given in Table 5.1. Therefore, one can discuss various leptonic scenarios to explain the observed VHE γ-ray signal from the direction of HESS J1741−302. Note that PSR 1741−3016 can be directly excluded from leptonic scenarios since it has a relatively low $\dot{E}$ value (5.2×10^{31} erg/s) and is an extremely old pulsar with a characteristic age of $\sim$3.3 Myr. Recall that pulsars with $\tau_c < 150$ kyr and with $\dot{E}/d^2 \approx 10^{34}$ erg s^{-1} kpc^{-2} are known to power PWNe that are detectable at very high energies [Carrigan et al. (2007)]. Although the other pulsar PSR J1739−3023 has a relatively high $\dot{E}$ value (3.0×10^{35} erg/s), the offset between the pulsar and the center-of-gravity of the VHE γ-ray emission from the direction of HESS J1741−302 is quite large. This offset is 0.35° corresponding to a projected distance of $\sim$21 pc for the given pulsar distance of 3.41 kpc. The corresponding $\dot{E}/d^2$ value for PSR J1739−3023 is 2.6×10^{34} erg s^{-1} kpc^{-2}. On the other hand, PSR B1737−30 has a reasonable $\dot{E}$ value (8.2×10^{34} erg/s) with two different distance approximations of 0.4 kpc and 3.28 kpc. These correspond to $\dot{E}/d^2$ values of 5.1×10^{35} erg s^{-1} kpc^{-2} and 7.6×10^{33} erg s^{-1} kpc^{-2} for 0.4 kpc and 3.28 kpc pulsar distances, respectively. In this subsection, two different leptonic scenarios including the pulsar PSR B1737−30 will be discussed.

6.1.1 Pulsar with an Offset PWN Scenario

As mentioned before (see Table 5.1), there is an offset of $\sim$0.19° between the pulsar PSR B1737−30 and the center-of-gravity of the VHE γ-ray excess from the direction of HESS J1741−302. Consequently, it is reasonable to discuss a leptonic scenario by taking into account a pulsar with an offset PWN. For this purpose, one can start with calculating the energy flux from HESS J1741−302 which is $F_{\gamma}(1{-}30 \text{ TeV}) \approx 7.45 \times 10^{-13}$ erg s^{-1} cm^{-2}. By using this energy flux value, γ-ray efficiencies between 1 TeV and 30 TeV for different pulsar distance approximations can be calculated by using the formula

$$\eta_{\gamma}(1{-}30 \text{ TeV}) = \frac{L_{\gamma}}{\dot{E}_{\text{PSR B1737}-30}} = \frac{4\pi F_{\gamma}(1{-}30 \text{ TeV}) d^{2}_{\text{PSR B1737}-30}}{\dot{E}_{\text{PSR B1737}-30}} \tag{6.1}$$

which leads to 0.017% and 1.17% for pulsar distances of 0.4 kpc and 3.28 kpc, respectively. The calculated efficiency value for the distance of 0.4 kpc (0.017%) would place PSR B1737−30 in the same realm as objects like Vela [H.E.S.S. Collaboration (2005)], Crab Nebula [Aharonian (2006b)] and G21.5−0.9 [Djannati-Atai et al. (2007)]. Recall that all of these objects have $\tau_c < 11$ kyr and are more energetic than PSR B1737−30. Therefore, a distance of few kpc appears more plausible if one takes into account the obtained γ-ray efficiency values of the PWN scenario.

The angular offset of 0.19° between PSR B1737−30 and HESS J1741−302 should be explained when taking into account the PWN scenario. This angular offset corresponds to 1.3 pc and 10.9 pc for 0.4 kpc and 3.28 kpc pulsar distances, respectively. Assuming that the pulsar PSR B1737−30 was born exactly at the position of the observed VHE excess from the direction of HESS J1741−302 with an initial kick velocity, one can make a simple test for deriving the required initial pulsar kick velocities for both pulsar distances taking into account the characteristic age of PSR B1737−30 ($\tau_c = 20.6$ kyr) to explain the observed offset.

One can see from Fig. 6.1 (upper panel) that the pulsar PSR B1737−30 is at 0.19° offset from HESS J1741−302 in the direction perpendicular to the galactic plane while Fig. 6.1 (lower panel) shows the schematic illustration of the simple test for deriving the required initial pulsar kick velocities for explaining the observed offset. Note that the lower panel shows the orientation of the objects that can be seen in Fig. 6.1 (upper panel) in the direction perpendicular to the paper plane. In this simple test, the initial pulsar kick angle β was changed between 5° and 175° for both pulsar distances (marked as D_{PUL}). Note that the VHE γ-ray excess position (marked as the blue cloud) can be anywhere on the line (marked as R_{EXCESS}) connecting it to the Sun. It is clear that the minimum pulsar kick velocity value would be obtained for $\beta = 90°$ while it takes its maximum values for the boundary angles ($\beta = 5°$ and $\beta = 175°$).

The outcome of the test can be seen in Fig. 6.2 for the pulsar distances of 0.4 kpc (blue line) and 3.28 kpc (red line). Consequently the angular offset of 0.19° between the pulsar and the center-of-gravity of the observed VHE γ-ray excess can be explained with the minimum initial pulsar kick velocities of 65 km/s and 540 km/s for the pulsar distances of 0.4 kpc and 3.28 kpc, respectively. It can also be seen from Fig. 6.2 that the pulsar kick-off velocities do not change significantly for a wide range of β values. Note that these

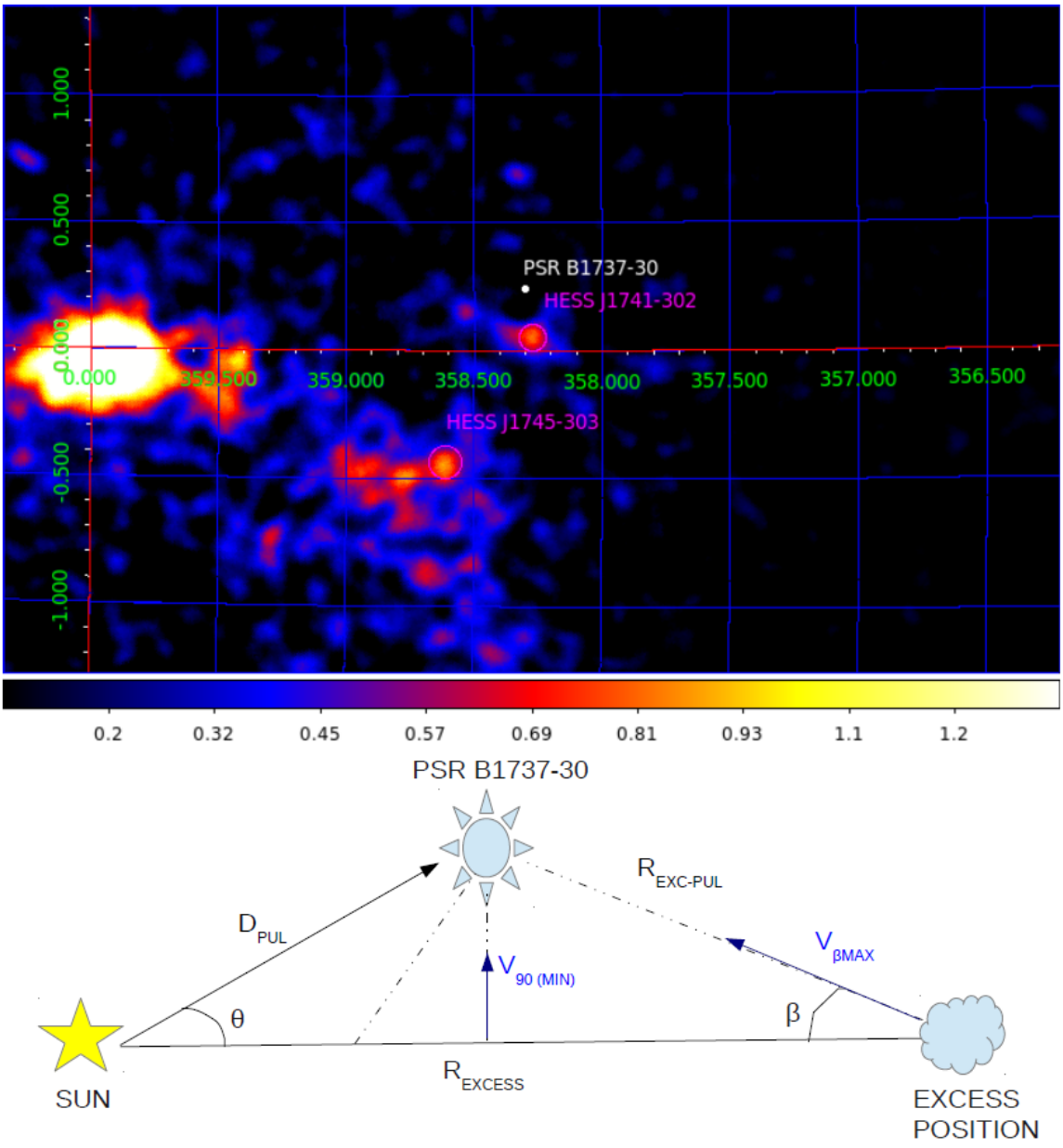

Figure 6.1: The upper panel shows the positions of HESS J1741−302, HESS J1745−303 (magenta circles) and the pulsar PSR B1737−30 (white dot) in the Galactic coordinate system. The bright GC ridge can also be seen around $l = 0°$, $b = 0°$. The lower panel is a schematic illustration of the simple test for deriving the required initial pulsar kick velocities. The yellow star indicates the Sun's position while the blue cloud indicates the observed VHE γ-ray excess position. The pulsar position is marked with the blue star. D_{PUL} is the distance to the pulsar PSR B1737−30, R_{EXCESS} is the distance to the observed VHE γ-ray excess position and $R_{EXC\text{-}PUL}$ is the distance between the pulsar and the excess position. The angle θ is the measured angular offset between the pulsar and the VHE γ-ray excess position while the angle β is the assumed initial pulsar kick angle.

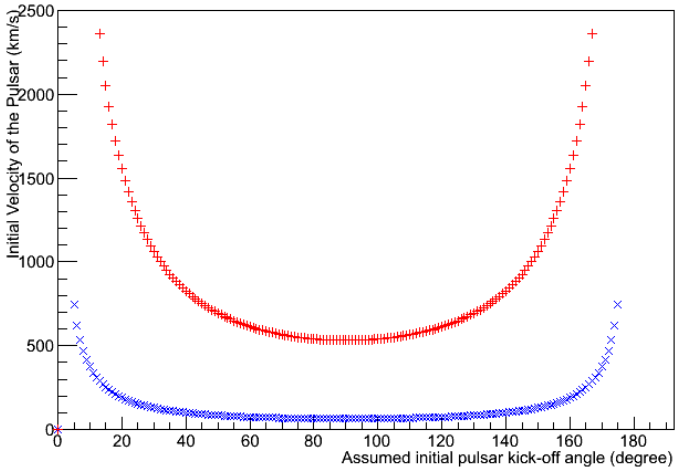

Figure 6.2: Plot showing initial pulsar kick velocities as a function of initial kick angle β. The blue line shows the initial pulsar kick velocities for the pulsar distance of 0.4 kpc while the red line shows the initial pulsar kick velocity for the pulsar distance of 3.28 kpc.

kick-off velocity values are quite reasonable [Hansen et al. (1997)], therefore a pulsar with an offset PWN scenario can not be excluded. However, no proper motion in right ascension (PM RA) or in declination (PM Dec) could be observed for the pulsar PSR B1737−30 [ATNF Pulsar Database].

Recall that in the case of a leptonic pulsar with an offset PWN scenario, there is a (still) bright VHE offset PWN while the X-ray PWN close to the pulsar is already dim. Consequently, one may expect to see a faint PWN in X-ray energies close to the pulsar PSR B1737−30. As discussed in the Section 5.4, the Suzaku observations showed neither significant X-ray emission around HESS J1741−302 nor from the position of the pulsar PSR B1737−30 [Uchiyama et al. (2011)] which is cross-checked with an independent X-ray data analysis performed by using the Swift XRT data in this thesis. For calculating the expected X-ray flux from the direction of the pulsar PSR B1737−30, one can use the phenomenological approach given by Mattana et al. (2009). Recall that the outcome of the study presented in Mattana et al. (2009) was that γ-ray luminosities (L_{γ}) do not show any correlation with pulsar spin-down luminosities nor they do with characteristic ages of pulsars while X-ray luminosities ($L_{X\text{-}ray}$) show correlation both with spin-down luminosities and characteristics ages of pulsars [Mattana et al. (2009)]. These correlations are given by

$$\log_{10}(L_{X\text{-}ray}) = (33.8 \pm 0.04) + (1.87 \pm 0.04)\log_{10}(\dot{E}_{37}) \quad \text{and} \tag{6.2}$$

$$\log_{10}(L_{X\text{-}ray}) = (33.7 \pm 0.04) - (2.49 \pm 0.06)\log_{10}(\tau_4) \tag{6.3}$$

where $\dot{E}_{37} = (\dot{E}_{Pulsar})/(10^{37}$ erg s$^{-1})$ is the scaled spin-down luminosity and τ_4 is the scaled characteristic age of the pulsar of interest given by $(\tau_c)/(10^4$ yr). Consequently, one can calculate the expected X-ray flux from the direction of PSR B1737−30 by using the known $\dot{E}$ and τ_c values taking into account both distance approximations. The expected fluxes in the 2−10 keV energy band for a PSR B1737−30 distance of 0.4 kpc were evaluated

as $F_{X\text{-}ray}(2-10\ \mathrm{keV}) = 1.4 \times 10^{-13}$ erg s^{-1}cm^{-2} and $F_{X\text{-}ray}(2-10\ \mathrm{keV}) = 5.1 \times 10^{-14}$ erg s^{-1}cm^{-2} by using τ_c and $\dot{E}$, respectively. On the other hand, for the PSR B1737−30 distance of 3.28 kpc, the expected fluxes are $F_{X\text{-}ray}(2-10\ \mathrm{keV}) = 2.1 \times 10^{-15}$ erg s^{-1}cm^{-2} (by using τ_c) and $F_{X\text{-}ray}(2-10\ \mathrm{keV}) = 7.6 \times 10^{-16}$ erg s^{-1}cm^{-2} (by using $\dot{E}$). Consequently, Mattana et al. (2009) predicts a faint X-ray PWN around the pulsar PSR B1737−30 which has not been detected at X-ray energies yet. This actually can explain the missing X-ray counter part. Recall that the flux upper limits evaluated for the pulsar PSR B1737−30 in Uchiyama et al. (2011) was given as $F_{X\text{-}ray}(1-9\ \mathrm{keV}) < 3.5 \times 10^{-13}$ erg s^{-1} cm^{-2} (derived from the Suzaku observations, assuminig a spectral index of 2.0). This flux upper limit corresponds to $F_{X\text{-}ray}(2-10\ \mathrm{keV}) < 2.55 \times 10^{-13}$ erg s^{-1} cm^{-2} in the 2−10 keV energy band[1]. Note that this limit is 2 times higher than the estimated flux (for the pulsar distance of 0.4 kpc) by using Eq. 6.3.

As explained in Section 5.4, the analysis of independent X-ray data from Swift XRT observations showed no X-ray emission from the direction of PSR B1737−30 either (see Fig. 5.20). Instead, an X-ray emission from the cataclysmic variable Suzaku J174035.6−301416 could be seen in the vicinity of the pulsar PSR B1737−30 as mentioned in Uchiyama et al. (2011). Note that the sensitivity of the Swift XRT[2] is comparable with the predicted fluxes for the pulsar distance of 0.4 kpc. These predicted fluxes from Mattana et al. (2009) include large errors and differ depending on the used property of the pulsar ($\dot{E}$ or τ_c). Consequently, the expected flux levels are at the limit of detectability and its not surprising that the Swift XRT could not detect any X-ray emission from the pulsar PSR B1737−30. Observation with deeper exposure can resolve the faint X-ray PWN around the pulsar PSR B1737−30. On the other hand, the expected X-ray flux from PSR B1737−30 for the distance of 3.28 kpc is still below the sensitivity level of the Swift XRT and therefore can not be detected.

6.1.2 IC Scattering of OH/IR Star's Radiation Field

Another leptonic scenario can be considered taking into account the powerful OH/IR star that is located in the vicinity of HESS J1741−302 as shown in Fig. 5.20. Recall that OH/IR stars are late type stars enshrouded in a dense dust shell which absorbs all the radiation emitted by the star and re-emits it in infra-red (IR) wavelengths. These strong IR photon fields of such stars can provide target photons for producing IC scattered γ-rays in the presence of relativistic electron populations. Consequently, in this scenario, the OH/IR star's strong IR radiation acts as target photons for IC scattering from the relativistic electron population provided by PSR B1737−30. It can be clearly seen from Fig. 6.3 (left) that the radiation field of the OH/IR star is very strong in IR wavelengths and dominates over the FoV. The spectrum of the OH/IR star is shown in Fig. 6.3 (right). One can estimate the energy density of this strong radiation field by using the integrated

[1]Note that the integral flux in the 1−9 keV energy band can be converted to the 2−10 keV energy band by multiplying the 1−9 keV integrated flux with ln(10 keV / 2 keV) / ln(9 keV / 1 keV) ≈ 0.73.

[2]The sensitivity of the Swift XRT is 2×10^{-14} erg s^{-1} cm^{-2} in 10^4 s [Burrows et al. (2000)].

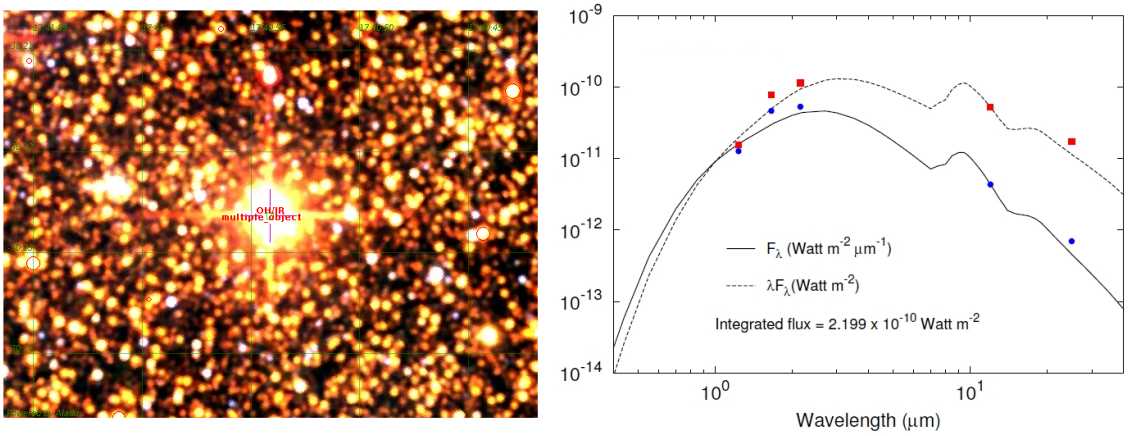

Figure 6.3: Left figure: The Two Micron All Sky Survey (2MASS) infra-red skymap of the region around the OH/IR star OH 358.23+0.11. Angular scale of the FoV is $0.1^\circ \times 0.08^\circ$ in R.A. and Dec., respectively. Right figure: The spectrum and the spectral energy distribution of the OH/IR star. The data points were taken from 2MASS [Skrutskie et al. (2006)]. The red points show the spectral energy distribution of the OH/IR star while the blue points show the measured flux from the direction of the OH/IR star. The OH/IR star emission model was fitted to the observed flux points by using the DUSTY framework (http://www.pa.uky.edu/ moshe/dusty/) and the model was normalized to the data at 12 μm. The black lines show the fitted model to the blue data points while the dashed black line show the fitted model to the red data points.

IR flux obtained from the spectrum of the OH/IR star as

$$U_{Rad} = \frac{4\pi}{c} F_{IR} \left[\frac{d}{R_{Shell}} \right]^2 \tag{6.4}$$

where U_{Rad} is the energy density (in eV cm^{-3}), F_{IR} is the integrated infra-red flux measured from the direction of the OH/IR star (2.2×10^{-10} Watt m^{-2}), d is the assumed distance to the OH/IR star and R_{Shell} is the shell radius of the OH/IR star. Note that a typical dust shell radius R_{Shell} for OH/IR stars is $\sim 5.0 \times 10^{16}$ cm which approximately corresponds to a radius of $\sim 1.6 \times 10^{-2}$ pc and is determined from the measurements of phase lag between red and blue-shifted OH maser emission [Herman et al. (1985)]. The distance to the OH/IR star is not very well constrained and was estimated as $4.5^{+1.4}_{-4.2}$ kpc by using the OH maser spectrum [Caswell (1998)] and the rotation curve of Wouterloot&Brand [Wouterloot et al. (1989)]. In this scenario, it is assumed that the OH/IR star and the pulsar PSR B1737−30 have similar distances from the Sun. Note that the pulsar distances of 0.4 kpc and 3.28 kpc can also be assumed for the OH/IR star distances since they are compatible with the estimated distance to the star. Consequently, by using the F_{IR} value obtained from the OH/IR star's spectrum, one can calculate the energy density of the OH/IR star's radiation field as 3.5×10^4 eV cm^{-3} and 2.3×10^6 eV cm^{-3} for the OH/IR star distances of 0.4 kpc and 3.28 kpc, respectively. Note that these values are extremely large when compared to the energy density of the CMB radiation field which has the energy density of 0.25 eV cm^{-3}.

Another important point of consideration in this scenario is whether or not the injected

electrons from PSR B1737−30 can reach the position of the OH/IR star. The angular distance between the pulsar PSR B1737−30 and the OH/IR star is 0.13°. Assuming that these two objects are located at the same distance from the Sun, the projected distances between these two objects correspond to 0.95 pc and 9.1 pc for the pulsar-OH/IR system distances of 0.4 kpc and 3.28 kpc, respectively. Recall that the evolution of PWN in a spherically symmetric case can be given as

$$\begin{aligned} R_{PWN} &\approx 1.5 \dot{E_0}^{1/5} E_{SN}^{3/10} M_{ej}^{-1/2} t^{6/5} \\ &\approx 1.1\text{pc} \left(\frac{\dot{E}_0}{10^{38}\ \text{erg s}^{-1}} \right)^{1/5} \left(\frac{E_{SN}}{10^{51}\ \text{erg}} \right)^{3/10} \left(\frac{M_{ej}}{10\ \text{M}_\odot} \right)^{-1/2} \left(\frac{t}{10^3\ \text{years}} \right)^{6/5} \end{aligned} \quad (6.5)$$

where R_{PWN} is the radius of the PWN forward shock at time t, $\dot{E}_0$ is the spin-down luminosity of the pulsar, E_{SN} is the explosion energy of the supernova and M_{ej} is the ejected mass released in the supernova explosion [Slane et al. (2006)]. For a basic estimation[3], assuming that $E_{SN} = 10^{51}$ erg, $M_{ej} = 10\ \text{M}_\odot$ and taking $t = \tau_c = 20.6$ kyr as the characteristic age of the pulsar PSR B1737−30 gives $R_{PWN} \approx 10$ pc. This estimated R_{PWN} value of 10 pc suggests that the pulsar PSR B1737−30 can actually fill a sphere with a radius of ∼10 pc with the injected electrons during the time period which is equal to its characteristic age. Since the estimated R_{PWN} value is in the order of the projected distance between the pulsar and the OH/IR star for both distances of 0.4 kpc and 3.28 kpc, one can conclude that the injected electrons from the pulsar can reach the OH/IR star's position within the characteristic age of the pulsar. Recall that several assumptions were made in Eq. 6.5 while calculating R_{PWN}, consequently this R_{PWN} value includes large errors but can still give an idea whether or not the injected electrons can reach the OH/IR star's position.

One can investigate the energetics of the IC scattering of OH/IR star's radiation field from the relativistic electrons injected by the pulsar PSR B1737−30 scenario or in other words, the required total energy of electrons which can give rise to the observed VHE γ-ray luminosity. Recall that the total energy of the electrons can be calculated by using the formula

$$E_{e,total} = L_\gamma \times \tau_{IC} \quad (6.6)$$

where L_γ is the VHE γ-ray luminosity of HESS J1741−302 and τ_{IC} is the characteristic time for IC scattering of an electron with energy E. Note that in this calculation, one assumes that L_γ is equal to the total energy loss rate for IC scattering of the whole population of electrons. The term τ_{IC} can be calculated as

$$\tau_{IC} = \frac{E}{dE/dt} \quad (6.7)$$

where the term E is the energy of an electron and the term dE/dt is the energy loss rate

[3]Note that in this estimation, it is assumed that the pulsar PSR B1737−30's progenitor is an undetected SNR.

of a single electron. In the Thomson regime, the energy loss rate of an electron is given by

$$\frac{dE}{dt} = \frac{4}{3}\sigma_T c U_{Rad} \gamma^2 \tag{6.8}$$

where σ_T is the Thomson cross-section and γ is the Lorentz factor of the electron. Table 6.1 shows the energy requirements for being able to produce the observed VHE γ-ray signal from IC scattering of both CMB photons and the IR photons from OH/IR star's radiation field from the assumed electron population injected by PSR B1737−30. Recall that the characteristic age of the pulsar is 6.3×10^{11} s which gives the maximum available pulsar energy of 5.2×10^{46} erg if one takes into account the spin-down luminosity of the pulsar. From Table 6.1, one can see that the scenario including IC scattering from CMB photons for the pulsar distance of 3.28 kpc can be directly excluded since the required energy in electrons is more or less in the order of the energy available in the pulsar while for the pulsar distance of 0.4 kpc, ∼1.5% of the energy available in the pulsar is required. Moreover, the energy requirements in the case of the scenario that takes into account the OH/IR star are significantly less when compared to the CMB only case. Therefore, the scenario of IC scattering of OH/IR photons from the electrons injected by pulsar PSR B1737−30 can not be excluded for both distance approximations from the energetics point of view.

IC Model	U_{Rad} (eV cm^{-3})	τ_{IC} (s)	$L_\gamma.\tau_{IC}$ (erg)	$\dot{E}.\tau_{IC}$ (erg)
CMB (0.4 kpc)	0.25	5.3×10^{13}	7.5×10^{44}	4.3×10^{48}
CMB (3.3 kpc)	0.25	5.3×10^{13}	5.0×10^{46}	4.3×10^{48}
OH/IR (0.4 kpc)	3.5×10^{4}	3.7×10^{8}	5.3×10^{39}	3.0×10^{43}
OH/IR (3.3 kpc)	2.3×10^{6}	5.5×10^{6}	5.3×10^{39}	4.5×10^{41}

Table 6.1: Energetics table for the leptonic scenario that takes into account the radiation field from the CMB and the OH/IR star. The U_{Rad} column shows the energy density in the radiation field. For the OH/IR star's radiation field, U_{Rad} was evaluated from the integrated flux obtained from OH/IR star's spectrum. The τ_{IC} column shows the characteristic time for IC scattering for an electron evaluated at 1 TeV while the $L_\gamma.\tau_{IC}$ column shows the required total energy in electrons to produce the observed VHE γ-ray signal. The $\dot{E}.\tau_{IC}$ column shows the total energy released by the pulsar during the corresponding τ_{IC}.

At this point one should also take into account that not all of the electrons injected by the pulsar interact with the OH/IR star's radiation field since they are not positionally coincident. Therefore, an additional treatment of the energetics may be needed. For this purpose, one should calculate the fraction of the total energy injected from the pulsar at the location of the OH/IR star. Recall that the assumed radius of the dust shell around the OH/IR star is $1.6\times\ 10^{-2}$ pc, while the distance between the OH/IR star and the pulsar is 0.95 pc (for the system distance of 0.4 kpc) and 9.1 pc (for the system distance of 3.28 kpc). Consequently, assuming that the injected energy (or in other words, relativistic

electrons) from PSR B1737−30 is distributed spherically symmetric around the pulsar, one can calculate the corresponding fraction of the injected energy at the location of the OH/IR star as $\sim$7.1 $\times$ 10^{-5} and $\sim$7.7 $\times$ 10^{-7} for the system distances of 0.4 kpc and 3.28 kpc, respectively. Combining these values with the previously calculated maximum available pulsar energy of 5.2 $\times$ 10^{46} erg gives 3.7 $\times$ 10^{42} erg for 0.4 kpc and 4.0 $\times$ 10^{40} erg for 3.28 kpc system distances, respectively. If one compares these maximum available pulsar energy values, which take into account the treatment of distance between the OH/IR star and the pulsar, with the total energy values given in Table 6.1, it is clear that the scenarios including the IC scattering of CMB photons can be directly excluded for both distance approximations while the IC scattering of the OH/IR star's radiation field scenarios for both distances still survive. Note that for the system distance of 0.4 kpc, $\sim$0.14% of the maximum energy available from the pulsar should be transferred into electrons while this efficiency value increases to $\sim$13% for the system distance of 3.28 kpc.

An important fact should be mentioned at this point. Recall that the OH/IR star is not located at the center-of-gravity of the VHE γ-ray excess observed from the direction of HESS J1741−302 but there is an angular offset around $\sim$0.08°. In the leptonic scenario which takes into account the IC scattering of OH/IR star's radiation field from the relativistic electron population injected by the pulsar PSR B1737−30, one expects that the center-of-gravity of the VHE γ-ray excess should be coincident with the OH/IR star's position where IC scattering takes place. Note that the angular offset of $\sim$0.08° is significantly larger than the systematic pointing error of the H.E.S.S. telescopes (20"). Consequently, this observed offset between HESS J1741−302 and the OH/IR star makes the scenario unlikely although this scenario is energetically reasonable.

For being able to investigate the properties of the relativistic electron population provided by the pulsar PSR B1737−30, a more sophisticated modeling of the pulsar-OH/IR system is required. For this purpose, the naima modeling package[4] was used. This package uses Markov Chain Monte Carlo (MCMC) fitting [MacKey (2003)] of non-thermal X-ray, GeV, and TeV spectra to constrain the properties of their parent relativistic particle distributions. The workhorse of naima is the emcee package [Foreman-Mackey et al. (2013)] which is an affine-invariant ensemble sampler for MCMC. For the modeling of IC emission, the naima package implements the analytical approximations to IC scattering of blackbody radiation developed by Khangulyan et. al (2014) given by Eq. 14 in their paper. This has the advantage of being computationally cheap compared to a numerical integration over the spectrum of the blackbody and remains accurate within one percent over a wide range of energies. Note that the seed photon field here can be a blackbody or a diluted blackbody (gray body) and the modeling of IC scattering also takes these effects into account. For deriving the properties of the relativistic electron population by using the analytical approximation suggested by Khangulyan et. al (2014), one needs to provide seed photon field's properties as input to the naima code. As it was explained before (see Table 6.1), the energy density of the OH/IR star's radiation field can be calculated by using two different distance assumptions. In addition to this energy density value, one needs to provide the photon gas temperature of this radiation field. Consequently, the parameters of the parent electron population's spectrum can be constrained.

[4]See http://naima.readthedocs.org/en/latest/index.html for the detailed description of naima package.

Note that in general for OH/IR stars, the photon gas temperature in the vicinity of the stellar surface is $T_{stellar} = \sim$2000 - 3000 K while this value decreases to $T_{shell} =$ 800 - 1000 K at the dust shell and even to around 100 K just beyond the dust shell [Goldreich et al. (1976)]. Since there is a quite high uncertainty in the determination of this photon gas temperature around the OH/IR star of interest, T_{gas} temperature was changed between 100 K and 1000 K for the modeling of the pulsar-OH/IR star system.

The results obtained from naima modeling are shown in Fig. 6.4 for two different pulsar-OH/IR system distances of 0.4 kpc (upper figures) and 3.28 kpc (lower figures). For modeling the IC spectra, a power law parent electron spectrum was assumed. Note that modeled IC spectra with an exponential cut-off power-law (ECPL) parent electron spectrum assumption can not be fitted to the observed H.E.S.S. flux points, consequently the fit does not converge[5]. As it can be seen from energetics plots (Fig. 6.4 left figures), the energy requirements are independent of the system distances. This fact was already predicted by the energetics study (see Table 6.1 $L_{\gamma}.\tau_{IC}$ column for OH/IR models) since L_{γ} scales with d^2 while τ_{IC} scales with d^{-2}. Note that there is at least a factor of $\geq$ 2 difference (for $T_{Gas} = 100$ K) between the theoretical energy requirements shown in Table 6.1 and the total energy results obtained from the modeling output. Recall that the energetics estimations shown in Table 6.1 are rough and include large errors. They also don't take into account the temperature of the photon gas and are calculated in the Thomson regime. When one takes into account the temperature of the radiation field, it can be seen from Fig. 6.4 (right figure) that as the temperature increases, the electron spectral index gets harder than the expected value in the Thomson regime of $\Gamma_{\gamma} = (1-\Gamma_e))/2$, which corresponds to $\Gamma_e \approx 3.6$ for the observed VHE γ-ray spectral index of $\Gamma_{\gamma} = \sim$2.3. This is basically because the scattering starts to occur in the Klein-Nishina regime.

Figure 6.5 shows the example output from the naima modeling of the IC scattering from OH/IR star's radiation field (for $T_{Gas} = 500$ K) for both pulsar-OH/IR star distances of 0.4 kpc and 3.28 kpc. As it can be seen from the left figures, the IC model can be fitted to the H.E.S.S. data points quite well. The corresponding parent electron spectra are given in the right figures. Consequently, the observed VHE γ-ray spectrum of HESS J1741−302 can be well reproduced by the IC scattering of OH/IR star's radiation field from the relativistic electron population injected by the pulsar PSR B1737−30.

Taking into account the energy output plot obtained from the naima IC modeling (see Fig. 6.4 left plots) and the maximum available pulsar energy of 3.7×10^{42} erg for 0.4 kpc and 4.0×10^{40} erg for 3.28 kpc system distances, one can conclude that the IC emission from the pulsar-OH/IR star system is energetically possible for all assumed T_{Gas} temperatures for 0.4 kpc while one can put an upper limit on the T_{Gas} around 100 - 200 K for the system distance of 3.28 kpc since the fraction of the total energy available in the pulsar into electrons gets larger than 20 - 25% above these photon gas temperatures.

[5]Recall that the ECPL model fit to the VHE gamma-ray flux points did not significantly improved the fit with respect to a power-law model (0.4σ). In the case one uses ECPL model for the parent electron spectrum in naima code for producing the IC spectrum, the cut-off parameter of the parent electron spectrum can not be constrained.

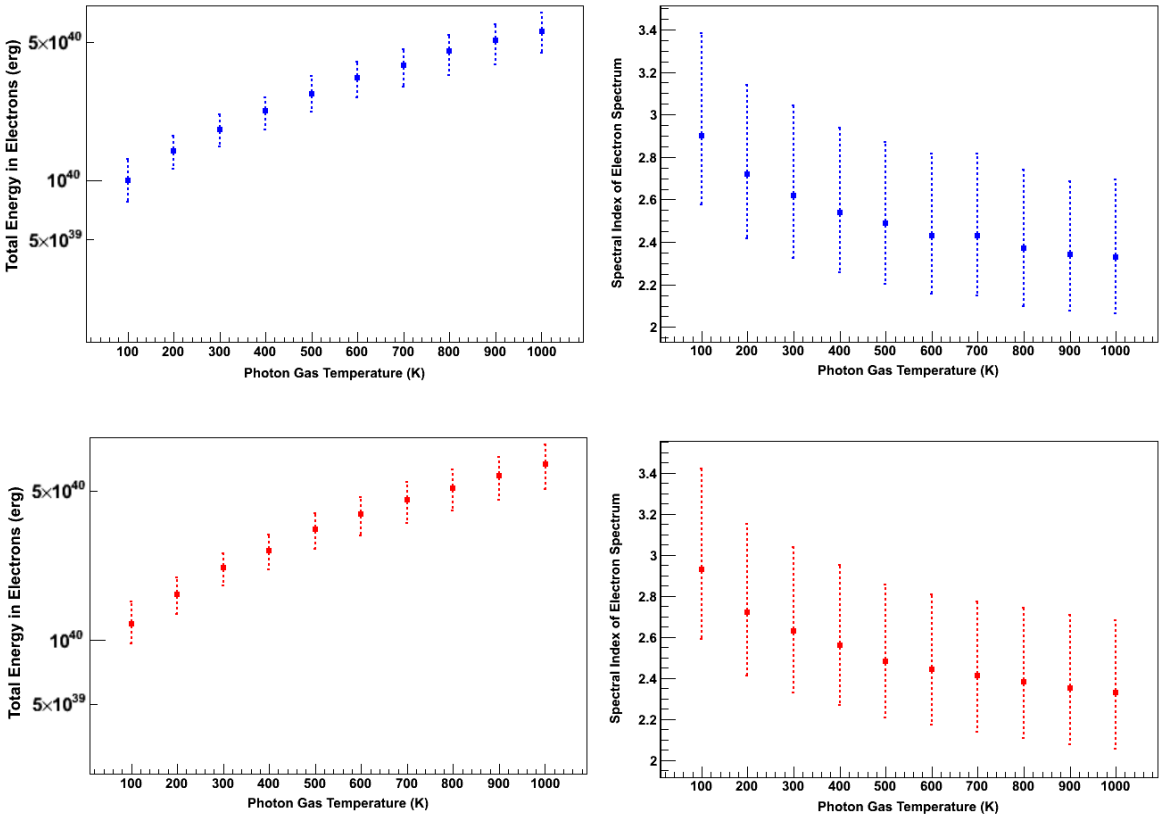

Figure 6.4: Results of modeling the IC scattering of OH/IR star's photon fields from the relativistic electrons injected by the pulsar PSR B1737−30. The upper plots show the results for the pulsar distance of 0.4 kpc (blue points) while the lower plots show the results for 3.28 kpc (red points). The left figures show the total amount of energy that the relativistic electrons should have for producing the observed VHE emission from the direction of HESS J1741−302 for different assumed photon gas temperatures of the OH/IR star's radiation field. Note that the energy density values given in Table 6.1 for different distances were used as input for this modeling. The right figures show the obtained spectral indexes of the electron spectra (average of 100 simulations) for different assumed photon gas temperatures.

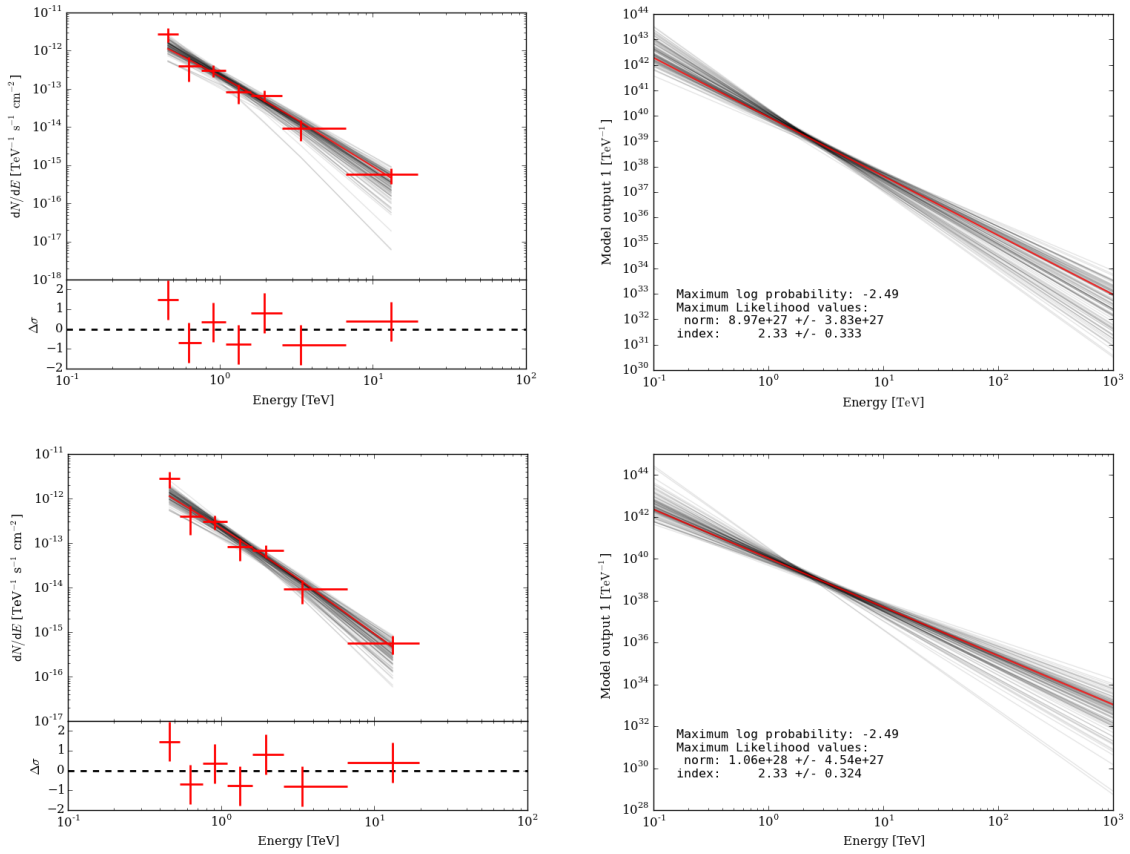

Figure 6.5: Example output IC spectrum from the naima modeling for a photon gas temperature of 500 K. The upper figures are for pulsar-OH/IR system distance of 0.4 kpc while the lower figures are for the distance of 3.28 kpc. The red data points in the left figures are the H.E.S.S. data points derived from the spectral analysis of HESS J1741−302 while the black lines show 100 simulated IC spectra assuming a power-law model for the parent electron spectrum. The red lines in the left figures show the best IC spectrum fitted to the H.E.S.S. data points. The black lines in the right figures show the corresponding 100 parent electron spectra that give rise to the IC spectra shown in the left figures while the red lines show the corresponding electron spectra that give rise to the best IC spectra fitted to the H.E.S.S data points in the left figures. The obtained best fit electron spectrum parameters are also given in the right figures.

6.2 Hadronic Scenarios

The investigation of HI and ^{12}CO data showed clear evidence (see Section 5.3 for more details) that there are several molecular clouds along the line of sight of HESS J1741−302. Moreover, the solid angle averaged H_2 column density of the HESS J1741−302 region was calculated as $\sim 6.5 \times 10^{22}$ cm^{-2} ($\sim 8.0 \times 10^{22}$ cm^{-2} for HI + ^{12}CO), which is relatively a high value when compared to other parts of the Galactic Plane. This relatively high column density value actually indicates that there is enough target material to produce hadronic emission when illuminated by protons (also by other hadrons).

Recall that there are no positionally coincident SNRs or powerful pulsars at the position of the observed VHE emission region. Consequently, an isolated VHE γ-ray emission was detected from this region that can support the idea of an interaction of protons accelerated by an undetected proton source with MCs along the line of sight. In this subsection, hadronic scenarios including illumination of MCs by the background galactic CRs and interaction of protons injected by an undetected local SNR inside or close to MCs will be discussed.

6.2.1 Illumination of MCs by the Background Galactic CRs

As discussed in Section 2.2, a significant fraction of the background galactic CRs is composed of hadrons (protons and heavy nuclei). The spectral index of background CRs in the energy range from several GeV to beyond 100 TeV is $\sim$2.7 [Particle Data Group (2014)] which is measured from the Earth. Therefore this value actually reflects the CR spectrum in the vicinity of the Earth. It is generally assumed that the local flux of CRs gives a correct approximation for the whole galactic population of relativistic particles although there can be small variations on large galactic scales, especially in the proximity of young CR accelerators. In this subsection, a hadronic scenario based on illumination of the MCs found along the line of sight of HESS J1741−302 by the background galactic CRs will be discussed.

HESS J1741−302 has a significantly harder VHE γ-ray spectrum ($\Gamma = 2.28 \pm 0.16_{\rm stat}$) with respect to the spectrum of background galactic CRs under a power-law assumption ($\Gamma = \sim 2.7$). Since it is expected that the observed γ-rays carry direct information about the spectrum of progenitor particles (see Section 2.3.2 for details), which are background galactic CRs in this case, one can conclude that the VHE emission is not expected to originate from the background galactic CRs interaction with MCs and directly exclude this scenario.

Moreover, it is quite common to use the cosmic-ray enhancement factor (K_{cr}) for each molecular cloud along the line of sight for quantifying the emissivities observed from the direction of MCs. Note that the K_{cr} values of unity (up to 3) can be interpreted as an indication of background galactic CRs interaction with molecular clouds, while a local CR source would be needed if the K_{cr} value significantly exceeds unity [Aharonian & Atoyan (1996)]. Recall that while calculating K_{cr} values for each molecular cloud along the line of sight of HESS J1741−302, it was assumed that all the observed VHE γ-ray flux originates from pp interactions of the background galactic CRs alone with the molecular cloud of interest. Consequently, these calculated K_{cr} values for each MCs

also support the idea of excluding this scenario since they are significantly higher than unity (see Table 5.5 for K_{cr} values).

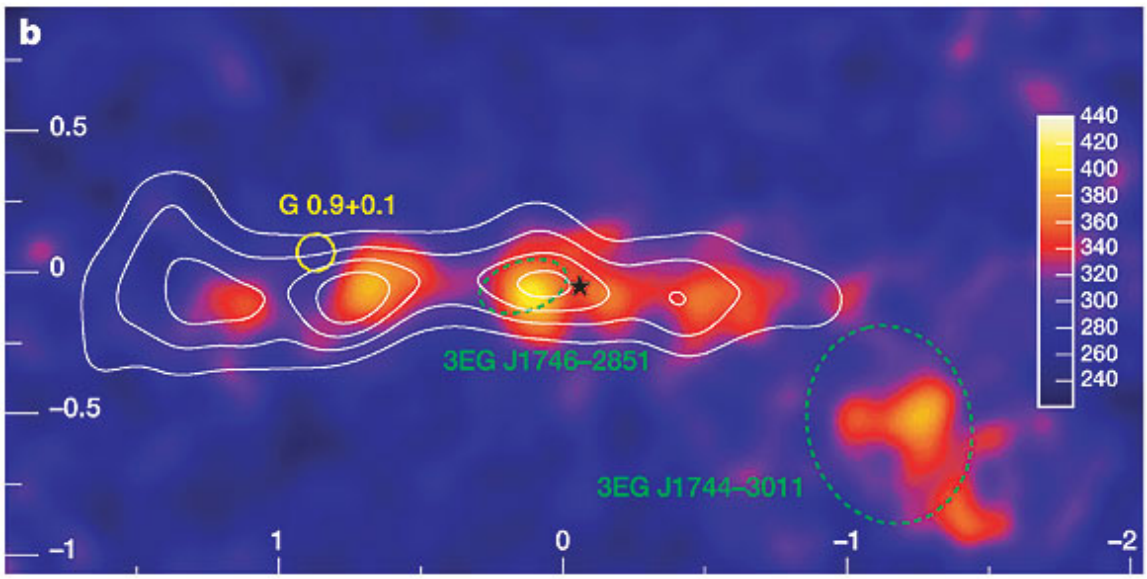

Figure 6.6: γ-ray count map of the GC region after subtraction of the two dominant point sources, showing an extended band of γ-ray emission. The axes are Galactic latitude (x) and Galactic longitude (y), units are degrees. The color scale is in events and is dimensionless. The white contour lines indicate the density of molecular gas, traced by its CS emission. The position and size of the composite supernova remnant G0.9+0.1 is shown with a yellow circle. The position of Sgr A* is marked with a black star. The 95% confidence region for the positions of the two unidentified EGRET sources in the region are marked as dashed green ellipses. These smoothed and acceptance-corrected images are derived from 55 hours of data consisting of dedicated observations of Sgr A*, G0.9+0.1 and a part of the data of the H.E.S.S. Galactic plane survey. Credit: [Aharonian (2006a)]

Recall that the H.E.S.S. Collaboration reported on the detection of diffuse γ-ray emission from the GC ridge [Aharonian (2006a)] and the derived spectrum can be seen in Fig. 2.3. In that study, the TeV γ-ray spectrum extracted from the region $-0.8^\circ < l < 0.8^\circ$, $|b| < 0.3^\circ$ and could be fitted well by a power-law model with a spectral index of $\Gamma = 2.29 \pm 0.07_{\rm stat} \pm 0.20_{\rm sys}$. The authors suggested that at least for $|l|$ <1°, there is a close match between the distribution of the VHE γ-ray emission and the distribution of dense interstellar gas as traced by CS emission which can be seen clearly from Fig. 6.6. They also suggested that the CRs accelerated by the galactic central source, with an age assumption of ∼10 kyr, can fill the region $|l|$ <1° but have not diffused yet beyond $|l|$ >1°. For this reason, although there is a perfect match between the observed spectral index of HESS J1741−302 ($\Gamma = 2.28 \pm 0.16_{\rm stat} \pm 0.20_{\rm sys}$) and the derived diffuse γ-ray spectral index for the GC ridge, since the projected distance of the cloud 6 from the GC is ∼260 pc ± 40 pc (corresponds to $l = \sim 1.7^\circ$), the scenario considering the illumination of cloud 6 by the CRs accelerated at the GC will be excluded and not be discussed in this thesis.

6.2.2 Local SNR inside or close to MCs

Although there are no detected SNRs in the (vicinity of) HESS J1741−302 region[6], one can still discuss a hadronic scenario assuming an undetected SNR located within or in the vicinity of one of the detected clouds since the calculated K_{cr} values suggest the existence of a local CR source. In this scenario, it is assumed that all the observed VHE γ-ray emission originated from pp interactions between the detected MCs along the line of sight of HESS J1741−302 and the injected protons from an undetected SNR.

There are several studies on the VHE γ-ray emission taking into account the hadronic scenarios based on SNR-MC interactions. One of them is the VHE γ-ray emission from the GC ridge [Aharonian (2006a)]. In that study, a cosmic-ray enhancement factor of 3 - 9 above 1 TeV is observed. Another example is the detected VHE γ-ray emission coincident with MCs from the W28 region [H.E.S.S. Collaboration (2008b)]. W28 is a mixed-morphology SNR, with radio size of 50'×45' and an estimated distance between 1.8 and 3.3 kpc [Lozinskaya (1981)]. It is an old SNR (35 to 150 kyr [Kaspi (1981)]), thought to have entered its radiative phase of evolution in which much of its CRs have escaped into the surrounding interstellar medium. In the case of a hadronic origin, the authors estimated the CR enhancement factor for E >1 TeV, assuming MC distances of 2 kpc and 4 kpc for the various cloud components found along the line of sight for W28, in the range between 13 to 32 (see Table 2 in that study). Another intriguing example of SNR-MC interaction is CTB 37A. The region of the SNR complex CTB 37 harbors three young SNRs while one of these remnants (SNR G348.5+0.1) is interacting with several molecular clouds. OH maser emission at 1720 MHz has also been detected [Frail et al. (1996)] at various locations towards the TeV γ-ray source HESS J1714−385 [Aharonian (2008b)]. In a recent study about the connection between interstellar gas towards CTB 37A and the TeV γ-ray source HESS J1714−385, the authors located several MCs by using several different molecular emission lines along the line of sight for HESS J1714−385 [Maxted et al. (2013)]. The corresponding K_{cr} values were found changing between 80 - 1100 for the calculated distances between 6.3 kpc an 7.9 kpc (see Table 7 in their paper).

As it can be understood from the given examples above, the K_{cr} values can have a quite wide range of values depending of the source of interest. It is expected since K_{cr} values depend on the properties of the assumed proton source and the assumed diffusion coefficient. Consequently, many parameters like the age and size of the SNR of interest, spectral index of the injected proton spectrum and properties of interstellar medium between SNR and MC come into play. Note that in Aharonian et. al. (1996), cosmic-ray enhancement factors were estimated between 80 - 300 for the SNR-MC interactions assuming an SNR with an age of 10^4 - 10^5 years with an injected proton spectrum ($\Gamma_{p,inj} = 2.2$) at a distance of 10 pc from a MC. In this estimation, the galactic cosmic-ray diffusion coefficient was taken as $D = 10^{26}$ cm^{2}s^{-1}. Recall that energy and magnetic field dependent diffusion

[6]The nearest detected SNRs in the vicinity of HESS J1741−302 are SNR G357.7+00.3 and SNR G357.7−00.1 both located ∼0.7° away from HESS J1741−302.

coefficient inside a molecular is given by

$$D(E,B) = \chi 10^{28} \left(\frac{E}{10\ \mathrm{GeV}}\right)^{0.5} \left(\frac{B}{3\mu\mathrm{G}}\right)^{-0.5} \quad \mathrm{cm^2 s^{-1}} \tag{6.9}$$

where χ is a factor that takes into account deviations from the average Galactic diffusion coefficient. Since the magnetic field scales roughly as the square root of the gas density, the magnetic fields inside the densest regions of a MC can reach mG levels. Consequently, the range of the parameters considered by Aharonian et al. (1996) does not suggest CR enhancement factors above ∼300. But K_{cr} values up to ∼1000 can be reasonable if the SNR-MC distance is smaller than 10 pc, which actually indicates that the SN explosion takes place in a MC.

It would be a reasonable approach to calculate the required energetics in such a hadronic scenario like it was done for the IC scattering of pulsar-OH/IR system in Section 6.1.2 as a starting point. A basic estimation of total energy required in protons can be calculated by

$$W_p = L_\gamma \times t_{pp} \tag{6.10}$$

where W_p is the total energy in protons giving rise to the observed γ-ray luminosity L_γ. The term t_{pp} is the cooling time of protons through the channel of π^0 production. This term is given by

$$t_{pp} = \frac{1}{n_{Gas} c \kappa \sigma_{pp}} \tag{6.11}$$

where n_{Gas} is the gas number density, c is the speed of light, σ_{pp} and κ are the cross-section and inelasticity of the pp process, respectively. For the calculation of t_{pp}, one can use a formally assumed energy independent pp cross-section of $\sigma_{pp} = 34$ mb since the cross section of the pp process does not significantly change over a broad range of proton energies from ∼1 GeV to hundreds of TeVs (see Fig. 2.9). The term κ, which is basically the fraction of kinetic energy of the proton transferred to γ-rays, can be taken as $\kappa = 0.17$ as it was suggested by Kelner et al. (2006). Consequently, Eq. 6.11 can be expressed only in terms of n_{Gas} as $t_{pp} = 5.76 \times 10^{15} \times (n_{Gas}/\mathrm{cm^{-3}})^{-1}$ s. Finally, one can calculate the total energy in protons (W_p) by using the Eq. 6.10 and the calculated n_{Gas} values for each molecular cloud given in Table 5.5. The obtained results are given in Table 6.2 for different γ-ray energy thresholds[7] of 0.35 TeV (HESS J1741−302 VHE data analysis threshold) and 1.0 TeV (for comparison with other studies).

Note that the estimated W_p values in Table 6.2 are significantly lower than the formally assumed SN explosion energy of 10^{51} erg. If one calculates the efficiencies by taking the ratio $W_p/(10^{51}$ erg), it can be seen that these efficiency values change between 0.04% - 0.2% depending on the cloud of interest. This basic calculation suggests that each molecular cloud found along the line of sight for HESS J1741−302 can give a rise to the observed VHE emission from the energetics point of view under the assumption of an undetected SNR located in the vicinity (or inside) of each molecular clouds.

There was a similar study done by Drury et. al (1994) for the estimation of the total

[7]Recall that the luminosity L_γ is calculated by taking into account the integrated energy flux from HESS J1741−302 above a certain γ-ray energy threshold.

MC Number	n_{Gas} (cm^{-3})	t_{pp} (s)	W_p (E_γ >0.35 TeV) (erg)	W_p (E_γ >1.0 TeV) (erg)
1	–	–	–	–
2	85 ± 22	6.78×10^{13}	$(2.10 \pm 0.68) \times 10^{48}$	$(1.42 \pm 0.46) \times 10^{48}$
3	175 ± 79	3.29×10^{13}	$(3.67 \pm 1.81) \times 10^{47}$	$(2.48 \pm 1.22) \times 10^{47}$
4	107 ± 25	5.39×10^{13}	$(7.50 \pm 2.29) \times 10^{47}$	$(5.08 \pm 1.55) \times 10^{47}$
5	74 ± 14	7.79×10^{13}	$(1.15 \pm 0.31) \times 10^{48}$	$(7.78 \pm 2.12) \times 10^{47}$
6	249 ± 35	2.31×10^{13}	$(4.01 \pm 0.97) \times 10^{47}$	$(2.71 \pm 0.65) \times 10^{47}$

Table 6.2: Energetics table for the hadronic scenario taken into account pp interaction between an undetected SNR and MCs found along the line of sight of HESS J1741−302. The MC Number column shows the clouds from Fig. 5.18 while the n_{Gas} column gives the corresponding gas number density for the cloud of interest. The t_{pp} column gives the characteristic cooling time for protons calculated by using Eq. 6.11. The fourth and fifth W_p columns give total energy in protons ($L_\gamma.t_{pp}$) above the γ-ray energy thresholds of 0.35 TeV and 1.0 TeV, respectively.

flux above a certain energy threshold taking into account SNR-MC interactions. In this study, the expected total flux at the Earth was given as

$$F(>E) \approx 9 \times 10^{-11} \left(\frac{E}{1 \text{ TeV}}\right)^{-1.1} \left(\frac{E_{SN}}{10^{51} \text{ erg}}\right) \left(\frac{d}{1 \text{ kpc}}\right)^{-2} \left(\frac{n_{Gas}}{1 \text{ cm}^{-3}}\right) \theta \quad (\text{cm}^{-2}\text{s}^{-1}) \tag{6.12}$$

where E_{SN} is the assumed SN explosion energy, d is the distance to the SNR of interest, n_{Gas} is the gas number density of the MC of interest and θ is the fraction of the total SN explosion energy transferred into CRs. Note that the derivation of Eq. 6.12 assumes a differential energy spectrum inside the remnant proportional to $E^{-2.1}$. Finally, one can calculate the parameter θ in Eq. 6.12 for each molecular cloud along the line of sight of HESS J1741−302 with the assumed SN explosion energy of 10^{51} erg. Note that in this calculation, the assumed SNR distance d is taken as the distance to the MC of interest since it is assumed that SNRs are located in the vicinity (or inside) of the MC of interest.

As it can be seen from the calculated W_p values in Table 6.3, they are also significantly lower than the formally assumed SN explosion energy of 10^{51} erg. When one compares the results for the total energy in protons given in Table 6.2 and Table 6.3, it can be seen that the results calculated from Drury et. al (1994) are slightly higher but still compatible. Recall that there are additional assumptions like the spectral index of the CR spectrum injected by the SN but this slight difference does not change the conclusions that each MC along the line of sight can produce the observed VHE emission if one assumes a SNR in the vicinity or inside the MC of interest.

MC Number	$\theta \times 10^{-4}$ (E>0.35 TeV)	W_p (E>0.35 TeV) (erg)	$\theta \times 10^{-4}$ (E_γ >1.0 TeV)	W_p (E_γ >1.0 TeV) (erg)
1	–	–	–	–
2	33.2 ± 10.4	(3.32 ± 1.04) × 10^{48}	34.8 ± 20.3	(3.48 ± 2.03) × 10^{48}
3	5.8 ± 2.2	(5.82 ± 2.22) × 10^{47}	6.1 ± 5.8	(6.09 ± 5.81) × 10^{47}
4	11.9 ± 3.5	(1.19 ± 0.35) × 10^{48}	12.4 ± 6.6	(1.24 ± 0.66) × 10^{48}
5	18.2 ± 5.1	(1.82 ± 0.51) × 10^{48}	19.0 ± 8.6	(1.90 ± 0.86) × 10^{48}
6	6.3 ± 1.6	(6.32 ± 1.61) × 10^{47}	6.7 ± 2.4	(6.67 ± 2.42) × 10^{47}

Table 6.3: Energetics table for the hadronic scenario derived from Eq. 6.12 for each MCs found along the line of sight of HESS J1741−302. The MC Number column shows the clouds from Fig. 5.18. The term θ in the second and fourth columns give the fraction of total energy in protons from SN explosion, calculated from Eq. 6.12 for the energies above 0.35 TeV and 1.0 TeV respectively. The W_p terms in the third and fifth columns give the corresponding energy in protons in terms of erg above the γ-ray energy thresholds of 0.35 TeV and 1.0 TeV, respectively, assuming an initial SN explosion energy of 10^{51} erg.

Chapter 7

Summary

Multi-wavelength data analysis of the unidentified VHE γ-ray source HESS J1741−302 and the interpretation of the VHE emission detected from the direction of this source were presented in this thesis. The additional work done on the software development for the MST prototype in Berlin-Adlershof was presented in Appendix B in detail.

The analysis of ∼145 hr good-quality data from H.E.S.S. phase I observations conducted within 2.0° radius around HESS J1741−302 resolved the morphology of this source in more detail with respect to the previous analysis presented in Tibolla et. al (2008). The morphology analysis of the HESS J1741−302 region has shown that the VHE source HESS J1741−302 and the nearby hotspot could be statistically discriminated from each other at the significance level of 4.0σ. The best fit centroid position of the Gaussian corresponding to the VHE γ-ray emission coming from the direction of HESS J1741−302 was found to be R.A.: $17^{\mathrm{h}}41^{\mathrm{m}}15.8^{\mathrm{s}} \pm 3.6^{\mathrm{s}}_{\mathrm{stat}} \pm 1.5^{\mathrm{s}}_{\mathrm{sys}}$, Dec.: $-30°22'37.2" \pm 50"_{\mathrm{stat}} \pm 20"_{\mathrm{sys}}$. No significant intrinsic extension of the source could be obtained, consequently HESS J1741−302 was found to be a point-like source. Recall that the results presented in Tibolla et. al (2008) suggested an extended morphology for HESS J1741−302 since the source and the nearby hotspot could not be statistically discriminated while the size of this extension was not mentioned.

The VHE γ-ray spectrum of HESS J1741−302 was extracted by using the updated best fit source position taking into account the point-like morphology of the source. With this choice of the extraction region, the source spectrum can be well described by a power-law model with a spectral index of $\Gamma = 2.28 \pm 0.16_{\mathrm{stat}} \pm 0.20_{\mathrm{sys}}$ and a normalization at 1 TeV of $\Phi_0 = (2.12 \pm 0.42_{\mathrm{stat}} \pm 0.42_{\mathrm{sys}}) \times 10^{-13}$ cm^{-2} s^{-1} TeV^{-1}. The integrated flux above 1 TeV is $\Phi(>1\ \mathrm{TeV}) = (1.65 \pm 0.28_{\mathrm{stat}} \pm 0.33_{\mathrm{sys}}) \times 10^{-13}$ cm^{-2} s^{-1} corresponding to ∼1% of the Crab Nebula flux at the same energies. A power-law with exponential cut-off model did not improve the fit significantly (0.4σ from LLRT), consequently the ECPL model was rejected. Recall that in Tibolla et. al (2008), the source spectrum was described by a power-law model with a spectral index of $\Gamma = 2.78 \pm 0.24_{\mathrm{stat}} \pm 0.20_{\mathrm{sys}}$. The choice of a point-like extraction region as opposed to Tibolla et. al (2008) for deriving the source spectrum led to a significantly harder spectrum.

Different leptonic and hadronic emission scenarios were discussed in this thesis for explaining the observed VHE γ-ray emission from the direction of HESS J1741−302. The investigated leptonic scenarios take into account the injection of relativistic electrons

provided by the relatively powerful nearby pulsar PSR B1737−30. As it was also discussed before in Tibolla et. al (2008), a pulsar with an offset PWN scenario can not be excluded. In the case the VHE emission is originated by a pulsar with an offset PWN, the efficiency calculations and the lack of emission in the X-ray energy band suggest that the PWN of interest should be located at a few kpc distance. Consequently, the VHE γ-ray emission from the assumed pulsar with an offset PWN located at a distance of 0.4 kpc is unlikely and can be excluded. Another leptonic scenario includes the IC scattering of the OH/IR star OH 358.23+0.11's radiation field from the injected relativistic electrons from PSR B1737−30. Basic energetic calculations and sophisticated modeling of the VHE γ-ray emission from the pulsar-OH/IR star system suggest that IC scattering of IR photons provided by the strong OH/IR star can explain the observed VHE γ-ray emission for the system distances of both 0.4 kpc and 3.28 kpc from the energetic and spectral points of view. But the observed $\sim$0.08° offset between HESS J1741−302 and the OH/IR star OH 358.23+0.11 disfavors the scenario from the morphology point of view since the $\sim$0.08° offset is significantly large when compared to the systematic pointing error of the H.E.S.S. telescopes. The leptonic scenario including IC scattering of the CMB photons from the relativistic electrons provided by PSR B1737−30 was also investigated, but energetically the distance of 3.28 kpc can be directly excluded since in this case, nearly all of the energy available from the pulsar should be transferred to electrons. On the other hand, the pulsar distance of 0.4 kpc is energetically reasonable since it requires $\sim$1.5% of the energy available from the pulsar. Note that if one takes into account the distance between the OH/IR star and the pulsar, since only fraction of injected electrons contributes to IC scattering, both leptonic CMB scenarios can be excluded energetically while the leptonic scenarios including the pulsar-OH/IR system can still give rise to the observed VHE γ-ray emission energetically.

The investigation of HI and ^{12}CO data showed clear evidence for the existence of molecular clouds along the line of sight for HESS J1741−302 with a solid angle averaged H_2 column density of $\sim 6.5 \times 10^{22}$ cm^{-2}. This suggests the existence of dense target material for hadronic interactions. Illumination of the MCs found along the line of sight by the galactic background CRs can be directly excluded since the calculated cosmic-ray enhancement factors (between $\sim$80 - 300) for each MC significantly exceed unity. The VHE γ-ray spectrum of HESS J1741−302 is significantly harder than the spectrum of the background galactic cosmic-rays which also supports this idea. A special case of illumination of MC 6 (which is found close to GC with a projected distance of $\sim$260 pc) by the CRs accelerated at the GC was not investigated in detail for this thesis since it was suggested that the propagation of CRs accelerated at the GC are not expected to reach the galactic longitudes beyond 1.0° [Aharonian (2006a)]. Instead, large K_{cr} values suggest the requirement of a cosmic-ray source in the vicinity (or inside) of the MCs found if one assumes that all the VHE γ-ray emission from the direction of HESS J1741−302 originates from pp interactions. The required energetics for each assumed SNR-MC system were calculated. The results suggest that the each MC found along the line of sight for HESS J1741−302 can give a rise to the observed VHE γ-ray emission if one assumes an undetected SNR in the vicinity (or inside) of each MCs.

Up to now, the H.E.S.S. observations conducted on HESS J1741−302 include $\sim$145 hr of good quality data. Because HESS J1741−302 is one of the faintest VHE γ-ray sources

detected, additional observations with H.E.S.S. will probably not place strict constraints on the emission scenarios discussed in this thesis unless the additional observation time significantly exceeds the existing amount of data. The possible future observations on this source that will be conducted by using the future Cherenkov Telescope Array can provide detailed morphology and spectral information about this source since CTA will be a factor of 10 more sensitive than any existing instrument and will have an angular resolution of $<0.02^{\circ}$. Recall that the morphology analysis of the HESS J1741−302 region performed by using a cut configuration that provides an angular resolution angular down to 0.08° (hi-res ζ) actually suggests a morphology model which is slightly extended along the Galactic plane for this source. With the improved angular resolution of CTA, this morphology model can be cross-checked in the future which can place constraints on the emission model and support the discussed hadronic scenario. By using CTA, more statistics at the high energy part of VHE γ-ray spectrum of HESS J1741−302 with respect to the current spectrum can be obtained which allows the determination of a cut-off in the VHE γ-ray spectrum. This cut-off energy can also be used for placing additional constraints on the emission scenarios and can resolve the question whether the VHE emission is hadronic or leptonic.

Appendix A

MST Prototype

This appendix gives a brief description about the motivation and the structure of the MST prototype. The author of this thesis has worked in the software development group for the MST prototype and the details of the work are given in Appendix B. Note that the detailed information given in this appendix about the instrumentation and the software framework used in MST prototype covers a wide range of research areas. Therefore, this appendix assumes that the reader is familiar with the concepts explained below.

In the future CTA project, each individual CTA telescope will be a complex system that has to operate in synchronization with other telescopes. A prototype of one of the design concepts of the MST, which is still under development and testing, was installed in Berlin at the end of 2012. The MST prototype is the first opportunity inside the CTA consortium to integrate a considerable number of hardware devices and to exercise the control software. This prototype is composed of the mechanical structure, drive system and mirror facets mounted with powered actuators to enable active controlling of mirror facets in 3D space. There are 84 hexagonal spherical type mirror facets mounted on the dish. Figure A.1 shows the design concept of the MST prototype. The MST prototype has a Davies-Cotton [Davies-Cotton (1957)] type reflector design with a diameter of 12 m and a focal length of 16 m. The prototype is not fully functional since it has no photo-multipliers in the camera housing and has only a fraction of real optical mirrors. A dummy camera of 2.5 tons, allowing functions such as operation of protective camera lids and temperature sensors, was mounted on the prototype to resemble and to test the structural effects of the real camera. Three Charge-Coupled Device (CCD) cameras mounted on the prototype allow measuring the performance of the instrument while a mounted weather station is being used for monitoring the environmental conditions. The Atacama Large Millimeter/sub-millimeter Array (ALMA) [Wrootten-Thomson et al.(2009)] Common Software (ACS) [Chiozzi, et al. (2004)] distributed control framework is decided by the CTA consortium to serve as the future array control middle-ware and is being used in the MST prototype control (See Appendix B for more details).

The main goal of the MST prototype is to prove the design concept and the confirmation of the steel structure design. Furthermore, different test of the drive system and a proof of the calibration methods are being studied. Measurements of static and dynamic deformations depending on azimuth and elevation motion, angular position and environmental conditions are being performed. While star visibility in Berlin is not optimal for

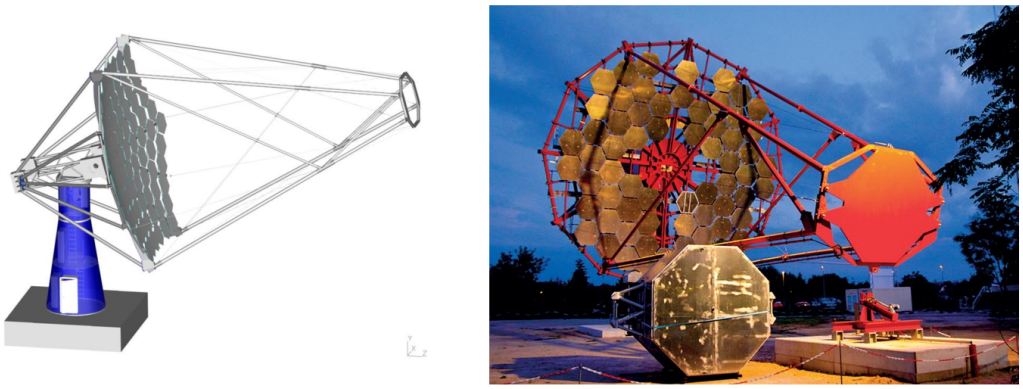

Figure A.1: Left figure: Sketch of the structure design of the MST, composed of a quadrupod (camera support), a dish structure, counterweights, a head (connecting the dish and the tower), and a tower with the foundation. Right figure: Photo of MST prototype in Berlin. In the foreground camera housing currently installed on the telescope can be seen. Credit: http://www-zeuthen.desy.de/

physics observations, the sky conditions are sufficient for accurate pointing measurements. The telescope pointing and the pointing calibration tests are an important part of the MST prototype program. The measurement of the point spread function (PSF), safety system tests, observation of weather conditions and related performance tests, testing of array control and proof of the mechanical concept are also included in the MST prototype program.

A.1 Drive System

The drive system of the MST prototype is designed to resemble and to test the expected operation modes of the CTA telescopes, allowing pointing of the prototype to any position and tracking any astronomical object. The prototype operates with the help of main two motors, one for azimuth and one for elevation motion. The drive system of the prototype is composed of 6 drive systems at a lower level, communicating via Bosch-Rexroth programmable logic controller[1]. Two drives are used for azimuth motion while four drives are used for elevation motion. The PLC runs the VxWorks real-time operating system and hosts an OPC-UA[2] server. This OPC-UA server can be accessed by using the prototype control software.

[1] A programmable logic controller (PLC) is a digital computer used for automation of typically industrial electro-mechanical processes, such as control of machinery.

[2] OPen Connectivity-Unified Architecture (OPC-UA), see http://www.opcfoundation.org for more information.

A.2 CCD Cameras

A crucial tool to check different aspects of the MST prototype is a set of CCD cameras housed in water-proof casing and installed on the prototype dish. Currently, three CCDs are used for pointing calibration. The central Lid CCD camera is mounted on the central plate, pointing at the dummy camera. The LEDs on the dummy camera lid allow the determination of the camera position with respect to the Lid CCD for the pointing accuracy measurement. This camera is also used for mirror alignment and measurement of the PSF. Another camera called "Sky CCD" is mounted on the edge of the dish 6 meters away from the center to take unobstructed images of the sky in the direction of the telescope pointing. The locations of Sky CCD and Lid CCD on the MST prototype can be seen at the left side of Fig. A.2.

The chosen CCD camera model, which is shown at the right side of Fig. A.2, is "Prosilica GC 1350" with a resolution of 1.4 Mpix (1360 $\times$ 1024) and a pixel size of 4.65 μm $\times$ 4.65 μm. For a large light collection area combined with a suitable field of view, the Sky CCD uses an 85 mm "Walimex Pro" aperture [Oya et al. (2012)]. The lens weighs about 480 g and requires a support structure within the camera housing to avoid bending or distortion of the CCD camera. The resulting total field of view is 4.26° $\times$ 3.21°, which is sufficient for astrometry measurements as well as single bright star observations. Sensors installed on the CCD cameras record temperature information to observe the effects of temperature changes such as CCD chip expansion due to heat. The output images are stored in a database for later image processing. These CCDs can operate at a rate up to 10 Hz and therefore generate the largest fraction of data volume of the prototype. The CCD cameras used in the MST prototype are interfaced via GigE Vision interface allowing up to 1000 Mbit/s on Gbit Ethernet. The Allied Vision Technologies (AVT) PvAPI SDK[3] allows to control and capture images from GigE Vision CCD cameras in a Linux environment. It is accessible by most of the programming languages such as C++ and Java.

The main goals of using CCD cameras are to test the structural design stability of the prototype under the effects of temperature, wind and other environmental and operational factors. For this purpose, the data taken from a weather station is being used. Additionally, the CCDs are used to perform mirror adjustments and allow the measurements of the optical point spread function.

A.3 Active Mirror Control

The design of the CTA telescopes makes use of a tessellated reflector composed of individual mirror facets [Föster, et al. (2012)]. Each individual mirror facet is attached to a triangular support called "Active Mirror Control" (AMC) unit, including two powered actuators and a fixed support. The AMC unit has the functionality to enable perfect mirror alignment in 3D space and to allow re-alignments of the reflectors since the deformation due to the weight of the telescope causes misalignments depending on the telescope elevation.

The dish of the MST prototype is completely covered by a combination of real and dummy mirrors. Several AMC units of two different designs are installed on the MST

[3]Software Development Kit (SDK).

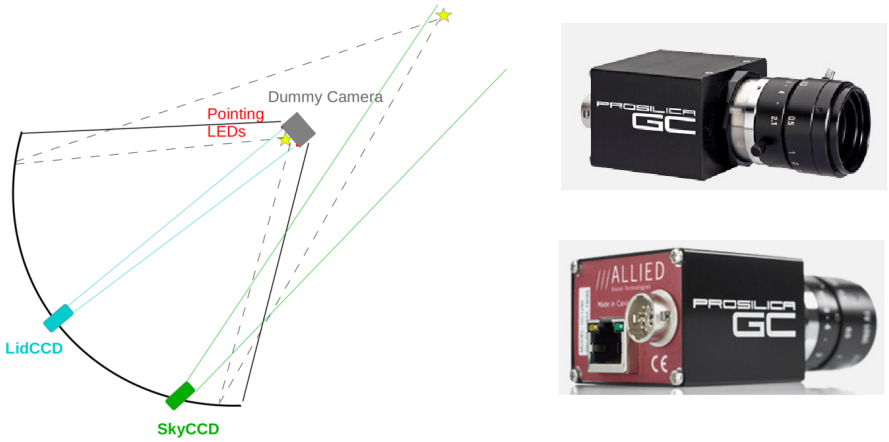

Figure A.2: Right figure: Sketch of the MST prototype showing the Lid and Sky CCDs shown on it. The pointing LEDs are shown with red dots while the star images shows the observed star for pointing calibration and the image of this star on the dummy camera. Left figure: Picture of Prosilica GC 1350 model CCD camera used for the Sky and Lid CCD.

prototype. One type of unit communicates via XBee radio modules[4], creating a Wireless Personal Area Network (WPAN) that is accessed via a XBee receiver connected to a PC via a USB or a RS-232 serial interface. The other type of unit is interfaced via Controller Area Network Bus (CAN-Bus) accessed via an Ethernet-CAN-Bus gateway.

A.4 Weather Station

A weather station (WS) has been acquired and installed close to the MST prototype for continuously monitoring the weather conditions. The chosen WS model is "Davis Vantage VUE" and can be seen in Fig. A.3. This WS is able to measure the wind speed and direction, as well as other quantities with the required accuracy and (measurement) rate. The instrument is composed of an outdoor unit communicating via a WPAN with an indoor unit, including a data-logger with limited internal storage capacity and equipped with a RS-232 serial interface. The WS is the least complex component of the MST prototype and for this reason, it was the first device installed on the prototype and read-out by using the ACS software. Starting from the lower level, an OPC-UA server has been implemented with the OPC-UA Java SDK which uses the RXTX library to communicate with the WS data-logger via the serial line. In a higher level, a Java ACS component was implemented using the UML[5] based code generation framework and tested with the ACS object explorer[6].

[4]See XBee from http://www.digi.com/ for detailed information.

[5]The Unified Modeling Language (UML) is a general-purpose modeling language in the field of software engineering which is designed to provide a standard way to visualize the design of a system. The Magic Draw software is used for generating the UML models. See https://www.magicdraw.com/ for details.

[6]ACS object explorer is a GUI which allows the monitoring of an ACS component's properties. In the case of WS ACS component, these properties are temperature, wind speed, wind direction and humidity.

Figure A.3: Davis Vantage VUE model weather station used in MST prototype.

Appendix B

ACS Control Software for the MST Prototype

This appendix concentrates on the work done in the software development group for the MST prototype by the author of this thesis. The software used for controlling the MST prototype is a complicated framework which is continuously developed by the software development group for the MST prototype. Therefore, not all the details of the software used in the MST prototype can be given in this appendix. The reader is assumed to be familiar with the control software explained in this appendix.

CTA will be composed of a large number of devices that in principle might use various types of hardware interfaces. For this reason, the MST prototype is a great opportunity to integrate various telescope hardware systems in advance to test the control software. In the future CTA project, a flexible way of accessing the hardware will be necessary for handling such a complex installation. Engineering side of this installation would require accessing the devices by using expert modes for hardware testing while scientist would require a user-friendly framework to operate an array composed of many telescopes without having any experience with the complex details of the devices. These requirements can be met by using a software based on the distributed computing paradigm and in particular, distributed object platform COBRA[1].

B.1 ALMA Common Software

The ALMA Control Software [Chiozzi, et al. (2004)] (ACS) is a general framework based on CORBA and C++, Java and Python languages. It provides a complete environment and structures at the base of application software developments. Since ACS is based on a distributed component model, ACS components can be implemented as CORBA objects in any of the supported programming languages. ACS components are the base for high level control entities and for the implementation of devices such as telescope drive system, CCD camera and weather station. It also provides common CORBA-based

[1]The Common Object Request Broker Architecture (CORBA) is a standard defined by the Object Management Group (OMG) designed to facilitate the communication of systems that are deployed on diverse platforms.

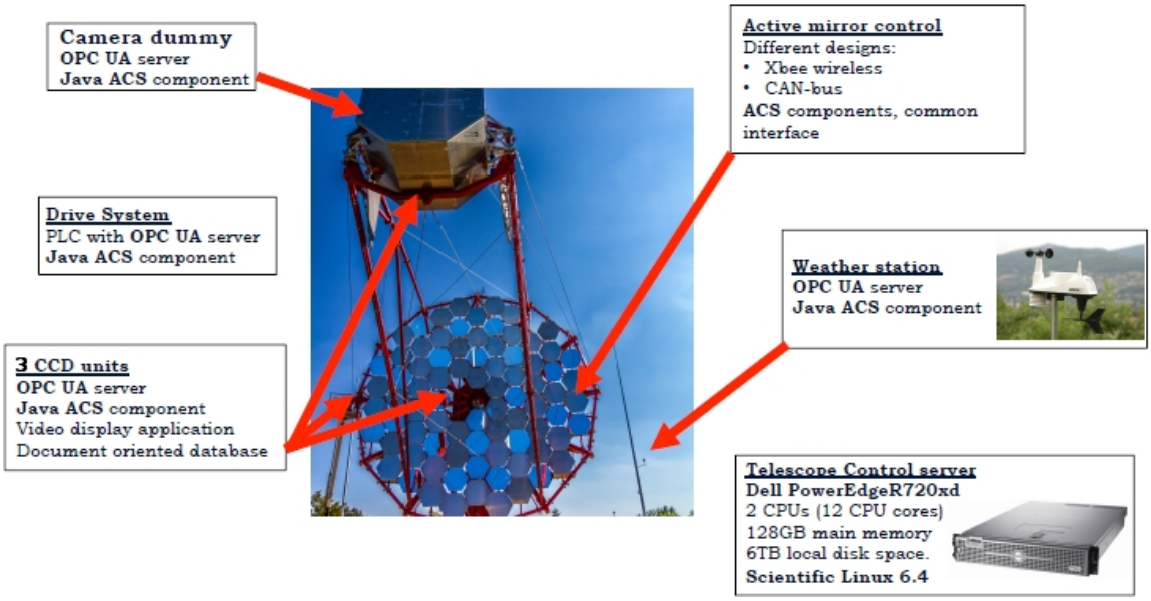

Figure B.1: The locations of the hardwares used in the MST prototype are indicated with the red arrows. The corresponding ACS components to these hardwares are also mentioned in the boxes. Credit: Oya et al., The MST Prototype – 11th ACS workshop, Nov. 2014 Garching

services such as logging, error and alarm management, configuration database and life-cycle management while hiding the complexities of CORBA programming from non-expert users. The ACS framework was originally developed for the ALMA project. Because of the similar complexity levels of the ALMA and CTA projects, ACS is decided to be the main control software in the future CTA project. Currently, ACS is being used for controlling the MST prototype. For accessing the hardware, the low level software interface protocol OPC-UA is being used. The hardware used in the MST prototype and the corresponding ACS components responsible for operating the MST instrumentations can be seen in Fig. B.1. Recall that each of these instruments used in the MST prototype was explained in Appendix A.

The schematic sketch of the data flow between the installed instruments and ACS is shown in Fig. B.2. Each of these hardware devices was connected to the ACS layer as it can be seen from the figure. Some of the ACS components like WS, CCD camera and LEDs are connected to the ACS layer by using an OPC-UA server while some of them (drive system, power supplies etc.) use PLC with an OPC-UA server. Additionally, there are some instrumentations coming with an embedded system[2] with OPC-UA server.

B.2 The Configuration Database in ACS

The Configuration Database (CDB) stores the information that the ACS system requires for starting up and initializing. These information include various telescope start-up

[2]See Raspberry Pi (https://www.raspberrypi.org/) for details.

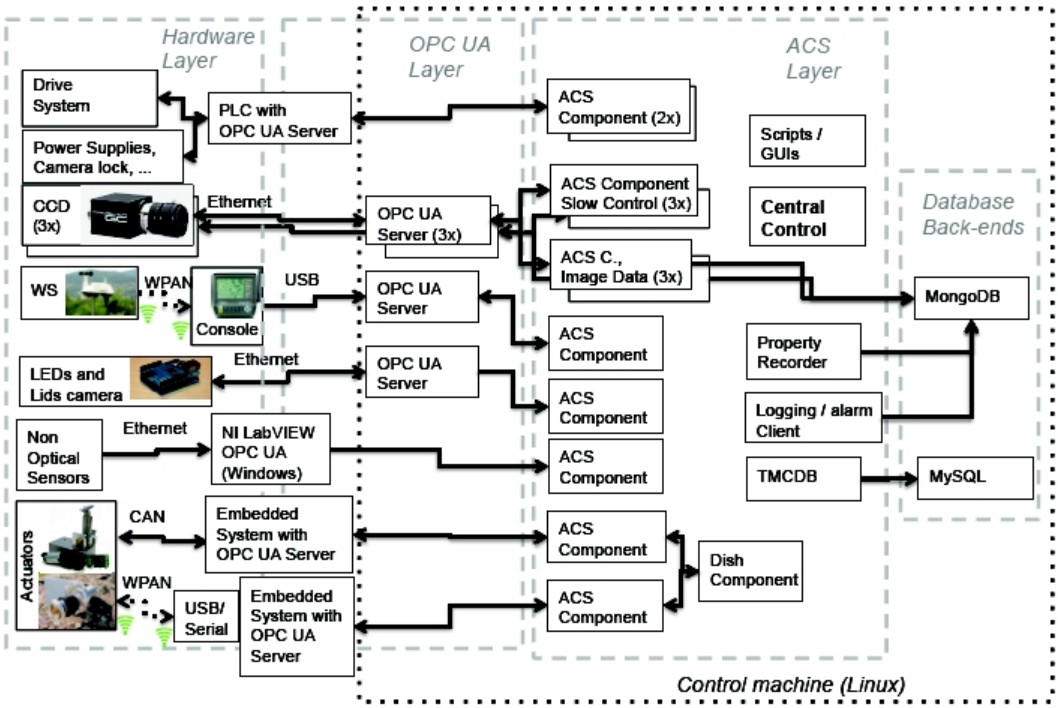

Figure B.2: The schematic sketch of the data flow between the installed hardware and the ACS. The whole system is composed of three sub-layers, namely hardware, OPC-UA and ACS layers. Databases used for storing telescope configurations and collected data are also shown. Credit: Oya et al., The MST Prototype − 11th ACS workshop, Nov. 2014 Garching

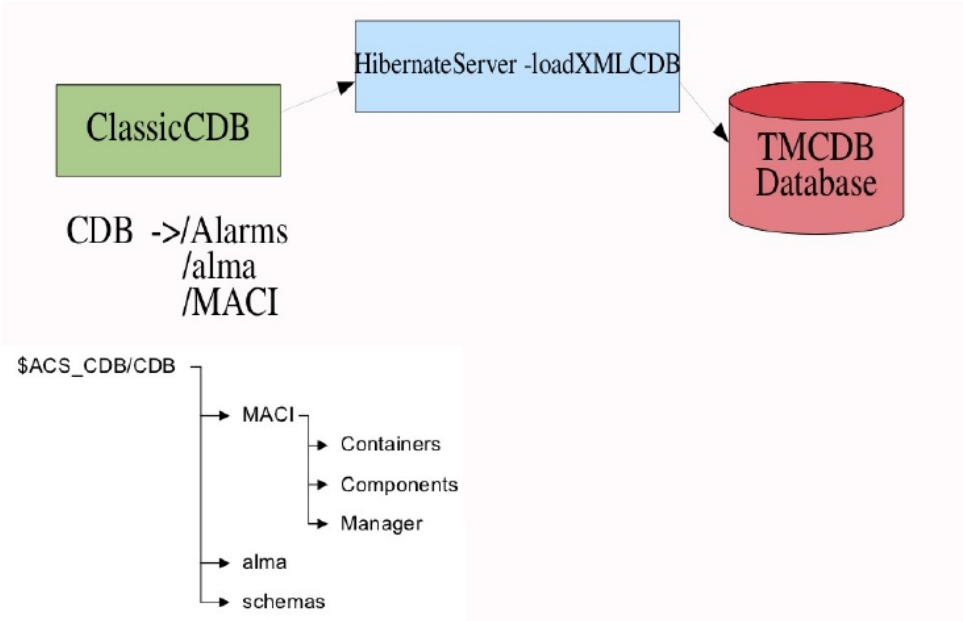

Figure B.3: Schematic sketch of the configuration data transfer process from a classical CDB in ACS to a TMCDB MySQL. Classical configuration data are stored in XML and XSD files located in the ACS configuration folder, under "Components", "Configurations" and "Manager" folders. The Hibernate framework was used for mapping and transferring the stored data located in the XML and XSD files under these folders.

configurations and deployment data for the components, the containers[3] and the ACS manager. The default implementation of CDB consists of a set of XML[4] files parsed against corresponding XSD[5] files.

Note that ACS provides an alternative implementation of the CDB that uses a relational database such as HSQLDB[6] or Oracle[7] to store configuration information. This alternative implementation method is called Telescope Monitoring and Configuration Database (TMCDB). The author of this thesis has worked on the project for modifying the ACS software to run with TMCDB MySQL[8] database implementation. This modification was suggested since the XML structures can be extremely complicated while dealing with a huge number of complicated ACS components. Using the TMCDB implementation provides access to the relational database tables of interest by using terminal or GUIs[9], otherwise one has to make the required modifications for each ACS components' prop-

[3]Note that ACS system has three different containers that allow components written in different programming languages to be implemented. These containers are "frodoContainer" (for Java), "bilboContainer" (for C++) and "aragornContainer" (for Python).

[4]Extensible Markup Language (XML) is a markup language that defines a set of rules for encoding documents in a format which is both human and machine readable.

[5]XML Schema Definition (XSD), a recommendation of the World Wide Web Consortium that specifies how to formally describe the elements in an XML.

[6]HSQLDB (Hyper SQL Database) is a relational database management system written in Java. It has a JDBC driver and supports a large subset of SQL formats. See www.hsqldb.org/ for more details.

[7]Oracle Database, commonly referred to as Oracle RDBMS or simply as Oracle, is an object-relational database management system produced and marketed by the Oracle Corporation. See http://www.oracle.com/ for more details.

[8]See http://www.mysql.com/ for more details.

[9]Graphical User Interface (GUI).

erties by changing the corresponding XML and XSD files manually with a text editor. Moreover, the TMCDB implementation provides easy maintenance of different telescope configurations and allows the initialization of ACS for different pre-defined configurations. In principle, any relational database could be used with TMCDB. The MySQL database was chosen for the MST prototype since it is freely available and a very-well documented user friendly database. For this purpose, the Hibernate framework[10] was used for mapping and transferring the data stored in XML and XSD files to the relational database tables of MySQL as illustrated in Fig. B.3. For the TMCDB implementation to work with MySQL database, some of the ACS source code had to be adapted. The source code locations and the reasons for adapting the code are listed below. Note that all of the modules listed below are located in the ACS source code. Therefore, after the changes are made, ACS should be compiled from scratch to make the TMCDB MySQL implementation work.

- CommonSoftware/jacsutil/src/alma/hibernate/util/jdbcNativeExtractor.java : Definition of additional function for returning the connection object for MySQL.

- CommonSoftware/`cdb_rdb`/src/com/cosylab/cdb/jdal/hibernate/DBUtil.java : Definition of additional function for connecting to MySQL database. Some definitions like back-end name were added.

- CommonSoftware/`cdb_rdb`/src/com/cosylab/cdb/jdal/hibernate/HibernateDBUtil.java : Definition of Hibernate dialect and MySQL driver to be used were added.

- CommonSoftware/`cdb_rdb`/src/com/cosylab/cdb/jdal/hibernate/plugin/PluginFactory.java : Modification for allowing MySQL driver was made in this source class.

- CommonSoftware/`cdb_rdb`/src/com/cosylab/cdb/jdal/HibernateWDALImp.java : Modifications for getting the configuration from XML files and place them into MySQL database tables in a correct way were done within this source class.

The list above gives a brief summary of the changes made in the ACS source code. Some other classes and XSD files were also modified in the "Codegen" module to create MySQL scripts required for creating the MySQL table templates. Executing these auto-generated MySQL scripts creates the required MySQL tables and columns in the database, consequently the data of interest can be stored in these tables. In additional to these changes, some environmental variables have to be exported for ACS to work with the TMCDB MySQL implementation. These environmental variables and their functions are listed below.

[10]Hibernate is an object-relational mapping library for the Java language, providing a framework for mapping an object-oriented domain model to a traditional relational database (http://hibernate.org/).

- export `ENABLE_TMCDB`=1 : This setting is mandatory and allows ACS to work with the TMCDB implementation. The default value of this environmental variable is "0" which starts ACS by using the classical CDB.

- export `TMCDB_CONFIGURATION_NAME`='<name>' : This setting is mandatory and allows any specific ACS configuration to be saved under a specific name. By changing the configuration name, many different TMCDB start-up configurations can be stored.

- export `LOAD_FROM_XML`=1 : This setting is only required for the first time when Hibernate reads the existing configuration of ACS from the XML files. After the first time reading from XML files and saving the configuration under a specific '<name>', the same configuration can be loaded later by just using the setting of this specific TMCDB configuration name. Therefore, this environmental variable should not be exported for starting ACS with an existing configuration name.

- export `ACS_CDB`='<Path.to.CDB>' : This setting is required only if one uses other CDB than the default CDB in ACS, it shows the path to XML and XSD files to be read.

B.3 Monitoring and Alarm Information in ACS

The ACS system produces unnumbered monitoring information about the condition of the whole system while it is in operation. These information is generated by the ACS components, containers or managers. Monitoring information can be used for maintaining the whole system structure and also for raising alarms in the case of unexpected system conditions. All the information messages and alarms raised by the corresponding components or containers are transmitted to a central information service that provides an interface for consumers of these data. This central service is called the 'ACS Central Logger". Two consumers, one for information messages and another one for alarms are realized for the MST control system. An external ACS java client was developed by the author of this thesis that can connect to the ACS central logger system, get the required monitoring information and alarm information from there and save the pre-selected information into a MongoDB[11] database. Note that every single information and alarm message produced by the ACS system has a priority level showing the importance of the message. The minimum level requirement for an information message to be saved into database can be determined from the client. The risk of filling up the storage system with excessive log information is excluded by using a capped collection or alternatively a "time of life" collection, provided by MongoDB. Basically, one can set up a maximum time

[11]MongoDB is a cross-platform document-oriented NoSQL database. MongoDB avoids the traditional table-based relational database structure in favor of a JSON-like documents with dynamic schemas (MongoDB calls the format BSON), making the integration of data in certain types of applications easier and faster. See http://www.mongodb.org/ for more details.

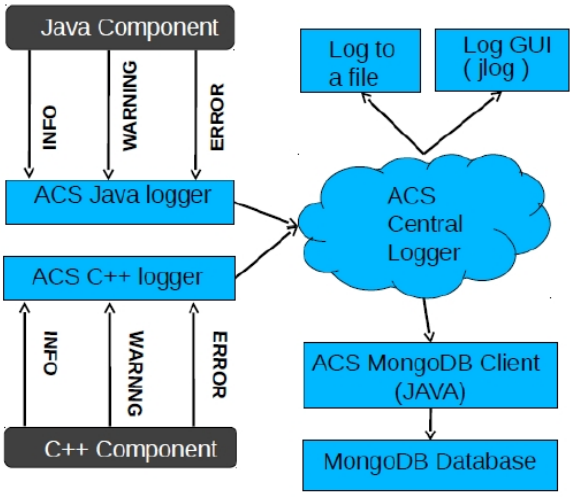

Figure B.4: Schematic sketch of log and alarm information transfer between various ACS components written in different languages and MongoDB database.

of life for any message that is stored in the database. After this time, the message will be deleted automatically. A schematic sketch of the java client can be seen in Fig. B.4.

Bibliography

[Abraham (2004)] Abraham, J., et al. Properties and performance of the prototype instrument for the Pierre Auger Observatory. NIM A, 523:5095, 2004.

[Abraham (2007)] Abraham, J., et al. Correlation of the Highest-Energy Cosmic Rays with Nearby Extragalactic Objects. Science, 318:938, 2007.

[Acero (2010)] F. Acero et al., Monthly Notices of the Royal Astronomical Society, Volume 402, Issue 3, pp. 1877-1882. (2010)

[Ackermann (2012)] M. Ackermann et al. (Fermi-LAT Collaboration), ApJS 203, 4 (2012), arXiv:1206.1896 [astro-ph.IM]

[Actis (2011)] M. Actis et al., Exp. Astron. 32 (2011) 193-316

[Aharonian & Atoyan (1996)] F.A. Aharonian, & A.M. Atoyan, A&A 309 (1996) 917

[Aharonian (2001)] Aharonian, F., Gamma Rays From Molecular Clouds. Space Sci. Rev. 99, 187-196 (2001)

[Aharonian (2004a)] Aharonian, F. Very High Energy Cosmic Gamma Radiation. World Scientific, 2004.

[Aharonian (2004b)] Nature, 432, 75

[Aharonian (2004c)] Aharonian et al., Calibration of cameras of the H.E.S.S. detector. Astroparticle Physics, 22, (2004).

[Aharonian (2005a)] Science, 307, 1938

[Aharonian (2005b)] Aharonian F. A. et al. H.E.S.S. Collaboration, Science 307, 1839, 2005

[Aharonian (2006a)] The H.E.S.S. Collaboration: F. A. Aharonian, et al. 2006, Nature 439:695-698,2006

[Aharonian (2006b)] Observations of the Crab nebula with HESS. A&A, 457:899915, October 2006a. doi: 10.1051/0004-6361:20065351.

[Aharonian (2006c)] Aharonian F. A. et al. 2006d, Science 314, 1424

[Aharonian (2006d)] F.Aharonian et al., The Astrophysical Journal, Volume 636, Issue 2, pp. 777-797. 2006

[Aharonian (2007)] F. Aharonian, A. G. Akhperjanian, A. R. Bazer-Bachi, et al. 2007, ApJ, 664, L71

[Aharonian (2008a)] Aharonian et al., A&A, 483, 509, (2008)

[Aharonian (2008b)] Aharonian, F. et al., A&A 490 p685-693 (2008)

[Aharonian (2009)] Aharonian F. A. et al. 2009b, ApJ Letters 695, L40

[Aharonian (2012)] Aharonian, F., Khangulyan, D., Malyshev D.: 2012, arXiv:1207.0458v1 [astro-ph.HE]

[Alexic (2010)] Aleksic J. et al. 2010b, ApJ Letters 723, 207

[Alexic (2012)] Aleksic J. et al. 2012, A&A Letters 539, 2

[Amano et al. (2014)] Takanobu Amano, Kazufumi Torii, Takahiro Hayakawa, Yasuo Fukui, 2014, Stochastic Acceleration of Cosmic Rays in the Central Molecular Zone of the Galaxy, accepted by PASJ Letters, arXiv:1110.3140 [astro-ph.HE]

[Anderhub (2013)] H. Anderhub et al., 2013, astro-ph/1304.1710

[ATNF Pulsar Database] http://www.atnf.csiro.au/research/pulsar/psrcat/ , Manchester, R. N., Hobbs, G. B., Teoh, A. & Hobbs, M., AJ, 129, 1993-2006 (2005)

[Atwood (2009)] W. B. Atwood et al. (Fermi-LAT Collaboration), ApJ 697, 1071 (2009), arXiv:0902.1089 [astro-ph.IM]

[Baade & Zwicky (1934)] Baade W., Zwicky F., 1934, Proceedings of the National Academy of Science, 20, 259

[Barnacka (2013)] Anna Barnacka, Ph.D thesis, Detection techniques for the H.E.S.S. II telescope, data modeling of gravitational lensing and emission of blazars in HE-VHE astronomy

[Berge (2006)] Berge, D. 2006, PhD thesis, Heidelberg University

[Berge & Funk & Hinton (2007)] D.Berge, S.Funk, J.Hinton, Background Modelling in Very-High-Energy gamma-ray Astronomy, Astron.Astrophys.466:1219-1229,2007

[Bergin (2004)] Bergin, E.A., Hartmann, L.W., Raymond, J.C., Ballesteros-Paredes, J., 2004, ApJ, 612, 921

[Bernlöhr (2000)] Bernlöhr, K., Monte Carlo images of air showers, http://www.mpi-hd.mpg.de/hfm/ bernlohr/HESS/

[Bernlöhr (2003)] K. Bernlöhr, O. Carrol, R. Cornils, et al. The optical system of the H.E.S.S. imaging atmospheric Cherenkov telescopes. Part I: layout and components of the system. Astropart. Phys., 20:111128, Nov. (2003)

[Bernlöhr (2008)] K. Bernlöhr. Simulation of imaging atmospheric Cherenkov telescopes with CORSIKA and simtelarray. Astroparticle Physics, 30, (2008).

[Bethe (1953)] H.A. Bethe, Moliere's Theory of Multiple Scattering, Phys. Rev. 89, 1256, 1953

[Blake (1987)] Blake et al. , ApJ, 315, 621 (1987)

[Blitz (1981)] Blitz, L., Shu, F. H., Astrophysical Journal, Part 1, vol. 238, May 15, 1980, p. 148-157

[Blumenthal & Gould (1970)] Blumenthal & Gould 1970, Rev. Mod. Phys., 42, 237

[Bolmont (2014)] Bolmont, J. et al. Nucl.Instrum.Meth. A761 (2014) 46-57 arXiv:1310.5877 [astro-ph.IM]

[Bolz (2004)] Bolz, O., PhD thesis, Heidelberg University (2004).

[Bothe & Kolhörster (1929)] W. Bothe and Kolhörster, W. Zeitschrift für Physik, 56:751, 1929.

[Böttcher & Reimer (2004)] Böttcher & Reimer et al. A. 2004, ApJ, 609, 576

[Burrows et al. (2000)] Burrows, D.N., et al. 2000, Proc., SPIE, 4140, 64

[Burrows et al. (2005)] David N. Burrows et al., SpaceSci.Rev.120:165,2005

[Burton & Gordon (1978)] Burton, W. B. & Gordon, M. A., A&A, 63, 7, (1978)

[Carrigan et al. (2007)] S. Carrigan, J.A. Hinton, W. Hofmann, K. Kosack, T. Lohse, O. Reimer, for the H.E.S.S. Collaboration, Proceedings of the 30th ICRC, Merida, Mexico

[Carrigan et al. (2013)] S. Carrigan, F. Brun, R.C.G. Chaves, C. Deil, A. Donath, H. Gast, V. Marandon, M. Renaud, for the H.E.S.S. collaboration, 33rd International Cosmic Ray Conference, Rio De Janeiro 2013

[Casanova (2010)] Casanova, S. et al., Publ. Astron. Soc. Japan 62, pp.769-777 (2010)

[Castellina (2012)] Castellina, Antonella; Donato, Fiorenza (2012). Oswalt, T.D McLean, I.S.; Bond, H.E.; French, L.; Kalas, P.; Barstow, M.; Gilmore,G.F.; Keel, W., ed. Planets, Stars, and Stellar Systems (1 ed.). Springer. ISBN 978-90-481-8817-8.

[Caswell (1998)] J.L.Caswell, MNRAS, 297 (1): 215-235. doi: 10.1046/j.1365-8711.1998.01468.x

[Chaves et al.(2009)] Tibolla,O.,Chaves,R.C.G.,deJager,O.,Domainko,W.,Fiasson,A.,Komin,N.,Kosack,K arXiv:0907.0574

[Chia-Chun Lu et al. (2013)] Chia-Chun Lu, Proceedings of the 33rd International Cosmic Ray Conference (ICRC2013), Rio de Janeiro (Brazil)

[Chiozzi, et al. (2004)] G. Chiozzi, et al., The ALMA Common software: a developer friendly CORBA based framework, SPIE Procs. 5496- 23 (2004).

[Clemens (1985)] D.P. Clemens, ApJ, 295, 422, (1985)

[Clifton & Lyne (1986)] T.R.Clifton & A.G.Lyne, Nature, 320, 43 (1986)

[CTA Consortium Home Page] https://portal.cta-observatory.org/Pages/Home.aspx

[CTA Consortium (2010)] CTA Consortium, "Design Concepts for the Cherenkov Telescope Array", arXiv:1008.3703, 2010.

[CTA Consortium (2011)] Experimental Astronomy (2011) 32:193-316, Design Concepts for the Cherenkov Telescope Array, The CTA Consortium (2011)

[Cutri et al. (2003)] 2MASS All Sky Catalog of point sources. CDS/ADC Collection of Electronic Catalogues, 2246, 0 (2003)

[Dame (2001)] T.Dame et al., ApJ, 547, 792 (2001)

[Daum (1997)] A. Daum et al.,First results on the performance of the HEGRA IACT array. Astroparticle Physics, 8:111, December 1997. doi: 10.1016/S0927-6505(97)00031-5.

[Daniel et al. (2004)] Schwartz, Daniel A., "The Development and Scientific Impact of the Chandra X-Ray Observatory". International Journal of Modern Physics D 13, 7

[Davies-Cotton (1957)] Davies J. M., Cotton E. S., 1957, Design of the quartermaster solar furnace J. Solar Energy Sci. and Eng. 1 16

[Davis et al. (2011)] Davis E. et al., 2011, Mechanical design of a medium-size telescope for CTA, CTA internal notes

[Deleglise (2013)] G. Deleglise, N. Geffroy, G. Lamanna for the CTA Consortium, Large Size Telescope camera support structures for the Cherenkov Telescope Array, arXiv:1307.4565

[Dermer (1986)] Dermer, C.D.:, Astron. Astrophys. 157, 223. (1986)

[Dermer (2009)] C. D. Dermer and G. Menon 2009, High Energy Radiation from Black Holes (Princeton University Press)

[Di Francesco (2006)] Di Francesco, J., et al. "An Observational Perspective of Low-Mass Dense Cores I: Internal Physical and Chemical Properties". Protostars and Planets V. (2006)

[Dickman (1978)] Dickman, R. L.: 1978, ApJS 37, 407

[Djannati-Atai et al. (2007)] H.E.S.S. collaboration, A. Djannati-Atai et al. , Proc. 30th International Cosmic Ray Conference, Merida, 2007, arXiv:0710.2247

[Doll (1990)] P. Doll, J. Engler, P. Gabriel, et al. Nuclear Physics B, 14:336, (1990).

[Doro (2012)] Doro et al., Astroparticle Physics 43 (2013) 189-214

[Drury et al. (1994)] L.O'C. Drury, F.A. Aharonian, H.J. Völk, 1994, A&A, 287,959-971

[Dunham (1937)] Dunham T. 1937. Publ. Astron. Soc. Pac. 49:2628

[Dyson & Williams (1980)] Dyson, J. E. & Williams, D. A., 1980, Physics of the Interstellar Medium (New York: Halsted Press)

[Egberts (2014)] Egberts K. et al. Diffuse γ-Ray Emission from H.E.S.S. Galactic Plane Survey Observations, Paper in preparation

[Eger et al. (2010)] P. Eger, G. Rowell, A. Kawamura, Y. Fukui, L. Rolland, C. Stegmann, A multi-wavelength study of the unidentified TeV gamma-ray source HESS J1626-490, doi:10.7529/ICRC2011/V07/0035 (2010)

[Eidelman (2004)] Eidelman et al. Particle Data Booklet. Physics Letters B, 592, (2004).

[Eidemüller (2002)] D. Eidenmüller. Hadron suppression using a cluster finder algorithm for the H.E.S.S. telescope system., Diploma Thesis, HU Berlin, 2002.

[Engel (2011)] Engel et al. Extensive air showers and hadronic interactions at high energy. Annual Review of Astronomy and Astrophysics, 61, (2011).

[Etten et al. (2009)] Adam Van Etten, Stefan Funk and Jim Hinton A Multi-wavelenght investigation of the unidentified gamma-ray source HESS J1708410, 2009 ApJ 707 1717 doi:10.1088/0004-637X/707/2/1717

[Ewen (1951)] H.I. Ewen, E.M. Purcell, Nature 168, 356 (1951)

[Fermi Collaboration (2013)] Fermi-LAT Collaboration: 2013, Phys. Rev. B 88, 082002

[Finkbeiner (2012a)] Finkbeiner, D.P., Su, M., Weniger, C.: 2012, arXiv:1209.4562v1 [astro-ph.HE]

[Finkbeiner (2012b)] Finkbeiner, D.P., Su, arXiv:1206.1616v2 [astro-ph.HE] (2012)

[Fletcher (1994)] R.S. Fletcher, T.K. Gaisser, P.Lipardi and T. Stanev, Phys. Rev. D50, 5710, 1994

[Foreman-Mackey et al. (2013)] Foreman-Mackey, D., Hogg, D.W., Lang, D., & Goodman, J. 2013, PASP, 125, 306, (2013)

[Föster, et al. (2012)] A. Föster, et al. "Mirror Development for CTA". Proc of the 32nd International Cosmic Ray Conference, Beijing, China, 2011.

[Frail et al. (1996)] Frail D.A. et al. 1996, AJ, 111, 1651F

[Freeman (2001)] Freeman, P., Doe, S., & Siemiginowska, A. 2001, Proc. SPIE, 4477, 76

[Funk (2004)] S. Funk, G. Hermann, J. Hinton, et al. The trigger system of the H.E.S.S. telescope array. Astropart. Phys., 22:285296, (2004).

[Funk (2005)] S. Funk, Ph.D. Thesis, A new population of very high-energy γ-ray sources detected with H.E.S.S. in the inner part of the Milky Way. (2005)

[Gabici (2012)] S.Gabici et al., Gamma-ray signatures of cosmic ray acceleration, propagation, and confinement in the era of CTA, arXiv:1209.0582 [astro-ph.HE] , 2012

[Ginzburg & Sryovatski (1967)] Ginzburg V. L., Syrovatskij S. I., 1967, in van Woerden H., ed., IAU Symposium Vol. 31, Radio Astronomy and the Galactic System. p. 411

[Glover (2010)] S. C. O. Glover, M. M. Mac Low, On the Relationship Between Molecular Hydrogen and Carbon Monoxide Abundances in Molecular Clouds, arXiv:1003.1340 (2010)

[Goldreich et al. (1976)] Goldreich, P., Scoville, N. (1976). "OH-IR stars. I - Physical properties of circumstellar envelopes". Astrophysical Journal 205: 144. DOI:10.1086/154257

[Goldsmith & Li (2007)] Goldsmith, P. F. & Li, D., Krco, M., ApJ, 654, 273, (2007)

[H.E.S.S. Collaboration (2005)] H.E.S.S. collaboration, F. Aharonian et al., Astron. Astrophys. 437 (2005) L7-L10

[H.E.S.S. Collaboration (2008a)] H.E.S.S. Collaboration, Energy spectrum of cosmic-ray electrons at TeV energies. Phys. Rev. Lett., 101, (2008).

[H.E.S.S. Collaboration (2008b)] H.E.S.S. collaboration, F. Aharonian et al., Discovery of very high energy gamma-ray emission coincident with molecular clouds in the W28 (G6.4-0.1) field, DOI: 10.1051/0004-6361:20077765

[Hansen et al. (1997)] B. M. S. Hansen , E. S. Phinney, Mon.Not.Roy.Astron.Soc. 291 (1997) 569

[Hauser & Dwek (2001)] Hauser M. & Dwek E. 2001, ARAA 39, 249

[Heck (1998)] D. Heck, J. Knapp, J. Capdevielle, et al. Corsika: A monte carlo code to simulate extensive air showers, thech. report,forschungszentrum, wissenschaftliche berichte, 1998. FZKA 6019 (1998).

[Heitler (1954)] W. Heitler. The Quantum Theory of Radiation. Oxford University Press, 3st edition, (1954).

[Herman et al. (1985)] Herman, J., Habing, H.J., 1985, A&A, Supplement Series, v. 59(3) p. 523-555; ISSN 0365-0138

[Hess (1912)] V. Hess. Physikalische Zeitschrift, 13:1084, 1912.

[Hillas (1985)] A. M. Hillas. Cerenkov light images of EAS produced by primary gamma. In F. C. Jones, editor, International Cosmic Ray Conference, volume 3 of International Cosmic Ray Conference, (1985).

[Hillenbrand (1993)] Hillenbrand, Lynne A.; Massey, Philip; Strom, Stephen E.; Merrill, K. Michael, Astronomical Journal (ISSN 0004-6256), vol. 106, no. 5, p. 1906-1946 (1993)

[Hinton & Hoffman (2009)] J. A. Hinton and W. Hofmann, Ann. Rev. Astron. & Astroph. 47 (2009) 523-565

[Hirayama (2005)] Hirayama et al. The EGS5 Code System. SLAC Report, SLAC-R-730, (2005).

[Höcker (2007)] Höcker, A., et al. , TMVA - Toolkit for Multivariate Data Analysis, [physics/0703039v4], 2007

[Huang (2003)] Proceedings of the 28th International Cosmic Ray Conference. July 31-August 7, 2003. Trukuba, Japan. Under the auspices of the International Union of Pure and Applied Physics (IUPAP). Editors: T. Kajita, Y. Asaoka, A. Kawachi, Y. Matsubara and M. Sasaki, p.2297

[Jackson (2004)] Jackson, J. M., Simon, R., Shah, R. Y., Rathborne, J. M., Heyer, M. H., Clemens, D. P., & Bania, T. M., in ASP Conf. Ser. 317 Milky Way Surveys: The Structure and Evolution of our Galaxy, ed. Clemens, D. P., Shah, R. Y., & Brainerd, T. G. (San Francisco: ASP), 49, (2004)

[Janssen (2006)] Janssen, G. H. & Stappers, B. W., 2006. 30 glitches in slow pulsars. A&A, 457, 611-618.

[Jelley (1958)] J.V. Jelley. Cerenkov Radiation and its Applications, chapter 9. Pergamon Press, Inc, (1958).

[Kalmykov (1997)] N.N. Kalmykov, S.S. Ostapchenkp, A.I. Pavlov, Nucl. Phys. Proc. Suppl. B52, 17, 1997

[Karachentsev (2006)] I. D. Karachentsev, Yu. N. Kudrya, V. E. Karachentseva, S. N. Mitronova, Astrophysics October 2006, Volume 49, Issue 4, pp 450-461

[Kaspi (1981)] Kaspi V.M., Lyne A.G., Manchester R.N., et al. 1993, ApJ 409, L57

[Kelner et al. (2006)] Kelner, S.R., Aharonian F. A. & Bugayov, V.V., 2006, Phys ReV D 74, 034018

[Kennel & Coroniti (1984)] Kennel, C. F. & Coroniti, F. V. 1984, ApJ, 283, 710

[Khangulyan et al. (2014)] Khangulyan, D., Aharonian, F. A., Kelner, S. R., The Astrophysical Journal, Volume 783, Issue 2, article id. 100, 11 pp. (2014)

[Klein & Nishina (1929)] Klein, O; Nishina, Y (1929). "Über die Streuung von Strahlung durch freie Elektronen nach der neuen relativistischen Quantendynamik von Dirac". Z. Phys. 52 (11-12): 853 and 869.

[Komin (2005)] N. Komin, Ph.D. Thesis, Detection of Gamma Rays from the Supernova Remnant RX J0852.0-4622 with H.E.S.S. (2005)

[Kothes-Doughterty et al. (2007)] A&A 468, 9931000 (2007), R. Kothes, S.M. Dougherty

[Koyama et al. (2007)] Koyama, K., et al. 2007, PASJ, 59, S23

[Kulkarni (1982)] Kulkarni, S. R., Blitz, L., Heiles, C., ApJ, 259, L63 (1982)

[Langer & Penzias 1990] Langer, W. D. & Penzias, A.A., ApJ, 357, 477 (1990)

[Lemoine-Goumard (2006)] Lemoine-Goumard, M., Degrange, B., Tluczykont, M., 2006, Astropart. Phys., 25, 195

[Leroy (2003)] Leroy et al., Calibration results for the first two H.E.S.S. array telescopes. In: Proc. 28th ICRC, Tsukuba, p. 2895. Univ. Academy Press, Tokyo, (2003).

[Li & Ma (1983)] T.-P. Li and Y.-Q. Ma. Analysis methods for results in gamma-ray astronomy. ApJ, 272:317324, Sept. 1983.

[Longair (1983)] Laing, RA; Riley, JM; Longair, MS (1983). "Bright radio sources at 178 MHz - Flux densities, optical identifications and the cosmological evolution of powerful radio galaxies". Monthly Notices of the Royal Astronomical Society 204: 151. Bibcode:1983MNRAS.204..151L. doi:10.1093/mnras/204.1.151.

[Longair (1992)] Longair, M.S. High Energy Astrophysics, vol 1. Cambridge University Press., 1992.

[Longair (2011)] M. Longair. High Energy Astrophysics. Cambridge University Press, 3rd edition, (2011)

[Lozinskaya (1981)] Lozinskaya T.A. 1981 Sov. Astron. Lett. 7, 17

[MacKey (2003)] Information Theory, Inference, and Learning Algorithms, ISBN: 9780521642989, 2003

[Mattana et al. (2009)] F. Mattana, M. Falanga, D. Götz, R. Terrier, P. Esposito, A. Pellizzoni, A. De Luca, V. Marandon, A. Goldwurm, P. Caraveo, Astrophys.J.694:12-17, 2009

[Maxted et al. (2013)] Nigel I. Maxted, Gavin P. Rowell, Bruce R. Dawson, Michael G. Burton, Yasuo Fukui, Andrew Walsh, Akiko Kawamura, Hirotaka Horachi, Hidetoshi Sano, Satoshi Yoshiike, Tatsuya Fukuda, DOI: 10.1093/mnras/stt1159 (2013)

[McClure-Griffiths (2009)] McClure-Griffiths et al., arXiv:0901.1159 [astro-ph.GA] (2009) GASS: The Parkes Galactic All-Sky Survey. I. Survey Description, Goals, and Initial Data Release

[McClure-Griffiths et al. (2009)] N. M. McClure-Griffiths, D. J. Pisano, M. R. Calabretta, H. A. Ford, F. J. Lockman, L. Staveley-Smith, P. M. W. Kalberla, J. Bailin, L. Dedes, S. Janowiecki, B. K. Gibson, T. Murphy, H. Nakanishi, K. Newton-McGee, Astrophys.J.Suppl.181:398-412 , 2009

[Mitsuda et al. (2007)] K. Mitsuda et al., Publ. Astron. Soc. Japan 59, S1-S7, 2007 January 25

[Mizukami et al. (2009)] T. Mizukami et al. CANGAROO-III Observations of HESS J1614−518, ICRC Proocedings (2009)

[Moderski et al. (2005)] R. Moderski, M. Sikora, P.S. Coppi, F. Aharonian, Mon. Not. R. Astron. Soc. 363, 954966 (2005) doi:10.1111/j.1365-2966.2005.09494.x

[Moderski (2013)] R. Moderski et al. (CTA Cons.), ICRC 2013 proc. 0840

[Monnier et al. (1999)] Monnier, J.D., Tuthill, P.G., Danchi, W.C., 1999, ApJ, 525, L97

[Mori (1997)] Mori M., ApJ, 307, 47, (1997)

[Morris (2002)] D.J. Morris et al., MNRAS, 335, 275 (2002)

[Mücke (2003)] Mücke, A. et al. 2003, Astropart. Phys., 18, 593

[Nakanishi et al. (2003)] H. Nakanishi and Y. Sofue, Publ. Astron. Soc. Japan 55, 191202, 2003

[NASA (2012)] NASA, Goddard Space Flight Center. Retrieved 31 October 2012.

[Naurois (2003)] de Naurois, M., et al. 2003, Proc. of 28th ICRC (Tsubaka), Vol .5, p.2907

[Naurois (2009)] Mathieu de Naurois, Loic Rolland (2009), A high performance likelihood reconstruction of gamma-rays for Imaging Atmospheric Cherenkov Telescopes, DOI: 10.1016/j.astropartphys.2009.09.001

[Nedbal (2008)] Discovery of VHE gamma-rays from the high-frequency-peaked BL Lac object RGB J0152+017, H.E.S.S. collaboration, F. Aharonian et al., arXiv:0802.4021

[Ohm (2009)] S. Ohm, C. van Eldik & K. Egberts, γ/hadron separation in very-high-energy γ-ray astronomy using a multivariate analysis method, Astroparticle Physics, 31 (2009), pp. 383391

[Oya et al. (2012)] Oya et al., 2012, International Conference on Computing in High Energy and Nuclear Physics 2012 (CHEP2012) IOP Publishing Journal of Physics: Conference Series 396 (2012) 012037 doi:10.1088/1742-6596/396/1/012037

[Pareschi (2013)] G. Pareschi et al. (CTA Cons.), ICRC 2013 proc. 0466

[Particle Data Group (2014)] K.A. Olive et al. Particle Data Group, Chin. Phys. C, 38, 090001, 2014

[Perades et al. (2013)] J.M. Paredes, C. H. Ishwara-Chandra, V. Bosch-Ramon, V. Zabalza, K. Iwasawa, M. Ribo, Deep GMRT radio observations and a multi-wavelength study of the region around HESS J1858+020, Accepted for publication in A&A, arXiv:1312.3752

[Persic (2013)] M. Persic, Nucl. Phys. B 239 (2013) 210-215

[Piron et al. (2001)] Piron, F., Djannati-Atai, A., Punch, M., et al. 2001, A&A, 374, 895

[Planck Collaboration (2013)] Planck Collaboration, Planck 2013 results. I. Overview of products and scientific results, DOI: 10.1051/0004-6361/201321529, arXiv:1303.5062

[Profumo (2012)] Profumo, S., Linden, T.: 2012, JCAP07, 011

[Prokoph (2009)] H. Prokoph, Diploma Thesis, Leipzig University, Investigations on gamma-hadron separation for imaging Cherenkov telescopes exploiting the time development of particle cascades, (2009)

[Ramana (1993)] Ramana Murthy, P.V. and Wolfendale, A.V. Gamma-Ray Astronomy. Cambridge University Press., 1993.

[Raue (2010)] M. Raue and D. Mazin 2010, APh, 34, 245

[Roman-Duval (2009)] Kinematic Distances to Molecular Clouds identified in the Galactic Ring Survey, Roman-Duval et al., ApJ 699:1153-1170, (2009)

[Rubio (1993)] Rubio, M., Lequeux, J., & Boulanger, F. 1993, A&A, 271, 9

[Sana (2009)] H. Sana, E. Gosset, C.J. Evans, The massive star binary fraction in young open clusters - II. NGC 6611 (Eagle Nebula), arXiv:0909.0486 (2009)

[Scoville & Solomon (1978)] Scoville, N. Z., & Solomon, P. M., ApJ, 220, L103 (1978)

[Serlemitsos et al. (2007)] Serlemitsos, P., et al. 2007, PASJ, 59, S9

[Shahinyan et al. (2015)] K. Shahinyan et al., VERITAS Observations of the Unidentified Point Source HESS J1943+213, 2014 Fermi Symposium proceedings - eConf C14102.1, arXiv:1502.03016

[Shettys et al. (2011)] Rahul Shetty, Simon C. Glover, Cornelis P. Dullemond, Eve C. Ostriker, Andrew I. Harris, Ralf S. Klessen, Monthly Notices of the Royal Astronomical Society. 2011; 415(4):3253 - 3274. DOI: 10.1111/j.1365-2966.2011.18937.x

[Simpson (1983)] Simpson J.A., 1983 Ann. Rev. Nuc. Part. Phys. 33, 323

[Skrutskie et al. (2006)] The Two Micron All Sky Survey (2MASS), M.F. Skrutskie, R.M. Cutri, R. Stiening, M.D. Weinberg, S. Schneider, J.M. Carpenter, C. Beichman, R. Capps, T. Chester, J. Elias, J. Huchra, J. Liebert, C. Lonsdale, D.G. Monet, S. Price, P. Seitzer, T. Jarrett, J.D. Kirkpatrick, J. Gizis, E. Howard, T. Evans, J. Fowler, L. Fullmer, R. Hurt, R. Light, E.L. Kopan, K.A. Marsh, H.L. McCallon, R. Tam, S. Van Dyk, and S. Wheelock, 2006, AJ, 131, 1163.

[Slane et al. (2006)] B.M. Gaensler, P.O. Slane, Ann.Rev.Astron.Astrophys.44:17-47,2006, DOI: 10.1146/annurev.astro.44.051905.092528

[Snyder & Buhl (1974)] Snyder, L. E., & Buhl, D., ApJ, 189, L31 (1974)

[SPLATALOGUE] http://www.cv.nrao.edu/php/splat/advanced.php

[Stahler (2004)] Stahler S., Palla F., 2004, The Formation of Stars. Wiley

[Strong (2007)] Strong, A. W., Moskalenko, I. V., & Ptuskin, V. S. 2007, Annu. Rev. Nucl. Part. Sci., 57, 285

[Swings (1938)] Swings P, Rosenfeld L. 1937. Ap. J. 86:48386

[Tacconi (1986)] Tacconi, L. J. & Young, J. S. Astrophysical Journal, Part 1 (ISSN 0004-637X), vol. 308, Sept. 15, 1986, p. 600-610.

[Taylor (1993)] Taylor, J. H. & Cordes, J. M., 1993. Pulsar Distances and the Galactic Distribution of Free Electrons. ApJ, 411, 674-684.

[Tempel (2012a)] Tempel, E., Hektor, A., Raidal, M.: 2012, JCAP 09, 032

[Tempel (2012b)] Hektor, A., Raidal, M., Tempel, E.: arXiv:1207.4466v3 [astroph.HE]

[Tempel (2012c)] Hektor, A., Raidal, M., Tempel, E.: 2012, arXiv:1209.4548v1[astroph.HE]

[Tempel (2012d)] Tempel, E., Hektor, A., Raidal, JCAP 1209 (2012) 032

[Tibolla et al.(2008)] O.Tibolla et al., AIP Conf. Proc. 1085, 249 (2008); doi: 10.1063/1.3076652, A new source discovered close to the Galactic Center: HESS J1741-302

[Uchiyama et al. (2011)] Uchiyama, H., Koyama, K., Tibolla, O., Matsumoto, H., Kaufmann, S., Wagner, S. "No X-ray excess from the HESS J1741-302 region, except for a new intermediate polar candidate" PASJ, 63, S865 (2011)

[Van De Hulst (1982)] Van De Hulst H.C. 1973 Op. Cit. Sulivan W. T. III (1982)

[Vassiliev (2007)] V. Vassiliev et al. 2007, Astropart. Phys. 28, 10

[Vincent (2003)] P. Vincent, J.-P. Denanca, J.-F. Huppert, and H.E.S.S. collaboration. Performance of the H.E.S.S. Cameras. In International Cosmic Ray Conference, volume 5 of International Cosmic Ray Conference, page 2887, (2003).

[Voelk (2009)] Heinrich J. Voelk, Bernlöhr, K., Imaging Very High Energy Gamma-Ray Telescopes, Exper.Astron. 25 (2009) 173-191

[Weekes (1989)] Weekes, T.C., et al. Observation of TeV gamma rays from the Crab nebula using the atmospheric Cerenkov imaging technique. ApJ, 342:379395, 1989.

[Weekes (2003)] T.C. Weekes. Very High Energy Gamma-Ray Astronomy. Institute of Physics Publishing, (2003).

[Weinreb (1963)] S. Weinreb, A.H. Barrett, M.L. Meeks, J.C. Henry, Nature 200, 829 (1963)

[Weniger (2012)] Weniger, C.: 2012, JCAP 1208, 007

[Wilson (2009)] Tools of Radio Astronomy Thomas L. Wilson, Kristen Rohlfs, Susanne Hüttemeister, ISBN: 978-3-540-85121-9, DOI 10.1007/978-3-540-85122-6, Astronomy and Astrophysics Library ISSN: 0941-7834

[Wouterloot et al. (1989)] Wouterloot, J.G.A., Brand, J., 1989, A&AS, 80, 149

[Wrootten-Thomson et al.(2009)] Wootten A. and Thomson A. R., 2009 The Atacama Large Millimeter/submillimeter Array IEEE Proc. 97 1463